BOUNDARY ELECTRON AND BETA DOSIMETRY - QUANTIFICATION OF THE EFFECTS OF DISSIMILAR MEDIA ON ABSORBED DOSE

By

Josane C. Nunes, M.Sc.

A Thesis
Submitted to the School of Graduate Studies
in Partial Fulfilment of the Requirements for the Degree
Doctor of Philosophy

McMaster University

BOUNDARY ELECTRON AND BETA DOSIMETRY

DOCTOR OF PHILOSOPHY (1992) McMaster University
(Physics) Hamilton, Ontario.

TITLE: Boundary Electron and Beta Dosimetry - Quantification of the Effects of Dissimilar Media on Absorbed Dose.

AUTHOR: Josane C. Nunes, B.Sc. (York University)
M.Sc. (McMaster University)

SUPERVISOR: Professor W. V. Prestwich

NUMBER OF PAGES: xxii, 267.

DOCTOR OF PHILOSOPHY (1992) McMaster University
(Physics) Hamilton, Ontario.

TITLE: Boundary Electron and Beta Dosimetry - Quantification of the Effects of Dissimilar Media on Absorbed Dose.

AUTHOR: Josane C. Nunes, B.Sc. (York University)
M.Sc. (McMaster University)

SUPERVISOR: Professor W. V. Prestwich

NUMBER OF PAGES: xxii, 267.

ABSTRACT

This work quantifies the changes effected in electron absorbed dose to a soft-tissue equivalent medium when part of this medium is replaced by a material that is not soft-tissue equivalent. That is, heterogeneous dosimetry is addressed.

Radionuclides which emit beta particles are the electron sources of primary interest. They are used in brachytherapy and in nuclear medicine; for example, beta-ray applicators made with strontium-90 are employed in certain ophthalmic treatments and iodine-131 is used to test thyroid function. More recent medical procedures under development and which involve beta radionuclides include radioimmunotherapy and radiation synovectomy; the first is a cancer modality and the second deals with the treatment of rheumatoid arthritis. In addition, the possibility of skin surface contamination exists whenever there is handling of radioactive material.

Determination of absorbed doses in the examples of the preceding paragraph requires considering boundaries or interfaces. Whilst the Monte Carlo method can be applied to boundary calculations, for routine work such as in clinical situations, or in other circumstances where doses need to be determined quickly, analytical dosimetry would be invaluable.

Unfortunately, few analytical methods for boundary beta dosimetry exist. Furthermore, the accuracy of results from both Monte Carlo and analytical methods has to be assessed.

Although restricted to one radionuclide, phosphorus-32, the experimental data obtained in this work serve several purposes, one of which is to provide standards against which calculated results can be tested. The experimental data also contribute to the relatively sparse set of published boundary dosimetry data. At the same time, they may be useful in developing analytical boundary dosimetry methodology.

The first application of the experimental data is demonstrated. Results from

two Monte Carlo codes and two analytical methods, which were developed elsewhere, are compared with experimental data.

Monte Carlo results compare satisfactorily with experimental results for the boundaries considered. The agreement with experimental results for air interfaces is of particular interest because of discrepancies reported previously by another investigator who used data obtained from a different experimental technique.

Results from one of the analytical methods differ significantly from the experimental data obtained here. The second analytical method provides data which approximate experimental results to within 30%. This is encouraging but it remains to be determined whether this method performs equally well for other source energies.

ACKNOWLEDGEMENTS

I would like to thank the members of my supervisory committee for their roles in overseeing this project, and the Physics Department for its financial support.

There are a number of people whose expertise and assistance have helped to establish a workable, safe and efficient experimental system. A special thanks to Gino Innocente of the Machine Shop in ABB for his sound advice concerning materials and design of several pieces of equipment.

I am grateful for the diligence of the Health Physics Department with regard to radiation protection; suggestions and assistance given willingly and good-naturedly over the years by Heinz Schlichting, Steve Staniek and Dr. J. Harvey have been greatly appreciated.

I am also indebted to Kenrick Chin for his help in implementing the word-processing system used for this document and in developing and maintaining equipment used in the experiments. It is a pleasure to acknowledge his technical wizardry.

Computer Information Services, C. I. S., have been a valuable resource with regard to using the VAX system at McMaster. I am particularly appreciative of the assistance given on numerous occasions by Dr. F. Kus.

Beginning with the cordial welcome with which he introduced me to McMaster, Dr. C. Webber has been a longstanding source of encouragement. I am grateful for his continued interest.

Most especially, I would like to thank my supervisor, Dr. Prestwich, for his guidance and help in all aspects of this project. Besides benefitting from his scholarly wisdom, I have learnt from the superb example that he sets; his enthusiasm for research and understanding, together with his kindness, are inspirational. I have been fortunate to have had this opportunity.

It is also with deep gratitude that I acknowledge the support of my sister, Ligia, and my parents. Their encouragement has kept me afloat when I have been caught in the undertow of this effort.

TABLE OF CONTENTS

PART I. INTRODUCTION

PART II. METHODOLOGY AND RESULTS

PART III. DISCUSSION AND CONCLUSIONS

LIST OF ILLUSTRATIONS

LIST OF TABLES

Table Page

PART I. INTRODUCTION

CHAPTER 1

INTRODUCTION

Radiation is energy, in the form of electromagnetic waves or charged particles, in transit. It is an intrinsic part of the earth's environment and therefore comes into contact with matter, both animate and inanimate. Consequently, it is of interest to understand how radiation interacts with matter and what the effects of these interactions are.

There are two types of radiation, ionizing and non-ionizing. Examples of the latter include microwaves, radiowaves, alternating current power, visible light and some ultra-violet light. Examples of ionizing radiation are neutrons, X-rays, gamma rays, alpha particles, energetic electrons and other charged particles.

Ionizing radiation is characterized by localized release of large amounts of energy (about 33eV), which can break chemical bonds. This harbours the potential for causing damage to the material exposed to such radiation. In living systems, there are two routes for biological damage - (i) direct breakage of chemical bonds in a critical target; (ii) creation of free radicals, such as $OH^{\cdot}$, which can in turn cause chemical and biological damage.

It is becoming increasingly commonplace for people and machinery to be exposed to ionizing radiation. This is attributed largely to technological advances; for example, space travel places equipment in the paths of fast charged particles; also, television sets, smoke detectors, nuclear reactors are sources of ionizing radiation; and medical diagnoses and treatments make use of X-rays, radioactive nuclides, fast electrons and other charged particles. Therefore, it is incumbent on us to study the interactions of ionizing radiation with matter in order to assess their beneficial and detrimental effects.

This work focuses on electron interactions with matter. These interactions are pervasive for they are initiated not only by incoming electrons but also by

indirectly ionizing radiation such as X-rays and gamma rays which, in the course of their interactions, produce energetic electrons that ultimately deposit energy in the medium.

Energy deposited is one parameter that is quantitated in the investigation of electron interactions with matter. In this work, a beta-emitting radioisotope is used as an electron source to study the energy deposition of electrons near the boundaries between different materials.

1.1 Beta Dosimetry

Beta dosimetry refers to methods used to quantitate absorbed doses due to radioactive beta sources. These methods include calculations or measurements or both, and they determine the energy deposited per unit mass of absorbing material. Results from beta dosimetry are used in areas such as radiation therapy, radiation protection and radiation biology.

In the context of dosimetry, absorbed dose refers to energy deposition in regions of super-cellular, as opposed to sub-cellular, dimensions. This is one feature which distinguishes the fields of dosimetry and microdosimetry. Despite similar nomenclature, they are inherently distinct because, whereas dosimetry solely quantitates the average energy deposited, microdosimetry deals with not only how energy is deposited in specific biological sites, but also how this energy deposition correlates with radiobiological effects. The present work does not include microdosimetry.

1.1.2 Overview of some of the work done in the experimental and analytical aspects of beta dosimetry

For purposes of clarity, this account addresses homogeneous and heterogeneous (or interface) beta dosimetry separately, and in that order. The term experimental beta dosimetry is self-explanatory; the meaning conferred upon analytical beta dosimetry is taken from Sherbini and Porter (Sherbini and Porter 1983).

Analytical beta dosimetry is the determination of absorbed doses from a given source geometry using calculations. It consists of empirical and theoretical methods. The former rely on experimental measurements and do not investigate thoroughly the underlying theory; the latter make use of physical principles to formulate theories from which, mathematical models, used to calculate absorbed

doses, are developed. (Sherbini and Porter 1983)

Early experiments which measured absorbed doses in a single medium include the works of Failla in the 1930's and 1960's, and Loevinger, Clark, Brar and Marinelli in the 1950's. Several experiments were done by Cross in the late 1960's.

One of Failla's major contributions was the invention of an extrapolation chamber, a detector which could be used to measure energy deposited by electrons in a medium. (Failla 1937) A most noteworthy characteristic of this detector was that it did not appreciably disturb the electrons which were depositing energy in the medium, and it could therefore accurately measure absolute ionization currents. Descendants of Failla's original chamber continue to be used in beta dosimetry today.

The dosimetry of uniformly distributed beta sources in infinite media was well-established by the 1950's. At this time, attention turned towards the dosimetry of small and non-uniform sources. Pioneering experiments with beta point sources in air were done by groups in Germany, England and America during the 1950's (Loevinger 1956) and later by Failla in 1960 (Cross 1967). In 1955, a group in America published results for the distribution of energy absorption in air around beta point sources such as Phosphorus-32 and Thallium-204 (Clark, Brar and Marinelli 1955). During this decade, Loevinger also measured energy absorption from plane beta sources (Loevinger 1950; Loevinger 1954). He constructed an extrapolation chamber for making some of these measurements, giving details of the chamber design in a publication (Loevinger 1953). Other names associated with this time period and type of experiment include Sommermeyer and Waechter, Emery, Jalbert, Sinclair and Blondel, Kastner and Greenberg.

Cross also contributed extensively to experimental beta dosimetry in single infinite media. He measured dose distributions around beta point sources in air, argon, ethane and expanded polystyrene (Cross 1967) and did similar experiments with extended plane sources (Cross 1969).

Additionally, both Loevinger and Cross made progress in analytical beta dosimetry. Loevinger showed that ionization current measurements made with

plane beta sources could be used to infer ionization currents around point beta sources (Loevinger 1950). He also empirically derived a beta point source kernel (that is, a formula for predicting the energy deposition around a point source of unit activity) which has since been much used. (Loevinger 1956) This formula can be integrated analytically to provide doses for source geometries other than points (Hine and Brownell 1956). It accounts for about 95% of the energy deposited but gives erroneous non-zero values at distances far from the source.

Cross compiled tables of dose rate distributions from point and plane beta sources in water and air (Cross 1967a; Cross 1967b). His calculations were based on dose distributions calculated by Spencer (Spencer 1955), and he had done calculations of this type previously in order to compare with his experimental work (Cross 1967; Cross 1969).

Besides Loevinger, in the 1950's Rossi and Ellis tackled beta dosimetry using the empirical approach. Parker in 1943 was a forerunner in this area and his counterpart in the theoretical approach was Roesch (Sherbini and Porter 1983). The results of these works were initiatory, albeit not remarkably successful.

Roesch used the age diffusion theory, developed for neutron transport, for electron transport. This theory treats the transport of electron energy as if the energy were diffusing, and the results obtained upon its application to beta sources are not good in the region near the source (Hine and Brownell 1956). Roesch's theory also invokes the severe approximation that electrons lose energy continuously along their path of interaction, and it does not include electron scattering. (Sherbini and Porter 1983; Hine and Brownell 1956)

The empirical approach has since been pursued; Radzievsky et al have formulated an analytical representation for beta dose point kernels, which they refer to as dose functions of the point source. Their approach is based on representing beta spectra as the summation of several constituent spectra (Radzievsky et al 1980).

Spencer developed a theory of electron transport in homogeneous, infinite media by solving the transport equation numerically, using the method of moments

(Spencer 1955; Spencer 1959). He also treated electron energy loss as occurring continuously, and included electron scattering via the Mott cross-section (Sherbini and Porter 1983).

Spencer's results were used by Berger in 1971 to calculate absorbed dose distributions around beta point sources in an infinite water medium. The compendium which Berger published was similar to Cross's compilations (Cross 1967a; Cross et al 1982).

Since the initiatory and educative work of Berger in 1963 (Berger 1963), interest and progress in the area of simulating electron transport using computers and the Monte Carlo technique have continued to the present. In 1973, Berger published dose distributions around monoenergetic electrons, similar to ones Spencer had calculated, but focused primarily on point sources in water. He showed their relevance to beta dosimetry as well (Berger 1973); and the computer code which he used was a precursor to a series of Monte Carlo codes which are currently used for calculations pertaining to beta dosimetry.

In general, the Monte Carlo method's results are more accurate than those provided by analytical methods but this is not the sole reason for its continued use in dosimetric calculations. Its applicability to the boundary problems (that is, heterogeneous beta dosimetry in finite media), and the concurrent lack of alternative comparably efficient methods, make it almost indispensable.

The study of interface or boundary dosimetry was undertaken as early as, if not prior to, 1949, when Spiers recognized that material inhomogeneities present in the body should not be neglected in dosimetric calculations; he attempted to calculate the dose near a bone/soft-tissue interface. Although the radiation source was X-rays or gamma rays, and not beta particles, which is the subject at hand, it is recognized that the issue of addressing material heterogeneity in dosimetric calculations was put on a solid footing at this time. (Spiers 1949)

In 1970, Charlton applied Spencer's monoenergetic electron dose distributions to the problem of electron energy deposition near material boundaries. However, the method is applicable only to media with similar electron scattering properties. (Charlton 1970)

Around this time, a theoretical model, referred to as the "one-group" method, was proposed. It provides a means of calculating doses at planar material interfaces from plane, infinite beta sources; other source geometries are dealt with as well. The theory assumes one representative energy for the beta source, and is based on an approximate solution of the transport equation (O'Brien et al 1964; O'Brien 1974).

Another analytical method is the "two-group" method. This is more of an empirical approach and is an extension of the work done with beta dosimetry of homogeneous media by this group. The basis of their method, besides the one mentioned earlier, is that the source fluence is treated as being comprised of direct and diffusional components. (Radzievsky and Komarov 1982) Although they claim that experimental data support their analytical results, implementation of their theory in the present work (Chapter 6) has provided contradictory evidence.

Electron dosimetry is not disparate from beta dosimetry. Developments in the former can promote progress in the latter. Consequently, it is appropriate to note the recent renewed interest and advances in electron beam dose calculations. Several groups are using and extending Fermi-Eyges multiple scattering theory to this end (Sandison and Papiez 1990; Bruivinis et al 1989; Jette 1983; Jette and Bielajew 1989; Jette 1988). Some are also addressing the inhomogeneity problem in this context (Jette et al 1989) and others are exploring new numerical techniques such as the phase-space-time evolution method for particle transport (Storchi and Huizenga 1989).

The work of Werner attests to the intertwinement of electron and beta dosimetry. His is a theoretical approach based on the energy averaged Boltzmann equation. He has applied it to calculating dose distributions in regions with high-energy electron sources, and to the dosimetries of beta-emitting radionuclides and plane uniform monoenergetic source distributions in infinite homogeneous media, as well as to spherical uniform monoenergetic isotropic source distributions in infinite homogeneous media. (Werner et al 1988) In addition, a combination of this model and one based on the diffusion approximation to the Boltzmann equation

have been used in handling electron dosimetry at material interfaces (Werner 1985).

Experimental work in interface electron dosimetry includes that of Eisen et al and Lockwood et al. The former used dye film dosimetry (Eisen et al 1972) and the latter, a calorimetric method (Lockwood et al 1980); these works constitute benchmark data against which analytical and numerical methods can be tested.

With regard to experimental interface beta dosimetry, contributions have been made by groups concerned with air interfaces in general (Osanov and Podsevalov 1971) and in particular with dose rates at skin/air interfaces (Pook and Francis 1975), by the proponents of the "one-group" and "two-group" methods mentioned earlier and by Kwok et al.

In the experiments of Kwok et al, point and plane beta sources were used at planar material interfaces to study dose perturbations arising from the presence of material boundaries; results were compared with Monte Carlo calculations (Kwok et al 1987; Kwok et al 1990). In related works, discrepancies between Monte Carlo and experimental results have been reported for plastic/air boundaries (Yu 1989).

The resolution of these discrepancies is one of the goals of this project. In addition, Monte Carlo codes will be tested against new benchmark experimental data concerned with interface beta dosimetry, and the "one-group"and "two-group" methods mentioned above will be examined further.

1.2 Rationale for the Project

Several objectives of the present work were the following: (i) to produce a set of benchmark data for testing analytical and numerical dosimetry calculations; (ii) to contribute towards developing clinical radioimmunotherapy; and (iii) to provide data relevant to the dosimetry of skin surface contamination by 'hot spots' of beta radionuclides.

The presence of material boundaries complicates dosimetric calculations. All analytical methods aimed towards this problem thus far are approximate; even Monte Carlo algorithms such as the ones used in this work implement electron

multiple scattering theories which are valid for homogeneous, infinite media. Consequently, the reliability and accuracy of these calculational methods are assessed by comparing their results with high quality experimental data. Since such data are relatively scarce, this project has aimed to furnish some.

To this end, experiments were designed * (i) to quantitate dose backscatter at planar material interfaces due to a beta source present at these boundaries; (ii) to investigate the dependence of dose enhancement on the atomic number of the backscattering material; (iii) to study the variation of dose perturbation with distance from the source, the source being fixed at a planar material interface; and (iv) to study the variation of dose perturbation with source displacement from the material interface. No other investigations which address these aspects of boundary beta dosimetry as thoroughly as does the present work have been found in the literature.

To illustrate the practical relevance of the type (i) experiments, one can imagine for example that radioactive beta sources are present at soft-tissue/cortical-bone boundaries or air/soft-tissue boundaries within the body as a result of nuclear medicine or radiotherapeutic procedures. These experimental data should help in understanding how doses in these situations are enhanced or reduced because of the presence of different media.

Contamination of the skin by beta sources, resulting in localized areas of high activity, or 'hot spots', provides a concrete example of application of one of these experiments. The experiment, type (iii) above, uses Mylar as a skin substitute and beta activity is present on the surface. The dose perturbation fall-off with depth in the Mylar is measured, and provides an estimate of how far below the skin surface the energy from surface contamination is deposited.

Figure 1.1 depicts another example of potential application *in vivo* for the type (iii) experiment. Here, the beta source is within a tumour that has partially invaded a segment of cortical bone. It is known that the bone enhances dose to the

**The inception of many of the ideas associated with these is due to Dr Prestwich.*

surrounding healthy soft-tissue because of excess electron scattering in cortical bone relative to soft-tissue. but how does this dose enhancement fall-off with increasing amounts of soft-tissue between the source at the interface and the point of interest?

Fig 1.1 *In vivo* relevance of type (iii) experiment

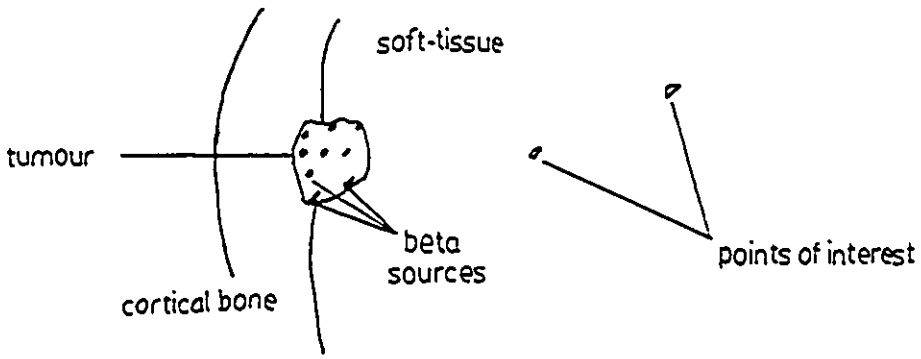

Figure 1.2 is a descriptive diagram which demonstrates an anatomical setting for a type (iv) experiment. Here, the source is embedded in a tumour which is some distance from a bone and there is intervening soft-tissue. A possible question is "how far from the radioactive site (the tumour) must the bone be in order not to appreciably increase the dose to the intervening healthy tissue?"

Fig 1.2 Sample illustration of applicability of type (iv) experiment

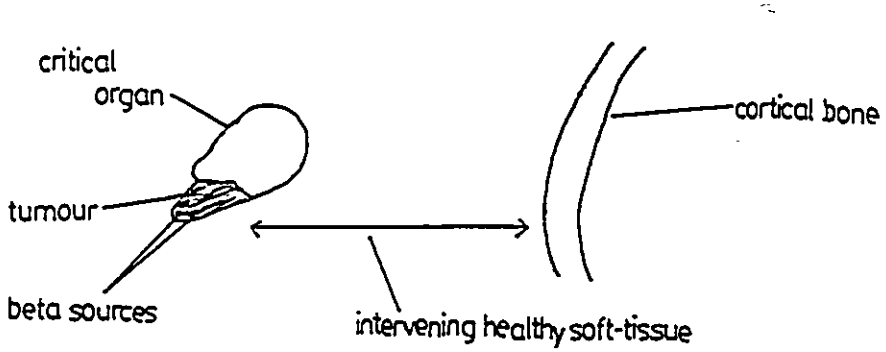

These diagrams are anatomically nebulous; their purpose is to demonstrate that, in addition to contributing towards fundamental research, these types of experiments have practical and potentially useful applicability.

The preceding illustrations also assume that beta radionuclides are present in tumours. One radiotherapeutic treatment, still in developmental stages, for accomplishing this, especially in metastases, is radioimmunotherapy. This is a treatment which uses monoclonal antibodies as selective vehicles for transporting radionuclides to specific tumours. Tumour associated antigens attract these radioactively labelled monoclonal antibodies which should destroy the targetted tumour while sparing healthy tissue.

The treatment owes its existence to the development of the hybridoma technique for producing monoclonal antibodies (Köhler and Milstein 1975), and has progressed in part because of advances in immunology, molecular biology and cancer research. Details of physiological and biological hindrances thwarting speedier progress and greater success of this treatment can be found in the literature (for example, Sharkey et al 1990; Wessels 1990; Vaughan et al 1987; Larson et al 1986; Eckelman et al 1980). Techniques for quantitating the radionuclide activity distribution *in vivo* will not be discussed here either, save to mention that single photon emission computerized tomography, SPECT, is currently being developed for uses such as this. (Leichner 1986; Jaszczak et al 1985)

Another factor upon which the eventuality of clinical, routine radioimmunotherapy relies is the development of the dosimetry associated with this treatment. That is, one should be able to reliably predict the doses which will be received by the patient as a result of the procedure. Dosimetry calculations also aid in selecting the most cost-effective radionuclide for the procedure (McGregor 1988). In view of this, the work done here may play a small but relevant role in optimizing clinical radioimmunotherapy.

Other works in interface beta dosimetry have reported discrepancies between Monte Carlo and experimental results at air/plastic interfaces (Yu 1989). These experiments used thermoluminescent dosimeters (TLDs) which may have

perturbed the electron fluence in the medium under investigation but since there was agreement between calculational and experimental results for aluminium/plastic interfaces, this explanation is questionable.

Similar and additional experiments have been done in the present work using an extrapolation chamber as the radiation detector; this affords a different and more sensitive approach with which to obtain the aforementioned benchmark data and attempt an explanation of the discrepancies noted above.

CHAPTER 2

ENERGY DEPOSITION BY ELECTRONS TRAVERSING MATTER

The following does not purport to be a complete account of electron interactions with matter. The basics of some of the interactions relevant to the present study are outlined, while derivations of cross-sections and indepth treatments of some physical processes are omitted. However, references which address these topics are included.

Naturally occurring processes which are sources of electrons include beta decay, internal conversion and the Auger effect. Beta particles are electrons that are emitted during one type of beta decay in which a neutron transmutes into a proton, and an electron and antineutrino are emitted from the radioactive nucleus [$n \rightarrow p + e^- + \bar{\nu}$]. As a result of beta decay, electrons of different energies are emitted. Therefore, beta decay is a source of polyenergetic electrons. The beta spectrum is usually characterized by a highest, or endpoint, energy, E_0 (this is 1.708MeV for ^{32}P) and an average energy, <E>, (694keV for ^{32}P).

Internal conversion electrons are monoenergetic and result from de-excitation of an excited nuclear state by emission of an atomic electron rather than by emission of a photon.

Auger electrons are also monoenergetic; they are atomic electrons which are emitted instead of characteristic X-rays when inner shell vacancies are filled by outer shell electrons.

Artificial means of producing energetic electrons include linear accelerators, betatrons and electron synchrotrons. (Enge 1966)

In traversing a medium, an electron suffers very many collisions. A 1MeV electron undergoes about 10^4 elastic collisions while slowing down to 1keV (Berger and Wang 1988). Consequently, an electron's path is tortuous, a feature

described as pathlength straggling. Energy-loss straggling is another characteristic of electron traversal through a medium; the manifestation of energy-loss straggling is that, for incident electrons of the same energy, there is, at any particular depth in the medium, an energy distribution of electrons.

As a result of these two features, the end-point of an electron's path, or its range, in a medium, is not distinct. Several functional definitions exist; three examples are the CSDA range, the practical or extrapolated range and the maximum range. The last is relevant to beta emissions; it is determined from transmission measurements and is the absorber thickness required to reduce the beta particle transmission to background levels. The practical range is determined from the transmission curves of monoenergetic electrons; the linear middle portion of these curves is extrapolated until the background level is intersected and the absorber thickness associated with this point of intersection is defined as the extrapolated range. (Evans 1955) The CSDA range is based on a model of electron transport called the continuous slowing down approximation and is the definition used in this work.

An electron's properties make it a very interactive projectile in a medium. It is a lepton; that is, it is a spin one-half particle that does not feel the strong nuclear force. It is also charged and interacts via the electromagnetic force. It is the lightest charged lepton, with a mass of 0.511MeV, and is identical to atomic electrons, which are some of its targets.

Because it is charged, the electron can interact with either the atomic electrons or the positively charged nucleus. The latter type of interactions are usually scatterings with not much energy loss because of the small mass of the electron (projectile) compared with that of the nucleus (target); bremsstrahlung radiation may be produced during these interactions as well. Electron-electron interactions involve particles with equal masses so that considerable energy loss can occur; in addition, the intrinsic angular momentum (that is, the spin) of the electrons has to be considered. The results of these various types of interactions are scatterings and energy losses inflicted on the electron.

The prevalence of one type of interaction is largely dependent on the energy of the incident electron and on the atomic number of the medium. For example, whereas at higher electron energies, electron-nucleus encounters resulting in bremsstrahlung must be considered along with ionization and excitation as energy loss mechanisms, in the region of interest for this work, namely, less than 3MeV, bremsstrahlung production as a means of energy loss is a distant second to ionization and excitation. The stipulated energy range of interest arises because most beta emitters have end-point energies in this region (Mladjenović 1973).

In order to construct a representative picture of electrons interacting with matter, one has to determine the direction taken after each interaction and the energy loss incurred there. The electron fluence, differential in angle and energy, at a particular point in a medium, is the quantity which describes this.

Electron fluence is the number of electrons passing through a particular area. This quantity, differential in angle and energy, is the number of electrons per unit area per unit solid angle per unit energy. It is a fundamental parameter of electron transport and its role in determining absorbed dose will be demonstrated in Section 2.2.

Another term worth defining at this time is cross-section. Loosely, it can be defined as describing the probability for an interaction to occur. It is not a physical property of the particles which are targets of the interaction but can be considered their 'effective areas'. The units of a cross-section are area per target particle. The following definitions are taken from Evans (Evans 1955).

Evans presents two concepts of a cross-section: one has its roots in wave theory, the other in particle theory.

In the wave model, a cross-section can be thought of as an area in the incident wave-front through which a specific amount of power flows; this is the power removed as a result of interaction with one target particle. This is equivalent to saying that there is an incident power intensity J_0 (power per unit area) and interaction with 'a target' results in removal of an amount of power I. The cross-section σ for this interaction is such that $I=\sigma J_0$ and is therefore the proportionality

constant between the incident power intensity and the power removed.

In the corpuscular model, a cross-section can be thought of as an area associated with each target particle; incident particles must pass through this area in order to undergo the interaction. The value of the cross-section represents the probability of 'a hit' on this target area. The cross-section, σ, multiplied by the areal density, nx, of target particles in a thin target (where n is the volume density of target particles and x is the target thickness), gives the probability that one incident particle will interact while passing through the target material.

Two examples are included for illustration. (a) A reaction occurs in which products that can be counted are formed - an incident fluence Φ results in P products for a target with N target particles; then, $P = \sigma\Phi N$, where σ is the cross section for this interaction. (b) A beam is incident on a target with areal density nx of target particles; the incident intensity J_0 is known and the transmitted intensity J is measured. Then, $J = J_0 - \Delta J$, where ΔJ is the intensity removed by the target such that the probability of removal, that is, the probability of interaction, is $\Delta J / J_0 = n \times \sigma$, where σ is the 'cross-section'. In keeping with the format of the first definition, $\Delta J / n x$ is the power removed I, such that $I = \sigma J_0$.

2.1 Electron Interactions with Matter

As a result of the various types of interactions undergone by electrons penetrating a medium, their fluence changes with depth of penetration and there are corresponding changes in the absorbed dose. An understanding of the fundamental interactions is therefore a prerequisite for determining absorbed dose.

Electron interactions are categorized using the sizes of impact parameters relative to those of atomic radii. An impact parameter is the closest distance achieved between the line of motion of an incident particle and the target particle. It is denoted here by b and the atomic radius by a.

When the impact parameter is very much larger than the atomic radius,

(b>>a), the encounters are called distant collisions or soft collisions. They are the most common type of interaction and account for about half of the energy lost by electrons in penetrating a medium (Attix 1986). The energy loss results from ionization or excitation of the atom.

In soft collisions, the electric field of the electron interacts with the entire target atom. The electron can be treated as a point charge and its magnetic properties can be neglected. This approximation is justifiable given the magnitude of the impact parameter and the fact that the force associated with a magnetic field falls off as the reciprocal of the cube of the distance whereas the electric force does so as the reciprocal of the distance squared (Rossi 1952).

Nonetheless, the theoretical treatment of soft collisions is complicated. Determination of cross-sections for inelastic collisions resulting in atomic excitation necessitates evaluating transition probabilities for all possible excited states. For fast electrons (that is, ones whose velocities exceed greatly the internal motion of the system) the method of the Born approximation suffices. However, for slow electrons, this approximation is not valid and other sophisticated treatments are needed. (Chap 11, Mott and Massey 1949) In addition, the density effect, which is defined next, must be considered in the case of relativistic incident electrons.

In condensed media, the electron's electric field is felt foremost by atoms nearest it; the resulting dipole distortion of these atoms weakens the electric field felt by atoms further away so that in effect, some of the atoms in the medium screen the electric field of the passing electron from others. (Attix 1986; Rossi 1952) The result is a decrease in energy loss by the electron. This phenomenon is pronounced in condensed media, such as liquids and solids, in which atoms are not as widely spaced as in gases and cannot be treated independently, and it is not negligible in any medium for the case of relativistic electrons (Berger and Seltzer 1983). It is called the density effect (Fermi 1940) or polarization effect, and is taken into account in assessing electron energy loss, as discussed later.

Electron energy loss as well as scattering can occur in encounters where impact parameters are about the size of atomic radii (b ~ a). These encounters are

called hard or knock-on collisions. The incident electron can engage in inelastic or elastic collisions. Atomic excitation and ionization are two types of inelastic interactions. The assessment of atomic excitation, for fast and slow incident electrons, is on par with that for soft collisions outlined above. Ionization can result from direct interaction of the incident electron and an atomic electron and is likely at these impact distances, hence the name knock-on collision.

The incident electron can also change places with an atomic electron in what is referred to as a rearrangement collision, or exchange interaction, which may be elastic or inelastic. The theoretical treatment of these interactions is complex (Chap 10.11 Mott and Massey 1949).

If the scattered electron (also called secondary or knock-on electron) in a knock-on collision has an energy much greater than the binding energy, the interaction is treated as if the scattered electron had been free. The electrons' magnetic moments and spins cannot be neglected at these small interaction distances. In addition, the indistinguishability of the incident and scattered electrons must be considered, and a relativistic treatment is in order since fairly low energy electrons are relativistic (for example, an electron of 1MeV kinetic energy has a speed slightly greater than 9/10 the speed of light).

These interactions are also called inelastic electron-electron scatterings. Their cross-section was derived by Møller and is usually referred to as the Møller cross-section.

Møller completed a relativistic quantum mechanical treatment of electron-electron collisions, in which the interaction between the two electrons is treated as a first-order perturbation. Dirac's theory for electron motion in an electromagnetic field was used (Chap 15, Mott and Massey 1949) and the atomic electron was assumed to be free. Although collisions of this type are not as frequent as the distant interactions described earlier, large energy losses can occur at each encounter because the colliding particles have equal masses.

Let T = kinetic energy of the incident electron in units of mc^2, where m is the electron mass and c the speed of light

Let xT = the smaller of the kinetic energies of the incident and scattered electrons, in units of mc^2

Then, $0 \leq x \leq 1/2$ since one cannot distinguish between the incident and scattered electrons. The cross-section per electron is

$$\frac{d\sigma}{dx} = 2\pi r_o^2 \frac{(T+1)^2}{T^2(T+2)}\left\{\frac{1}{x^2} - \frac{1}{x(1-x)}\frac{(2T+1)}{(T+1)^2} + \frac{1}{(1-x)^2} + \frac{T^2}{(T+1)^2}\right\} \qquad (2.1)$$

where r_o is the classical electron radius, e^2/mc^2. (Zerby and Keller 1967; Roy and Reed 1968)

Equation 2.1 gives the probability of fractional energy loss x by the electron. If the particle emerging with the higher energy is taken to be the incident or primary electron, its energy loss is therefore xT. The cross-section also increases with decreasing incident electron energy T. Consequently, low energy electrons lose energy faster than high energy ones as a result of electron-electron collisions.

The angular deflections of the electrons can also be determined. The differential scattering cross-section derived by Moller is as follows. It gives the probability of scatter into solid angle $d\Omega^*$, defined by Θ^* to $\Theta^* + d\Theta^*$.

$$\frac{d\sigma}{d\Omega^*} = r_o^2 \frac{\gamma+1}{2\gamma^2\beta^4}\left[\csc^4\frac{\Theta^*}{2} + \sec^4\frac{\Theta^*}{2} - \csc^2\frac{\Theta^*}{2}\sec^2\frac{\Theta^*}{2} + \left(\frac{\gamma-1}{\gamma}\right)^2(1+4\csc^2\Theta^*)\right] \qquad (2.2)$$

where r_o is the classical electron radius

$\beta = v/c$, the ratio of electron speed to that of light

$$\gamma = \frac{1}{\sqrt{1-\beta^2}}$$

Θ^* is the scattering angle in centre of mass coordinates.
(Roy and Reed 1968)

This form of the scattering cross-section is instructive because the various terms can be associated with physical processes. The fourth term in the square brackets is a consequence of the electrons' spins; without it, the equation would represent the result of a collision between two identical particles with no spin. The third term accounts for the identical nature of the particles and their possible interchange. Without the third and fourth terms, Equation 2.2 is referred to as the relativistic Rutherford cross-section; that is, it is the cross-section for the interaction between two unlike charged particles. In the non-relativistic limit, it reduces to the form of the Rutherford scattering cross-section (Roy and Reed 1968).

Scattering angles determined from the Møller cross-section are as follows. For the higher energy or primary electron,

$$\cos\Theta_h = \left[\frac{(1-x)(T+2)}{(1+x)T+2}\right]^{1/2} \qquad (2.3)$$

where Θ_h is the angle of scatter between the higher energy electron's scattered direction and its original direction.
For the lower energy or secondary electron,

$$\cos\Theta_l = \left[\frac{x(T+2)}{xT+2}\right]^{1/2} \qquad (2.4)$$

where Θ_l is the angle of scatter between the secondary electron's direction and the original direction of the primary electron.
(Zerby and Keller 1967).

From these relationships, it can be seen that for energy losses up to a maximum of 1/2 T, $\cos\Theta_h \geq \cos\Theta_l \geq 0$, implying that the primary electron suffers a smaller, if not equal, deflection compared with the secondary.

The Møller cross-section, Equations 2.1 and 2.2, is finite for the incident electron energies of interest here and increases with decreasing electron energy. This implies that an electron undergoes successive interactions of this type, losing a fraction of its energy each time. The magnitude of the angular deflection at each collision depends on the incident electron energy and the fraction of this energy that is lost (Equation 2.4). Most of the deflections are small but there are large ones at times (Zerby and Keller 1967).

Energy losses incurred in electron interactions of the above two types are called collisional energy losses. As seen earlier, knock-on collisions can result in scattering as well as energy loss. However, the interaction discussed next results primarily in scattering for the incident electron energies of interest here. Radiative energy losses do occur but the probability of their being large is low. In addition, it is estimated that these radiative phenomena do not affect the electrons' deflections by more than three percent (Mott 1931). Therefore, scatter can be treated separately from energy loss. The scatterings are referred to as nuclear elastic scatterings or nuclear Coulomb scatterings.

Impact parameters of electron-nucleus interactions are smaller than the atomic radius ($b<<a$), so the interactions are called close collisions. The electron is scattered by the nucleus and there is a small chance that a photon will be emitted; the photon constitutes radiative energy lost by the electron, and is expected according to classical theory which proposes that whenever a charged particle is accelerated, it should radiate. The cross-section for this radiative phenomenon is 1/137 times that for elastic scatter (Evans 1955). However, when a radiative interaction occurs, a photon (bremsstrahlung radiation) is emitted, the electron is deflected and can lose up to all of its kinetic energy to the photon (Evans 1955; Attix 1986;Rossi 1952). As discussed later, radiative energy loss is not significant, given the electron energies of interest here.

Elastic nuclear scattering, or Rutherford scattering, is largely responsible for the characteristic zig-zag path of electrons penetrating a medium. Classical and quantum mechanical derivations of the cross-section give the same result, a

situation peculiar to fields in which the force varies as the reciprocal of the distance squared, as is the case for the electric field. (Appendix C, Evans 1955)

The classical derivation considers the effect of the Coulomb force on an electron which passes near a nucleus of charge Ze. Use is made of the impact parameter, b, to delineate a ring or differential cross-section within the effective target area. In addition, the impact parameter is related to the scattering angle, θ, giving the following expression for the differential cross-section per unit solid angle for elastic nuclear scattering.

$$\frac{d\sigma}{d\Omega} = \frac{1}{4}\left(\frac{Ze^2}{mv^2}\right)^2 \frac{1}{\sin^4\frac{\theta}{2}} \qquad (2.5)$$

where e is the electron charge and mv is the momentum of the incident electron. (Rutherford 1911; Chap 13, French 1971)

The quantum mechanical approach involves solving Equation 2.7, below. This is the time-independent (Schrodinger) wave equation for the outgoing wave, ψ, which is the result of scatter of an incident wave ψ_{inc} by a scattering potential. Elastic nuclear scattering can be considered as the scattering of an incident beam of electrons by a small, spherically symmetric region where the potential energy is non-zero. The scattering potential is denoted by $V(\vec{r})$, the scattered wave by ψ_{scat}, such that

$$\psi = \psi_{inc} + \psi_{scat} \qquad (2.6a)$$

where $\psi_{inc} = e^{-ikz}$ (2.6b)

$$\psi_{scat} = f(\theta)\frac{e^{ikr}}{r} \quad \text{for large } r \qquad (2.6c)$$

and ψ, the total or outgoing wave, is the solution of

$$\nabla^2\psi + k^2\psi = \frac{2m}{\hbar^2}V(\vec{r})\psi \qquad (2.7)$$

where k is the wave number: $k = \frac{2mE}{\hbar^2}$; E is the kinetic energy of the system, and m, the reduced mass.

The problem, then, is to find $f(\theta)$ in Equation 2.6c. This quantity is the scattering amplitude. Its square is the differential cross-section for scattering into the element of solid angle representing scatter through angle θ.

The wave equation, Equation 2.7, can be solved exactly and approximately. The method of partial waves, which involves expanding the wave function in spherical harmonics and using the asymptotic form of Equation 2.6c, gives an exact solution. The Born approximation method, which treats the scattering potential as a perturbation, is valid for fast incident electrons; the magnitude of the scattering potential must be considerably less than the kinetic energy of the incident particle. The appropriate wave equation is solved via the method of Green's functions (Chap 16, Arfken 1985) to give $f(\theta)$. (Mott and Massey 1949; McGervey 1983)

The Born approximation method gives the result that the scattering amplitude is the Fourier transform of the scattering potential with respect to momentum transfer. Using a Coulomb potential, $V(r)=Ze^2/r$, one obtains Equation 2.5 for $|f(\theta)|^2$.

Equation 2.5 is valid for two point charges interacting but the nucleus consists of a distribution of protons and neutrons. A form factor is used to modify the cross-section in order to accommodate the extended charge distribution arising from the protons. A form factor gives the ratio of the scattering amplitude for an extended charge distribution to that for a point charge. Here, it is called the nuclear form factor $F_N(q)$, and it is the Fourier transform of the charge distribution with respect to momentum transfer. Therefore, the elastic nuclear scattering cross-section becomes

$$\frac{d\sigma}{d\Omega} = |F_{N(q)}|^2 \left(\frac{d\sigma}{d\Omega}\right)_{point} \qquad (2.8)$$

where $\left(\frac{d\sigma}{d\Omega}\right)_{point}$ is given by Equation 2.5.

As stated earlier, the Born approximation method can be applied to elastic collisions between fast electrons and atoms (collision category b>a). Here, atomic electrons shield the nuclear charge from the incident electron, and the differential cross-section for this interaction is Equation 2.5 with Z^2 replaced by $[Z-F(q)]^2$, where F(q) is the atomic form factor.

Inelastic collisions between fast electrons and atoms are also treated by approximate methods. The optical transition probabilities for resulting atomic excited states must be determined; these probabilities are used to define generalized oscillator strengths. The differential cross-section for a particular atomic transition is determined from the generalized oscillator strength associated with that excitation. From this, it can be shown that, for small momentum transfers, the differential cross-section is related to the dipole moment corresponding to the atomic excitation. (Chap 11, Mott and Massey 1949; Gasiorowicz 1974)

Derivation of the Mφller cross-section requires making the spatial part of the wave function for the electron symmetric or anti-symmetric, depending on whether the total spin of the two electrons is even or odd. This follows from the requirement that the total wave function be antisymmetric. The consequences are observable in the fourth term of the differential cross-section (Equation 2.2), as outlined earlier. (Gasiorowicz 1974; Landau and Lifshitz 1976)

The cross-sections of Equations 2.2 and 2.5 indicate that an electron undergoes many successive collisions during the course of its penetration in a medium. Analytical models have been developed to describe the cumulative effect of many or multiple electron interactions. Multiple scattering theories address the angular deflection resulting from many electron interactions; these will be discussed further in Chapter 3. Energy loss is also described by analytical models, and one example is the continuous slowing down approximation (CSDA).

As indicated earlier, there are collisional and radiative energy losses, but the

latter constitute a small fraction of the total for the energies of interest here. An estimate of bremsstrahlung production is obtained from the radiative yield, $\gamma(E)$; this is the fraction of the incident electron's kinetic energy E that is converted to bremsstrahlung. It is approximately

$$\gamma(E) = \frac{3 \times 10^{-4} ZE}{1 + 3 \times 10^{-4} ZE}$$ (Zerby and Keller 1967),

where E is in units of mc^2, and Z is the atomic number of the medium. For E=700keV, the approximate average energy of ^{32}P, and bismuth (Z=83), since this was the highest atomic number material worked with here, $\gamma(E) \approx 3\%$.

Each energy loss suffered by an electron is the result of an individual collision. Energy loss is therefore a discrete phenomenon. However, since successive collisions occur and at many of them only a small fraction of the electron's energy is lost, the energy loss can be described, albeit approximately, as taking place continuously. This is the essence of the CSDA model for energy loss and although it ill-represents physical reality, it is widely used. The model neglects energy loss straggling and it becomes increasingly inappropriate for electrons in the low keV range since these are more likely to lose large fractions of their energy in single encounters.

A parameter of this model is the stopping power, S(E). It gives the energy loss per unit pathlength travelled by an electron of a given initial energy. The CSDA range, R_o, is the distance over which an electron of initial energy E_o loses all of its energy, according to this model. It is determined by

$$R_o = \int_0^{E_o} \frac{1}{S(E)} dE$$

where the stopping power S(E) is defined as follows.

$$\frac{1}{\rho}S(E) = -\frac{1}{\rho}\frac{dE}{dx} = N\int W\frac{d\sigma}{dW}dW$$

where $\frac{d\sigma}{dW}$ is the cross-section for inelastic scattering resulting in energy loss W, ρ is the medium density and N is the number of electrons per gram. $\frac{1}{\rho}S(E)$ is referred to as the mass stopping power.

If $\frac{d\sigma}{dW}$ is the cross-section for collisional type energy loss, $-\frac{1}{\rho}\frac{dE}{dx}$ is called the mass collisional stopping power. If it is the cross-section for radiative energy loss, $-\frac{1}{\rho}\frac{dE}{dx}$ is the mass radiative stopping power. That is,

$$S(E)_{total} = S(E)_{collisional} + S(E)_{radiative}$$

Collisional energy loss is separated into two types, namely, that resulting from hard collisions (b~a) and from soft collisions (b>a). Soft collisions are defined to be those where the ejected electron's energy is less than a pre-chosen value η. Conversely, hard collisions result in ejected electrons with energy greater than η. η is arbitrarily chosen under two conditions; one, that it is sufficiently large so that all hard collisions can be analyzed as if the atomic electrons were free, and two, that it is small enough so that the soft collisions can be treated as if the electron were a point charge. (Rossi 1952)

From the preceding section, it is evident that the Møller cross-section is used for evaluating hard collision stopping power and that the soft collision stopping power requires evaluation of the transition probabilities for various possible excited atomic states. That is,

$$S_{coll}^{hard}(E) = \int_{\eta}^{E_m} W\left(\frac{d\sigma}{dW}\right)_{Moller} dW$$

where E_m = 1/2 the incident electron energy.

$$S_{coll}^{soft}(E) = \int_0^{\eta} W\left(\frac{d\sigma}{dW}\right)_{ionic\ excit} dW$$

and

$$S_{coll} = S_{coll}^{hard} + S_{coll}^{soft}.$$

The soft collisional stopping power was first evaluated by Bethe (Berger and Seltzer 1983) using the Born approximation. The limitations of this method for handling electron-atom collisions have been briefly mentioned. The shell correction term, C/Z, in Equation 2.9 below, corrects for the invalidity of the Born approximation for incident electrons with velocity not much greater than that of the atomic electrons. The name for the correction is explanatory since electron velocities in the different orbitals vary, with the K-shell electrons being the fastest.

The mass collisional stopping power for electrons is given by

$$\frac{1}{\rho}S_{coll} = \frac{1}{\rho}\frac{dE}{dx}_{coll} = k\left[\ln\frac{\tau^2(\tau+2)}{2\left(\frac{I}{mc^2}\right)^2} + F^-(\tau) - \delta - \frac{2C}{Z}\right], \text{ where} \qquad (2.9)$$

$$k = 2\pi\frac{N_A Z}{A}r_o^2\frac{mc^2}{\beta^2},$$

with r_o= the classical electron radius,

$N_A Z/A$ =the number of electrons per gram of medium,

β=v/c; v is the electron speed. The presence of β in the denominator indicates that the energy loss per unit pathlength increases with decreasing electron energy.

mc^2 = rest mass energy of the electron

τ = kinetic energy of electron in units of mc^2

δ = correction for the density effect discussed earlier

C/Z = shell correction described above

and $$F^-(\tau) = 1 - \beta^2 + \frac{\frac{\tau^2}{8} - (2\tau+1)\ln 2}{(\tau+1)^2}$$ (Chap 8, Attix 1986).

I is the mean excitation energy of the medium. Although not shown explicitly here, the density effect term also depends of I which therefore plays a key role in evaluating collisional stopping power.

For gases, mean excitation values are determined from optical dipole oscillator strength densities, which are proportional to photoelectric cross-sections. In condensed media, the dielectric response function, which is related to the index of refraction, is used to determine I. (Berger and Wang 1988) The development of stopping power theory is not simple, particularly for low-energy electrons for which, the Born approximation that underlies the theory of Equation 2.9, is invalid. This is consequently an area of current research interest (for example, Nieminen 1988).

Section 2.1 should have provided some insight into the various interaction processes which electrons undergo. It should have enhanced an appreciation for the theoretical treatments necessary for determining cross-sections, the usage of which in analytical theories and Monte Carlo codes (Chapters 6 and 3) would otherwise be perfunctory. In addition, Section 2.1 has shown that energy loss can be treated separately from angular deflection.

2.2 Calculation of Energy Deposited

Absorbed dose is the quantity of primary interest for practical purposes. The absorbed dose at a particular point in a medium is the product of the electron fluence at that point and the appropriate collisional stopping power. The relationship between absorbed dose, D, and electron fluence, Φ, is given by

$$D(\vec{r}) = -\int_0^{E_o} \{\frac{dE}{dx}\Phi_{E,r}(\vec{r}) + E\frac{d\Phi_{E,r}(\vec{r})}{dx}\}dE \qquad (2.10)$$

where the first term within the brackets is the contribution from electrons which deposit some of their energy as they pass through dx and the second term is due to electrons coming to rest in dx (ICRU35 1984).

Evaluating Equation 2.10 requires knowledge of the electron fluence as a function of depth or distance r from a source. This is an extremely difficult parameter to determine analytically for a realistic situation given the enormous amount of electron scatter which takes place, the statistical fluctuations in the energy losses of successive collisions, and the presence of boundaries. To date, an analytical approach towards an exact solution remains intractable. However, there are approximate methods which are useful. One example is the continuous slowing down approximation (CSDA) to the radiative transport or Boltzmann equation.

2.2.1 The Boltzmann equation and methods for its solution

The time-independent or steady state Boltzmann equation describing electron transport gives the fluence as a function of energy and angle at any point in a medium, as shown below.

$$\vec{\nabla}\cdot\Phi(\vec{r},E,\vec{\Omega})\vec{\Omega} + \mu\Phi(\vec{r},E,\vec{\Omega}) = Y(\vec{r},E,\vec{\Omega}) + \int dE'\int d\vec{\Omega}' n\sigma(\vec{\Omega}'\rightarrow\vec{\Omega},E'\rightarrow E)\Phi(\vec{r}',E',\vec{\Omega}') \qquad (2.11)$$

For a volume of interest at $\vec{r}$, the terms on the left of Equation 2.11 represent electron losses and the terms on the right, gains or additions. Specifically,

$Y(\vec{r},E,\vec{\Omega})$ is a source of electrons at $\vec{r}$, with energy E and in direction $\vec{\Omega}$; Y is a number density;

n is the number of scatterers at $\vec{r}$ and $\sigma(\vec{\Omega}'\rightarrow\vec{\Omega},E'\rightarrow E)$ is the differential

cross-section for scatter of electrons travelling in direction $\vec{\Omega}'$ and with energy E' into angle $\vec{\Omega}$ with energy E. Therefore, $n\sigma\Phi$ gives the number of electrons per unit volume at $\vec{r}$, with angular direction $\vec{\Omega}$ and energy E that have been scattered into the volume of interest.

μ is the interaction coefficient, representing the probability per unit length of electron loss from the volume of interest at $\vec{r}$,

and the first term on the left describes the transport of electrons through and out of the volume of interest.

For electron transport in the CSDA, energy loss is treated separately from scatter; that is, elastic collisions causing angular deflections are segregated from inelastic collisions that are assumed to not cause angular deflections. The energy loss is described using a stopping power as discussed in Section 2.1. In this approximation, Equation 2.11 becomes

$$\vec{\Omega}\cdot\nabla\Phi(\vec{r},E,\vec{\Omega}) + \mu\Phi(\vec{r},E,\vec{\Omega}) = Y(\vec{r},E,\vec{\Omega}) + \frac{\partial(S(E)\Phi(\vec{r},E,\vec{\Omega}))}{\partial E} + \int d\vec{\Omega}'\, n\sigma(\vec{\Omega}'\rightarrow\vec{\Omega})\Phi(\vec{r}',E,\vec{\Omega}') \qquad (2.12)$$

where the second term on the right is called the slowing down term.

For an isotropic point source of monoenergetic electrons in an infinite homogeneous medium that is purely absorptive, Equation 2.12 gives the following result for the electron fluence at $\vec{r}$.

$$\Phi(\vec{r},E) = \frac{Y_o(E)}{4\pi r^2}e^{-\mu r} \qquad (2.13)$$

where Y_o is the total source strength: $Y(E,\vec{\Omega}) = \frac{Y_o(E)}{4\pi}$,

and $E = E' - \int_0^r S(E)\,dx$, where E' is the initial electron energy.

Equation 2.13 can be used in Equation 2.10 to estimate the absorbed dose.

In addition to being developed under the CSDA, Equations 2.12 and 2.13 are for infinite, homogeneous media. For heterogeneous media, there is the complication of material boundaries. An analytical method in interface beta dosimetry that is based on an approximate solution of the Boltzmann equation is that of O'Brien et al (O'Brien et al 1964). This method, which will be discussed further in Chapter 6, is based on Lewis' solution of the transport equation (Lewis 1950).

Other methods for handling electron transport at boundaries include the Monte Carlo method, the adjoint Monte Carlo method and the method of discrete ordinates. In this work, the Monte Carlo method and two analytical methods are used for dosimetric calculations. For completeness, a further note is made regarding the other two methods since they are topical and will not be discussed hereinafter.

The adjoint Monte Carlo method tracks electrons backwards (that is, from lower to higher energies) from the point of interest (for example, the detector) to the source. It has found applicability in the analysis of space systems exposed to electrons (Jordan 1986) and may be useful in optimizing dose distributions in radiotherapy (Mackie 1990).

The discrete ordinates or S_n method is a numerical means of solving the transport equation. It involves deriving a set of equations that describe the problem and developing procedures to solve these equations. The equations may be derived in various ways; for example, they can be formulated for finite cells in phase space or derived from analytical forms of the transport equation. Procedures for solving these equations use physical principles to ensure and hasten convergence of the solution and involve approximations. (Carlson and Lathrop 1968)

CHAPTER 3

MONTE CARLO SIMULATION OF ELECTRON TRANSPORT

In general, the Monte Carlo method "is used to predict the outcome of a series of events, each of which has its own probability" (McCracken 1955). With regard to electron transport, the events are the various interactions discussed in Chapter 2 and the probability of occurrence of an interaction is given by its cross-section. Consequently, the problem of solving the transport equation, Equation 2.11, lends itself to the Monte Carlo method.

A sample of source electrons is followed via a computer simulation which effects physical interactions by using computer-generated (pseudo-)random numbers to sample probability distributions that are based on cross-sections. Energy deposited in a medium is a typical example of a quantity which is scored. Source electrons are referred to as (case) histories and it follows that the more histories used, the smaller the sampling error and the longer the computing time.

Two Monte Carlo codes, EGS4 and Cyltran, are addressed in the following. They are different algorithms for simulating electron and photon transport in matter.

3.1 Simulation of Electron Transport - The Condensed History Technique

As noted in Chapter 2, electrons suffer many collisions per unit length of medium traversed. Owing to the multitude of interactions, analog Monte Carlo is not performed; that is, each interaction is not simulated (Nelson, Hirayama and Rogers 1985). Rather, the simulation is done in segments, where each segment consists of a series of interactions and the cumulative effects of these multiple

interactions are assessed theoretically. This is referred to as condensed history Monte Carlo which therefore is a combination of theory and conventional Monte Carlo.

Unique to condensed history simulation, then, is the need to assess energy loss and angular deflection resulting from a series of interactions. The energy loss can be dealt with by using, for example, the continuous slowing down model described in Section 2.1, or energy loss distributions such as the Landau distribution (Landau 1944). The net angular deflection is determined using multiple scattering theories.

3.1.1 Multiple scattering of electrons

A few examples of multiple scattering theories in the literature are those due to Goudsmit and Saunderson (Goudsmit and Saunderson 1940), Molière (Bethe 1953), Fermi-Eyges, Lewis (Lewis 1950) and Snyder and Scott. (Scott 1963) All are applicable to infinite, or semi-infinite, homogeneous media, a limitation which poses conflicting requirements when dealing with electron transport near material boundaries. The electron segment or step should be small enough so that it appears to be taking place in an infinite medium and it should be sufficiently long so as to contain multiple (>20) interactions.

Of the above list, only the Fermi-Eyges theory addresses energy loss (Eyges 1948) in addition to lateral displacement and scattering. The Fermi-Eyges diffusion equation for the scattering angle distribution can be derived from the Boltzmann equation (Scott 1963). Renewed interest in it is due to the pencil electron beam dose distribution work of Jette et al and others.

Neglecting energy-loss, using two dimensions, that is, the xz plane, and denoting the electron direction by an angle θ with respect to the z-axis, Equation 2.11 becomes

$$\sin\theta\frac{\partial\Phi}{\partial x} + \cos\theta\frac{\partial\Phi}{\partial z} = \int\mu(\theta' \rightarrow \theta)\Phi(\theta')d\theta' - \int\mu(\theta \rightarrow \theta')\Phi(\theta)d\theta \qquad (3.1)$$

Let the next scatter angle be ζ, such that $\theta' = \theta + \zeta$, and let in-scatter and out-scatter probability be equal: $\mu(\theta \rightarrow \theta') = \mu(\theta' \rightarrow \theta) = \mu(\zeta)$. Invoke the small-angle approximation, $\cos\theta \sim 1$, $\sin\theta \sim \theta$. Then, Equation 3.1 becomes

$$\theta\frac{\partial\Phi}{\partial x} + \frac{\partial\Phi}{\partial z} = \int\mu(\zeta)[\Phi(\theta + \zeta) - \Phi(\theta)]\,d\zeta$$

which can be reduced to the following equation using a Taylor expansion of $\Phi(\theta+\zeta)$ and the definitions of mean scatter angle, $\langle\zeta\rangle$, mean square scatter angle, $\langle\zeta^2\rangle$, and the variance in the scatter angle, $\langle\zeta^2\rangle - \langle\zeta\rangle^2$, which follow from the fact that each scatter is independent of the other. Assuming a Gaussian distribution for $\langle\zeta\rangle$, one obtains

$$\frac{\partial\Phi}{\partial z} = -\theta\frac{\partial\Phi}{\partial x} + \frac{\mu\langle\zeta^2\rangle}{2}\frac{\partial^2\Phi}{\partial\theta^2} \qquad (3.2)$$

where $\mu\langle\zeta^2\rangle$ is the linear scattering power, defined as that which causes an increase, $\Delta\langle\theta^2\rangle$, in the mean square scatter angle over a pathlength element Δl, given the scattering coefficient per unit pathlength μ –: $\Delta\langle\theta^2\rangle = \mu\langle\zeta^2\rangle\,\Delta l$.

Lewis also addresses multiple scattering from the standpoint of the transport equation. His approach does not proceed from a specific single scattering cross-section and makes no small-angle approximation. The angular distribution obtained is equivalent to that of Goudsmit and Saunderson (Lewis 1950; Roy and Reed 1968), and evaluation of the distribution in the small angle approximation gives the Molière distribution (Bethe 1953; Lewis 1950).

The Goudsmit-Saunderson distribution function for angles resulting from multiple scatterings is a Legendre series. The single scattering cross-section is incorporated in evaluating the coefficients of the series. (Goudsmit and Saunderson 1940) The distribution is a function of step-length as well as angle and numerical

evaluation of it can be lengthy (Zerby and Keller 1967). Therefore, random sampling of the Goudsmit-Saunderson distribution is more readily accomplished by sampling from stored multiple-scattering distributions calculated for pre-determined step-sizes (Berger and Wang 1988). This is the approach adopted in the Cyltran Monte Carlo code which uses the Goudsmit-Saunderson multiple scattering formalism.

The EGS4 code uses the Molière multiple scattering formalism. The latter was developed in the small angle approximation and has since been modified so as to improve its performance at large scattering angles (Bethe 1953). However, at very large scattering angles, in particular for 180° scattering or backscattering, the modified expression is inaccurate (Bethe 1953). In comparison, the Goudsmit-Saunderson formalism is exact for all scattering angles (Goudsmit and Saunderson 1940).

Like the Goudsmit-Saunderson theory, any single scattering cross-section can be employed in evaluating the Molière distribution equation (Bethe 1953). However, evaluation of the Molière theory is commonly taken as it was done in the original work, where a single-scattering theory developed by Molière was used. This theory does not include relativistic effects and it incorporates nucleus screening by atomic electrons for a Fermi-Thomas atom. The Molière distribution, derived in this way, is then given in terms of a scaled scatter angle. (Bethe 1953) This form is conducive to random sampling using variable step-sizes, a feature relevant to EGS4.

Although the theories of Goudsmit-Saunderson and Molière do not give very different results in general (Bethe 1953; Rogers and Bielajew 1988), it has been suggested that the Molière theory may be inappropriate for handling electron backscattering, particularly for low energy electrons off high atomic number media (Berger and Wang 1988; Rogers and Bielajew 1988). This is consistent with the improper behaviour of the Molière theory at very large scattering angles which was noted earlier. However, this suggestion awaits further clarification. In addition, possible effects on results from the EGS4 code, which uses the Molière formalism,

have yet to be ascertained.

3.2 Two Types of Algorithms for Electron Transport Simulation

Most electron transport simulations make use of the condensed history technique and treat energy loss separately from angular deflection. Existing Monte Carlo codes for the transport of electrons below 10MeV can be categorized as Class I or Class II (Berger 1963; Schneider and Cormack 1959). The former type of algorithm is used in Cyltran, the latter in EGS4.

3.2.1 Class I and Class II algorithms

The two approaches differ in their treatments of energy lost by a primary electron. The Class I algorithm lacks correlation between secondary or knock-on electron production and the primary electron; the energy lost by a primary as a result of all types of interaction along a path segment is determined at a single time. However, the energy lost by a primary in a Class II algorithm is determined by partitioning electron interactions such that ones which produce secondaries with energies greater than specified thresholds are treated discretely or individually whilst the others are treated in a grouped or continuous manner.

Class I procedures can use energy loss models such as the CSDA or sample from energy loss distributions. An advantage of the latter is that they can include the fluctuations in energy losses characteristic of electron transport. The Landau-Blunck-Leisegang theory used in Cyltran is an example of a distribution which incorporates energy loss straggling.

Class II procedures, or mixed procedures, incorporate energy loss fluctuations in electron transport explicitly for the interactions handled discretely. For the grouped interactions, a restricted energy-loss straggling theory can be

implemented (Andreo 1988); otherwise, the energy loss is handled in the CSDA as is done in EGS4. (Rogers and Bielajew 1990; Berger 1963)

The following clarifies the differences between the two approaches to electron transport with specific regard to how they are used in EGS4 and Cyltran, respectively.

Let the distance to a discrete interaction be t. At the discrete interaction, Møller and bremsstrahlung cross-sections are sampled. In order for the interaction to be discrete, the secondary electron or photon produced must have energy greater than a predetermined threshold, designated here as AE or AP, for electrons and photons, respectively. Consider that a secondary electron, with energy $E_\delta > AE$, is produced. Meanwhile, energy deposited along step, length t, is assessed in the CSDA; it is $t\,L^{AE}$, where L^{AE} is the restricted stopping power for energy loss less than AE. Consequently, the energy lost by the primary as a result of the catastrophic or discrete interaction plus the multiple interactions along t is $t\,L^{AE} + E_\delta$, and the energy of the primary is $E' = E_o - t\,L^{AE} - E_\delta$, where E_o is the original or initial primary electron energy.

In the other approach, a step length t , which is pre-determined, is divided into substeps. At each substep, an energy-loss distribution is sampled to give ΔE_{lost}, and secondary electrons or photons are generated according to Møller or bremsstrahlung cross-sections. At the end of step t, $E' = E_o - \Delta E_{lost}(t)$. The energy deposited along t is the energy lost, $\Delta E_{lost}(t)$, less the energy of any secondaries produced along t, E_δs. The secondaries can originate anywhere along a substep and their production sites are not correlated physically with the primary's interactions.

In both codes, the angular deflections undergone during t are assessed using multiple scattering theories (Section 3.1.1). (Rogers and Bielajew 1988, 1990; Berger 1963)

3.3 EGS4 and Cyltran - Two Widely Used Monte Carlo Codes for Coupled Electron-Photon Transport Simulation

Both systems consist of three units. One unit prepares cross-section data for the energies and materials of the problem. Another performs the Monte Carlo proper in that it does the simulation of radiation transport by tracking case histories and sampling probability distributions. The third unit is tailor-made for the problem being addressed by the user; it scores quantities of interest and defines material geometries and other input parameters.

The EGS4 System (Ford and Nelson 1978; Nelson, Hirayama and Rogers 1985; Rogers 1984) and the ETRAN-based system (Berger 1963; Halbleib and Vandevender 1976; Berger 1968) are the Monte Carlo codes proper used in this work. Their names are acronyms for Electron Gamma Shower and Electron Transport.

Cross-section data, representative of an understanding of radiation interaction with matter, are generated by algorithms called PEGS4 and XGEN for the two systems. The data are processed into forms which are accessible by the main codes (unit two) during simulations.

Units two and three, the Monte Carlo machinery and the user code, are often combined into single packages geared for specific problems. This is the case for the two packages used in this work - EGS4/Dosrz and Cyltran.

With regard to the present investigation, EGS4/Dosrz (Bielajew 1991) allows one to simulate an axisymmetric material geometry with a radiating isotropic disc of specified dimensions as the source. The standard features of the EGS4 system, including electron transport to 1keV, electron-electron scattering, multiple scattering, bremsstrahlung production and energy loss, are present. Additionally, the PRESTA algorithm (Bielajew and Rogers 1987), which reduces the dependence of electron transport on electron step-size, is used.

Cyltran, Cylindrical transport, is a package which belongs to a collection referred to as ITS (Halbleib, Mehlhorn and Kensek 1987; Halbleib and Mehlhorn

1984). Like EGS4/Dosrz, it simulates a cylindrical material geometry with axial symmetry. Its radiation transport features are fully described in the preceding reference and they include the various types of electron interactions discussed in Section 2.1; energy loss is handled as outlined in Section 3.2.1.

Cyltran is written in FORTRAN and EGS4/Dosrz in MORTRAN3, which is an extended FORTRAN. Both systems use multiplicative congruential random number generators. The EGS4 random number generator is an 'on-line' one whereas Cyltran uses the VAX random number generator. The codes were run on a VAX6420 computer at McMaster University.

Each electron is followed until its energy falls below a value ECUT which is specified by the user. The energy loss per electron step is also user-controlled. In EGS4, this is done by specifying ESTEPE, the fraction of an electron's energy that is lost per step; this allows step sizes to be controlled. In Cyltran, the equivalent of ESTEPE is fixed at 8%. The implementation of PRESTA in EGS4/Dosrz further controls electron step sizes; an example of this is that extremely short step sizes, which effectively turn off multiple scattering because they violate requirements of Molière's theory, are prevented from occurring.

EGS4/Dosrz and Cyltran differ in their termination of electron histories and in their handling of energy-loss straggling. The latter was discussed in Section 3.2.1, where differences between Class II and Class I algorithms were noted. An electron history is terminated when the electron energy is less than a previously specified value, ECUT. When this occurs at some point along an electron's step in EGS4, the electron's energy is deposited over the remaining step length. In Cyltran, the energy is deposited at some location along a straight line directed from the point at which ECUT was reached; the location is chosen randomly from a uniform distribution of distances which vary from 0 to the electron range corresponding to ECUT. (Rogers and Bielajew 1990)

Electron steps are terminated at material boundaries in both codes. In Cyltran, the pre-set electron step is shortened and energy loss determined; the deflection angle is sampled from a Gaussian distribution instead of the Goudsmit-Saunderson

distribution because deflection angles have been determined from the latter using a set of pre-determined step-lengths. In EGS4, variable step sizes are possible, and the PRESTA algorithm alleviates some of the problems associated with seriously violating the applicability of the Molière theory. (Rogers and Bielajew 1990)

Both codes have been tested against experimental electron broad beam data for 1 and 2 MeV electrons incident on homogeneous two-slab or three-slab media (Seltzer and Berger 1987; Rogers and Bielajew 1990). A comparison of the two codes with one of these experimental data sets (Eisen et al 1972) is included in Chapter 8. The case of polystyrene/vacuum media, which is not addressed in earlier comparisons, is of particular interest.

The experiments described in Chapter 4 will also test the codes' handling of boundary crossings. In addition, the electron sources are located at the material boundaries, a situation which is not feasible in electron beam experiments; a series of electron source energies, from 0 to 1.7 MeV, will be used. It will be of interest to see how the two codes compare at lower (that is, less than 1MeV) source energies.

A logic flow diagram which summarizes the salient features of electron transport simulation is given in Rogers and Bielajew 1990.

PART II. METHODOLOGY AND RESULTS

CHAPTER 4

THE EXPERIMENTS *

Heterogeneous or interface beta dosimetry was investigated in the various experiments described below. In addition to providing some new data in this area, the experiments are considered to be references against which the results of calculations can be tested. In essence, they address the transport and energy deposition of low energy (< 2MeV) electrons across material boundaries.

4.1 Experimental Objectives

A radioactive beta source located between two planar material slabs produces doses in each. If the materials are identical, so are the doses. Designate one of the slabs, one which is replaceable, as the scatterer, and the other, which remains in place, as the base. Let D_h be the dose in the base.

If the scatterer is a material which reflects or backscatters more electrons into the base than vice versa, then the dose in the base is increased to fD_h, where $f>1$, particularly in the region of the base that is adjacent to the material boundary. Conversely, if the scatterer is a material which backscatters less into the base than vice versa, then the dose in the base, particularly in the region near the material interface, is fD_h, where $f<1$.

* *Names and addresses of companies from which some of the materials were obtained are given in Appendix A.*

The quantity f is a measure of how much the dose in the base is changed when the scatterer is a material different from the base. It is the dose ratio of the scatterer to the base, R_{sb}. It can be seen that dose ratios of one scatterer to another, $R_{s_1s_2}$, can be obtained as well; for example, if scatterer s_1 changes the dose in the base to f_1D_h, and scatterer s_2 changes it to f_2D_h, then $R_{s_1s_2} = f_1/f_2$.

In addition to determining dose ratios at different material interfaces, the fall-off of these dose ratios with increasing distance from the scatterer, and therefore from the source, is also of interest. The first situation is referred to as the Zeroeth geometry and the second as the ASD geometry. Another type, the ASB geometry, considers dose ratios as a function of increasing source separation from the scatterer. Reasons for these names are elucidated shortly.

Two source geometries, point and planar, were used in the experiments. A point source is taken here to be one the dimension of which is considerably less than that of the detector. The source diameter was between 1mm and 2mm and the diameter of the sensitive portion of the detector was 1.05cm. A plane or distributed source is defined here as a broad, thin source, the dimension of which is comparable to or greater than that of the detector. The source used was 4.0cm in diameter. It covered the detector entirely and its diameter was roughly four times that of the sensitive area of the detector. ^{32}P was the beta source used.

4.2 Explanation of the Experiments

Dose backscatter factors, B, are defined by

$$B_{ih} = D_i/D_h - 1 \qquad (4.1)$$

where D_i is the dose in the base due to scatterer i and D_h is the dose in the base due to scatterer h.

It follows that the dose ratio R_{ih} for an interface created by materials i and h

is given by

$$R_{ih} = D_i / D_h \,. \qquad (4.2)$$

In practice, ionization currents are measured using an extrapolation chamber which can be assumed not to perturb the electron fluence appreciably. That is, it is a Bragg-Gray cavity, from which it follows that the absorbed energy (or dose) is proportional to the total ionization in the cavity (Failla 1937; Loevinger 1953). Therefore, determining the ratio of ionization currents suffices for determining dose ratios. The dose ratio of the above material interface is

$$R_{ih} = I_i / I_h \qquad (4.3),$$

where I_i and I_h are the ionization currents measured for scatterers i and h, respectively. In the experiment, the 'base' referred to in the description above is the collecting electrode of the ionization chamber. Different interfaces are created by changing the scatterer. A list of the interfaces for which dose backscatter factors were measured is provided in Table 4.1. Descriptions of the scatterers are also included.

The experiments are categorized for purposes of clarity.

'Zeroeth' measurements and 'absorber' measurements were done.

Zeroeth measurements determined dose backscatter factors at the interfaces for various two-component material slabs, as described above. The results are tabulated in Table 4.2.

Two types of absorber measurements were done. Mylar absorbers of different thicknesses were placed in two orientations. One, referred to as the ASD geometry, is that in which the absorbers were placed between the source and the detector. The other, referred to as the ASB geometry, is that where the absorbers were placed between the source and the (back)scatterer. In each of these geometries, dose backscatter factors were measured as functions of increasing

absorber thickness. The interfaces which were investigated are given in Table 4.1.

Measurements were made using different sensitive detection volumes or chamber thicknesses.

In addition, ASB type measurements were done with lucite absorbers for an air/lucite interface. The measurements were not as detailed as for the Mylar absorber measurements because lucite sheets less than 12mg/cm^2 thick were not obtainable. Mylar sheets as thin as 1.78mg/cm^2 are readily available commercially.

Another variation of the ASB type measurement was to use aluminium foils of varying thicknesses as absorbers. Aluminium and mylar scatterers were used to create an aluminium/mylar interface.

The Zeroeth, ASD and ASB type experiments correspond to those referred to as types (i), (iii) and (iv) in Chapter 1, where their possible applicability to biomedical situations was put forth.

Table 4.1 (a) Experimental Geometries

Source Geometry: Point

Experimental Geometry	Zeroeth	ASD	ASB
Interfaces:	aluminium/lucite	aluminium/mylar	aluminium/mylar
	air/lucite	air/mylar	air/mylar
	aluminium/mylar		aluminium/lucite
	air/mylar		air/lucite
	aluminium/A-150plastic		
	air/A-150plastic		
	cortical bone/soft-tissue (equivalent plastics)		
	air/soft-tissue (equivalent plastic)		
	copper/lucite		
	copper/mylar		
	cadmium/lucite		
	cadmium/mylar		
	tungsten/lucite		
	tungsten/mylar		
	bismuth/lucite		
	bismuth/mylar		
	carbon/lucite		
	carbon/mylar		

Table 4.1 (b) Experimental Geometries (continued)

Source Geometry:	Distributed	
Experimental Geometry	Zeroeth	ASD
Interfaces:	aluminium/lucite	bismuth/mylar
	air/lucite	aluminium/mylar
	aluminium/mylar	air/mylar
	air/mylar	
	aluminium/A-150plastic	
	air/A-150plastic	
	cortical bone/soft-tissue (equivalent plastics)	
	air/soft-tissue (equivalent plastic)	
	copper/lucite	
	copper/mylar	
	cadmium/lucite	
	cadmium/mylar	
	tungsten/lucite	
	tungsten/mylar	
	bismuth/lucite	
	bismuth/mylar	
	carbon/mylar	

Table 4.1 (c) Compositions of Scatterers

Scatterer	*Fraction by Weight of Constituent Elements*	*Effective Atomic No**	*Density (g/cm^3)*	*Dimensions (cm)*
Aluminium	Al: 1.0	13	2.69	7.62 x 7.62 x 1.2
Lucite, Perspex or PMMA $(C_5H_8O_2)_n$)	H:0.0805; C:0.5998;O:0.3196	5.85	1.17	7.62 x 7.62 x 1.8
Mylar or Melinex $((C_{10}H_8O_4)_n)$	H:0.042; C:0.625;O:0.333	6.24	1.4	7.62 x 7.62 x 0.85
A-150 or Shonka plastic	H:0.102;C:0.768; N:0.036;O:0.059; F:0.017;Ca:0.018	5.49	1.12	7.7 x 7.6 x 2.7
Copper	Cu: 1.0	29	8.93	5.08 x 5.08 x 0.3
Cadmium	Cd: 1.0	48	8.65	5.08 x 10.16 x 0.1
Tungsten	W: 1.0	74	19.3	5.08 x 5.08 x 0.075
Bismuth	Bi: 1.0	83	9.8	disc, 6.2cm diameter, 0.6cm thick
Carbon	C: 1.0	6	2.3	5.08 x 5.08 x 0.5
Air	N:0.755;O:0.232; A:0.013	7.36	1.23 $x10^{-3}$	
Cortical bone equivalent plastic[1]	H:0.025;C:0.286; N:0.009;O:0.404; Cl:0.005;Ca:0.268; Mg:0.003;S:0.004	10.3	1.9	7.62 x 7.62 x 0.6
Soft-tissue equivalent plastic[1]	H:0.102;C:0.745; N:0.019;O:0.133; Cl:0.001	5.35	1.05	7.62 x 7.62 x 1.6

[1] *Donated for experimental use by C.Kwok.*

"The effective atomic number in the preceding table is given by

$$\bar{Z} = \frac{\sum_{i=1}^{n} p_i \frac{Z_i^2}{M_{A_i}}}{\sum_{i=1}^{n} p_i \frac{Z_i}{M_{A_i}}}$$

where Z_i is the atomic number of element i

p_i is the fraction by weight of element i

M_{A_i} is the atomic mass of element i

n is the total number of elements in the medium.

4.3 Materials and Methods

A large part of the experimental work was done in a fumehood. This provided an environment that was convenient to use and sufficiently contained so that it afforded some protection in the event of spillage of radioactive solution. The window of the fumehood could be partially lowered to provide shielding when the source was not covered.

Photograph #1 on the following page is of the equipment in its working position. The extrapolation chamber, that is, the detector, is shown in Figure 4.1. In Photograph #1, the detector is upright, clamped in a lucite stand which was made for this purpose. Black coaxial cable can be seen leading from a small box near the lower end of the detector to the electrometer, which is the brown-covered, rectangular box on the table. The cable is partly wrapped in foam and the lucite stand in the fumehood sits on Styrofoam; these were found to reduce fluctuations in the currents.

Photograph #1 The Experimental Arrangement

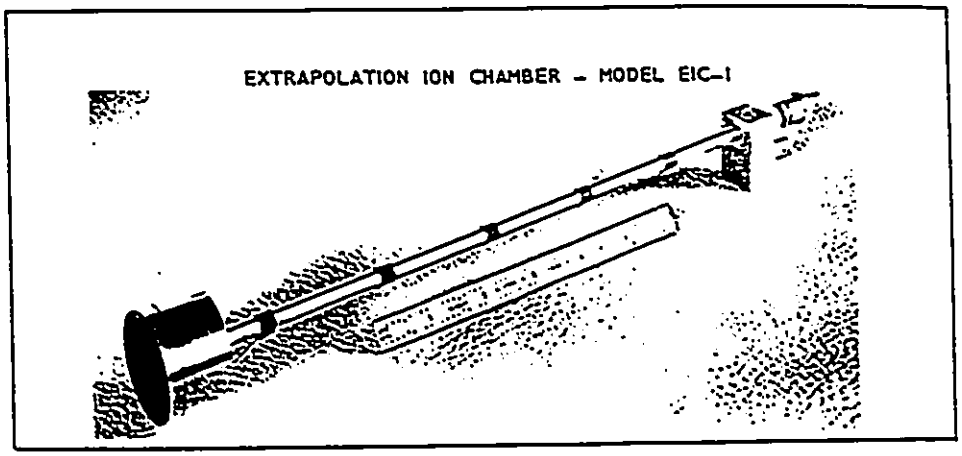

Fig 4.1 The Extrapolation Chamber (*courtesy* Far West Technology Inc.)

The computer on the table is interfaced* to the electrometer. This facilitated data collection and analysis.

The source mount, shown on its own in Photograph #2, is in place on top of the detector in Photograph #3. It is not readily discernible but is located directly below the lucite scatterer. Figure 4.2 is a side and top view of the source mount, illustrating the recess into which the detector fits and the open region over which a Mylar sheet, acting as a source substrate, is placed. It is made of aluminium alloy and screws into the lucite stand which holds the detector.

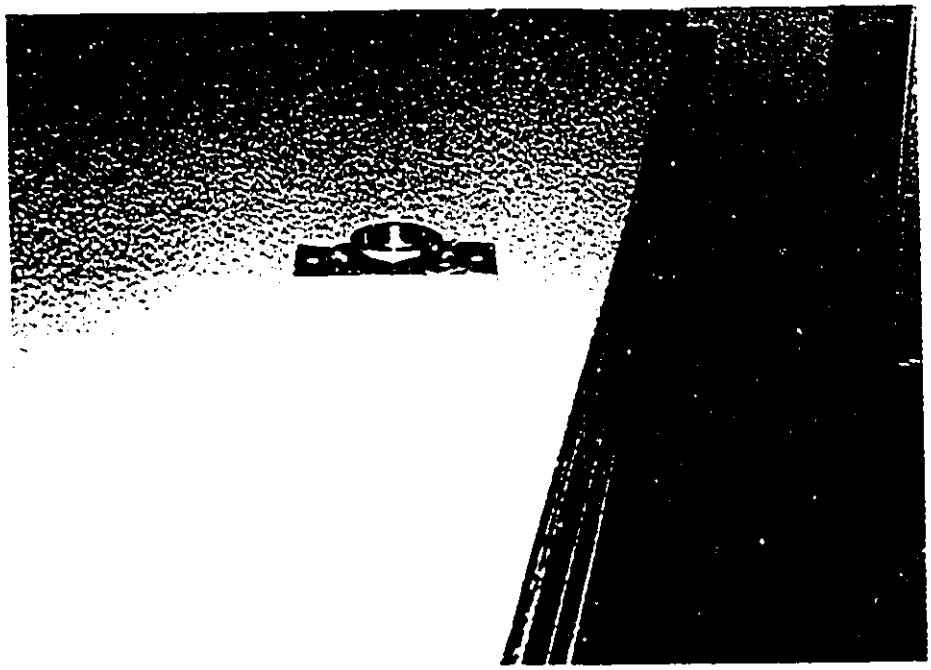

Photograph #2 The Source Mount

* *A special thanks to Kenrick Chin who did this and therefore improved the efficiency of the data collection.*

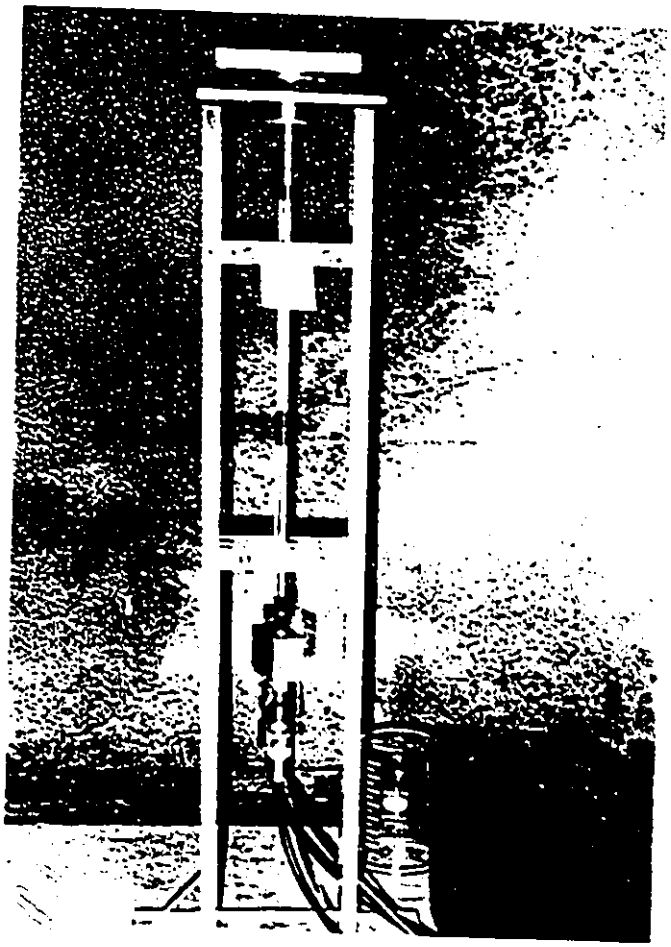

Photograph #3 Extrapolation Chamber in its lucite stand with source mount and a scatterer in place.

Fig 4.2 The Source Mount

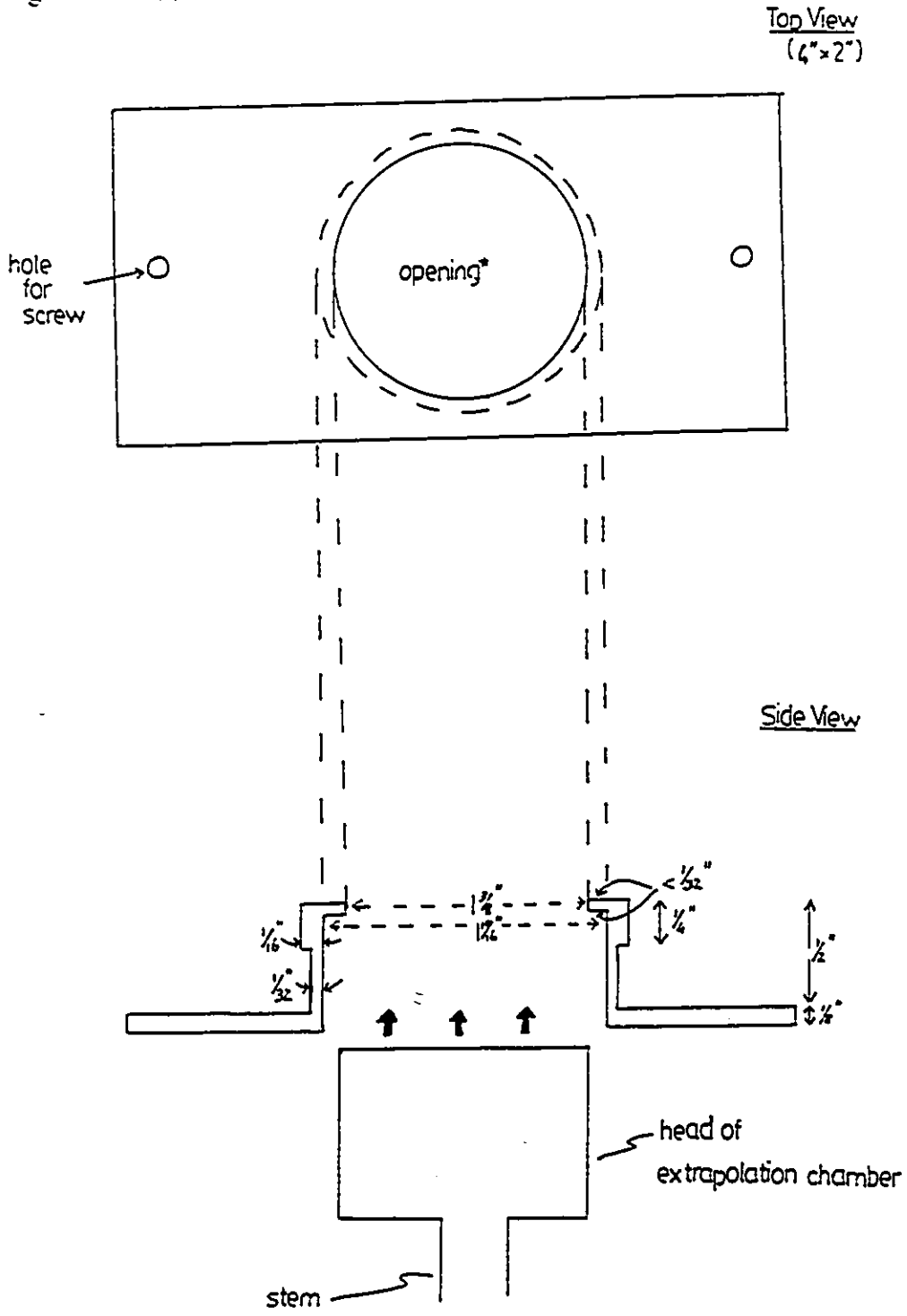

*Mylar substrate over opening, held taut by O-rings

Figure 4.3 shows the detector and source mount relationship. The point source was deposited on the Mylar substrate with the source mount already clamped in position. This allowed an immediate check on the chamber response and electrometer, and measurements could be started without having to reinstall the source mount.

The scatterers were changed remotely, using tongs about 1/2 m long. Zeroeth measurements were therefore not technically difficult. ASB type measurements were less simple; mylar or lucite absorbers were placed, using tongs, on the source and below the scatterer. The ASD type measurements were the most demanding; each measurement required, in addition to positioning absorbers, as for the ASB measurements, that the source mount be unscrewed, removed and then reinstalled.

These experiments therefore tested source integrity, which was of concern because the source was deposited on, and covered by, Mylar about 0.35mg/cm^2 (that is, 2.5μm) thick. Experimental reproducibility in general, and in particular, as being affected by repositioning of the scatterers, were also addressed. Each backscatter factor measurement was repeated at least once and scatterer repositionings were taken into account during each measurement.

Each measurement required at least 15 minutes, with more time being needed for the 'absorber' measurements. A typical experimental protocol is outlined shortly. Every backscatter factor determined involved obtaining 800 current samples for each of the pair of scatterers. A set of 100 current samples was taken at a time and the mean and standard deviation determined; this was done for positive and negative polarities applied to the detector and for four repositionings of each scatterer. The arithmetic mean and standard deviation of the currents from reversed polarities were calculated. The weighted average over the four scatterer positionings was obtained, and effects due to these repositionings were incorporated into the overall uncertainty by Chi-square analysis. The computer programme used for data acquisition and analysis is included in Appendix B.

Fig 4.3. Detector/Source-Mount/Scatterer Relationships

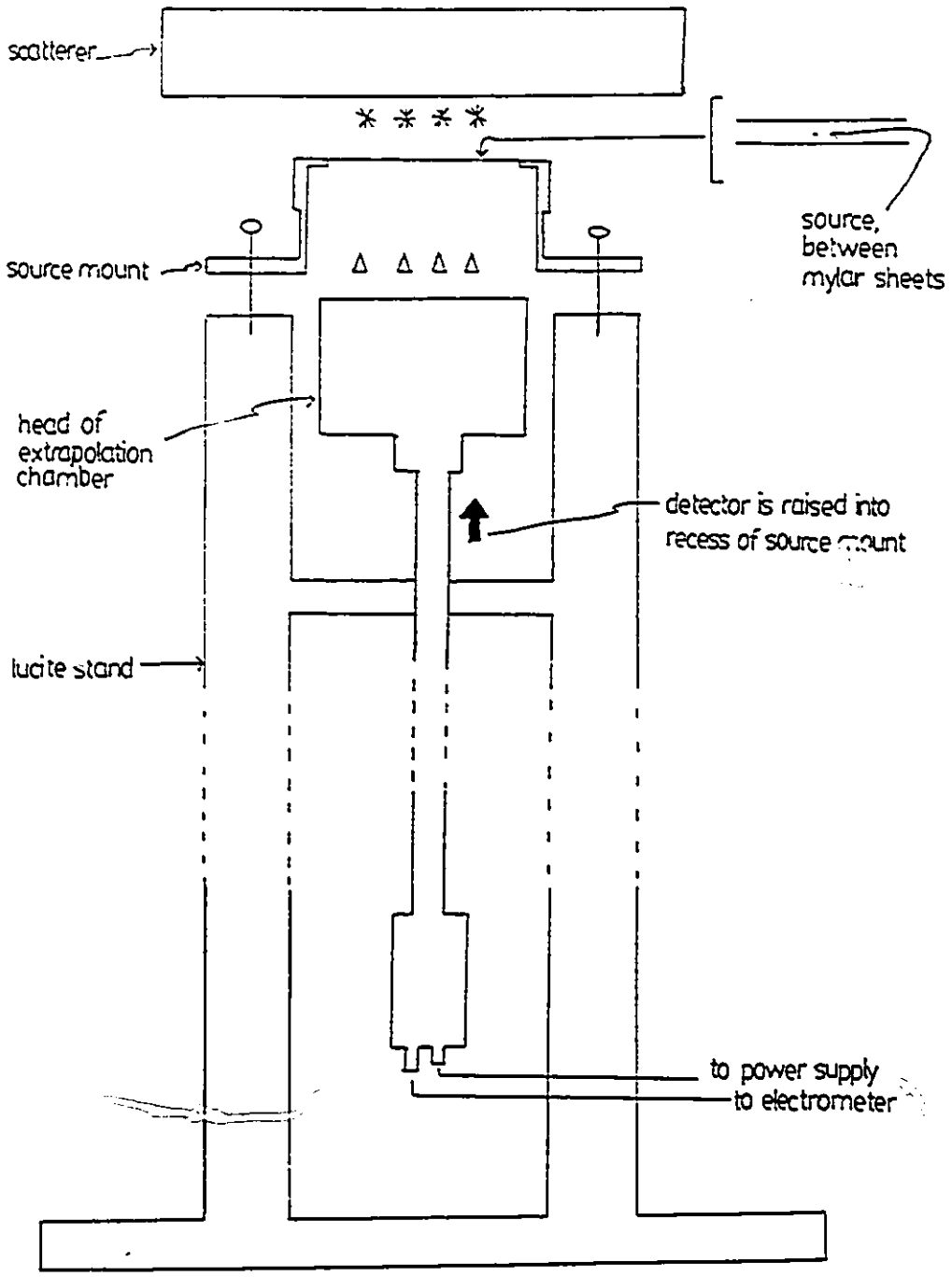

The experimental procedure for determining the dose backscatter factor for the aluminium/Mylar (Al/M) interface is as follows. The sequence of polarity and scatterer changes was intended to offset any linear drifts in the current collection system.

Experimental Protocol for Al/M Interface:

Repositioning Tally	Scatterer in Place	Polarity*	Ionization Current Sampled	
1^{Al}	Al	+	100 samples)	Arithmetic
		-	100 samples)	mean taken
1^{M}	M	-	100 samples)	"
		+	100 samples)	
2^{M}	M	+	100 samples)	"
		-	100 samples)	
2^{Al}	Al	-	100 samples)	"
		+	100 samples)	
3^{Al}	Al	+	100 samples)	"
		-	100 samples)	
3^{M}	M	-	100 samples)	"
		+	100 samples)	
4^{M}	M	+	100 samples)	"
		-	100 samples)	
4^{Al}	Al	-	100 samples)	"
		+	100 samples)	

* *A battery power supply was used to provide a + or - 90V potential across the electrodes.*

The currents measured at reversed polarities were different. The disparity increased with measured ionization current with the largest differences on the order of about 3% - that is. 3pA differences in nominal 100pA readings.

This change in current with polarity is mentioned in the literature (Boag 1964; Boag 1963; van der Zwan and Geiger 1986). It is referred to as a 'polarity current' or 'polarity effect' and is caused by various conditions. It can be caused by beta particles and secondary electrons trapped in the collecting electrode or be the result of change in the effective detector volume which could arise from space charges distorting the electric field between the electrodes (Boag 1964). The ionization current taken as being "correct" is the arithmetic mean of the two currents measured at reversed polarities (van der Zwan and Geiger 1986).

Throughout the experiments, ambient temperature and pressure were monitored and dose backscatter factors were found to be independent of them. This is because the backscatter factor is a ratio of currents; effects which temperature and pressure changes have on the absolute currents measured cancel out when the ratio is determined, particularly since the ratio is obtained in a period which is sufficiently short so that severe fluctuations in temperature and pressure do not occur.

4.3.1 The extrapolation chamber

The ionization method of dosimetry was used. An ionization chamber is a device or cavity which can be used to determine the energy absorbed per unit mass (that is, the dose) in the medium in which it is placed. The Bragg-Gray principle is invoked if the cavity is so small that is does not disturb the electron fluence traversing the cavity; it is as though the cavity were absent. Then, the relation between the ionization measured in the cavity and the absorbed dose in the medium is given by

$$E_m = J_m [\langle W_{air}(S/\rho)_{MA} \rangle] \qquad (4.4)$$

where E_m is the energy absorbed per unit mass or absorbed dose,

J_m is the number of ion pairs per unit mass of air in the cavity,

W_{air} is the energy required per ion pair formed in air,

and $(S/\rho)_{MA}$ is the ratio of mass stopping power of the medium to that of air.

The extrapolation chamber, invented by Failla, is a type of ionization chamber which satisfies the conditions for Equation 4.4 to hold. It provides a means of measuring ionization in a very thin layer of air, and is ideal for surface and depth dose measurements. The distinguishing feature of an extrapolation chamber is that the sensitive volume or air gap is variable.

The ionization per unit volume of air, J_v, is determined as a function of gap spacing d, such that $J_m = \frac{1}{\rho_{air}} \lim_{d \to 0} [J_v(d)]$, where ρ_{air} is the density of air. In practice, one can measure ionization current I as a function of gap spacing d; the limiting slope of such an extrapolation curve is used to calculate the ionization per unit mass of air in a vanishingly small cavity, namely, J_m. Hence, one can infer absorbed dose for the case of no cavity present. (Loevinger 1953; Failla 1937)

The small size of an extrapolation chamber's sensitive volume allows one to assume that it does not disturb the electron fluence. At the same time however, the small ion collection volume produces low ionization currents. Values from 10 to 100 pA were typical of the experiments performed here. The consequent demands placed on the current measuring system are outlined in the following section.

Figure 4.1 shows the extrapolation chamber purchased from Far West Technology, Inc. for use in these experiments. It is 35.0cm (13 3/4 ins) long, including the connectors. The stem is 29.2cm (11 1/2 ins) long, and the head, about 2.3cm (0.9 ins) long, with a diameter of 3.81cm (1 1/2 ins). It weighs 150g (0.33 lbs).

The air gap spacing is continuously variable; the space is between the entrance window, which is one electrode, and the collecting electrode. The

aluminium casing of the head supports the entrance window. This aluminium casing, which is cylindrical, turns on a brass sleeve, thereby allowing the spacing between the electrodes to be changed. There is a reference mark on the casing and the sleeve which facilitates reproducing air gap spacings. Zeroeth measurements, as described in Section 4.2, were made at 1, 2, 3 and 4 turns' settings of the aluminium casing. These correspond to air gap spacings of 1, 2, 3 and 4 mm, respectively.

There are two entrance windows which can be used. One is made of conductive polyethylene and is 6.9mg/cm^2 thick. The other is made of graphite coated polypropylene and is 0.2mg/cm^2 thick. The collecting electrode and guard ring are made of A-150 plastic, which is a soft-tissue equivalent material. A guard ring prevents leakage current from reaching the collecting electrode and it maintains a uniform electric field between the electrodes; it also defines the sensitive (detection) volume of the chamber. (Boag 1964) The sensitive region of the chamber used here is a right circular cylinder, diameter 1.05cm and height equivalent to the air gap spacing.

A sketch of the extrapolation chamber's interior, showing several of the features described above, is given in Figure 4.4. It was graciously made available for inclusion in this document by a representative of Far West Technology, Inc.

Fig 4.4. Interior of Extrapolation Chamber (*courtesy* Far West Technology Inc)

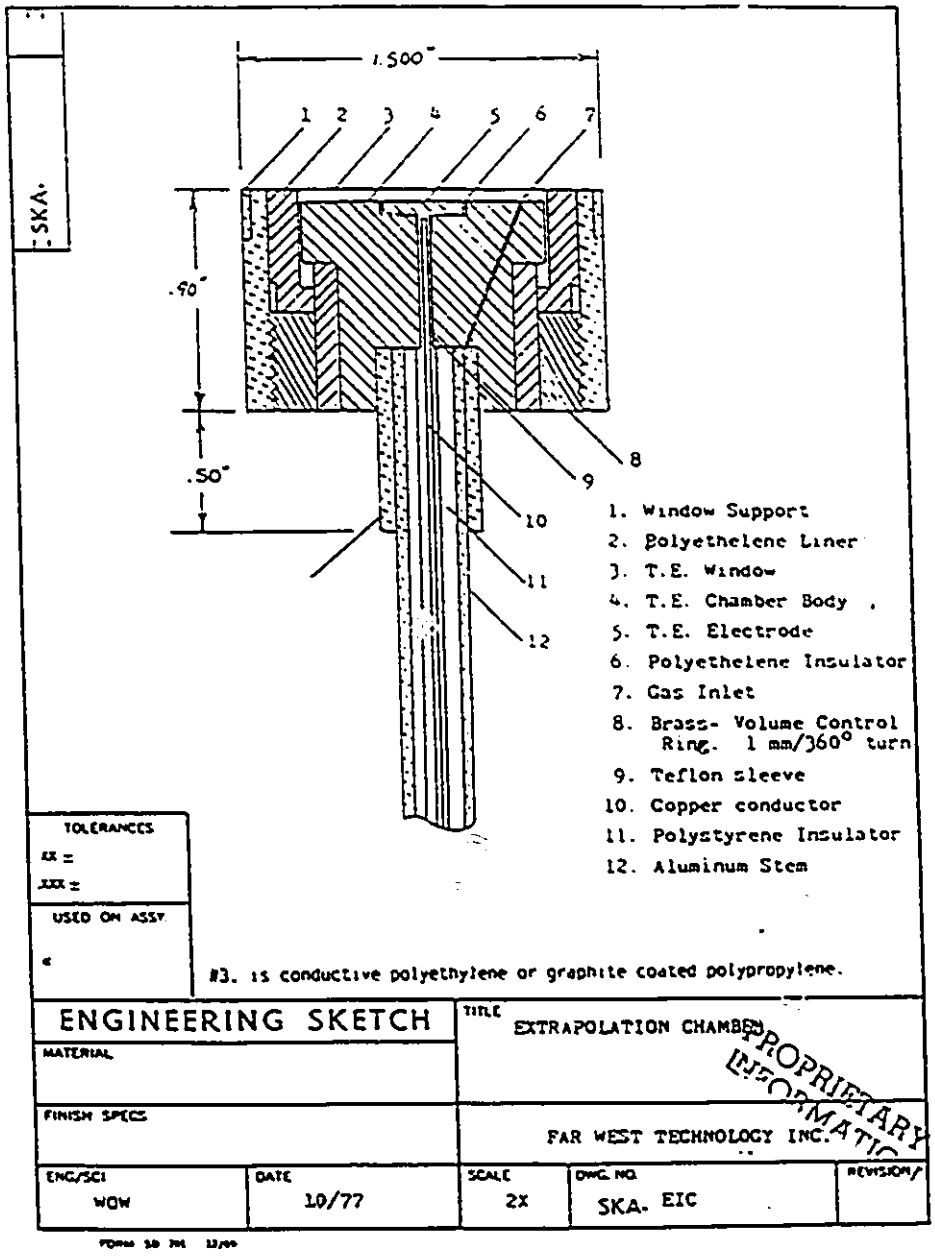

4.3.2 The electrometer

A Keithley614 electrometer was used for measuring ionization currents. It is a compact instrument, 12.7cm x 21.6cm x 35.9cm (5in x 8 1/2in x 14 1/8in), and weighs 3.3kg (7.2lbs). It can be either line or battery powered, and was operated on line throughout the experiments. The digital output was sampled by computer via an interfacing of the computer and the electrometer. This improved data collection and permitted immediate data analysis.

The electrometer is sensitive to 10^{-14}A and has a resolution of 0.1pA on the 200pA output range and 0.01pA on the 20pA output range. The work done here required accuracy in current readings of better than 1% in the pA range. This requirement was fulfilled by the Keithley614. For example, backscatter factors of about 8% with an absolute uncertainty of ~0.1% were measured. This translates into an uncertainty in the current of about 0.07%. The time constant of the electrometer, that is, the time required to respond to an input signal, is about 400ms.

Ion pairs produced in the ionization chamber are collected during a certain sampling time to give an ionization current. Shot noise is associated with the discrete nature of the ion pairs (Evans 1955), and it is estimated to be 0.02% at 50pA here. It is therefore negligible. This calculation is included in Appendix D.

The diagram below shows some of the relevant electrical connections in the experimental set-up. The power supply was a series of batteries, and a switch allowed polarity reversal of this high voltage.

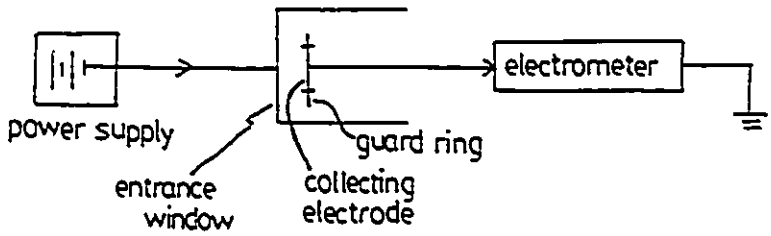

Sporadic current fluctuations were observed occasionally. Their occurrence was rare at high source intensity and became more frequent at lower ionization currents, particularly below 10pA. Consequently, making measurements at these low currents was kept minimal. It was found that wrapping the cable connecting the chamber to the electrometer in foam helped the current stability. Other than on-line interference in the building power supply, no plausible explanations are offered to account for these current spurts. Their existence is documented, and apart from having had to repeat several measurements because of a few of these current spurts, the current collection went smoothly and the electrometer was, for the most part, convenient and reliable.

4.3.3 Data collection and analysis

A sample experimental procedure was given in Section 4.3. Similar protocols were followed for measuring ionization current ratios for all the interfaces listed in Table 4.1. The computer programme, written in BASIC, to sample the ionization current, average over reversed polarities and over scatterer repositionings, as well as to do an error analysis on the current ratio, is listed in Appendix B. As already mentioned, a dose backscatter factor and its uncertainty can be obtained in about twenty minutes and a record of the experimental data is kept on diskette. The computer interfaced to the electrometer is a Xerox, model 6060, IBM compatible personal computer.

4.3.4 Source preparations

(i) ^{32}P point source preparation

Five millicuries (5mCi) of ^{32}P as orthophosphoric acid in 0.041mls of

water were purchased from New England Nuclear (DuPont). In its vial, the sample was reduced to approximately 10µl by evaporation for two hours under a heat lamp which was 13ins above the vial.

Half of the reduced volume, that is, 5µl, was placed, using a pippette, onto the Mylar substrate of the source mount (shown in Figures 4.2 and 4.3). This was dried in open air, in the fumehood, for about one hour. The dried point source, diameter about 2mm, was sealed with another sheet of Mylar. A ring of polyurethane spray was used as a glue to seal the covering Mylar sheet onto the substrate. The source, in the centre of the substrate, was not covered by the polyurethane spray. The covering Mylar sheet, sprayed with the sealant, was held taut in a 3in diameter embroidery hoop that was placed over the source: a secure seal between the Mylar substrate and cover was achieved within 10 minutes. The excess covering Mylar sheet and accompanying embroidery hoop were then cut away.

The Mylar supporting and covering the source was obtained from Steinerfilm Inc. Its mass thickness was measured as 0.35mg/cm^2. The Mylar substrate was held in place by rubber O-rings on an aluminium mount, as shown in Photograph #2. A strip of Aquadag, a colloidal graphite suspension, provided a conductive pathway between the source and the aluminium source mount which was always in electrical contact with the high voltage exterior of the detector's head. In this way, charge build-up in the source (Braden et al 1948), which could alter current collection, was prevented.

The sealed source on its aluminium mount fit over the extrapolation chamber as shown in Figure 4.2. Although the source mount was removed and reinstalled at least twenty times during the series of experiments in order to change the detector's chamber thickness (that is, air gap spacing) and to insert absorbers between the source and the detector (that is, ASD experiments), the integrity of the source was not compromised.

(ii) ^{32}P distributed source preparation

A thin beta source distributed over a circular area four centimetres in diameter was prepared with ^{32}P-orthophosphoric acid in aqueous solution.

The aluminum mount described above was used here as well. The substrate for the source was aluminized Mylar, thickness 0.35mg/cm^2, and the cover was a Mylar sheet of the same thickness.

The source was a grid of fifty ^{32}P point sources. Each point source was made from 5µl of radioactive solution. The total activity of the distributed source was estimated to be 3.6mCi at the time of preparation.

A 250µl syringe with a repeating dispenser that delivered 0.02 of the total syringe capacity at each dispensation was used to deposit 5µl droplets of source solution onto the substrate.

The source mount, which held the substrate as described earlier, was positioned on a micrometer table. The latter was screwed into the base of a custom-made lucite box. The lucite container provided radiation protection and was constructed by Mr. K.Chin.

The left wall of the box was absent in order to allow placement and removal of items such as the vial of radioactive liquid and the source mount. The two arms of the micrometer table were accessible from outside the box via holes in the right and front walls. These arms or handles were equipped with vernier scales which allowed 0.01mm adjustments, in the x and y directions, of the micrometer table.

The syringe-dispenser apparatus was suspended directly above the source mount by means of two holes in the roof of the box, and the source mount could be moved up to about 4cm in the x and y directions by turning the micrometer table handles. Depressing a button on the dispenser delivered a 5µl aliquot from the syringe. This was done remotely by moving a lucite rod, attached to the roof of the box, so that it depressed the button.

The micrometer table was lent by Sciencetech for use in this work. It was rectangular and was 14cm by 12 cm. The encasing lucite container was 25cm

wide, 20 1/2cm high and 22 1/2 cm deep. The lucite rod, which extended 17cm beyond the right wall of the box, was 31cm long.

Both filling of the syringe and dispensing of the radioactive solution were done within the lucite container. There was minimal personal radiation exposure. In order to provide containment in the event of spillage of the radioactive solution, the source preparation was done in a fumehood.

A grid of ^{32}P droplets was made by depositing 5µl aliquots at 5mm intervals over the source mount Mylar surface. The fifty drops were left to dry for about five hours, and the source was covered in the manner used for the point source.

As for the point source, integrity of the distributed source remained intact throughout the experiments.

Uniformity of the distributed source was assessed in two ways. The source was surveyed using a Geiger-Müller detector with a 1cm diameter window; and an autoradiograph of the source was made and the optical densities of each droplet measured. The first method gave a variation in count rate of about 10% and the second method indicated that the optical densities of the droplets varied about 20%. These are one standard deviation estimates obtained from ten and forty-five measurements, respectively.

The distributed source approximates a plane source. Each droplet contains roughly the same activity, and the number of droplets present in concentric rings around the centre of the source increases with distance from the centre.

4.4 Results for ^{32}P, Point Source

Results from the various types of experiments are presented in different subsections for purposes of organization and clarity. Evidence for the dependence of dose backscatter factor on chamber thickness (that is, inter-electrode spacing) is given in Section 4.4.1. The subsequent section summarizes the results of the

geometry experiments, and the last two sections describe the ASD and ASB experimental results. General trends of these latter results are conveniently summarized by "relaxation lengths".

A relaxation length is defined here to be the absorber thickness which reduces a dose backscatter factor by 1/e, where e~2.718. It is used to describe, quantitatively, the fall-off of dose backscatter factor with absorber thickness and is denoted here by v. v_{ASD} and v_{ASB} values are summarized in Sections 4.4.3 and 4.4.4.

4.4.1 Dependence of backscatter factor on chamber thickness

Dose backscatter factors, B, were found to be independent of chamber thickness when the thick detector window (6.9mg/cm^2) was used, and dependent on chamber thickness when the thin window (0.2mg/cm^2) was used. This difference is due to the filtering out of low energy electrons by the thick window. Evidence for the dependence and lack of it, for the cases of thin and thick detector windows, is given shortly.

Zeroeth measurements were done with both windows. Extrapolation of thin window data, which varied with inter-electrode spacing, to infer B values for the case of zero inter-electrode spacing, provided dose enhancement and reduction factors at about 1.4μm from the interface. Such extrapolated values are referred to as 'true interface values' in this work.

Only the thick window was used for experiments investigating the variation of B with distance from the interface because a thin window broke after use in a few experiments, demonstrating that it could not withstand the trauma of many source mountings. The replacement thin window was therefore saved for Zeroeth measurements.

(a) The Thick Window -

Preliminary measurements at air/soft-tissue-equivalent plastic interfaces indicated that backscatter factors did not vary with chamber thickness. An intensive investigation was carried out in order to confirm this.

ASD type measurements with polyethylene absorbers at an aluminium/lucite interface were done at 1, 2, 3, and 4 turns of the chamber. These turns correspond to electrode spacings of 1, 2, 3 and 4 mm, respectively, as mentioned earlier. Figure 4.5 demonstrates that there is no dependence of backscatter factor on chamber thickness since the four curves lie almost one on top of the other.

Similar experiments were done with Mylar absorbers for aluminium/Mylar and air/Mylar interfaces. Extreme inter-electrode or air-gap spacings of 1 and 4 mm were used. Figures 4.6 and 4.7 show no difference between the backscatter factor curves for the two electrode spacings.

Dose backscatter factor, B, was defined by Equation 4.1. Values of dose backscatter factors in this report are denoted frequently as %B, which means B x 100%.

ASB type measurements for aluminium/Mylar and air/Mylar interfaces, with Mylar absorbers, were done at 1 and 4 turns chamber thickness. The resulting backscatter factor curves, Figures 4.8 and 4.9, do not indicate that the backscatter factors vary with electrode spacing.

Relaxation lengths were determined from the ASD and ASB data. They are listed in the table below. ASD relaxation lengths for the two inter-electrode spacings agree for both interfaces, while ASB relaxation lengths for the air/Mylar interface appear to be different. The difference is attributed to fluctuations in the experimental data which are larger than calculable uncertainties. Additionally, the ASB relaxation lengths for the aluminium/Mylar interface are not markedly disparate. Therefore, the ASB and ASD experimental data strengthen the plausibleness of the assertion that backscatter factors do not vary with inter-electrode spacing.

Relaxation Lengths ν (mg/cm^2 Mylar)

Experimental Geometry:	ASD		ASB	
Interface:	Aluminium/ Mylar	Air/ Mylar	Aluminium/ Mylar	Air/ Mylar
Electrode Spacing				
4turns (4mm)	169 [6]*	213 [5]	30 [1]	28 [1]
1turn (1mm)	179 [10]	213 [5]	23 [1]	64 [14]

* *Bracketed quantities are uncertainties*

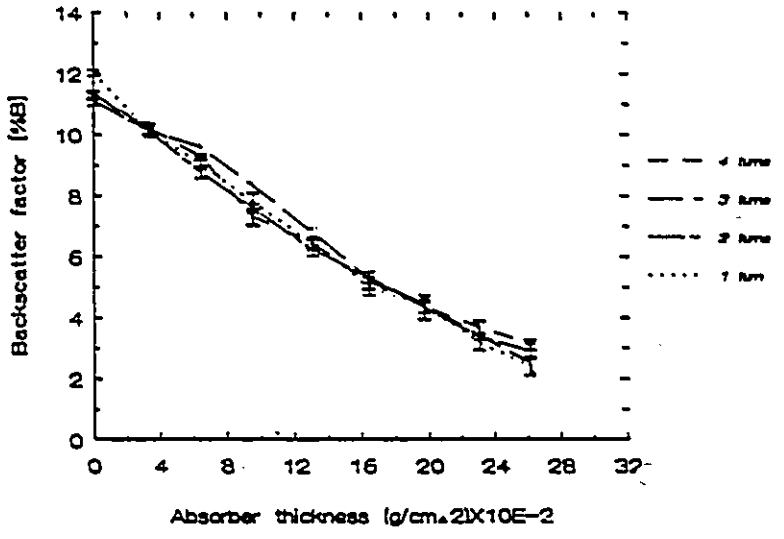

Fig 4.5 Aluminium/lucite backscatter factor variation with polyethylene absorbers between source and detector for four electrode spacings.*Note: %B = B x100%*

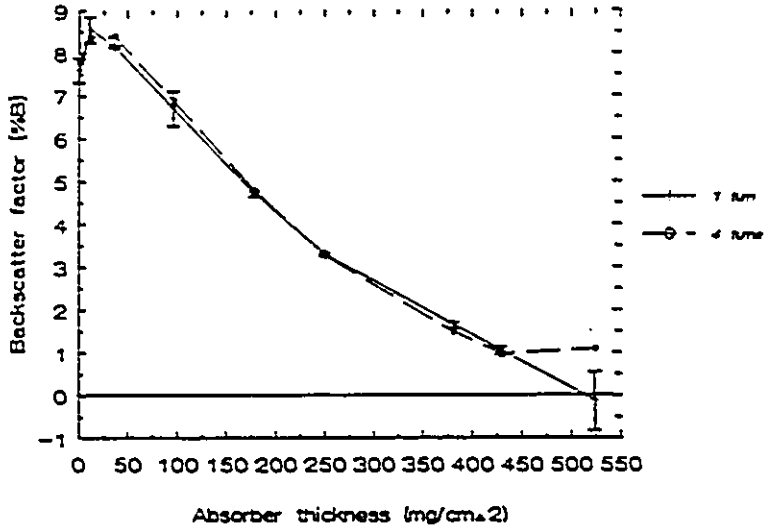

Fig 4.6 Aluminium/Mylar backscatter factor variation with Mylar absorbers between source and detector, for two electrode spacings.

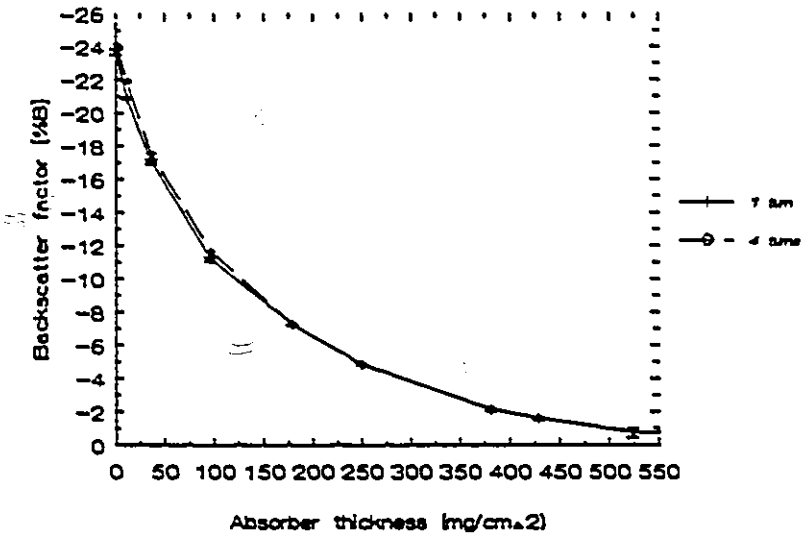

Fig 4.7 Air/Mylar backscatter factor variation with Mylar absorbers between source and detector, for two electrode spacings.

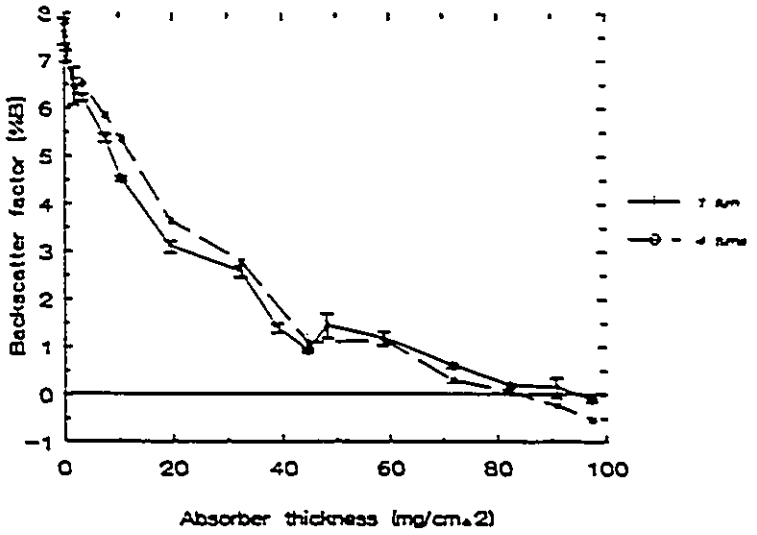

Fig 4.8 Aluminium/Mylar backscatter factor variation with Mylar absorbers between source and scatterer, for two electrode spacings.

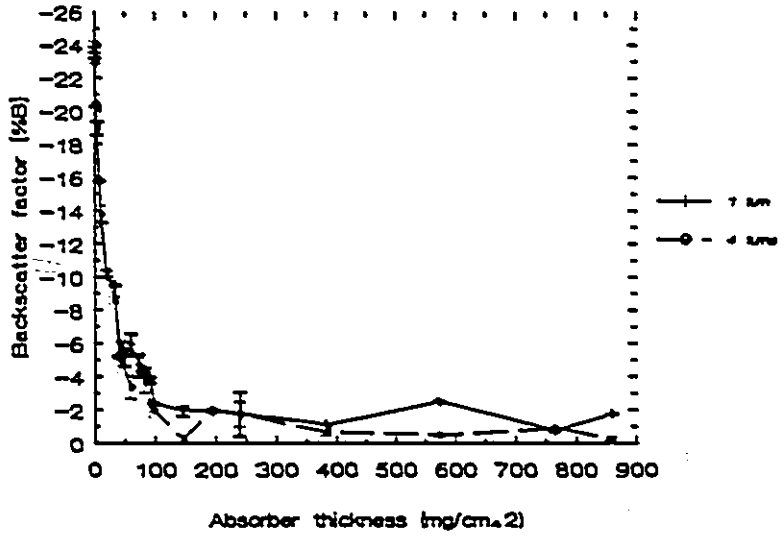

Fig 4.9 Air/Mylar backscatter factor variation with Mylar absorbers between source and scatterer, for two electrode spacings.

The final and most extensive piece of evidence to substantiate the claim of backscatter factors being independent of chamber thickness came from Zeroeth measurements. Backscatter factors were determined for 18 material interfaces; at each interface, backscatter factors were measured for at least three different inter-electrode spacings.

The experimental data were subjected to a one-way analysis of variance (ANOVA) test. The question at hand was presented in the following null hypothesis - that a backscatter factor at 1mm inter-electrode spacing is not different from that at 2mm, 3, or 4mm inter-electrode spacings -

$$H_o: B_1 = B_2 = B_3 = B_4.$$

The alternative hypothesis was

$$H_1: B_1 \neq B_2 \neq B_3 \neq B_4.$$

The raw data of the ANOVA are included in Appendix C. The null hypothesis could not be rejected at a 95% confidence level for 15 out of 18 cases. The probability of making a type I error (that is, of rejecting the null hypothesis when it is true) was α=0.05, and the probability of making a type II error (that is, of not rejecting the null hypothesis when it is false) was β=0.20; the power of the test was 80%, for detecting at least a difference of 0.3 among the backscatter factors.

The three anomalous cases were air/Mylar, bismuth/Mylar and bismuth/lucite interfaces. These data were examined for trends in the variation of backscatter factor with inter-electrode spacing since rejection of the null hypothesis meant solely that backscatter factors at various spacings were not the same. No trends were evident in the air/Mylar case. However, they were evident in data from both bismuth interfaces. Backscatter factors here decrease with decreasing inter-

electrode spacing: the values at 1mm and 4mm spacings differ by roughly 5%. This variation of backscatter factor with chamber thickness can be explained by the following.

Bismuth has the highest atomic number and scattering power of the scatterers used. Electrons backscattered from it are more energetic than ones backscattered from the other elements. Therefore, although low energy electrons are stopped by the thick window so that a variation of backscatter factor with inter-electrode spacing for most scatterers is clear only when the thin window is used, it is not unreasonable that such a trend could be evident only for the scatterer giving the largest backscatter factor when the thick window is used.

(b) The Thin Window -

The one-way ANOVA described above was also performed on these data. Raw data for the 17 interfaces considered are included in Appendix C. The null hypothesis, that B values for the different inter-electrode spacings are equal, could not be rejected at the 95% confidence level for 6 out of the 17 cases. The 6 cases were tungsten/Mylar, tungsten/lucite, cadmium/lucite, aluminium/lucite, air/lucite and bone/soft-tissue.

For a majority of the cases, however, it was clear that there was a variation of B with inter-electrode spacing. The trends could also be discerned in several of the six cases noted above, but with considerably less clarity. The variations observed were the following - that dose enhancement decreased with decreasing inter-electrode spacing and that dose reduction increased with decreasing inter-electrode spacing.

The distributed source data in Section 4.5.1 provide further evidence to support the observations noted here. That is, backscatter factors vary with inter-electrode spacing.

Consequently, these thin window data were extrapolated to determine "true

interface values". The latter, for a ^{32}P point source, are tabulated in the following section.

The variation of backscatter factor with chamber thickness is not severe. Differences in backscatter factors measured at 1mm and 4mm inter-electrode spacings range from less than one percent to about ten percent for the interfaces considered. Figure 4.10 illustrates these observations for several air and solid material interfaces, for a ^{32}P point source; the zero values are the results of linearly extrapolating the data obtained for finite chamber thicknesses.

Electrons with energy less than about 70keV are not detected with the thick window. The contribution of these low energy electrons, allowable by the thin window, must account for the dependence of backscatter factor on chamber thickness (that is, inter-electrode spacing) when the thin window is used.

Electrons backscattered from lower atomic number scatterers are lower in energy than ones backscattered from higher atomic number scatterers. This is consistent with the observation that the energy spectrum of ^{32}P electrons backscattered from low atomic number materials is diminished in the high energy region compared with similar backscattered spectra from high atomic number scatterers. (Chap 6, Mladjenović 1973)

Low energy electrons do not travel as far as more energetic electrons, and they deposit their energy within smaller distances from the starting point than more energetic electrons. Therefore, the energy deposited by electrons backscattered from lucite or Mylar constitutes a greater fraction of the energy deposited by electrons backscattered from higher atomic number scatterers when there is a smaller measurement region. This means that dose enhancement is smaller with a smaller detection volume; that is, backscatter factors decrease with decreasing chamber thickness. The converse relationship is expected for air interfaces.

Implicit in the above is that a greater number of electrons less energetic than 70keV are backscattered from lucite or Mylar than from higher atomic number scatterers. Many of these 'sub-70keV' electrons, after traversing the thin window,

are less than about 15keV, and the lowest energies are the most abundant. The electrons are therefore stopped at different distances within a 4mm air gap, with smaller stopping distances being more common than longer ones. Consequently, dose enhancement is reduced with decreasing inter-electrode spacing, as suggested in the preceding paragraph.

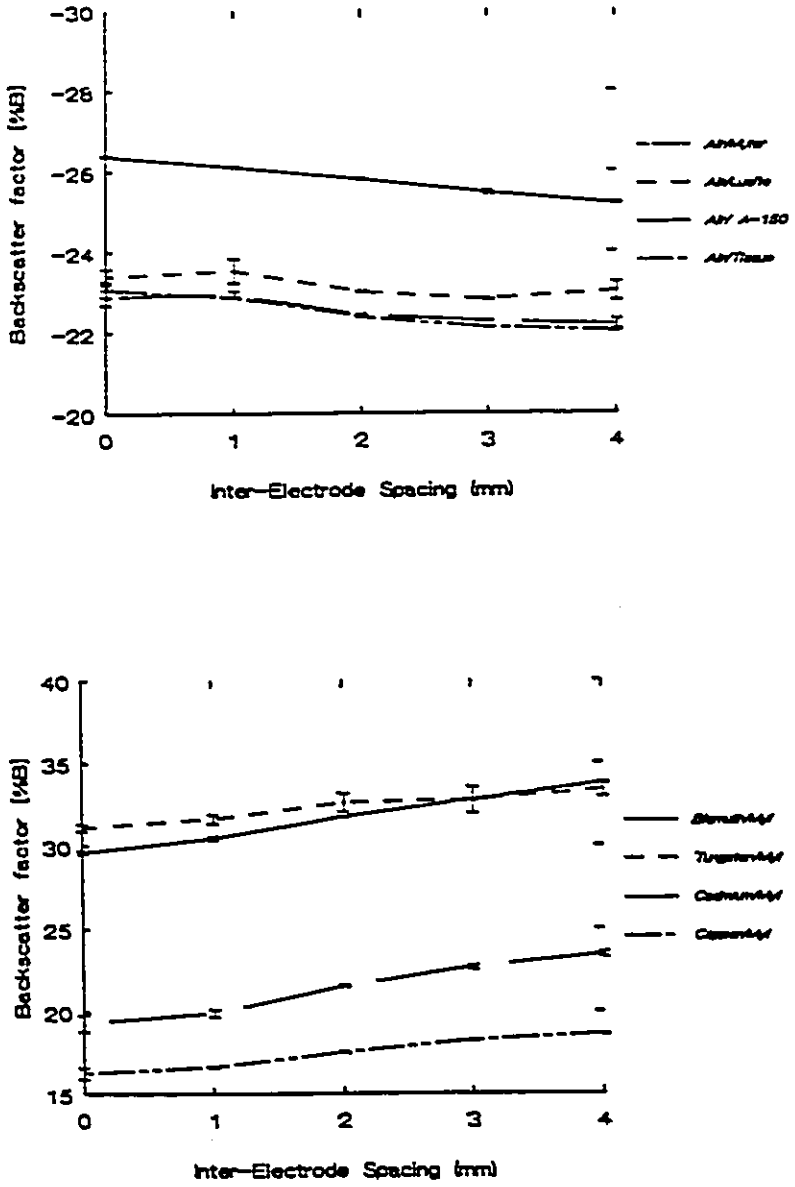

Fig 4.10 Variation of backscatter factor with inter-electrode spacing for a ^{32}P point source. Upper: air interfaces; Lower: solid material interfaces. Points at zero inter-electrode spacing are obtained by linear extrapolation of the other data points.

4.4.2 Zeroeth measurements

(a) Thick Window Values -

Table 4.2a gives the backscatter factors measured for the material interfaces listed in Table 4.1. The values are averages of data accumulated for different electrode spacings.

Backscatter factors increase with scatterer atomic number. This is attributed to more nuclear scattering, the cross-section for which goes as Z^2 (Section 2.1). Of greater interest is that the backscatter factor, B, is directly proportional to $\sqrt{\frac{Z(Z+1)}{M}}$, where Z and M are the atomic number and atomic mass of the scatterer. Figure 4.11a illustrates the straight line relationship, which is not surprising since a similar relationship between reflection coefficients and $\sqrt{\frac{Z(Z+1)}{M}}$ for various beta emitters has been documented (Chap 6, Mladjenović 1973), and B is essentially a measure of dose enhancement due to reflected or backscattered electrons. Following another proposed relationship between backscattered electrons and scatterer atomic number, (Baily 1980), B has been found to be proportional to log(Z+1) - Figure 4.11b.

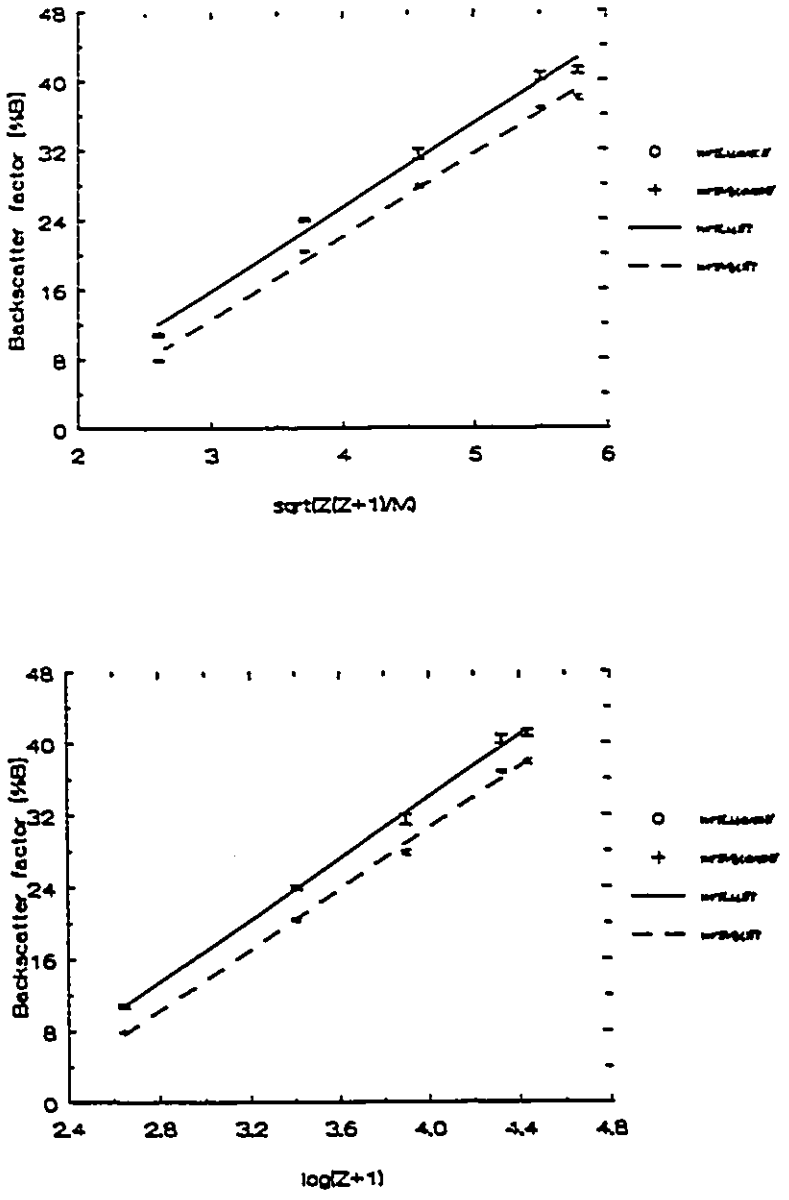

Fig 4.11 Dose backscatter factor relationships with scatterer atomic number. (a) Upper: Dose backscatter factor is proportional to $[Z(Z+1)/M]^{1/2}$; (b) Lower: dose backscatter factor is proportional to log(Z+1). *Explanation of legend: wrtLu = with respect to lucite; wrtMy =with respect to Mylar; exptl = experimental.*

No physical explanations are offered for these relationships. Although they are empirical, they are predictive and may be useful. It is also noted that the 'reference', Mylar or lucite, in the material interfaces considered, manifests itself in a vertical translation of the data. Backscatter factors with respect to lucite are higher than those with respect to Mylar. This finding parallels the observation that Mylar has greater scattering power than lucite.

Scattering power is a measure of how rapidly the mean scattering angle undergone by electrons increases with distance travelled in a medium. It is denoted by $\mu<\zeta^2>$ in the Fermi-Eyges multiple scattering theory outlined in Chapter 3. A relationship between backscatter factors and scattering power ratios has been found: the scattering power ratio is the ratio of scattering powers of the scatterers under consideration.

Scattering power data were taken from ICRU35 (ICRU35 1984). Although these vary with electron energy, the ratios for all scatterers considered here were fairly constant over a large energy interval. Specifically, scattering power ratios for several elements and compounds, with respect to lucite and Mylar, were constant between 100keV and 2MeV. Below 100keV, the ratios were constant to within 10%, with the variation most pronounced at low energies.

Figures 4.12 and 4.13 demonstrate the relationship between B and scattering power ratio. The scattering power ratio in Figure 4.12 is with respect to Mylar and that in Figure 4.13 is with respect to lucite. In both cases, $\ln(B) \propto (\text{scatt pwr ratio})^{1/6}$. Again, this relationship is entirely empirical.

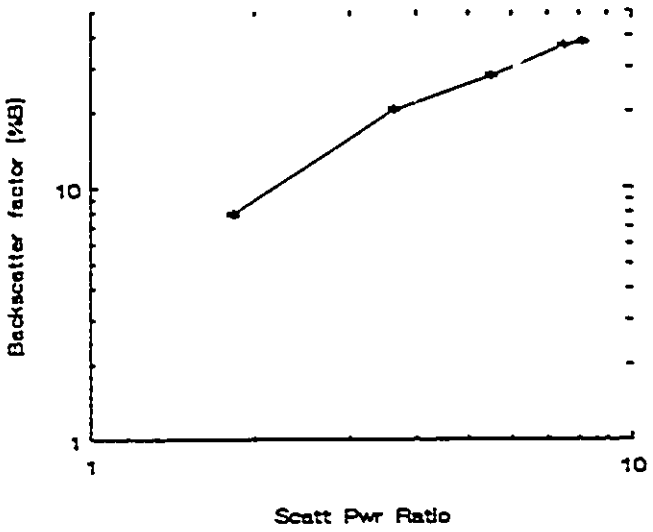

Fig 4.12 Dose backscatter factor as a function of scattering power ratio, with respect to Mylar.

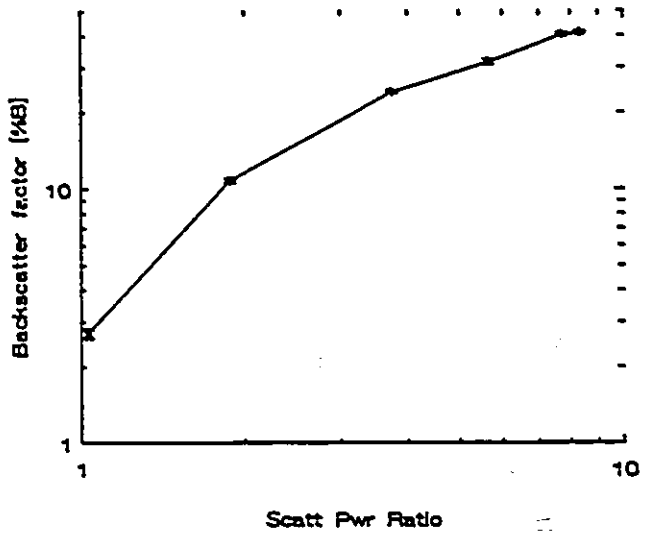

Fig 4.13 Relationship between dose backscatter factor and scattering power ratio, with respect to lucite.

Table 4.2 (a) Backscatter Factors for Zeroeth Geometry, Thick Window.

Source: ^{32}P

Source Geometry: Point

Interface	%B	[uncertainty]
Bismuth/Mylar	37.94	[0.29]
Tungsten/Mylar	36.75	[0.19]
Cadmium/Mylar	27.77	[0.28]
Copper/Mylar	20.44	[0.25]
Aluminium/Mylar	7.86	[0.09]
Bismuth/lucite	41.09	[0.36]
Tungsten/lucite	40.44	[0.49]
Cadmium/lucite	31.50	[0.60]
Copper/lucite	23.98	[0.24]
Aluminium/lucite	10.80	[0.21]
Cortical bone/soft-tissue*	8.24	[0.05]
Aluminium/A-150 plastic	11.77	[0.06]
Air/soft-tissue*	-20.23	[0.02]
Air/A-150 plastic	-20.75	[0.03]
Air/lucite	-21.39	[0.12]
Air/Mylar	-23.41	[0.13]
Carbon/Mylar	-3.16	[0.14]
Carbon/lucite	-0.54	[0.19]

* *tissue equivalent plastics*

(b) Thin Window "true interface values" -

Table 4.2b lists backscatter factors for the interfaces investigated with the thin window. The values are the results of linearly extrapolating the backscatter factors, as functions of inter-electrode spacing, to zero inter-electrode spacing.

When the thin window is used, the point of measurement is closer to the interface than when the thick window is used. Measured values of dose enhancement are smaller for the thin window than for the thick window, and the converse is the case for measured dose reduction factors (Tables 4.2 a and b). These observations are consistent with the results of the ASD geometry experiments described in the following section.

The data in Table 4.2b exhibit similar trends to those in Table 4.2a, namely, that dose enhancement increases with atomic number of the scatterer, and that dose enhancement factors with respect to lucite are larger than those with respect to Mylar.

Table 4.2 (b) "True Interface" Backscatter Factors

Source: ^{32}P

Source Geometry: Point

Interface	%B	[uncertainty]
Bismuth/Mylar	29.65	[0.12]
Tungsten/Mylar	31.07	[0.24]
Cadmium/Mylar	19.30	[0.48]
Copper/Mylar	16.27	[0.35]
Aluminium/Mylar	5.46	[0.11]
Bismuth/lucite	35.04	[0.35]
Tungsten/lucite	34.35	[0.65]
Cadmium/lucite	24.49	[0.30]
Copper/lucite	21.25	[0.69]
Aluminium/lucite	10.48	[0.57]
Cortical bone/soft-tissue*	7.47	[0.24]
Aluminium/A-150 plastic	9.94	[0.18]
Air/soft-tissue*	-23.15	[0.24]
Air/A-150 plastic	-22.93	[0.25]
Air/lucite	-23.41	[0.17]
Air/Mylar	-26.44	[0.02]
Carbon/Mylar	-4.60	[0.33]

* *tissue equivalent plastics*

4.4.3 *ASD measurements*

The fall-off of backscatter factor with intervening Mylar between source and detector in Figures 4.6 and 4.7 is roughly a decreasing exponential.

There is an initial rise in dose enhancement, to a maximum located between 10 1/2 and 35 mg/cm^2 absorber thickness, prior to the exponential decrease, for the aluminium/Mylar interface (Figure 4.6). The initial rise can be explained qualitatively by the following facts. Electrons reflected from aluminium have higher energy than those reflected from Mylar; aluminium, a higher atomic number material, is a stronger reflector of electrons; and the rate of energy loss (that is, the stopping power) is larger for lower energy electrons.

The higher energy electrons can penetrate the absorbers and reach the detector, where they deposit energy, while the electrons scattered from Mylar lose more of their energy in the absorbers, before reaching the detector. This greater filtration of Mylar scattered electrons continues for absorber thicknesses up to a certain point such that the ratio of backscattered doses increases initially.

With increasing intervening Mylar absorber, the measured differences between Mylar and aluminium backscattered spectra decrease, since electrons scattered from both materials lose increasingly more of their energy before reaching the detector. Consequently, the dose backscatter factor falls off with increasing absorber thickness; it is ~1% at 500mg/cm^2 of absorber.

The following is a pictorial description to supplement the explanation given above for the features of the aluminium ASD profile and to rationalize using sums of exponentials to fit the experimental data. The relative lengths of the arrows denote the relative energy depositions, as functions of absorber thickness x, from the three contributing elements.

The energy depositions are described as follows: $f_d(x)$, the 'direct' energy deposition from ^{32}P source electrons; $f_m(x)$, the energy deposited by electrons backscattered from Mylar; and $f_s(x)$, the energy deposited by electrons from the

scatterer.

'Direct' contribution ——————————————→ $f_d(x)$

Scatterer contribution ——————————→ $f_s(x)$

Mylar contribution ——————→ $f_m(x)$

Let $f_d(x) = A_o e^{-\mu x}$

$f_s(x) = r_s A_o e^{-\mu_s x}$

$f_m(x) = r_m A_o e^{-\mu_m x}$.

Then, the backscatter factor as a function of absorber thickness x is

$$B(x) = \frac{r_s e^{-\Delta\mu_s x} - r_m e^{-\Delta\mu_m x}}{1 + r_m e^{-\Delta\mu_m x}},$$

where $\Delta\mu_m = \mu_m - \mu$ is the difference between the absorption coefficients from the Mylar and 'direct' elements.

For $r_m e^{-\Delta\mu_m x} << 1$

$$B(x) \approx r_s e^{-\Delta\mu_s x} - r_m e^{-\Delta\mu_m x},$$

which fits experimental ASD profiles reasonably well. The criterion that $r_m e^{-\Delta\mu_m x} << 1$ is also satisfied by fits to experimental data.

However, the model is perhaps too simple. It suggests a single decreasing exponential for air interface ASD profiles whereas experimental observations indicate that two exponentials are more appropriate. Some solid material interface data shown later also lend support for this opinion regarding the model; they are best fit by the sum of three exponentials.

The variation of dose backscatter factor with distance from an air/Mylar interface, Figure 4.7, appears to be a combination of two exponentials decreasing at different rates.

Figures 4.14 and 4.15 show fits to the aluminium/Mylar and air/Mylar ASD

data, respectively. The fits are of the form

$$\%B = A_1 e^{-x/v_1} + A_2 e^{-x/v_2}, \qquad \text{and } 1 - \%B = A_1 e^{-x/v_1} + A_2 e^{-x/v_2},$$

for the aluminium and air scatterers, respectively. For the first case, v_2 represents a relaxation length and v_1, the rate at which the initial rise in the data occurs. In the second case, v_1 and v_2 are both relaxation lengths, with v_1 being representative of the initial faster fall-off portion of the curve.

The relaxation length for the aluminium scatterer in this geometry was about 174mg/cm^2. For the case of no scatterer, the initial fast fall-off of backscatter factor was characterized by a relaxation length of 33mg/cm^2, followed by a slower fall-off with a relaxation length of 213mg/cm^2. Table 4.3 summarizes the fitted parameters.

Table 4.3 Parameters of Fits to Experimental ASD Data, point source.

Interface	A_1	v_1 (mg/cm^2)	A_2	v_2 (mg/cm^2)
Aluminium/ Mylar	-6.1 [0.8]	50 [5]	13.9 [0.9]	174 [6]
Air/Mylar	5.8 [0.6]	33 [4]	19.1 [0.2]	213 [5]

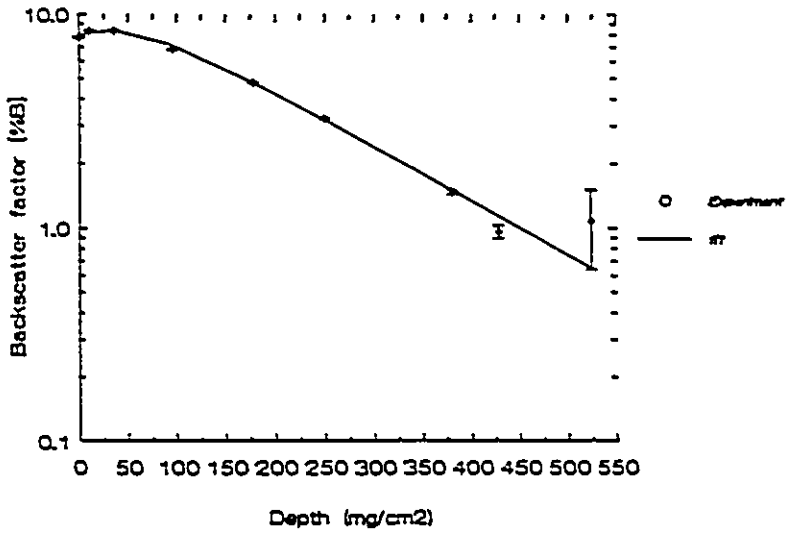

Fig 4.14 Fit to dose backscatter factor variation with absorber between source and detector, aluminium/Mylar interface.

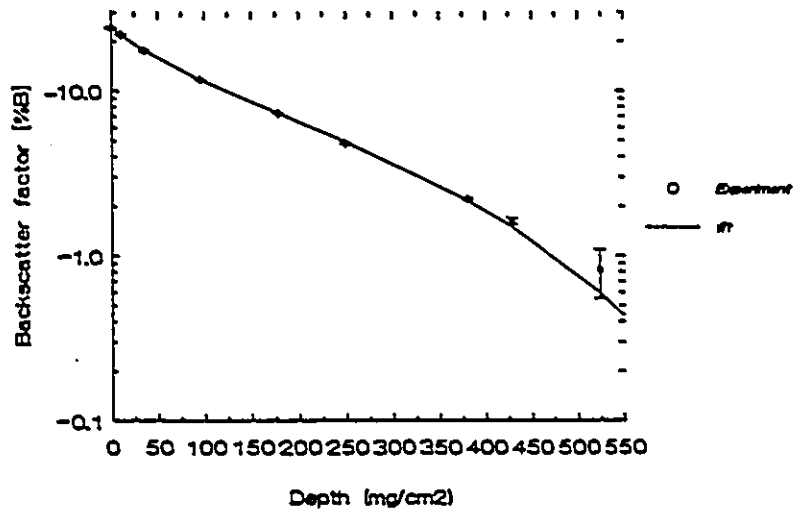

Fig 4.15 Fit to dose backscatter factor variation with absorber between source and detector, air/Mylar interface.

4.4.4 ASB measurements

The fall-off of dose enhancement or reduction with absorbers between source and scatterer is much more rapid than for the ASD geometry. Relaxation lengths for the ASB geometry are approximately 1/6 those in the preceding section.

Figure 4.8, for an aluminium/Mylar interface, shows a single exponential fall-off, with a relaxation length of about 26mg/cm^2. The fit, shown in Figure 4.16, is of the form

$$\%B = A_1 e^{-x/v_1}, \qquad \text{for } 0 \le x \le 60\text{mg/cm}^2,$$

$$\text{and} \quad \%B = ax + d, \qquad \text{for } x > 60\text{mg/cm}^2.$$

Dose enhancement ceases at about 90mg/cm^2 for this interface.

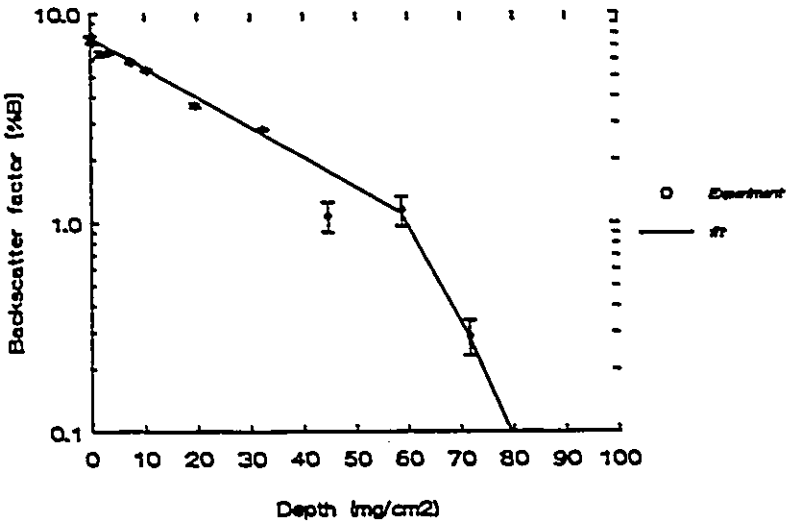

Fig 4.16 Fit to dose backscatter factor variation with absorber between source and scatterer, aluminium/Mylar interface.

In addition to a double exponential fall-off up to about 100mg/cm^2, which is similar to that observed in the preceding section for the air scatterer, the corresponding ASB curve, Figure 4.9, shows a lingering dose reduction factor well beyond this thickness. This is referred to as a 'trailing edge'. The fit to the ASB air scatterer data is of the form

$$1 - \%B = A_1 e^{-x/v_1} - A_2 e^{-x/v_2} + \delta,$$

and is shown in Figure 4.17a. Figure 4.17b illustrates the double exponential fit out to 100mg/cm^2 more clearly.

The 'trailing edge' was thought to have been caused by air spaces between Mylar discs which had to be stacked in order to construct thick absorbers. However, this explanation was shown to be incorrect. Solid lucite absorbers were used, instead of Mylar absorber discs, in an otherwise identical experiment. The results, shown in Figure 4.18, exhibit a 'trailing edge'.

The absorber thicknesses at which this lingering dose reduction factor is observed exceed the CSDA range for 2MeV electrons. That is, no backscattered electrons should be "seen" by the detector. Although the 'trailing edge' remains unexplained at the present time, it is a small effect; the backscatter factors are about -1/2% to -1 1/2%.

ASB type experiments were also done using aluminium absorbers. Figure 4.19 shows the variation of backscatter factor with aluminium thickness. An exponential decline, followed by a linear drop to zero, similar to Figure 4.16, are seen. The relaxation length was 35mg/cm^2, which roughly agrees with the corresponding experiment that used Mylar absorbers.

Table 4.4 lists the parameters of the fits for the ASB geometry. Relaxation lengths are convenient quantities which concisely describe the variation of dose enhancement or reduction with absorber thickness. They are about 30mg/cm^2 for this geometry, which is roughly 1/6 of the nominal 200mg/cm^2 for the ASD geometry, for aluminium and air scatterers.

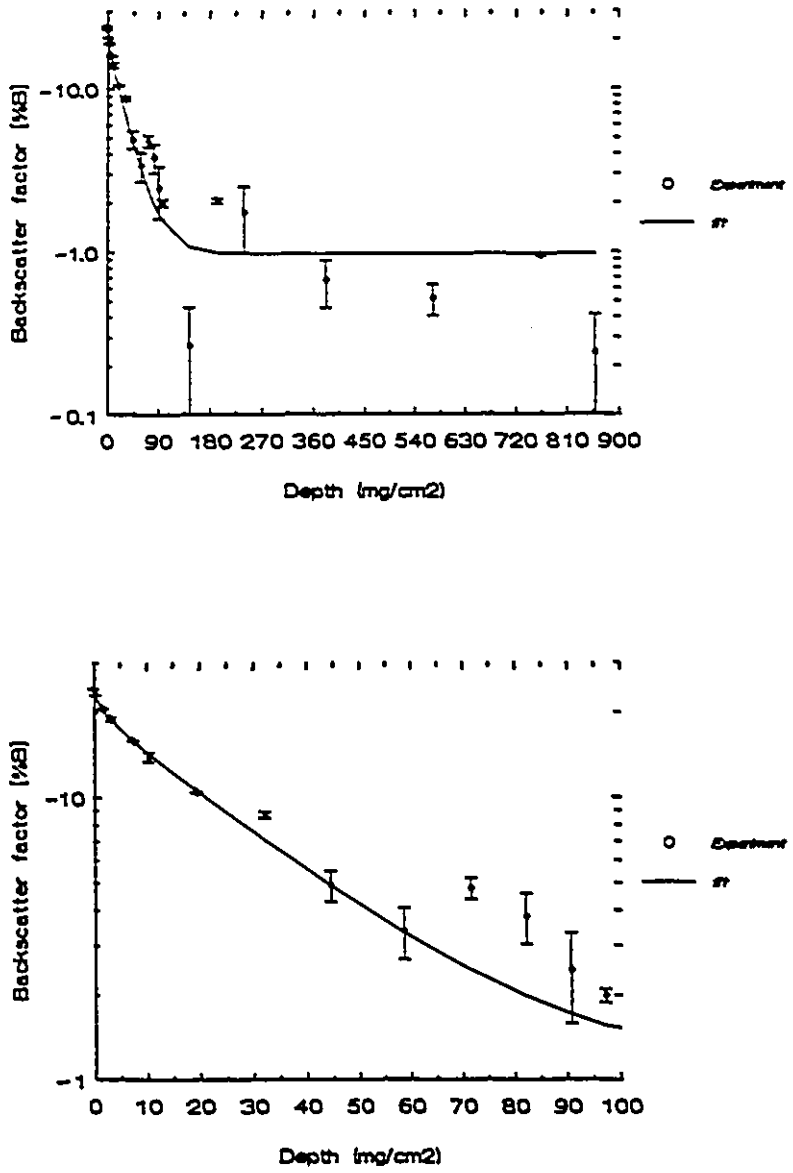

Fig 4.17 Fit to dose backscatter factor variation with absorber between source and scatterer. air/Mylar interface. (a) Upper graph; (b) Lower graph.

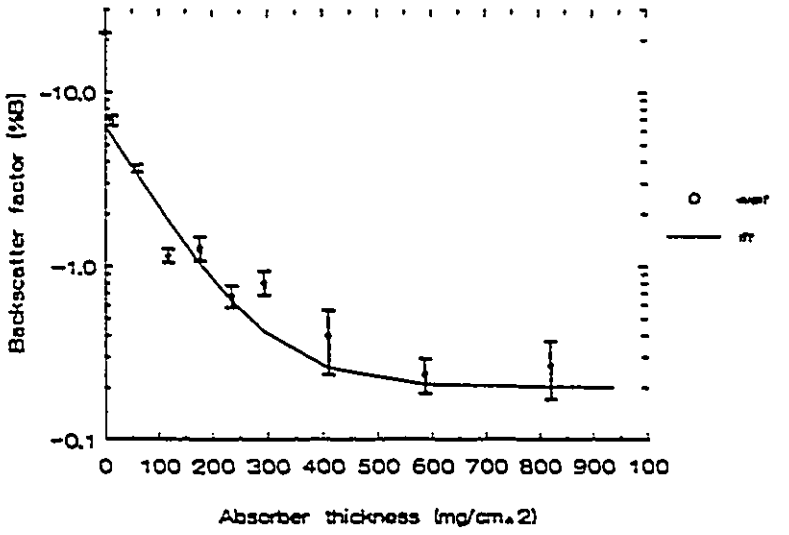

Fig 4.18 ASB type experiment with lucite absorbers, air/lucite interface. Note occurrence of 'trailing edge'.

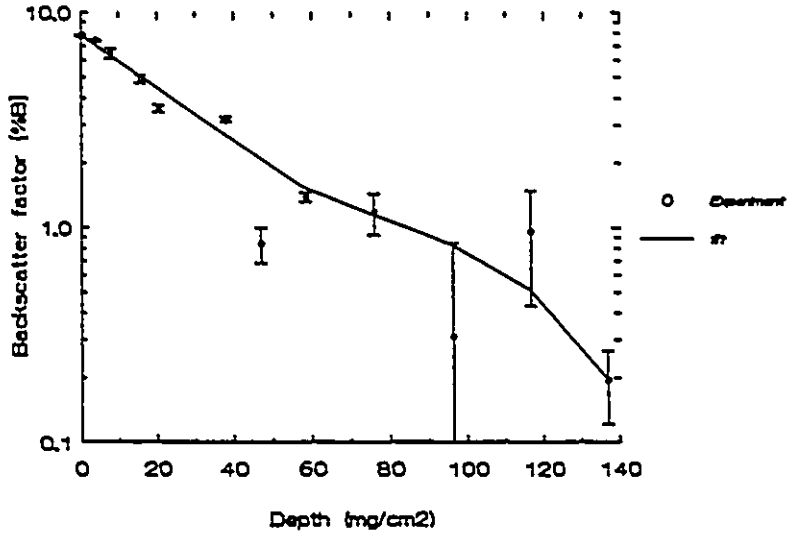

Fig 4.19 ASB type experiment with aluminium absorbers, aluminium/Mylar interface.

Table 4.4 Parameters of Fits to Experimental ASB Data. point source

Interface	A_1	v_1 (mg/cm^2)	a	d	A_2	v_2 (mg/cm^2)	δ
Air/Mylar	4 [1]	2 [1]			19 [1]	28 [1]	2.0 [0.5]
Aluminium/ Mylar	7.4 [0.2]	26 [4]	-0.04 [0.8]	3.0 [1.0]			
Aluminium/ Mylar (Al absorbers)	7.8 [0.1]	35 [2]	-0.02 [1.8]	2.3 [1.8]			

4.5 Results for ^{32}P, Distributed Source

Dependence of backscatter factor on chamber thickness for the case of the thin detector window is demonstrated in Section 4.5.1. The subsequent section deals with Zeroeth measurements for both detector windows. These data are used later for assessing the effects of source geometry on dose enhancement and reduction at material interfaces.

ASD experimental results are described in Section 4.5.3. Relaxation lengths determined here are larger than their point source counterparts, indicating a slower fall-off of backscatter factor with distance from an interface where a distributed source, rather than a point source, is located.

4.5.1 Dependence of backscatter factor on chamber thickness

The variation of backscatter factor with inter-electrode spacing described for the point source, thin window was also observed for the distributed source, thin window. As for the point source, the distributed source data were subjected to the aforementioned one-way ANOVA.

The null hypothesis was rejected in 15 out of 17 cases considered. The 15 cases exhibited definite variation of backscatter factor with chamber thickness. The two remaining cases were cortical bone/soft-tissue and aluminium/A-150 plastic; variation of backscatter factor with chamber thickness could be discerned in the latter case, while there was no dependence evident in the former. The data are included in Appendix C for reference.

Data for each interface were extrapolated to determine "true interface values".

4.5.2 Zeroeth measurements

Backscatter factors measured using the thick detector window are listed in Table 4.5. "True interface" backscatter factor values are also included in this table. As for the point source data, dose backscatter factors increase with scatterer atomic number, dose enhancement factors are larger for interfaces created with lucite than ones created with Mylar, and "true interface"backscatter factors are smaller than thick window values.

Table 4.5 Zeroeth Thick Window and "True Interface" Backscatter Factors.

Source: ^{32}P

Source Geometry: Distributed

Interface	*Thick Window* %B	[uncertainty]	*Thin Window* %B	[uncertainty]
Bismuth/Mylar	36.22	[0.05]	27.55	[0.35]
Tungsten/Mylar	35.30	[0.04]	27.70	[0.21]
Cadmium/Mylar	27.78	[0.03]	21.63	[0.32]
Copper/Mylar	20.07	[0.02]	15.78	[0.08]
Aluminium/Mylar	8.085	[0.045]	6.38	[0.03]
Bismuth/lucite	38.25	[0.03]	29.44	[0.30]
Tungsten/lucite	37.14	[0.11]	29.39	[0.30]
Cadmium/lucite	29.44	[0.03]	23.10	[0.22]
Copper/lucite	21.83	[0.04]	17.68	[0.14]
Aluminium/lucite	9.64	[0.02]	7.96	[0.08]
Cortical bone/soft-tissue*	7.47	[0.12]	6.01	[0.14]
Aluminium/A-150 plastic	10.51	[0.10]	8.66	[0.06]
Air/soft-tissue*	-23.47	[0.37]	-26.34	[0.14]
Air/A-150 plastic	-24.015	[0.375]	-26.70	[0.15]
Air/lucite	-24.31	[0.37]	-27.15	[0.14]
Air/Mylar	-25.71	[0.32]	-28.26	[0.11]
Carbon/Mylar	not available		-2.14	[0.32]

* *tissue equivalent plastics*

4.5.3 ASD measurements

The variation of backscatter factor with distance from an interface where a distributed ^{32}P source is located is similar to that observed for the case in which a point ^{32}P source is located at the interface. Dose enhancement increases to a maximum then decreases exponentially with increasing distance from the interface, and dose reduction decreases exponentially with increasing distance from the interface.

Figure 4.20 shows fits to the ASD curves for aluminium/Mylar, air/Mylar and bismuth/Mylar interfaces. The fits are of the form

$$\%B = A_1 e^{-x/v_1} + A_2 e^{-x/v_2} + A_3 e^{-x/v_3}$$

for the bismuth and aluminium interfaces, and

$$1 - \%B = A_1 e^{-x/v_1} + A_2 e^{-x/v_2}$$

for the air interface.

Maxima on the bismuth and aluminium curves occur between 65-80mg/cm^2 and 30-43mg/cm^2 from the interfaces, respectively. The bismuth peak occurs further from the interface than does the aluminium peak because more electrons with greater energy are backscattered from bismuth than from aluminium. Also, the fall-off of backscatter factor beyond the peak is slower for bismuth than for aluminium, as demonstrated by the larger relaxation length of the former.

As for the point source, with an air interface, dose reduction fall-off with distance from the interface is characterized by two decreasing exponentials. There is an initial faster decline, followed by a more moderate decrease.

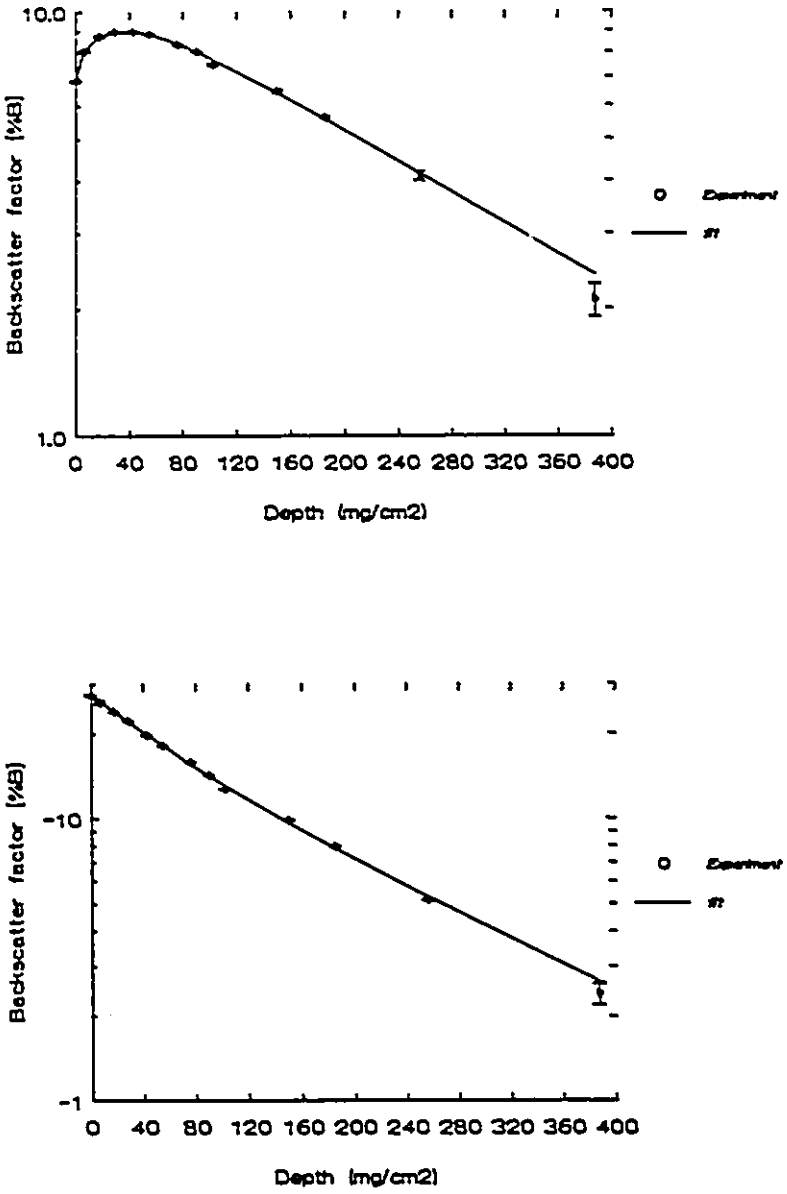

Fig 4.20 Fits to dose backscatter factor variation with absorber between distributed source and detector. Upper: aluminium/Mylar interface; Lower: air/Mylar interface.

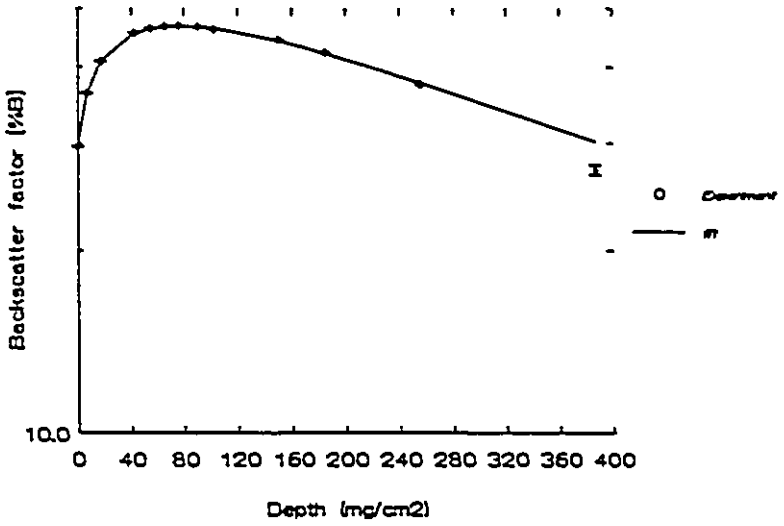

Fig 4.20 continued. Fit to dose backscatter factor variation with absorber between distributed source and detector, bismuth/Mylar interface.

Parameters of the fits for the three interfaces are given in Table 4.6. Relaxation lengths for bismuth and aluminium were 588[70]mg/cm^2 and 238[11]mg/cm^2, respectively. The two-component decline of the air interface was described by relaxation lengths of 88.5[24.3]mg/cm^2 and 294[138]mg/cm^2.

Table 4.6 Parameters of Fits to Experimental ASD Data, distributed source.

Interface	A_1	v_1 (mg/cm^2)	A_2	v_2 (mg/cm^2)	A_3	v_3 (mg/cm^2)
Aluminium/ Mylar	-4.2 [0.3]	33 [6.]	-1.2 [0.4]	5 [2]	12.1 [0.4]	238 [11]
Bismuth/ Mylar	-20 [2]	53.5 [13]	-9.8 [2.0]	10 [2]	58.8 [3.0]	588 [69]
Air/ Mylar	16 [8]	88.5 [24]	13 [8]	294 [138]		

Figure 4.21 compares ASD curves for distributed and point ^{32}P sources, for aluminium/Mylar and air/Mylar interfaces. As noted earlier, the shapes are similar, and the rate of decrease of backscatter factor with distance from the interface is slower for the distributed source. The latter observation is less evident in the air interface curve than in the aluminium curve, but is corroborated by the relaxation length values.

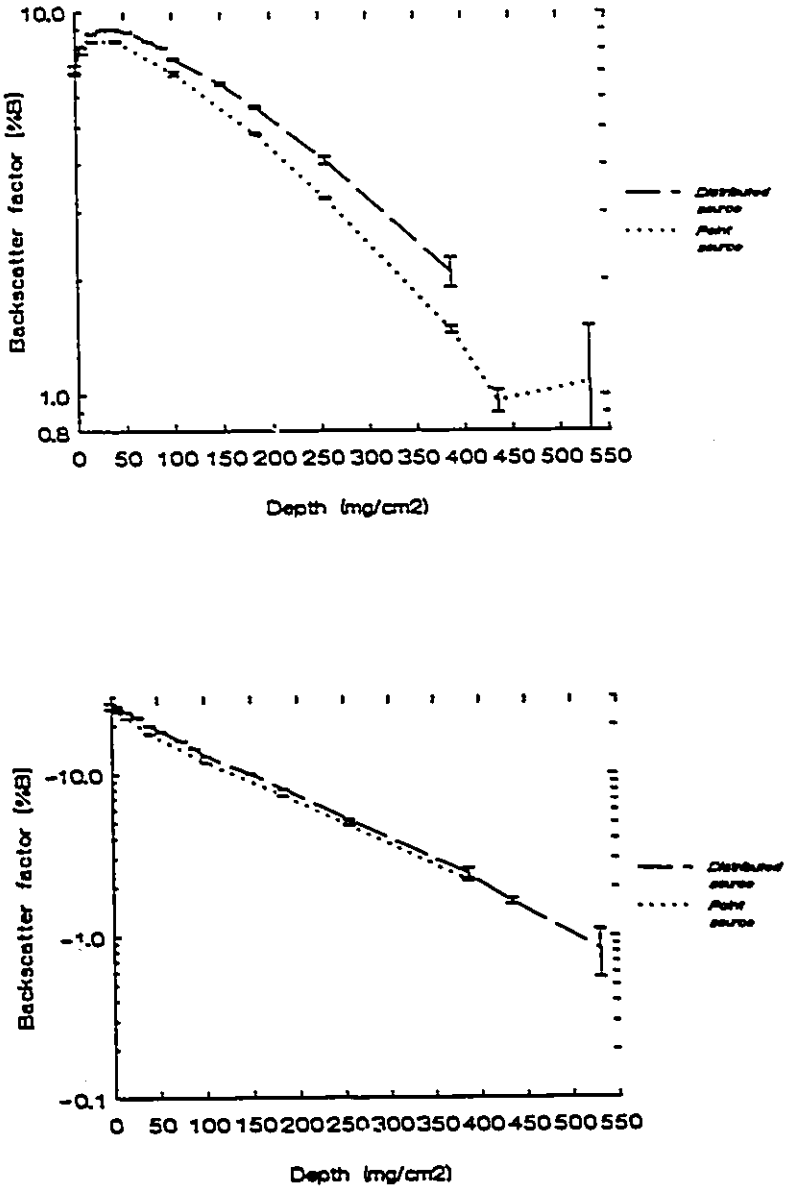

Fig 4.21 Effect of source geometry on backscatter factor variation with distance from an interface where a source is located. Upper: aluminium/Mylar interface; Lower: air/Mylar interface.

4.6 Effect of Source Geometry on Dose Backscatter Factor

Point source dose backscatter factors have been found to be larger than distributed source dose backscatter factors. Ratios of point source backscatter factor to distributed source backscatter factor are larger for interfaces created with lucite than ones created with Mylar. These ratios also vary with scatterer atomic number. Backscatter factor fall-off with distance from an interface, and therefore from the source, is slower for a distributed source than for a point source.

Table 4.7 lists ratios of backscatter factors for point to distributed sources for several interfaces. The thick detector window was used.

Point source dose backscatter factors exceed distributed source dose backscatter factors by about 1% to 5% for solid material/Mylar interfaces, and the point source backscatter factor is about 9% less than the distributed source backscatter factor for the air/Mylar interface. Corresponding values for solid material/lucite interfaces are about 8% to 10%, and 12% for the air/lucite interface.

Table 4.7 also lists point to distributed source backscatter factor ratios for several interfaces using the thin detector window.

Here, point source data exceed distributed source data by about 1% to 10% for solid material/Mylar interfaces, except for the cases of aluminium and cadmium. Point to distributed source backscatter factor ratios are less than unity for these two. Whilst such dramatic deviations are not observed among the lucite data, the cadmium/lucite interface does stand apart from other members of the data set. It shows a point source backscatter factor 6% larger than that for a distributed source, while the other materials show a corresponding value of about 20%.

At air/Mylar and air/lucite interfaces, point source backscatter factors are 6% and 14% less than distributed source backscatter factors, respectively. Perhaps most striking in Table 4.7 is the point to distributed source backscatter factor ratio of two for the carbon/Mylar interface.

Table 4.7 Point to Distributed Source Backscatter Factor Ratios.

	Thick Window		*Thin Window Extrapolated Values*	
Interface	Ratio, $B_{point}/B_{distributed}$		Ratio, $B_{point}/B_{distributed}$	
Bismuth/Mylar	1.05	[0.01][1]	1.07	[0.01]
Tungsten/Mylar	1.04	[0.01]	1.12	[0.01]
Cadmium/Mylar	1.00	[0.01]	0.89	[0.03]
Copper/Mylar	1.02	[0.01]	1.03	[0.02]
Aluminium/Mylar	0.97	[0.01]	0.86	[0.02]
Bismuth/lucite	1.07	[0.01]	1.19	[0.02]
Tungsten/lucite	1.09	[0.01]	1.17	[0.03]
Cadmium/lucite	1.07	[0.02]	1.06	[0.02]
Copper/lucite	1.10	[0.01]	1.20	[0.04]
Aluminium/lucite	1.12	[0.02]	1.32	[0.07]
Cortical bone/soft-tissue*	1.10	[0.02]	1.24	[0.05]
Aluminium/A-150 plastic	1.12	[0.01]	1.15	[0.02]
Air/soft-tissue*	0.86	[0.01]	0.88	[0.01]
Air/A-150 plastic	0.86	[0.01]	0.86	[0.01]
Air/lucite	0.88	[0.01]	0.86	[0.01]
Air/Mylar	0.91	[0.01]	0.94	[0.01]
Carbon/Mylar	not available		2.15	[0.36]

[1] bracketed quantities are uncertainties

** tissue equivalent plastics*

Existing experimental results on reflection coefficients for electron backscattering are predictive of the observation made here that point source backscatter factors are larger than distributed source backscatter factors at solid material interfaces.

The reflection of monoenergetic electrons from thick targets is dependent on angle (for example, Mladjenović 1973; Dressel 1966; Everhart 1960). The reflection coefficient (that is, the ratio of backscattered to incident electrons) varies with angle for scatterers or targets such as carbon, aluminium, copper, silver and lead. The variation is such that the reflection coefficient decreases with decreasing angle (Dressel 1966), where the angle is measured between the target's surface and the reflected electrons' direction. That is, for electrons incident normally on a target, fewer electrons are reflected at small or glancing angles to the target surface than at 90° to the target surface.

More directly related to the present work are the results of backscattering experiments done with a ^{32}P point source on planar scatterers. ^{32}P reflected electrons at the 90° position defined above are very dependent on scatterer atomic number, with considerably more electrons being reflected from high atomic number materials than from low atomic number materials. ^{32}P reflected electrons at small angles are less dependent on scatterer atomic number, with almost the same number of electrons being backscattered from low and high atomic number materials. (Mladjenović 1973; Seliger 1952)

Point and distributed sources are used in the experiments done in this work. A distributed source consists of a collection of point sources, with the number of point sources increasing with distance from the centre of the distributed source area. In addition, the distributed source diameter is greater than that of the detector's sensitive region, whereas the point source diameter is considerably smaller than that of the detector's sensitive region. Therefore, more electrons reflected at small or glancing angles are detected in the case of the distributed source than in the case of the point source.

Since the backscattered spectrum at small angles is almost independent of

scatterer atomic number, it follows that backscatter factors at glancing angles are smaller than those at larger angles. Consequently, a distributed source backscatter factor is smaller than that of a point source because the former results from more small angle contributions than the latter.

The approximate lack of dependence of small-angle scattering on atomic number has been rationalized by proposing that an electron is as likely to emerge from a low atomic number material as from a high atomic number one at small angles. (Seliger 1952)

Backscattered electrons from low atomic number scatterers are lower in energy than those from high atomic number scatterers, particularly at the 90° position, because elastic nuclear scattering is more prevalent than inelastic scattering in the latter case. The Coulomb scattering cross-section varies as the square of the atomic number whereas the inelastic scattering cross-section varies as the atomic number. (Seliger 1952)

In light of the preceding discussion, the variation of point to distributed source backscatter factor ratio with scatterer atomic number is not inconceivable. However, a quantitative explanation for the variety that was noted earlier in the values of Table 4.7 is not available at present.

It was noted before that backscatter factors with respect to lucite are greater than those with respect to Mylar. It is appropriate to mention here that these differences are larger for point sources than for distributed sources. Backscatter factors with respect to lucite exceed those with respect to Mylar by 18% to 80% for scatterers ranging from bismuth to aluminium, for a ^{32}P point source, and by 6% to 24% for the same scatterers , for a ^{32}P distributed source. These observations indicate that the angular dependence of backscattered electrons is different for Mylar and lucite.

The fall-off of backscatter factor with distance from an interface where a distributed source is located is slower than that measured for the case where a point source replaces the distributed one. Energy depositions by backscattered electrons are relevant to determining backscatter factors.

For a low atomic number scatterer such as Mylar, more electrons are backscattered at glancing angles to the scatterer surface than at 90° to the scatterer surface. The opposite is the case for high atomic number scatterers. (Seliger 1952) Additionally, backscattered spectra are less degraded at small angles than at 90° (Seliger 1952; Mladjenović 1973).

Therefore, more higher energy electrons are backscattered from a low atomic number material (for example, Mylar) using a distributed source than using a point source. This distributed source backscattered energy thus not only constitutes a larger fraction of the energy deposited by a high atomic number scatterer (for example, bismuth) but does so until further away from the interface. That is, the distributed source ASD backscatter factor fall-off is slower than that for a point source.

Larger ASD relaxation lengths were obtained from experimental distributed source data than experimental point source data. The values were 238[11]mg/cm^2 and 174[6]mg/cm^2 for an aluminium/Mylar interface, for distributed and point sources, respectively. Corresponding values for an air/Mylar interface were 294[138]mg/cm^2 and 213[5]mg/cm^2.

The source geometry effect is crudely summarized in the following statement which ignores the observed variation of this effect with scatterer atomic number. Zeroeth point source dose backscatter factors are larger than distributed ones by about 10% for solid material/Mylar interfaces and by 20% for solid material/lucite interfaces. Zeroeth point source backscatter factors are 6% and 14% less than distributed source ones for air/Mylar and air/lucite interfaces, respectively.

It will be of interest to compare Monte Carlo results from the following chapter with these findings.

CHAPTER 5

SIMULATION OF THE EXPERIMENTS

Experiments of the Zeroeth geometry type, described in Chapter 4, were simulated for point and distributed sources using both Monte Carlo codes. Dose backscatter factors for ^{32}P, $\bar{B}$, were calculated for the interfaces aluminium/Mylar, aluminium/lucite, bismuth/Mylar, bismuth/lucite, copper/Mylar, copper/lucite, air/Mylar and air/lucite. This constituted a rigorous comparison of the Monte Carlo codes with experimental data.

ASB type simulations were done for aluminium and air scatterers, using EGS4/Dosrz. As for the Zeroeth simulations, these duplicated the experiment in great detail. A simpler geometry was simulated for the ASD type experiments; although the extrapolation chamber was not in this simulation, it nonetheless answered the question of how the backscatter factor varies with distance from an interface where a source is fixed. The simulations are described further in Section 5.2.

For Zeroeth geometry, point source simulations, beta dose backscatter factors from the two Monte Carlo codes agree within uncertainties for four of eleven interfaces studied; discrepancies between results from the two codes for the remaining seven interfaces are less than twenty percent. In these cases, dose enhancements predicted by Cyltran are larger than ones predicted by EGS4/Dosrz, and dose reductions determined using Cyltran are smaller than ones determined using EGS4/Dosrz. For Zeroeth geometry, distributed source simulations, beta dose backscatter factors from the two codes agree within uncertainties; eight interfaces were investigated.

Monte Carlo-calculated beta dose backscatter factor data are determined from monoenergetic electron source data by integration over the beta spectrum of

interest, as described in Section 5.6. The monoenergetic data are therefore a crucial component in calculating beta dose backscatter factors. Furthermore, consideration of monoenergetic data from the two codes not only provides diagnostic information concerning the similarities and differences observed between beta dose backscatter factors, but it also permits a more elemental comparison of the two codes. Although the latter is a task that is not an explicitly stated objective of the present work, because of their availability, monoenergetic data are included in Section 5.7.

In general, Monte Carlo Zeroeth beta dose backscatter factors agree well with experimental data for the interfaces investigated. With the exception of results from several aluminium interfaces, agreement between Monte Carlo and experimental values is to within about fifteen percent or better.

Results from both codes for aluminium interfaces exceed experimental values. The magnitude of the discrepancy is more pronounced for Cyltran point source data than for EGS4/Dosrz point source data. For bismuth interfaces, this trend reverses; results from both codes are smaller than experimental values, and EGS4/Dosrz data underestimate the experimental backscatter factors more than Cyltran data do. For copper interfaces, backscatter factors from EGS4/Dosrz are in excellent agreement with experimental values. This is also the case for Cyltran point source data, while Cyltran distributed source data underestimate the experimental values. At air interfaces, dose reduction factors predicted by both codes agree exceptionally well with experimental data for the distributed source. For the point source, Monte Carlo dose reduction factors exceed experimental values by ten to fifteen percent except for one case in which the value predicted by Cyltran agrees with the experimental result.

Relaxation lengths as defined in Chapter 4 were determined from Monte Carlo data. Comparison of these with their experimental counterparts, for both ASD and ASB geometries, was favourable.

5.1 *Uncertainties Associated with the Monte Carlo Output*

The uncertainty estimates given by the Monte Carlo codes are estimates of the standard error in the mean value scored, where the mean is taken over a specified number of batches. (Rogers and Bielajew 1990; Halbleib, Mehlhorn and Kensek 1987) Each Monte Carlo calculation, called a run, consists of a number of histories, n. The n histories are divided equally into N batches. In this work, individual runs were such that n=100000 and N=10.

Let E_i = energy deposited in the scoring region for batch i

$< E_N >$ = average energy deposited per batch, $\frac{1}{N}\sum_{i=1}^{N} E_i$

$< E_N^2 >$ = mean square energy deposited per batch, $\frac{1}{N}\sum_{i=1}^{N} E_i^2$.

The uncertainty in $< E_N >$ is given by $\frac{1}{< E_N >}\sqrt{\frac{< E_N^2 > - < E_N >^2}{N-1}}$.

The statistical uncertainty in a run varies as $1/\sqrt{n}$. Therefore, to reduce an uncertainty associated with n histories by half implies that 4n histories must be used. Uncertainty estimates for Zeroeth simulations were on the order of 1% to 2% or less for point sources and ranged from 1% to 20% for distributed sources.

5.2 *Adjunct Notes Regarding the Simulations*

Computing time required for the simulations varied with source energy - longer times were needed for higher energies. More time was also taken for simulations using higher atomic number scatterers. In general, run times varied from 1 to 5 cpu hours.

Scoring regions used in the simulations correspond to the sensitive volume of the extrapolation chamber. The fraction of electron source energy deposited per

incident electron, $\varepsilon(E)$, was determined. This quantity facilitates studying how the different source energies contribute to the total energy deposited.

Monte Carlo data from monoenergetic electron sources, $\varepsilon(E)$, were accumulated and later integrated over the ^{32}P beta spectrum. This approach, instead of sampling from the spectrum during the simulation, was adopted for reasons of efficiency. The monoenergetic data are multi-purpose in that they can be applied to any beta spectrum, the end-point energy of which is less than or equal to that of ^{32}P.

Eleven electron source energies ranging from 70keV to 1.7MeV were used for thick detector window simulations. Twelve source energies, sampled from 10keV to 1.7MeV, were used for thin detector window simulations. The lower limits were chosen because less energetic electrons do not penetrate the detector windows and therefore do not contribute to energy deposited in the chamber.

Six scatterers and point and distributed sources were simulated, costing roughly 1000cpu hours for all the Zeroeth simulations using both Monte Carlo codes. Three scatterers, two source geometries and thirteen or fifteen source energies were used in ASD type simulations; about 400cpu hours were needed. ASB simulations, done for a point source, seven absorber thicknesses, two scatterers and several energies, took approximately 250cpu hours.

Figures 5.1 and 5.2 are schematics of Zeroeth and ASD simulation geometries. ASB simulations used the geometry shown in Figure 5.1, with Mylar absorbers of different thicknesses between the source cover and the scatterer.

The material compositions which were used to generate cross-section data for use in the Monte Carlo codes are listed in Table 4.1.

Electron and photon histories were terminated at 10keV and 1keV, respectively, in Cyltran simulations. Secondary particle production thresholds for EGS4/Dosrz (Class II algorithm), defined in Section 3.2.1, were 10keV and 1keV for electrons and photons, respectively; also, in EGS4/Dosrz simulations, the maximum fractional energy loss along an electron's condensed history step was 4%, and case histories were terminated at 1keV.

Fig 5.1 Zeroeth or ASB Simulation Geometry*

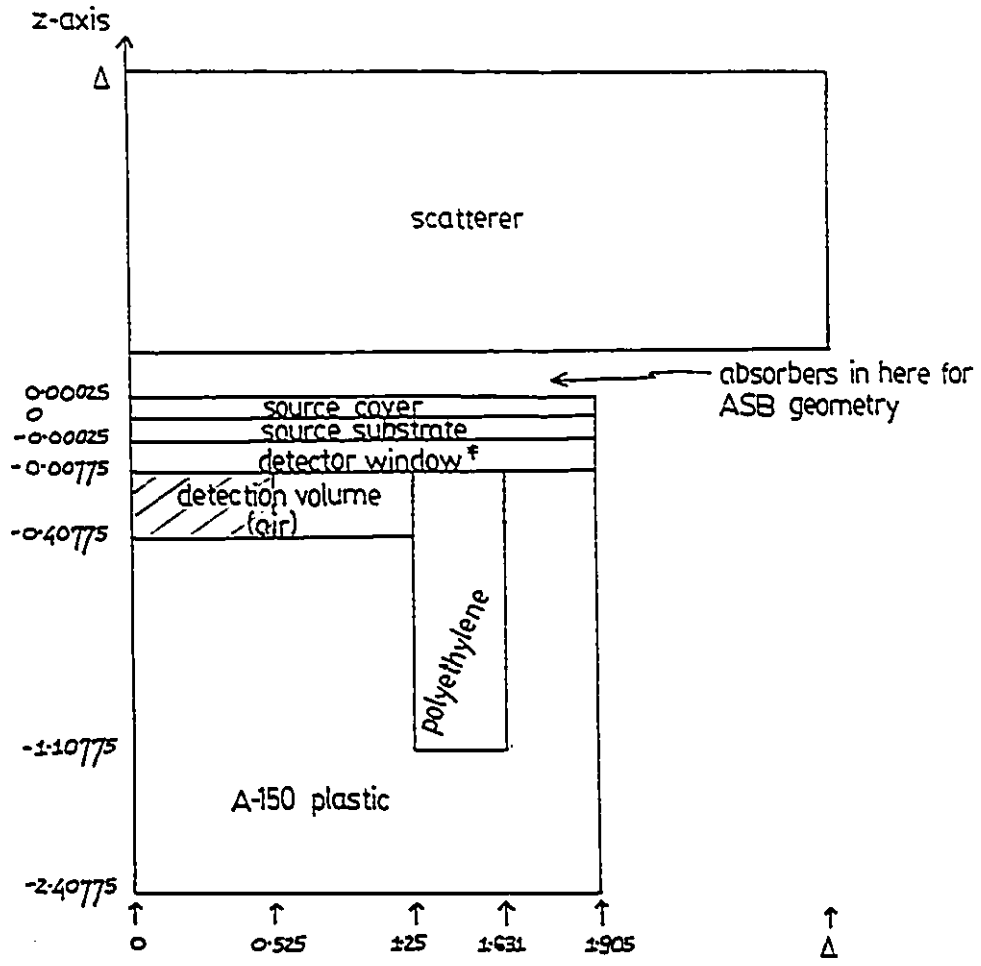

▨: scoring region

Δ: Dimensions of scatterer are ≥ CSDA range of 2MeV electrons in that medium.

† Thick detector window is illustrated here. The thin window is 2.22μm in z dimension.

** half the geometry is shown since it is symmetric about the z, or reference, axis indicated. Dimensions are in cm.*

Fig 5.2 ASD Simulation Geometry*

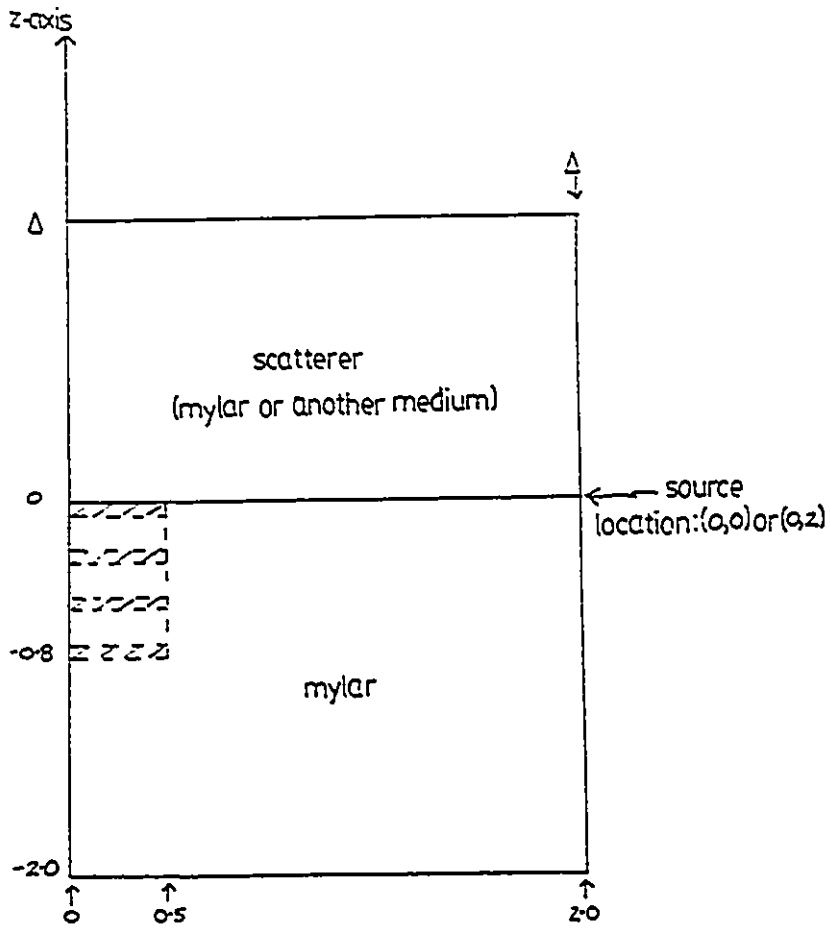

ZZZ: Twenty scoring regions at various depths are chosen between 0 and 0.8cm. Height of scoring region = 0.5mg/cm^2 Mylar.

Δ: Dimensions of scatterer are ≥ CSDA range of 2MeV electrons in that medium or 2.0cm. whichever is larger.

* *half the geometry is shown since it is symmetric about the z or reference, axis indicated. Dimensions are in cm.*

5.3 *Zeroeth Geometry*

Monoenergetic electron sources were used in simulations described by the geometry of Figure 5.1. The fractional energy deposited per electron, $\varepsilon(E)$, in the sensitive detector volume was scored. These data were integrated over the energy spectrum of ^{32}P by the methods outlined in Section 5.6 in order to determine beta dose backscatter factors, $\bar{B}$.

5.3.1 *Beta point source, ^{32}P*

(a) Thick Window -

Beta dose backscatter factors obtained from Monte Carlo simulations are given in Table 5.1. Table 5.2 compares results from the codes with experimental data from Chapter 4. In addition to percentage discrepancy between Monte Carlo and experimental data, a factor, F, which compares the difference between Monte Carlo and experimental backscatter factors to their combined uncertainty, is included.

Agreement between Monte Carlo and experimental data is generally within about twenty percent. However, the following criterion establishes a more rigorous means of comparison. Agreement between Monte Carlo and experimental data is considered poor if the discrepancy between the data is greater than ten percent and if the magnitude of the difference between the data is greater than twice the combined uncertainty of the data. That is, poor agreement is indicated if "discrepancy > 10% and F > 2".

Therefore, agreement between EGS4/Dosrz and experimental beta dose backscatter factors is poor for bismuth/Mylar and bismuth/lucite interfaces, air/Mylar and air/lucite interfaces and for the aluminium/Mylar interface. The good agreement exhibited for the aluminium/lucite boundary is inconsistent with the

preceding observation. Good agreement is also obtained between EGS4/Dosrz and experimental values for copper interfaces.

Poor agreement between Cyltran and experimental beta dose backscatter factors is shown for the aluminium/Mylar interface, the copper/Mylar interface and the air/lucite interface. Good agreement is exhibited for the bismuth interfaces as well as for the copper/lucite and air/Mylar interfaces. Observations for these latter two boundaries are at odds with the good agreement already noted for copper/Mylar and air/lucite interfaces.

Therefore, the degree of agreement obtained between Monte Carlo and experimental data for a scatterer/Mylar interface may be different from that obtained for a scatterer/lucite interface. This finding is consistent with the fact that although the codes do predict larger beta dose enhancement factors for interfaces which use lucite compared with ones which use Mylar, the differences are not as large as those observed experimentally.

There is also reasonable agreement between the data from the two codes. Beta dose backscatter factors from the two codes agree, within uncertainties, for aluminium and air interfaces. For bismuth and cooper interfaces, values from Cyltran are about ten percent larger than values from EGS4/Dosrz.

Table 5.1* Beta Dose Backscatter Factors for ^{32}P, point source, Zeroeth geometry. Thick Detector Window.

Scatterer:	Bismuth (Z=83)			Aluminium (Z=13)		
	EGS4/Dosrz	Cyltran	Expt	EGS4/Dosrz	Cyltran	Expt
% $\bar{B}$, with respect to Mylar	33.6 [0.5]	35.4 [0.9]	37.9 [0.3]	10.3 [0.4]	11.0 [0.8]	7.9 [0.1]
% $\bar{B}$, with respect to Lucite	35.0 [0.5]	37.1 [0.9]	41.1 [0.4]	11.4 [0.4]	12.4 [0.9]	10.8 [0.2]
Scatterer:	Copper (Z=29)			Air		
	EGS4/Dosrz	Cyltran	Expt	EGS4/Dosrz	Cyltran	Expt
% $\bar{B}$, with respect to Mylar	20.9 [0.4]	22.6 [0.8]	20.4 [0.2]	-26.2 [0.3]	-25.5 [0.6]	-23.4 [0.1]
% $\bar{B}$, with respect to Lucite	22.2 [0.4]	24.2 [0.9]	24.0 [0.2]	-25.4 [0.3]	-24.5 [0.6]	-21.4 [0.1]

** bracketed quantities are uncertainties.*

Table 5.2 Comparison of Monte Carlo Zeroeth $\bar{B}$ Values with Experimental Data. Thick Detector Window. ^{32}P point source.

Scatterer:	Bismuth (Z=83)		Aluminium (Z=13)	
	EGS4/Dosrz	Cyltran	EGS4/Dosrz	Cyltran
Discrepancy; F with respect to Mylar	11%; 7.4	7%; 2.6	-30%; 5.8	-39%; 3.9
Discrepancy; F with respect to lucite	15%; 9.5	10%; 4.1	-6%; 1.3	-15%; 1.7
Scatterer:	Copper (Z=29)		Air	
	EGS4/Dosrz	Cyltran	EGS4/Dosrz	Cyltran
Discrepancy; F with respect to Mylar	-2%; 1.1	-11%; 2.7	-12%; 8.9	-9%; 3.5
Discrepancy; F with respect to lucite	7.5%; 4.0	-1%; 0.2	-19%; 12.7	-14%; 5.1

Discrepancy = [(Experimental $\bar{B}$ - Monte Carlo $\bar{B}$) / (Experimental $\bar{B}$)] x 100%.

$$F = \left| \frac{\text{Experimental } \bar{B} - \text{MonteCarlo } \bar{B}}{\sqrt{\sigma^2_{\text{Expt},\bar{B}} + \sigma^2_{\text{MonteCarlo}\,\bar{B}}}} \right| .$$

(b) Thin Window

Zeroeth geometry, point source simulations using the thin detector window were done for bismuth/Mylar, aluminium/Mylar and air/Mylar interfaces. Agreement between results from these calculations and experimental results is similar to that obtained for the thick window for bismuth/Mylar and aluminium/Mylar. Differences between Monte Carlo and experimental data are smaller for thin window air/Mylar simulations than for thick window air/Mylar simulations.

Beta dose backscatter factors for a point source of ^{32}P and the thin window are listed in Table 5.3. Monte Carlo and experimental data are compared in Table 5.4.

Backscatter factors from both codes are smaller than experimental values for bismuth. However, according to the criterion established earlier, the agreement between the value from Cyltran and the experimental value is good and the agreement between the EGS4/Dosrz value and the experimental value is poor. Experimental, Cyltran and EGS4/Dosrz dose enhancement factors are 33.8%, 31.8% and 26.1%, respectively, for the bismuth/Mylar interface.

Backscatter factors from both codes substantially overestimate the experimental value for the aluminium/Mylar interface. Similar trends were noted for the thick window. For the thin window, experimental, Cyltran and EGS4/Dosrz values are 7.05%, 9.9% and 8.05%, respectively.

There is excellent agreement between Cyltran and experimental dose reduction factors for the air/Mylar interface. Although less spectacular, agreement between EGS4/Dosrz and experimental values is also good. Experimental, Cyltran and EGS4/Dosrz dose reduction factors are 25.2%, 24.9% and 27.2%, respectively.

Table 5.3* Beta Dose Backscatter Factors, % $\bar{B}$, for ^{32}P, point source. Zeroeth Geometry, Thin Detector Window.

Interface	EGS4/Dosrz	Cyltran	Experiment
Bismuth/ Mylar	26.1 [0.4]	31.8 [0.9]	33.77 [0.01]
Aluminium/ Mylar	8.05 [0.3]	9.9 [0.7]	7.09 [0.15]
Air/ Mylar	-27.2 [0.2]	-24.9 [0.6]	-25.20 [0.02]

Table 5.4 Comparison of Monte Carlo and Experimental $\bar{B}$ Zeroeth Values from Table 5.3.

Interface	EGS4/Dosrz Discrepancy[1]; F[1]	Cyltran Discrepancy[1]; F[1]
Bismuth/Mylar	23%; 19	6%; 2.2
Aluminium/Mylar	-13.5%; 2.9	-40%; 3.9
Air/Mylar	-8%; 10	1%; 0.5

* *bracketed quantities are uncertainties;* [1] *as defined for Table 5.2.*

5.3.2 *Distributed beta source, ^{32}P*

Beta dose backscatter factors with respect to Mylar and lucite were determined using Zeroeth geometry, distributed source and thin detector window for bismuth, copper, aluminium and air scatterers. The source had a diameter equal to that of the extrapolation chamber, namely, 3.81cm. Within uncertainties, results from the two Monte Carlo codes agree. Monte Carlo and experimental data are listed in Table 5.5 and are compared in Table 5.6.

As for the point source, Cyltran results agree better with experimental results for the high atomic number scatterer, bismuth (Z=83), than do EGS4/Dosrz results. Agreement between EGS4/Dosrz and experimental results is poor; EGS4/Dosrz data underestimate experimental values by about seventeen percent.

For the intermediate atomic number scatterer, copper (Z=29), whereas results from both codes agree very well with experimental results for the point source (Tables 5.1, 5.2), for the distributed source, only EGS4/Dosrz data exhibit the same calibre of agreement with experimental data. At the copper/Mylar boundary, the backscatter factor from Cyltran is about twenty percent less than the experimental. Reasons for this source geometry bias are not known.

Results for the low atomic number scatterer, aluminium (Z=13), are consistent with observations made in previous sections which dealt with point sources in that there is a tendency for backscatter factors from both codes to be larger than experimental values. However, the size of the discrepancies between calculated and experimental values is tempered by relatively large uncertainties associated with the calculated data, as shown by the small F values in Table 5.6.

For air interfaces, results from both codes agree well with experimental values. It is interesting but perhaps not significant to note that while EGS4/Dosrz dose reduction factors are larger than experimental ones for a point source (Tables 5.1 through 5.4), for a distributed source, EGS4/Dosrz values are slightly smaller than experimental values. Although Cyltran results behave similarly to this for the copper/Mylar boundary, as mentioned above, such is not the case for air interfaces.

Table 5.5* Beta Dose Backscatter Factors for ^{32}P, distributed source, Zeroeth geometry. Thin Detector Window.

Scatterer:	Bismuth (Z=83)			Aluminium (Z=13)		
	EGS4/Dosrz	Cyltran	Expt	EGS4/Dosrz	Cyltran	Expt
% $\bar{B}$, with respect to Mylar	24.3 [1.2]	25.5 [2.1]	29.57 [0.03]	7.67 [1.11]	7.06 [1.65]	6.86 [0.02]
% $\bar{B}$, with respect to Lucite	26.3 [1.3]	28.4 [2.2]	31.30 [0.02]	9.42 [1.13]	9.53 [1.69]	8.27 [0.02]
Scatterer:	Copper (Z=29)			Air		
	EGS4/Dosrz	Cyltran	Expt	EGS4/Dosrz	Cyltran	Expt
% $\bar{B}$, with respect to Mylar	15.8 [1.3]	13.0 [1.8]	16.79 [0.06]	-26.3 [0.8]	-27.9 [1.5]	-27.27 [0.06]
% $\bar{B}$, with respect to Lucite	17.7 [1.3]	15.6 [1.8]	18.24 [0.04]	-25.1 [0.8]	-26.2 [1.6]	-26.36 [0.02]

* *bracketed quantities are uncertainties.*

Table 5.6 Comparison of Monte Carlo Zeroeth $\bar{B}$ Values with Experimental Data. Thin Detector Window. ^{32}P distributed source.

Scatterer:	Bismuth (Z=83)		Aluminium (Z=13)	
	EGS4/Dosrz	Cyltran	EGS4/Dosrz	Cyltran
Discrepancy; F with respect to Mylar	18%;4.4	14%; 1.9	-12%; 0.7	-3%; 0.12
Discrepancy; F with respect to lucite	16%;3.9	9%;1.3	-14%; 1.0	-15%; 0.75
Scatterer:	Copper (Z=29)		Air	
	EGS4/Dosrz	Cyltran	EGS4/Dosrz	Cyltran
Discrepancy; F with respect to Mylar	6%; 0.8	23%; 2.1	4%; 1.2	-2%; 0.4
Discrepancy; F with respect to lucite	3%; 0.4	14.5%; 1.5	5%; 1.6	0.6%; 0.1

Discrepancy = [(Experimental $\bar{B}$ - Monte Carlo $\bar{B}$) / (Experimental $\bar{B}$)] x 100%.

$$F = \left| \frac{\text{Experimental } \bar{B} - \text{MonteCarlo } \bar{B}}{\sqrt{\sigma^2_{\text{Expt.B}} + \sigma^2_{\text{MonteCarloB}}}} \right| .$$

5.3.3 *Effect of source geometry on beta dose backscatter factors*

Three Monte Carlo cases studied are candidates for assessing the effect of source geometry on beta dose backscatter factors. They are the bismuth/Mylar, aluminium/Mylar and air/Mylar interfaces. Their data, for point and distributed ^{32}P sources, in Tables 5.3 and 5.5, are used.

There is no clear evidence of a difference between point and distributed source backscatter factors determined using EGS4/Dosrz. Ratios of point to distributed source backscatter factors for bismuth, aluminium and air interfaces are 1.07[0.06], 1.05[0.16] and 1.03[0.03], respectively. Bracketed quantities are absolute uncertainties.

However, data from Cyltran do exhibit differences between point and distributed source backscatter factors. Ratios of point to distributed source backscatter factors for bismuth, aluminium and air interfaces are 1.25[0.11], 1.41[0.34] and 0.89[0.05]. That is, dose enhancement factors are larger for a point source than for a distributed source, and dose reduction is smaller for a point source than for a distributed source. Similar observations were made experimentally, as noted in Section 4.6.

5.4 ASD Geometry

The lack of severe disagreement between results from the Monte Carlo codes in the preceding section provides the basis for the decision to use one code for the ASD type simulation and one for the ASB type simulation. Cyltran was chosen for the former and EGS4/Dosrz for the latter.

Figure 5.2 describes the ASD geometry which was simulated. Fractional energy deposited for monoenergetic electron sources was scored as a function of distance from the interface, where the source was fixed. That is, $\varepsilon(E,d)$ values were obtained. These data were integrated over the ^{32}P beta spectrum in order to determine backscatter factors as a function of distance from the interface, $\bar{B}(d)$.

5.4.1 Beta point source, ^{32}P

Figure 5.3 consists of graphs of $\bar{B}(d)$ versus distance from the interface for aluminium/Mylar, air/Mylar and bismuth/Mylar interfaces. These graphs closely resemble the experimental ASD curves of Section 4.4.3.

The aluminium/Mylar and bismuth/Mylar graphs show an initial increase in dose enhancement, to a maximum, followed by a decrease in dose enhancement. These curves may be adequately modelled by a combination of two exponentials.

Relaxation lengths, defined in Section 4.4, were determined from the Monte Carlo data. They were calculated from the slopes of the exponential fits shown in Figure 5.3, and were found to be 357[51]mg/cm^2 and 909[165]mg/cm^2 for aluminium and bismuth scatterers, respectively. The dose reduction profile exhibited a faster fall-off near the interface, followed by a more moderate decrease; relaxation lengths were 31[11]mg/cm^2 and 208[39]mg/cm^2 for the air/Mylar profile.

Parameters of the fits to experimental and Monte Carlo data are listed in

Table 5.7.

Table 5.7 Parameters of Fits to Experimental and *Monte Carlo* Backscatter Factor Data, ASD Geometry*, ^{32}P point source.

Scatterer		Parameters			
		A_1	v_1 (mg/cm^2)	A_2	v_2 (mg/cm^2)
Al	Expt	-6.1 [0.8]	50 [5]	13.9 [0.9]	174 [6]
	Calc	*-5.7 [0.5]*	*8 [2]*	*11.9 [0.5]*	*357[51]*
Bi	Expt		not available		
	Calc	*-29.2 [1.4]*	*12 [1]*	*50.6 [1.3]*	*909 [165]*
Air	Expt	5.8 [0.6]	33 [4]	19.1 [0.2]	213 [5]
	Calc	*9.5 [3.5]*	*31 [11]*	*25.2 [3.5]*	*208 [39]*

* *Fits are of the form* $\%B = A_1e^{-x/v_1} + A_2e^{-x/v_2}$ for solid interfaces and $1 - \%B = A_1e^{-x/v_1} + A_2e^{-x/v_2}$ for air interfaces and x is the distance from the interface in mg/cm^2.

There is excellent agreement between relaxation lengths derived from experimental and Monte Carlo data for the air/Mylar interface. For the aluminium/Mylar interface, the Monte Carlo relaxation length is considerably larger than the experimental value, indicating that the rate of decrease of dose enhancement predicted by the calculation is slower than that obtained experimentally.

There were no experimental data for the bismuth scatterer, but it is not unreasonable that relaxation lengths are larger for this scatterer than for aluminium. Electrons backscattered from the higher atomic number element have larger energies and can penetrate further into the Mylar absorbers which are between the source and the point of measurement. Consequently, not only is the Zeroeth backscatter factor larger for bismuth than for aluminium, but the region of maximum backscatter factor occurs at a depth further from the interface and the rate of fall-off of backscatter factor with depth is slower.

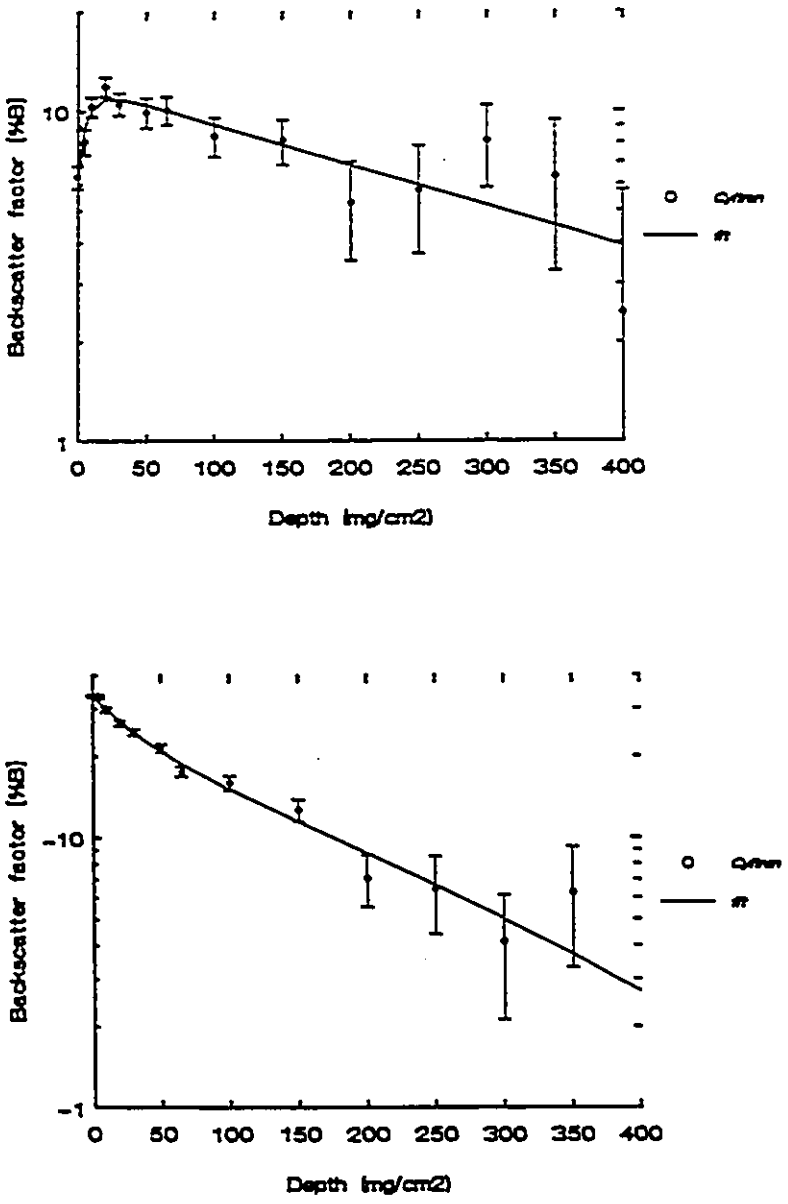

Fig 5.3 Variation of backscatter factor with distance from interfaces, ASD geometry, ^{32}P point source. Upper: aluminium/Mylar interface; Lower: air/Mylar interface.

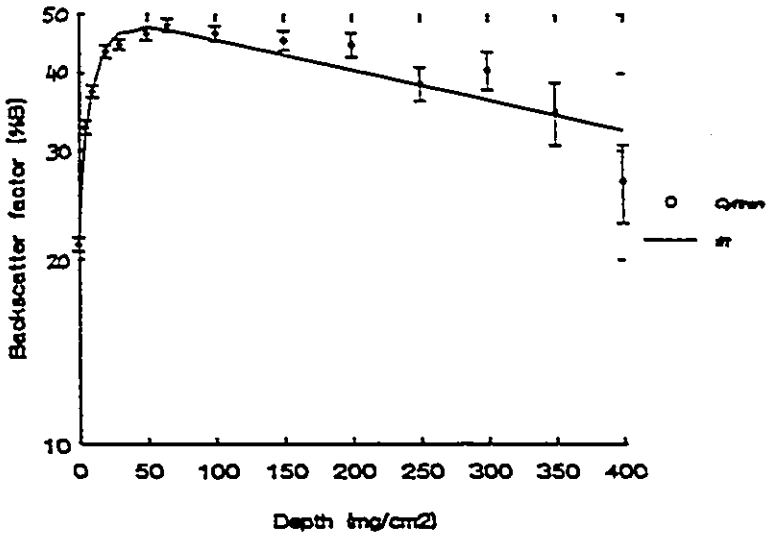

Fig 5.3(continued) Variation of backscatter factor with distance from a bismuth/Mylar interface, ASD geometry, ^{32}P point source.

Although the experimental and Monte Carlo $\bar{B}(d)$ data do not agree within uncertainties, as is evident from Figure 5.4, and Table 5.8, the Cyltran code has been effective in reproducing the general trends of the experimental backscatter factor depth profiles.

Furthermore, the position of the maximum on the aluminium/Mylar curve agrees with that on the experimental one. The former occurs around 20 to 30

mg/cm^2. The latter is observed between 10½ and 35mg/cm^2 absorber thickness (Section 4.4.1), but this translates into a depth between 18 and 43 mg/cm^2 since the detector window and source substrate and cover occupy 7.7mg/cm^2.

As mentioned earlier, this simulation was intended to investigate the variation of dose backscatter factors with distance from an interface where a ^{32}P point source was located. It does not replicate the experimental geometry as do the simulations of the preceding section. However, consistent with the results for the Zeroeth geometry, Cyltran beta dose backscatter factors in this geometry are larger than experimental values for the aluminium and air interfaces, as seen in Figure 5.4. In spite of this, the qualitative similarity between the Monte Carlo and experimental ASD curves for both of these interfaces, and the quantitative agreement between experimental and Monte Carlo relaxation lengths for the air interface, are positive indicators of the code's reliability.

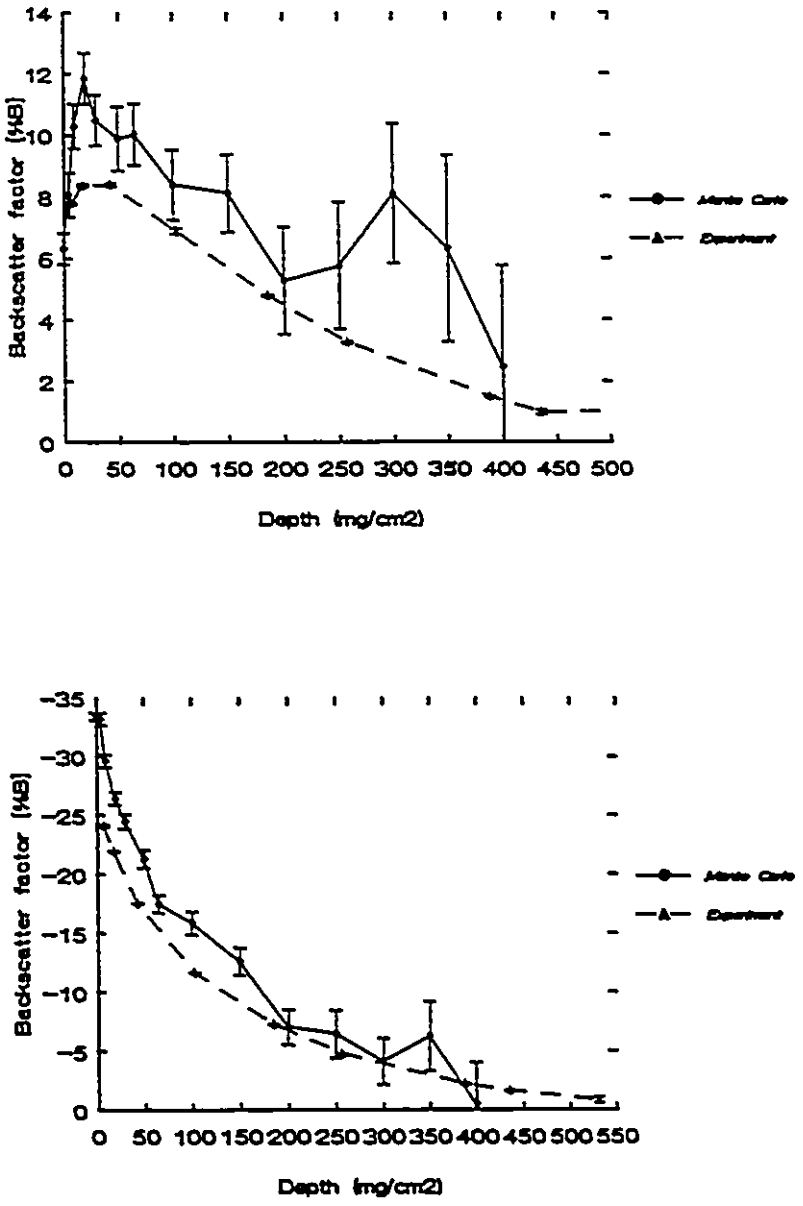

Fig 5.4 Comparison of experimental and Monte Carlo ASD curves for ^{32}P point source. Upper: aluminium/Mylar interface; Lower:air/Mylar interface.

Table 5.8 Experimental and Monte Carlo ASD Backscatter Factors for ^{32}P point source.

	Aluminium/Mylar				Air/Mylar			
Depth	Cyltran		Experiment		Cyltran		Experiment	
(mg/cm^2)	%B	[uncert]*	%B	[uncert]	%B	[uncert]	%B	[uncert]
0	6.31	[0.52]			-33.4	[0.3]		
5	8.05	[0.73]			-33.1	[0.6]		
7.7			7.9	[0.1]			-23.4	[0.1]
10	10.3	[0.7]			-29.6	[0.6]		
18.3			8.36	[0.05]			-21.91	[0.02]
20	11.8	[0.8]			-26.4	[0.6]		
30	10.5	[0.8]			-24.4	[0.7]		
43.3			8.39	[0.05]			-17.51	[0.03]
50	9.9	[1.1]			-21.3	[0.8]		
65	10.0	[1.0]			-17.5	[0.8]		
100	8.4	[1.1]			-15.9	[1.0]		
103.1			6.87	[0.09]			-11.66	[0.02]
150	8.1	[1.3]			-12.6	[1.2]		
185.7			4.77	[0.03]			-7.27	[0.02]
200	5.3	[1.8]			-7.0	[1.5]		
250	5.75	[2.1]			-6.4	[2.1]		
256.9			3.25	[0.02]			-4.77	[0.04]
300	8.09	[2.3]			-4.1	[2.0]		
350	6.3	[3.0]			-6.3	[3.0]		
387.9			1.47	[0.03]			-2.20	[0.04]
400	2.4	[3.3]			-0.4	[3.7]		
435.6			0.96	[0.07]			-1.62	[0.07]
531			1.08	[0.44]			-0.82	[0.27]

* uncert = uncertainty

5.4.2 Distributed beta source, ^{32}P

Figure 5.5 illustrates dose backscatter factor fall-off with distance from a ^{32}P distributed source at aluminium/Mylar, air/Mylar and bismuth/Mylar interfaces. Errors are larger in these data than in the point source simulation data. This is because of poorer statistics or the relatively fewer events which occur in the scoring region when a source broader than this region is used. Smaller uncertainties necessitate prohibitively long computing times.

Fits to the data are also shown in Figure 5.5. The parameters are listed in Table 5.9, along with corresponding experimental values for comparison.

Relaxation lengths for the aluminium/Mylar and bismuth/Mylar ASD profiles shown in Figure 5.5 are 263[90]mg/cm^2 and 435[132]mg/cm^2. These agree with experimental values of 238[11]mg/cm^2 and 588[69]mg/cm^2, within uncertainties. Positions of maxima on the simulated ASD curves agree with experimental maxima positions for the aluminium profile, but not for bismuth profile. The maxima on experimental and Monte Carlo ASD aluminium/Mylar profiles occur around 30mg/cm^2 from the interface; the maximum on the experimental bismuth/Mylar curve occurs between 65-80mg/cm^2 and slightly further from the interface on the Monte Carlo curve, at about 100-150mg/cm^2.

The experimental ASD curve for the air interface exhibits a two-component exponential decline which is characterized by two relaxation lengths of magnitudes 88.5[24.3]mg/cm^2 and 294[138]mg/cm^2. However, the Monte Carlo backscatter factor fall-off is better represented by a single exponential with a relaxation length of 147[19]mg/cm^2.

Experimental and Monte Carlo ASD profiles are compared in the graphs of Figure 5.6, and these data are listed in Table 5.10. There is satisfactory agreement between experimental and Monte Carlo results in these three profiles.

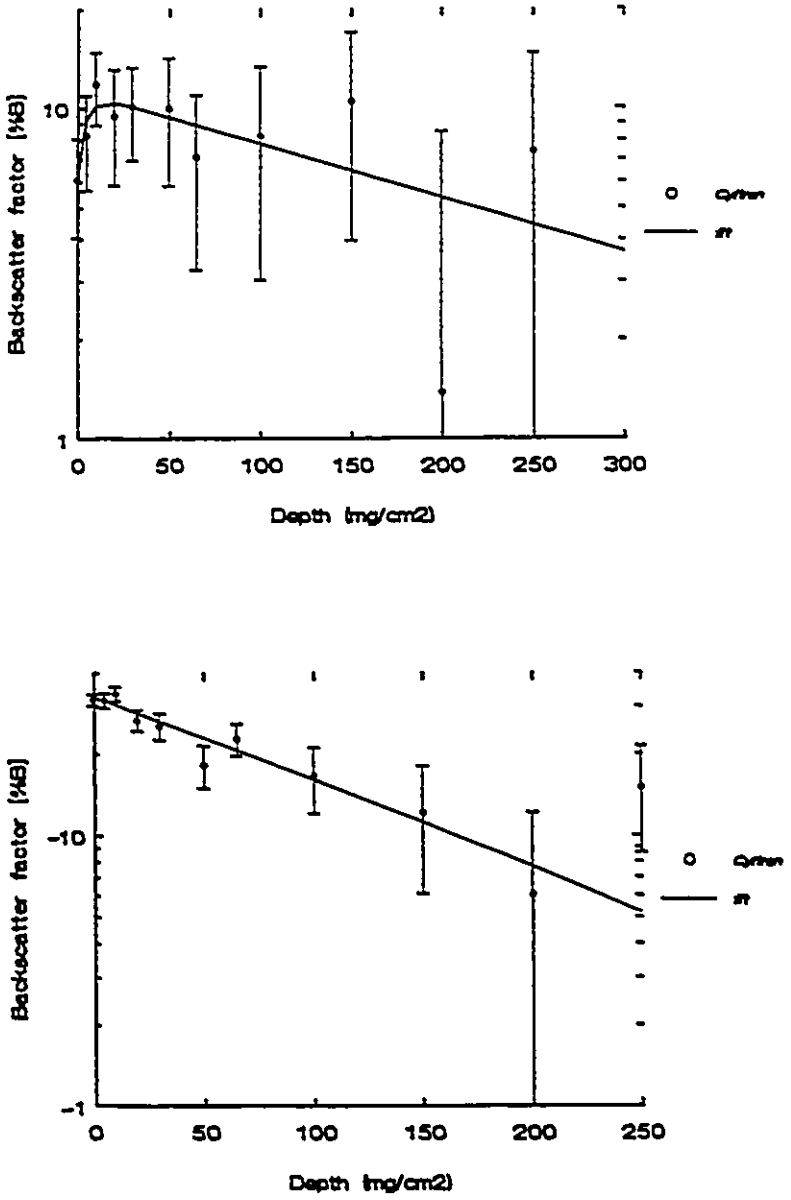

Fig 5.5 Monte Carlo backscatter factor variation with distance from interfaces, ASD geometry, for a ^{32}P distributed source. Upper: aluminium/Mylar interface; Lower: air/Mylar interface.

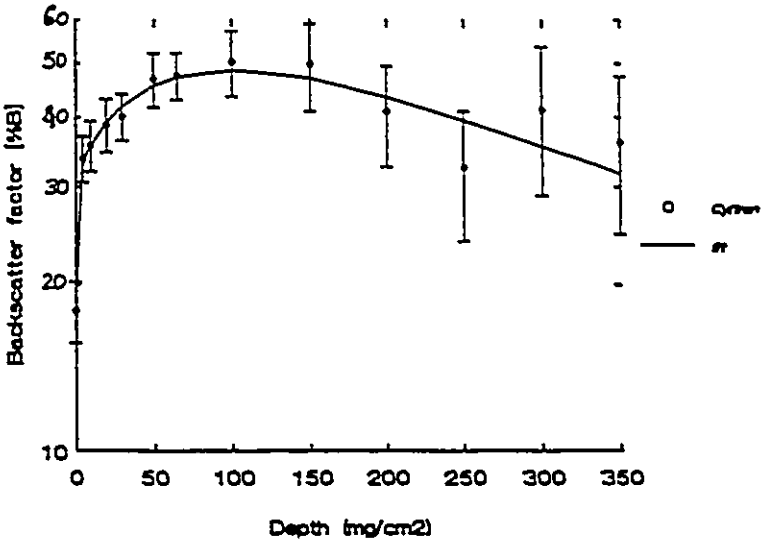

Fig 5.5(continued) Monte Carlo backscatter factor variation with distance from a bismuth/Mylar interface, ASD geometry, for a ^{32}P distributed source.

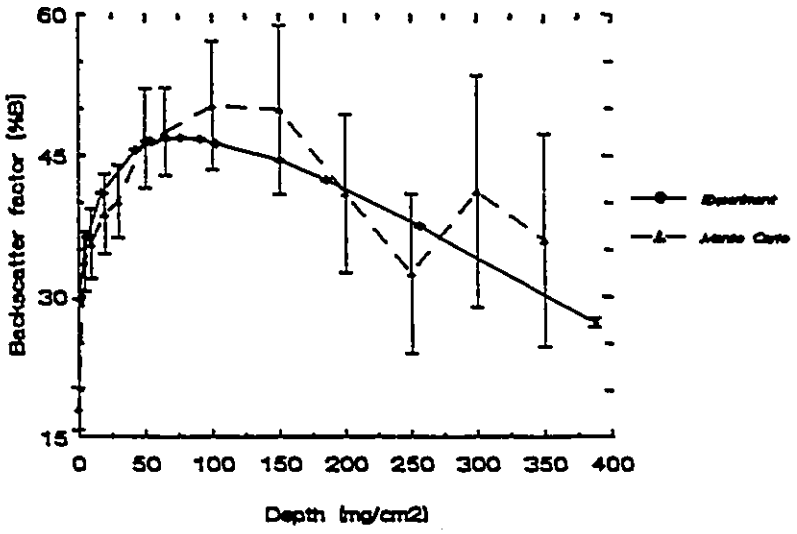

Fig 5.6 Comparison of experimental and Monte Carlo ASD curves for ^{32}P distributed source. Bismuth/Mylar interface.

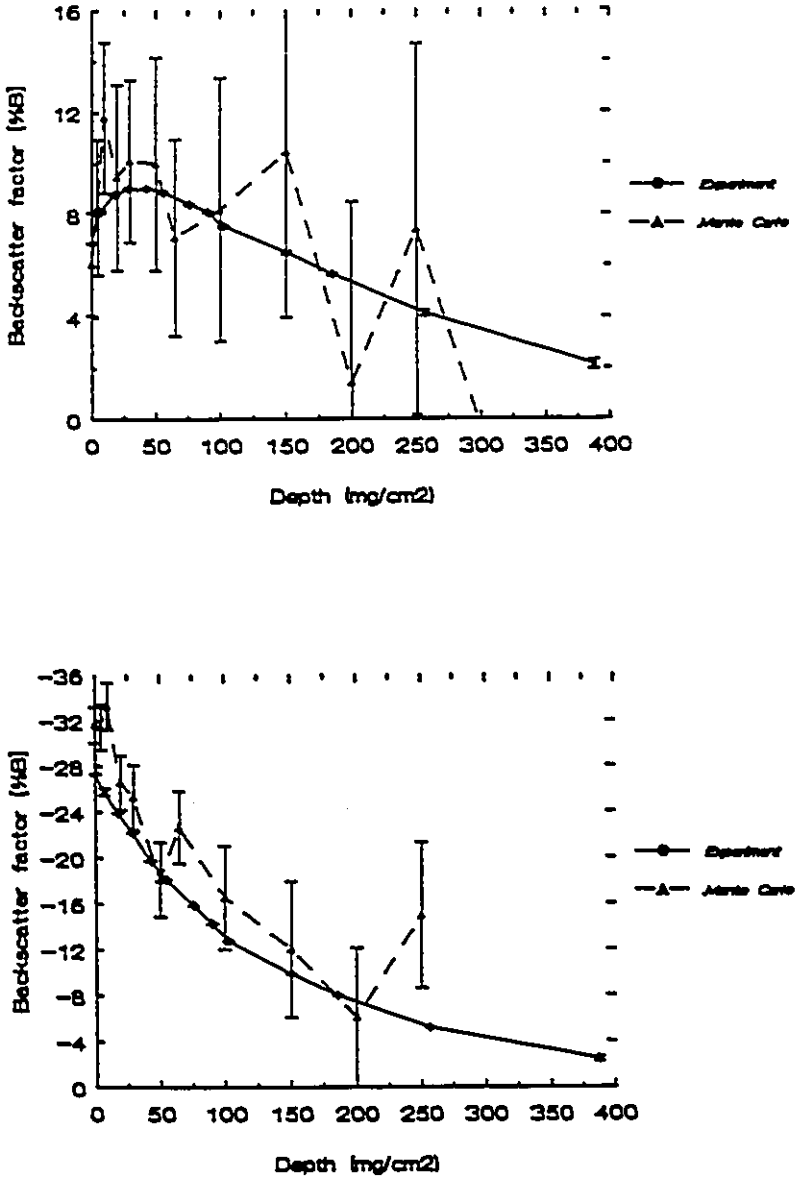

Fig 5.6(continued) Comparison of experimental and Monte Carlo ASD curves for ^{32}P distributed source. Upper: aluminium/Mylar interface; Lower: air/Mylar interface.

Table 5.9 Parameters of Fits to Experimental and *Monte Carlo* Backscatter Factor Data, ASD Geometry*, ^{32}P distributed source.

Scatterer		Parameters					
		A_1	v_1 (mg/cm^2)	A_2	v_2 (mg/cm^2)	A_3	v_3 (mg/cm^2)
Al	Expt	-4.2 [0.3]	33 [6]	-1.2 [0.4]	5 [2]	12.1 [0.4]	238 [11]
	Calc			*-5.3[1.2]*	*5[3]*	*11[1]*	*263[90]*
Bi	Expt	-20.0 [1.6]	53.5 [13]	-9.8 [2.0]	10.4 [1.9]	58.8 [3.0]	588 [69]
	Calc	*-40 [13]*	*61 [20]*	*-13.0[1.3]*		*71 [14]*	*435[132]*
Air	Expt			15.6 [8]	88.5 [24]	13[8]	294[138]
	Calc			*32.2[0.8]*	*147[19]*		

* *Fits are of the form* $\%B = \sum_i A_i e^{-\frac{x}{v_i}}$ for solid interfaces and

$1 - \%B = \sum_i A_i e^{-\frac{x}{v_i}}$ for air interfaces.

x is the distance from the interface in mg/cm^2.

Table 5.10 Experimental and Monte Carlo ASD Backscatter Factors for ^{32}P distributed source.

	Aluminium/Mylar		Bismuth/Mylar	
Depth (mg/cm^2)	Cyltran %B [uncert]*	Experiment %B [uncert]	Cyltran %B [uncert]	Experiment %B [uncert]
0	6.0 [2.0]		17.9 [2.3]	
0.55		6.86 [0.02]		29.57 [0.03]
5	8.2 [2.7]		33.6 [3.2]	
7.25		8.085 [0.05]		36.22 [0.05]
10	11.8 [3.0]		35.5 [3.7]	
17.85		8.76 [0.03]		40.87 [0.01]
20	9.4 [3.7]		38.6 [4.3]	
28.85		8.98 [0.03]		
30	10.05 [3.2]		40.0 [3.9]	
42.85		8.98 [0.03]		45.52 [0.02]
50	9.9 [4.2]		46.7 [5.3]	
54.95		8.86 [0.03]		46.36 [0.04]
65	7.1 [3.8]		47.4 [4.7]	
65.55				46.74 [0.05]
76.15		8.36 [0.03]		46.80 [0.02]
90.55		8.055 [0.01]		46.63 [0.04]
100	8.15 [5.2]		50.2 [6.9]	
102.65		7.49 [0.05]		46.14 [0.02]
150.35	10.4 [6.5]	6.47 [0.06]	49.7 [9.0]	44.36 [0.04]
185.25		5.61 [0.04]		42.26 [0.05]
200	1.4 [7.1]		40.8 [8.5]	
250	7.4 [7.3]		32.3 [8.6]	
256.45		4.08 [0.10]		37.36 [0.08]
300			41.1 [12.4]	
350			35.9 [11.4]	
387.45		2.1 [0.2]		27.1 [0.5]

* uncert = uncertainty

Table 5.10(continued) Experimental and Monte Carlo ASD Backscatter Factors for ^{32}P distributed source.

	Air/Mylar Interface	
Depth (mg/cm^2)	Cyltran %B [uncert]*	Experiment %B [uncert]
0	-31.55 [1.6]	
0.55		-27.27 [0.06]
5	-31.4 [2.0]	
7.25		-25.7 [0.3]
10	-33.2 [2.1]	
17.85		-23.84 [0.02]
20	-26.5 [2.4]	
28.85		-22.12 [0.01]
30	-25.2 [2.9]	
42.85		-19.68 [0.05]
50	-18.1 [3.3]	
54.95		-18.02 [0.02]
65	-22.6 [3.2]	
76.15		-15.80 [0.03]
90.55		-14.18 [0.02]
100	-16.5 [4.5]	
102.65		-12.69 [0.02]
150.35	-12.0 [5.9]	-9.82 [0.03]
185.25		-7.93 [0.04]
200	-6.0 [6.1]	
250	-14.9 [6.4]	
256.45		-5.13 [0.04]
387.45		-2.4 [0.2]

* uncert = uncertainty

5.5 *ASB Geometry, Point Source, ^{32}P*

Monte Carlo calculation of one backscatter factor in this configuration was accomplished by placing a Mylar absorber of a known thickness between the source and scatterer in the geometry of Figure 5.1. Several monoenergetic electron sources were used for each absorber thickness d and fractional energy deposited in the detector, $\varepsilon(E,d)$, scored. These were integrated over the ^{32}P beta spectrum to determine beta dose backscatter factors as a function of absorber thickness, $\overline{B}(d)$, for aluminium and air scatterers.

The backscatter factor depth profiles for these two cases are illustrated in Figure 5.7. The profile for the aluminium scatterer resembles its experimental counterpart. Although it is fitted by two exponentials and the experimental curve is modelled by one exponential, their relaxation lengths are not tremendously different. The dominant relaxation length obtained from the Monte Carlo data is 36[1]mg/cm^2 and the experimental value is 26[4]mg/cm^2. The second profile in Figure 5.7, for the case of no or air scatterer, is represented by two decaying exponentials, a trend exhibited by the experimental curve as well (Section 4.4.4).

However, the lingering dose reduction factor observed in the air interface experimental data, to well beyond 400mg/cm^2, is not obtained in the Monte Carlo results. At 400mg/cm^2, no dose reduction is predicted by EGS4/Dosrz. Nonetheless, the slower declining exponential has a relaxation length of 39[3]mg/cm^2 which roughly approximates the experimental value of 28[1]mg/cm^2.

Parameters of the fits to Monte Carlo and experimental ASB backscatter factor depth curves are given in Table 5.11. The backscatter factor data are listed in Table 5.12 and the profiles are compared graphically in Figure 5.8.

Comparison of EGS4/Dosrz and experimental ASB backscatter factor data is acceptable. Backscatter factor depth profiles from the code not only exhibit trends observed in the experimental curves, but they also predict rates of decrease of backscatter factor with depth which approximate experimental values; for the air and aluminium interfaces investigated, EGS4/Dosrz and experimental relaxation

lengths are about 36mg/cm^2 and 28mg/cm^2, respectively.

Table 5.11 Parameters of Fits to Experimental and *Monte Carlo* Backscatter Factor Data, ASB Geometry, ^{32}P point source.

		Parameters						
		A_1	v_1 (mg/cm^2)	a	d	A_2	v_2 (mg/cm^2)	δ
Scatterer								
Al	Expt	7.4 [0.2]	26 [4]	-0.04 [0.8]	3.0 [1.0]			
	Calc	*8.9 [0.1]*	*36 [1]*			*1.4 [0.2]*	*1.7 [0.4]*	
Air	Expt	4 [1]	2[1]			19 [1]	28 [1]	2.0[0.5]
	Calc	*11[1]*	*5[1]*			*16[1]*	*39[3]*	

Fits are of the form $\%B = A_1 e^{-x/v_1} + A_2 e^{-x/v_2}$ for the aluminium/Mylar interface and $1 - \%B = A_1 e^{-x/v_1} + A_2 e^{-x/v_2}$ for the air/Mylar interface. x represents the absorber thickness. Experimental fits are as detailed in Section 4.4.4.

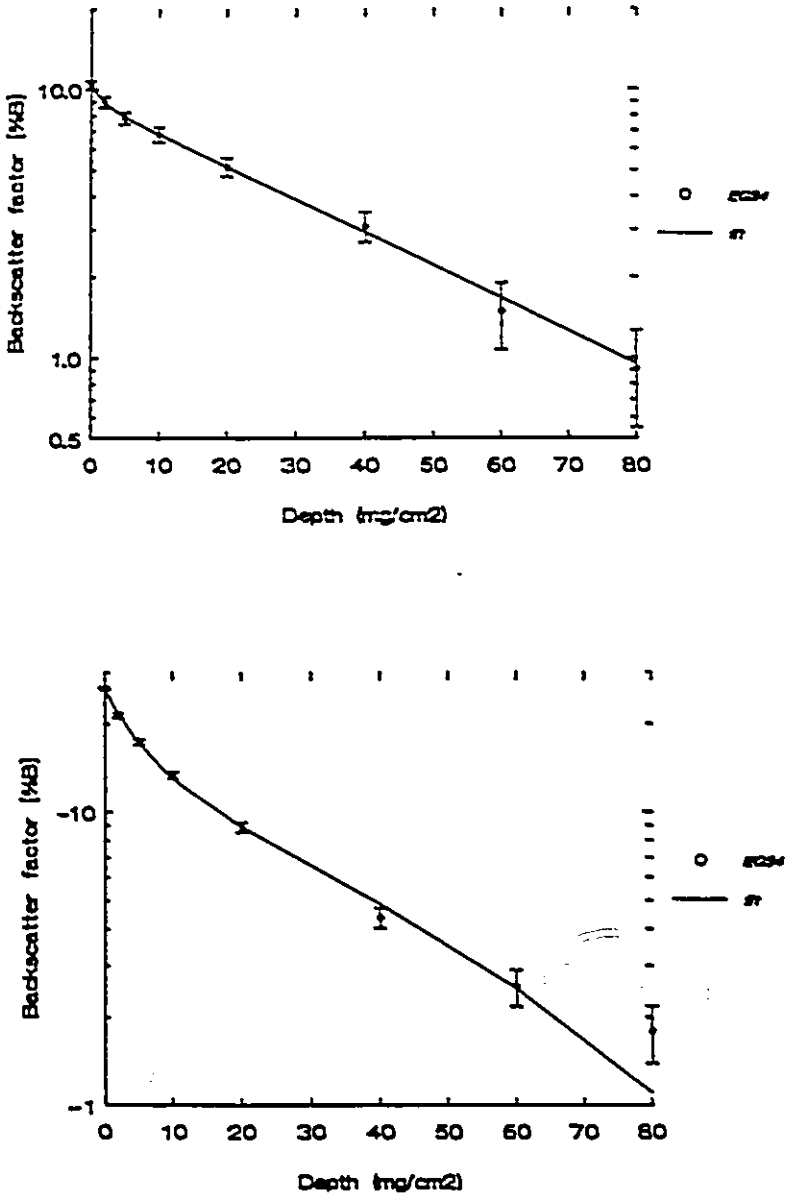

Fig 5.7 Monte Carlo backscatter factor variation with distance from interfaces, ASB geometry, for a ^{32}P point source. Upper: aluminium/Mylar interface; Lower: air/Mylar interface.

Table 5.12 Experimental and Monte Carlo ASB Backscatter Factors for ^{32}P point source.

	Aluminium/Mylar		Air/Mylar	
Depth (mg/cm^2)	EGS4/Dosrz %B [uncert]*	Experiment %B [uncert]	EGS4/Dosrz %B [uncert]	Experiment %B [uncert]
0	10.3 [0.4]	7.9 [0.1]	-26.2 [0.3]	-23.4 [0.1]
0.35		7.27 [0.08]		-22.88[0.02]
1.78		6.44 [0.17]		-20.47[0.02]
2.0	8.87 [0.44]		-21.1 [0.3]	
3.3		6.51 [0.11]		-18.84[0.28]
5	7.71 [0.41]		-17.1 [0.4]	
7.45		5.83 [0.06]		-15.76[0.03]
10	6.71 [0.42]		-13.2 [0.4]	
10.4		5.34 [0.08]		-13.78[0.54]
19.48		3.63 [0.08]		-10.38[0.04]
20	5.08 [0.41]		-8.8 [0.3]	
32.15		2.79 [0.03]		-8.59 [0.23]
40	3.05 [0.40]		-4.3 [0.3]	
44.48		1.07 [0.18]		-4.9 [0.6]
58.65		1.14 [0.19]		-3.35 [0.7]
60	1.47 [0.41]	-	-2.5 [0.4]	
71.55		0.29 [0.06]		-4.75 [0.42]
80	0.90 [0.36]		-1.8 [0.4]	
82.15		0.04 [0.08]		-3.78 [0.78]
90.75				-2.44 [0.87]
97.18				-1.98 [0.11]
144.88				-0.27 [0.19]
192.58				-2.05 [0.07]

* uncert = uncertainty

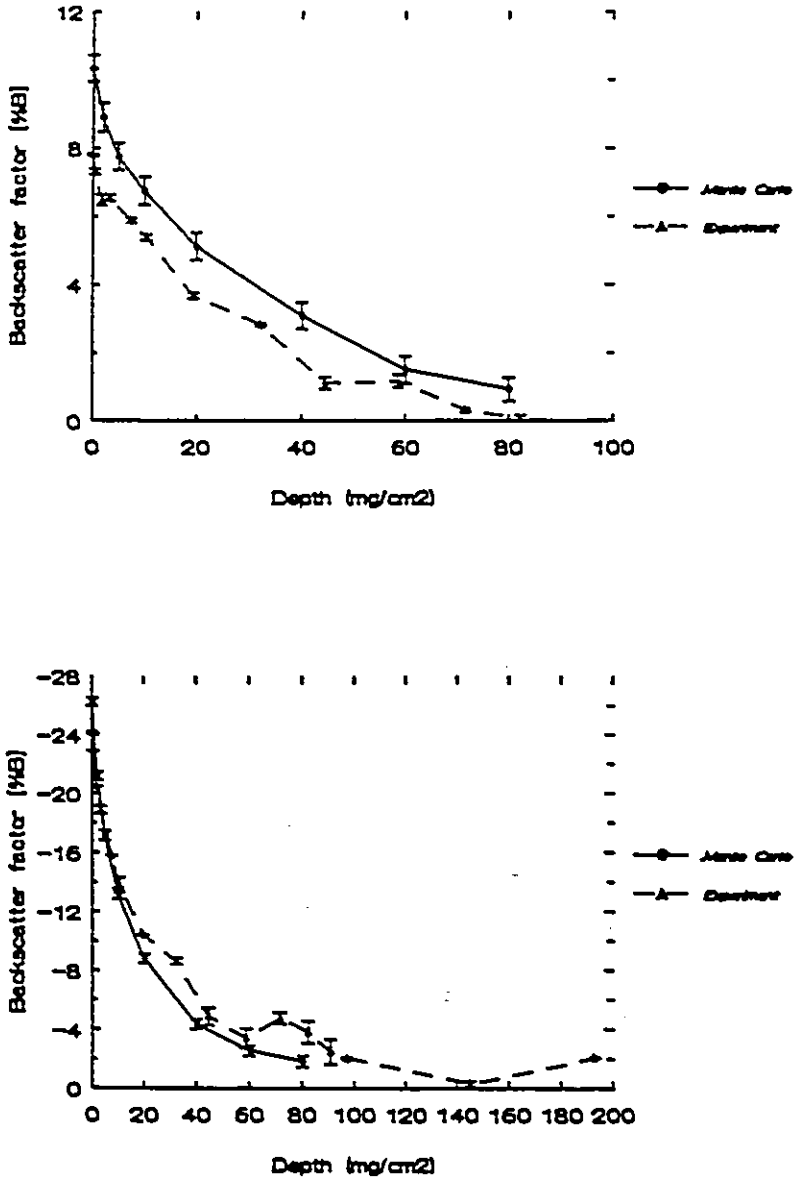

Fig 5.8 Comparison of experimental and Monte Carlo ASB curves, for a ^{32}P point source. Upper: aluminium/Mylar interface; Lower: air/Mylar interface.

5.6 *Determination of $\bar{B}$, the Beta Dose Backscatter Factor*

Dose backscatter factors were defined in Chapter 4. Since both beta sources and monoenergetic electron sources are dealt with here, dose backscatter factors due to the former are denoted by $\bar{B}$ and those due to the latter are denoted by B(E). Similarly, $\bar{R}$ and R(E) represent dose ratios for beta and monoenergetic electron sources, respectively.

$\varepsilon_S(E)$ is the fraction of monoenergetic electron source energy E deposited in the scoring region when material or scatterer S is in position. $\varepsilon_M(E)$ is defined in a parallel manner, except material M replaces S. The dose ratio at an interface created by materials S and M, and due to a monoenergetic electron source of energy E, is

$$R_{SM}(E) = \frac{\varepsilon_S(E)}{\varepsilon_M(E)} \qquad (5.1).$$

and the dose backscatter factor is $B_{SM}(E) = R_{SM}(E) - 1.$ (5.2)

The dose ratio for a beta source and the same material interface is obtained by summing or integrating the monoenergetic energy deposited data, $E\varepsilon_S(E)$ and $E\varepsilon_M(E)$, over the beta spectrum of interest, S(E). This gives the total energy deposited by a beta source for the two scatterers, $E_{tot,S}$ and $E_{tot,M}$. The dose ratio is the ratio of these. That is,

$$\bar{R}_{SM} = \frac{E_{tot,S}}{E_{tot,M}} = \frac{\int E\varepsilon_S(E)\, S(E)\, dE}{\int E\varepsilon_M(E)\, S(E)\, dE} \qquad (5.3).$$

The beta dose backscatter factor is given by $\bar{B}_{SM} = \bar{R}_{SM} - 1.$ (5.4)

Equation 5.4 can be rewritten as follows.

$$\bar{B}_{SM} = \frac{\int B_{SM}(E) E\varepsilon_M(E)\, S(E)\, dE}{\int E\varepsilon_M(E)\, S(E)\, dE} \qquad (5.5).$$

Three methods of integrating monoenergetic fractional energy deposited data over the beta spectrum were carried out in order to evaluate Equation 5.3. Numerical means for determining S(E) was available from a previously developed computer programme (Prestwich 1986).

The first method consisted of fitting the fractional energy deposited data, $\varepsilon(E)$, as functions of source energy E and using a fine energy bin width ($E_o/500$ or 3.4keV for ^{32}P) to integrate over the spectrum. The linear least -squares fits achieved are illustrated in Figure 5.9. Although they appear reasonable, errors in the fitted parameters were such that uncertainties in the fitted values were sometimes considerably larger than those in the input data. The fits were of the form

$$\varepsilon(E) = e^{-\sum_{i=1}^{4} \alpha_i E^{i-1}} \qquad \text{for } E \geq 100\,\text{keV}, \text{ and}$$

$$\varepsilon(E) = e^{-\sum_{i=1}^{3} \beta_i E^{i-1}} \qquad \text{for } E < 100\text{keV}.$$

The shapes of the fractional energy deposited profiles are similar for the five scatterers shown in Figure 5.9. The data are from Zeroeth type, thick window simulations; beta dose backscatter factors determined from these data are detailed in Section 5.3.1.

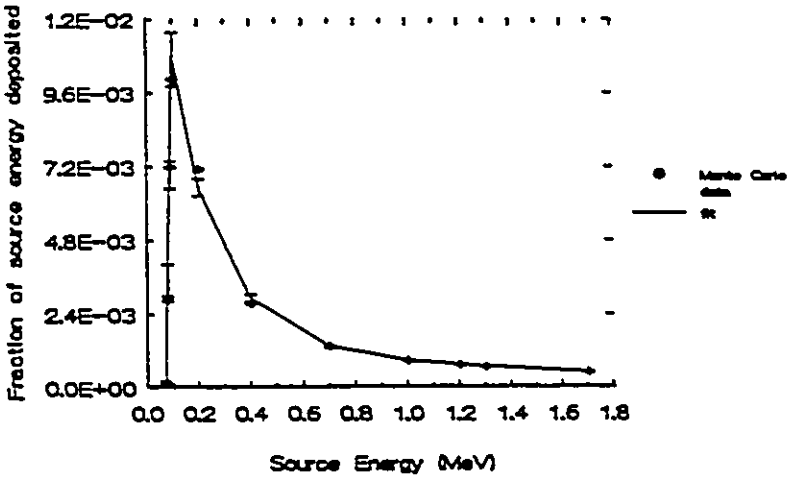

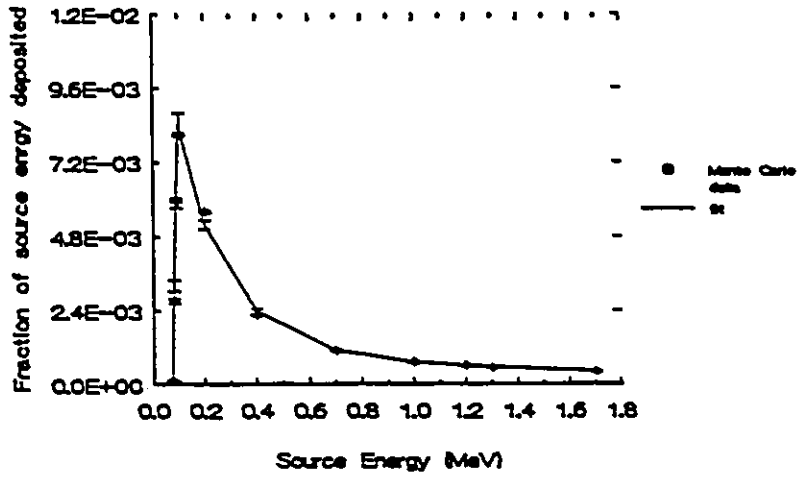

Fig 5.9 Fractional energy deposited by monoenergetic electron point sources in Zeroeth geometry simulations. (a) Upper: Bismuth scatterer; (b) Lower: aluminium scatterer.

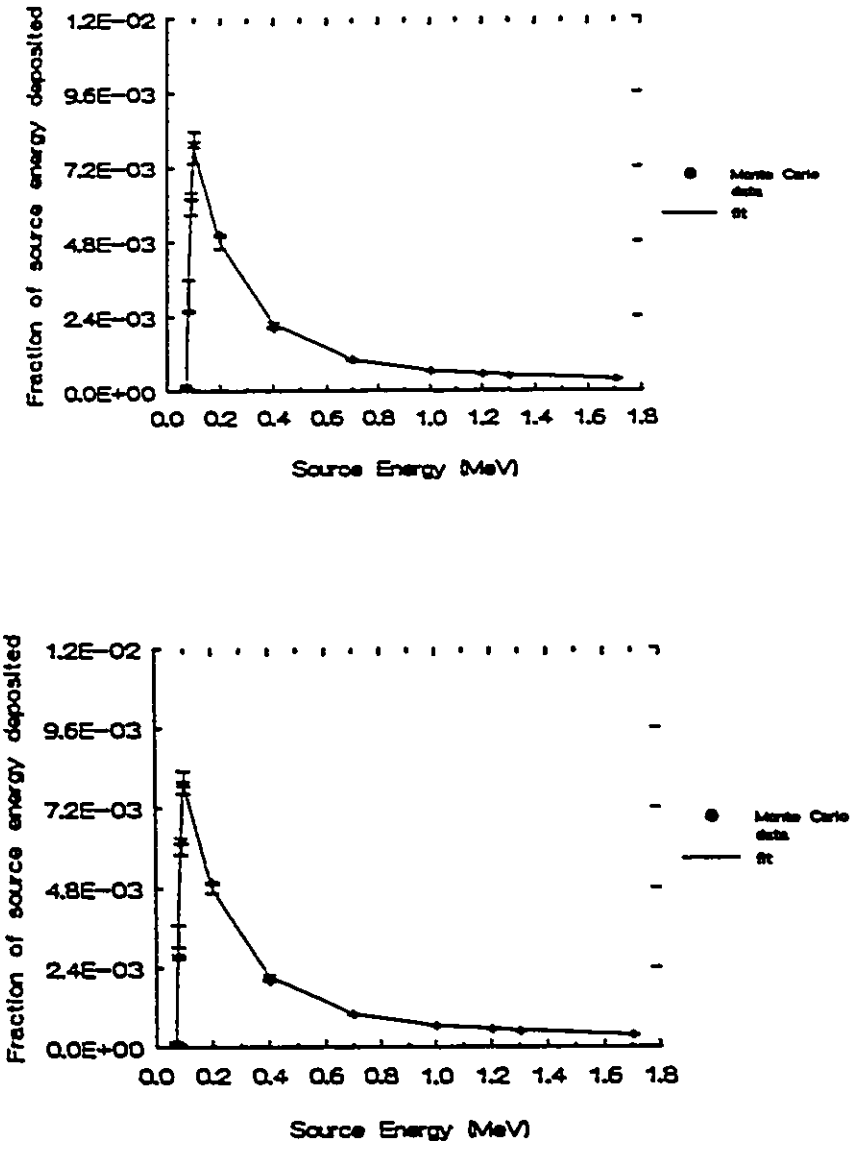

Fig 5.9(continued) Fractional energy deposited by monoenergetic electron point sources in Zeroeth geometry simulations. (c) Upper: Mylar scatterer; (d) Lower: lucite scatterer.

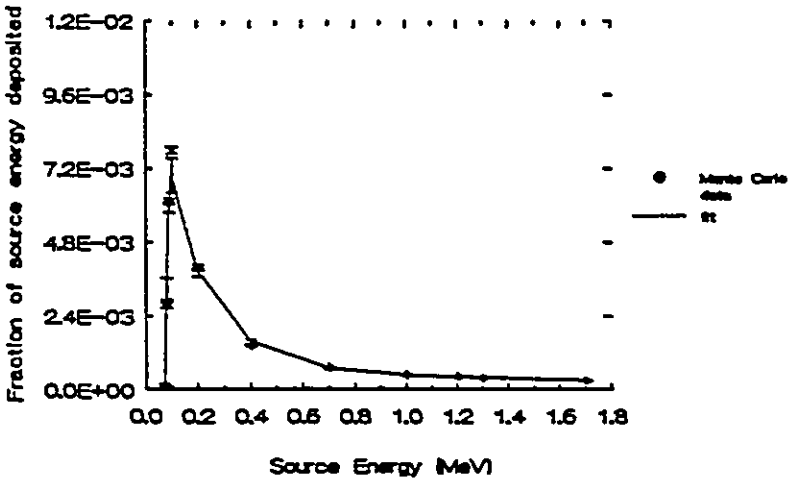

Fig 5.9(continued) (e) Fractional energy deposited by monoenergetic electron point sources in Zeroeth geometry simulations, air scatterer.

The second method of integrating monoenergetic fractional energy deposited data over the beta spectrum was a linear interpolation between the Monte Carlo calculated $\varepsilon(E)$ values and integration over the beta spectrum using the small binning described above.

The third method was a coarse summation. The individual Monte Carlo monoenergetic data, ε_i, were summed over the beta spectrum. That is,

$$E_{tot,S} = \sum_i E_i \varepsilon_{i,S} S_i \Delta_i \qquad (5.6)$$

and

$$E_{tot,M} = \sum_i E_i \varepsilon_{i,M} S_i \Delta_i \qquad (5.7),$$

where Δ_i, the bin width used in the summation, was considerably larger than 0.2% of the end-point energy which was used in the other two methods.

Uncertainties in E_{tot} were determined by

$$\sigma^2_{E_{tot},S} = \sum_i S_i^2 \Delta_i^2 E_i^2 \sigma^2_{\varepsilon_i,S} \qquad (5.8)$$

and

$$\sigma^2_{E_{tot},M} = \sum_i S_i^2 \Delta_i^2 E_i^2 \sigma^2_{\varepsilon_i,M} \qquad (5.9).$$

These reflect the uncertainties associated with the input Monte Carlo monoenergetic fractional energy deposited data, ε_i.

Beta dose backscatter factors were also calculated using Equation 5.5. Monoenergetic backscatter factors, B(E), from Zeroeth geometry, thick window, point source simulations, were fitted as polynomials in E. This approach was pursued because B(E) data, shown in Figure 5.10, were fit better than ε(E) data.

Beta dose backscatter factors obtained from the second and third methods agreed very well. Agreement between these values and those obtained from the fitting methods was reasonable over-all. It was exceptional for those cases where the fits were good and somewhat mediocre for the cases where the fits were poorer.

These methods, of varying complexity, served to show that the straightforward summation method, Equations 5.6 and 5.7, was adequate. Consequently, the summation method was used exclusively to determine beta dose backscatter factors for those cases which had not already been subjected to the four procedures described above.

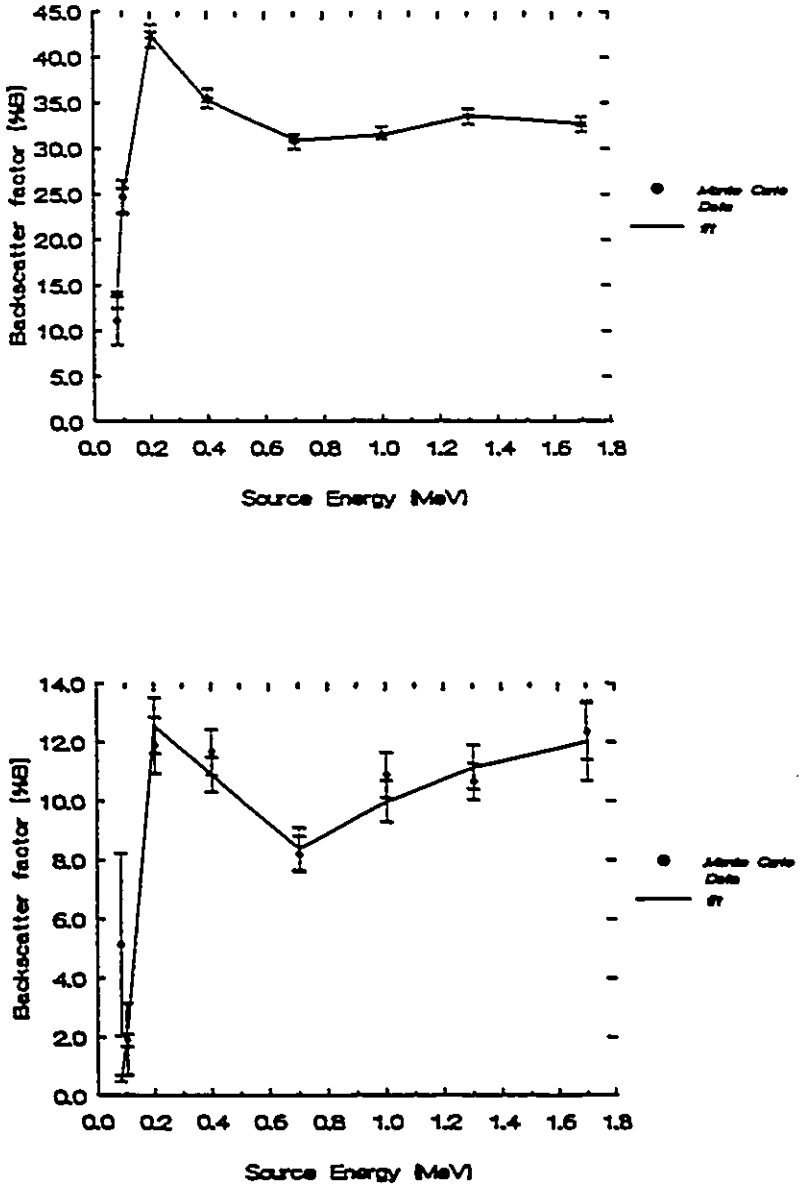

Fig 5.10 Monoenergetic dose backscatter factor variation with source energy. Upper: bismuth/Mylar interface; Lower: aluminium/Mylar interface.

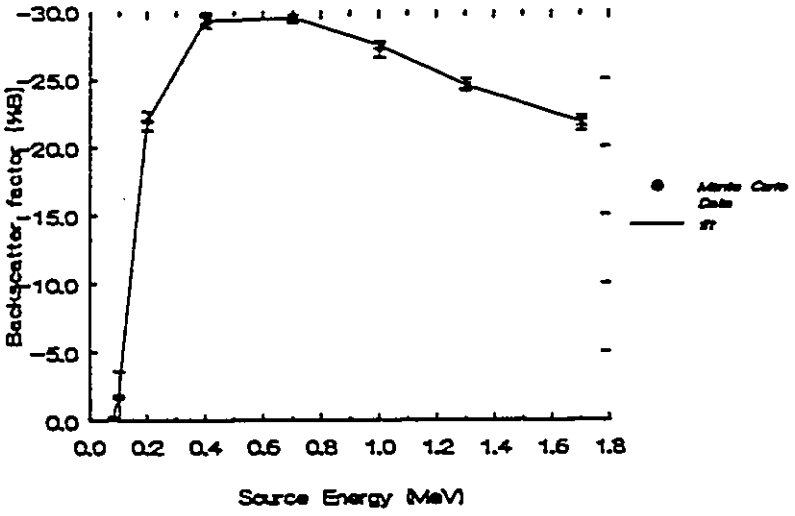

Fig 5.10(continued) Monoenergetic dose backscatter factor variation with source energy for an air/Mylar interface.

5.7 Monoenergetic Electron Source Results

It was pointed out in the introductory portion of this chapter and later demonstrated in Section 5.6 that monoenergetic data are fundamental to calculating beta dose backscatter factors. In addition, although it is the latter results which are compared with experimental values, a comparison of monoenergetic data from the two Monte Carlo codes is worthwhile because it can provide information that is not obtainable by comparing beta dose backscatter factors from the two codes. Section 5.7.1 is therefore devoted to such a comparison.

Figure 5.11 consists of fractional energy deposition profiles for bismuth, copper, aluminium, air, Mylar and lucite. The data are from Zeroeth geometry, thin window, distributed source simulations; beta dose backscatter factors determined from these data are given in Section 5.4.2.

Although source geometry and window thickness used in the simulations are different, the fractional energy deposition profiles shown in Figure 5.9 have the same shapes as those in Figure 5.11. The profiles exhibit a steep rise from no energy deposited by source electrons with energy less than a cut-off value, E_{cut}, to a peak, followed by an exponential-like decrease. Source electrons which create the peak deposit the largest fraction of their energy in the detector, compared with other incident electrons. The deposition of smaller amounts of energy by higher energy electrons is consistent with stopping powers predicted by the CSDA model.

A cut-off energy exists in these profiles because electrons with less energy than E_{cut} are unable to penetrate the detector window. For the thick window, E_{cut} is about 70keV, and for the thin window, it is about 15keV. Since more lower energy electrons enter the detector when the thin rather than the thick window is used, the peaks in the thin window profiles, Figure 5.11, occur at a source energy which is smaller than that at which the peaks in the thick window profiles, Figure 5.9, occur. Fractional energy deposition peaks at 50keV in Figure 5.11, and at 100keV

in Figure 5.9.

Figures 5.9 and 5.11 also demonstrate that the fraction of source energy deposited in the detector is typically less than 1%. At the same time, however, the profiles indicate that the amount of energy deposited increases with scatterer atomic number. It is also of interest to note that the fractional energy deposited by 20keV source electrons in the profiles of Figures 5.11 (a), (c), (e) is considerably smaller than the fractional energy deposited by 20keV source electron in the profiles of Figures 5.11 (b), (d), (f). The latter profiles are Cyltran data and the former are EGS4/Dosrz data. The difference is not related to the atomic number of the scatterer because Figures 5.11 (a), (c), (e) are for bismuth, aluminium and Mylar scatterers and Figures 5.11 (b), (d), (f) are for copper, air and lucite scatterers. Possible causes of this difference are suggested in Section 5.7.1, where a quantitative comparison of the data is given.

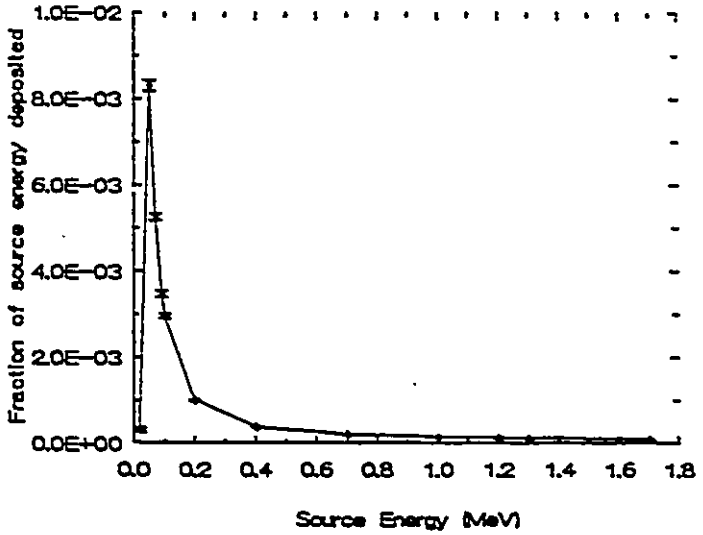

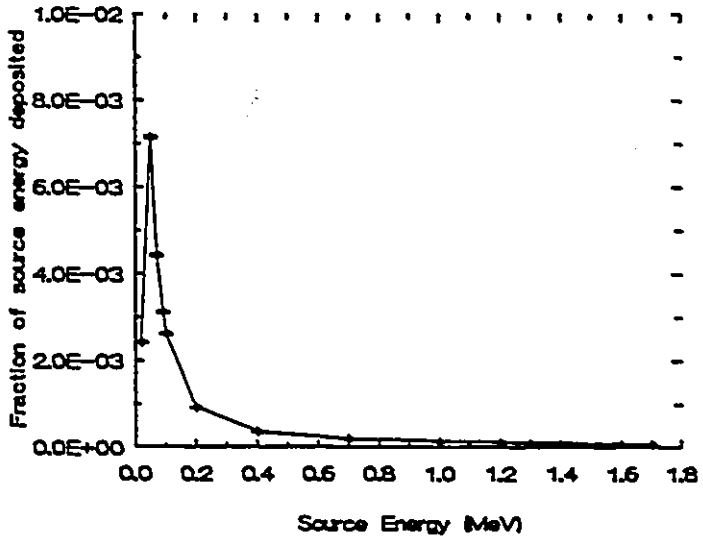

Fig 5.11 Fractional energy deposited by monoenergetic electron distributed sources in Zeroeth geometry, thin window simulations. (a) Upper: bismuth scatterer; (b) Lower: copper scatterer.

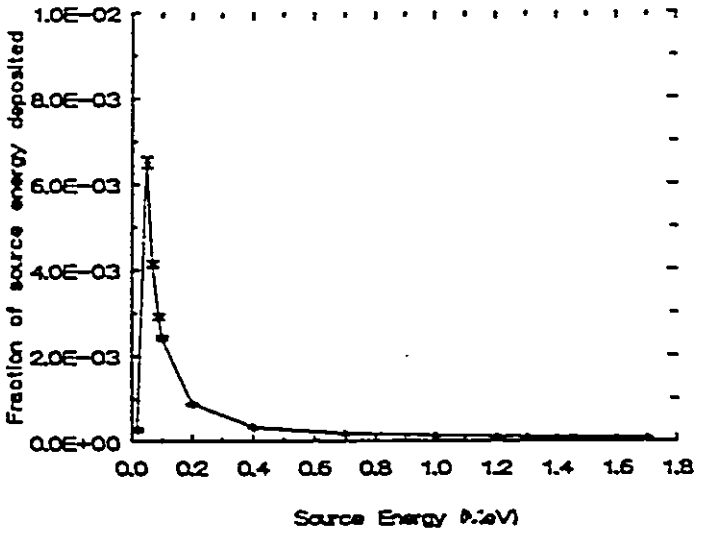

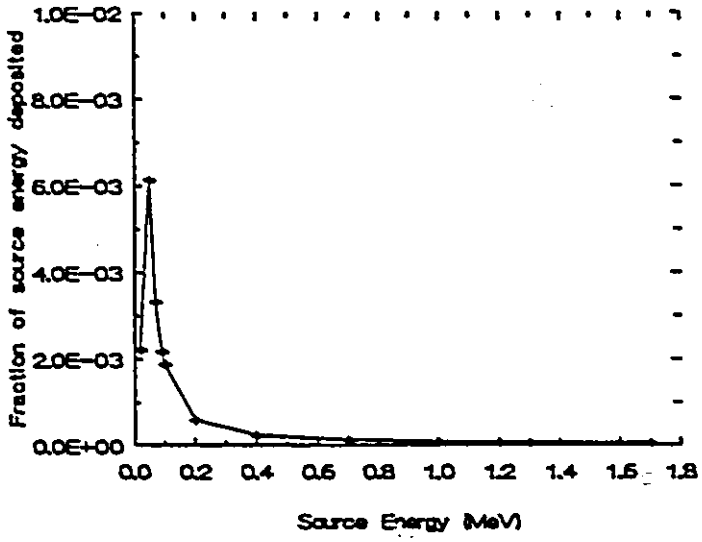

Fig 5.1-1(continued) Fractional energy deposited by monoenergetic electron distributed sources in Zeroeth geometry, thin window simulations. (c) Upper: aluminium scatterer; (d) Lower: air scatterer.

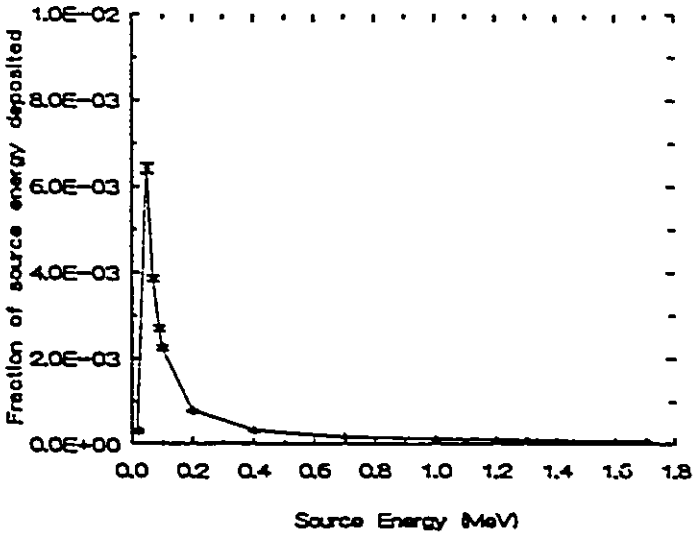

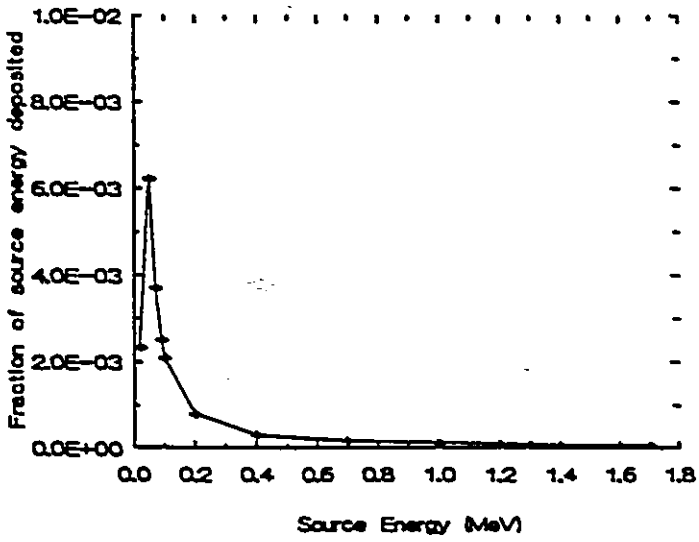

Fig 5.11(continued) Fractional energy deposited by monoenergetic electron distributed sources in Zeroeth geometry, thin window simulations. (e) Upper: Mylar scatterer; (f) Lower: lucite scatterer.

Figures 5.12 and 5.13 illustrate monoenergetic dose backscatter factors from EGS4/Dosrz and Cyltran, respectively, for several interfaces. These data are from Zeroeth geometry, distributed source, thin window simulations.

The graphs of Figure 5.12 are for scatterer/Mylar interfaces. The solid material/Mylar graphs show somewhat similar trends in the variation of backscatter factor with electron source energy. Dose enhancement increases with source energy, peaks around 100 or 200 keV, then decreases to a minimum after which it increases again. The valleys in these graphs occur between 200keV and 700keV. Magnitudes of the dose enhancement factors and locations of peaks differ with scatterer atomic number. Dose reduction at the air/Mylar interface increases with source energy, to a maximum at around 400keV, followed by a very slight decrease with increasing source energy.

Monoenergetic backscatter factors for scatterer/lucite interfaces are shown in Figure 5.13. Trends shown in these graphs differ from those in Figure 5.12. Dose enhancement increases with electron source energy, to a peak in the neighbourhood of 100keV, and then decreases with increasing source energy, except of the persistently large dose enhancement factor at 1.3MeV. Dose reduction at the air/lucite interface increases with source energy in two stages; the first is a rather sharp increase between 0 and 200keV, and the second is more gradual so that the dose reduction in this latter stage may almost be constant. As for the solid material interface data, however, the large uncertainties associated with these values prohibit describing these monoenergetic backscatter factor profiles clearly.

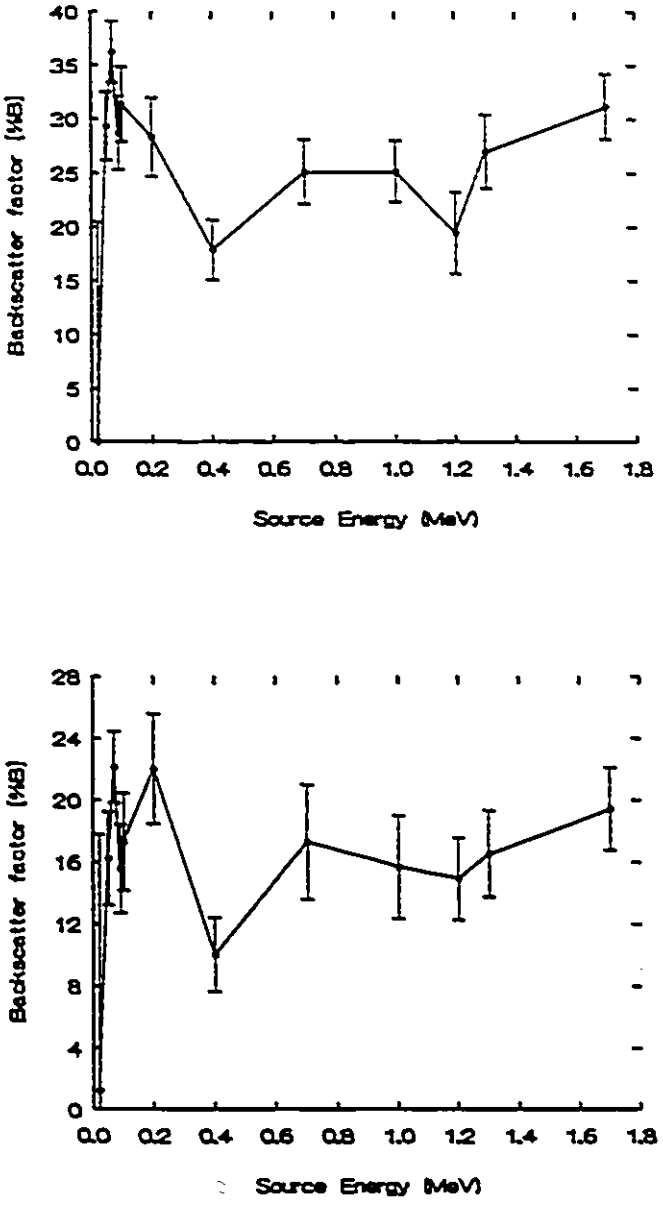

Fig 5.12 (a) Distributed source monoenergetic dose backscatter factors from EGS4/Dosrz. Upper: bismuth/Mylar interface; Lower: copper/Mylar interface.

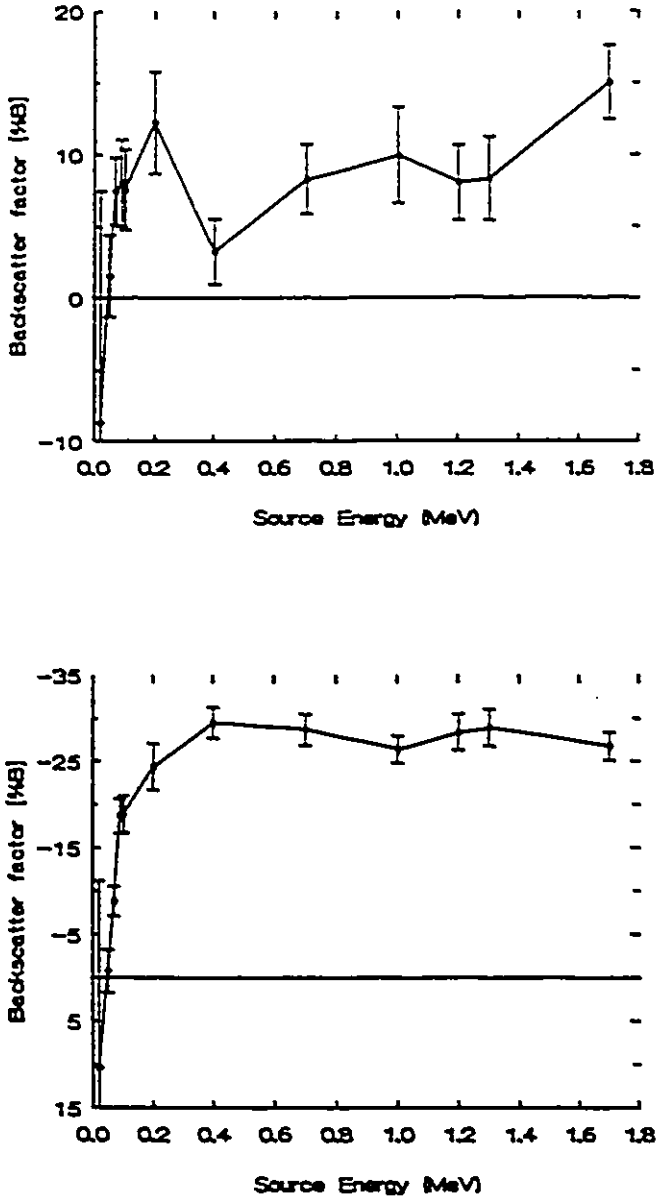

Fig 5.12 (b) Distributed source monoenergetic dose backscatter factors from EGS4/Dosrz. Upper: aluminium/Mylar interface; Lower: air/Mylar interface.

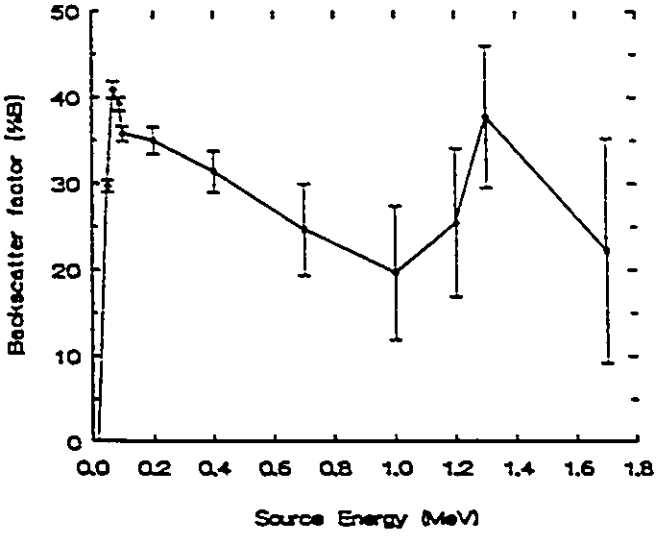

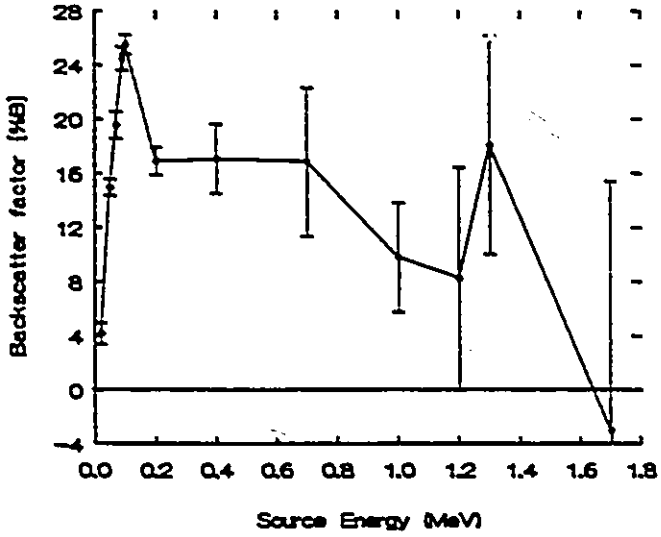

Fig 5.13 (a) Distributed source monoenergetic dose backscatter factors from Cyltran. Upper: bismuth/lucite interface; Lower: copper/lucite interface.

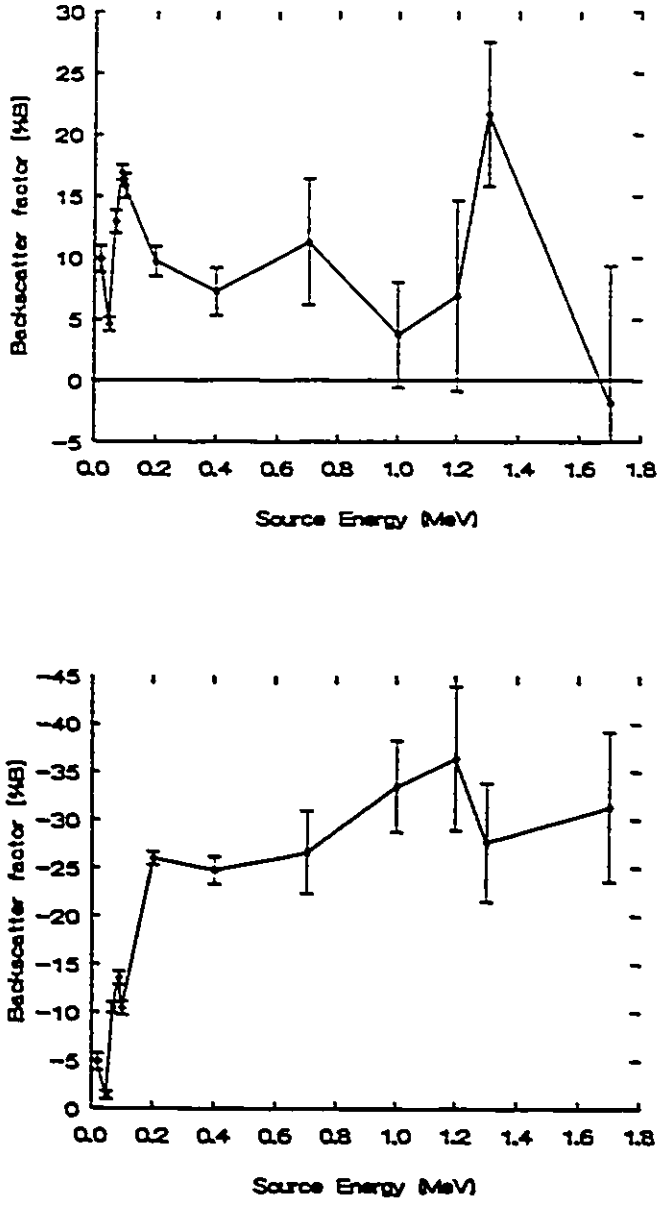

Fig 5.13 (b) Distributed source monoenergetic dose backscatter factors from Cyltran. Upper: aluminium/lucite interface; Lower: air/lucite interface.

5.7.1 Comparison of EGS4/Dosrz and Cyltran results

Fractional energy deposited per incident electron, $\varepsilon(E)$, and monoenergetic dose backscatter factors, B(E), from several Zeroeth simulations and one ASD simulation are compared. Both Monte Carlo codes were used for each calculation.

To be more specific, monoenergetic results from Zeroeth geometry, point source calculations with thick and thin detector windows are compared; beta dose backscatter factors derived from these data are given in Section 5.3.1. Next, monoenergetic data from Zeroeth geometry, distributed source, thin window simulations are considered; beta dose backscatter factors from these data are detailed in Section 5.3.2. Lastly, a comparison of results from an ASD type simulation, done for one source energy, is given.

Zeroeth Geometry, point source

(a) Thick Detector Window -

For source energies greater than, or equal to, 100keV, EGS4/Dosrz and Cyltran $\varepsilon(E)$ data agree to within 3% for aluminium, Mylar and lucite scatterers. This also holds for the case of no or air scatterer, except at 1.7MeV, where there is a 7% discrepancy. Agreement between the two codes is within 4% for bismuth and copper scatterers.

Differences noted in the preceding paragraph are such that Cyltran values exceed those from EGS4/Dosrz. This trend is evident in Figure 5.14 where ratios of "EGS4 $\varepsilon(E)$ to Cyltran $\varepsilon(E)$" for aluminium, air and Mylar scatterers are shown as functions of source energy. For source energies 100keV and greater, these ratios are less than, or equal to, 1.

Below 100keV, data are sparse since only source energies 70keV and greater are of physical relevance in this simulation. Energy deposited data at 80keV

are about 7% different for a few scatterers. These discrepancies are such that EGS4/Dosrz values are larger than those from Cyltran; this is the reverse of the trend noted before for higher energies, and is visible in Figure 5.14 as well.

Although not shown in Figure 5.14, Cyltran predicts a small but finite fractional energy deposited for 70keV source electrons for the aluminium and copper scatterers whereas EGS4/Dosrz predicts none. The CSDA range corresponding to this source energy is 7.3mg/cm^2 in polyethylene; the detector window and source substrate are about 7.25mg/cm^2 thick. The discrepancy between the two codes here may be a manifestation of different treatments of either energy-loss straggling or termination of electron histories, or both.

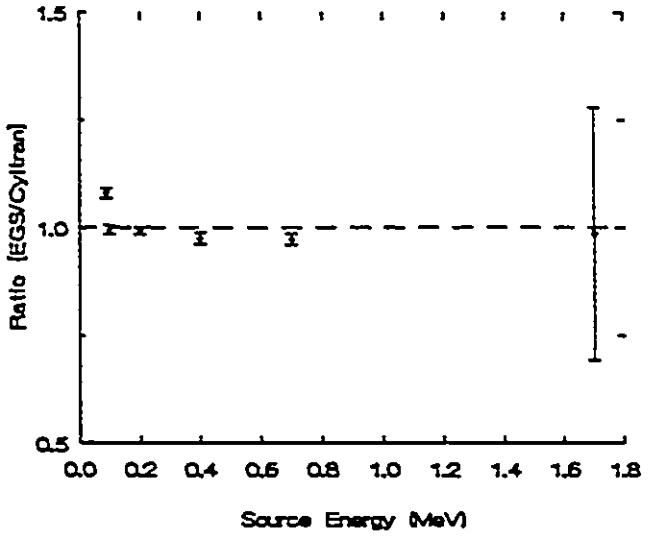

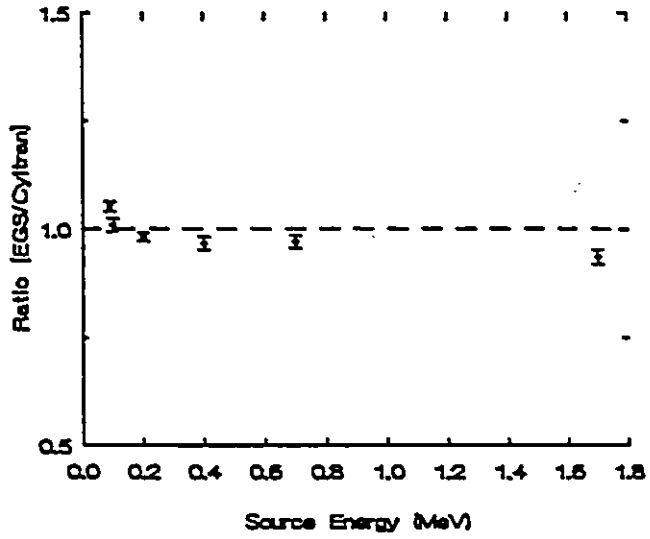

Fig 5.14 Ratio of fractional energy deposited, Thick detector window, point source Zeroeth simulations. Upper: aluminium scatterer; Lower: air scatterer.

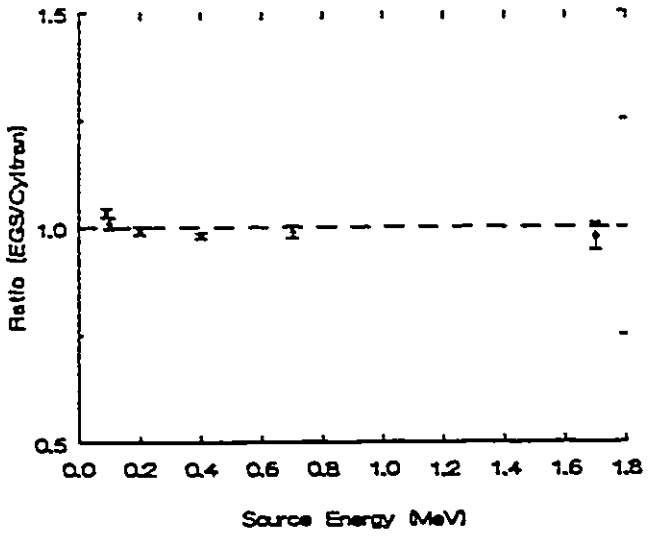

Fig 5.14(continued) Ratio of fractional energy deposited, Thick detector window, point source Zeroeth simulations. Mylar scatterer.

Monoenergetic dose backscatter factors predicted by the two codes for six material interfaces are compared in Figures 5.15 and 5.16. Ratios of EGS4/Dosrz B(E) values to Cyltran B(E) values are shown as functions of source energy E.

The bismuth/Mylar, aluminium/Mylar and air/Mylar interface data shown in Figure 5.15 exhibit agreement to within about 10% between the two codes, in the region 100keV $\leq$ E $\leq$ 1.7MeV. The bismuth/lucite interface in Figure 5.16 shows a 15% discrepancy at 100keV; otherwise, data from the codes agree to within 10%. Agreement between results from the codes is also within 10% for aluminium/lucite

and air/lucite interfaces, except at 100keV in the first and 1.7MeV in the second.

These findings are consistent with the agreement exhibited between the beta dose backscatter factors from the two codes (Table 5.1).

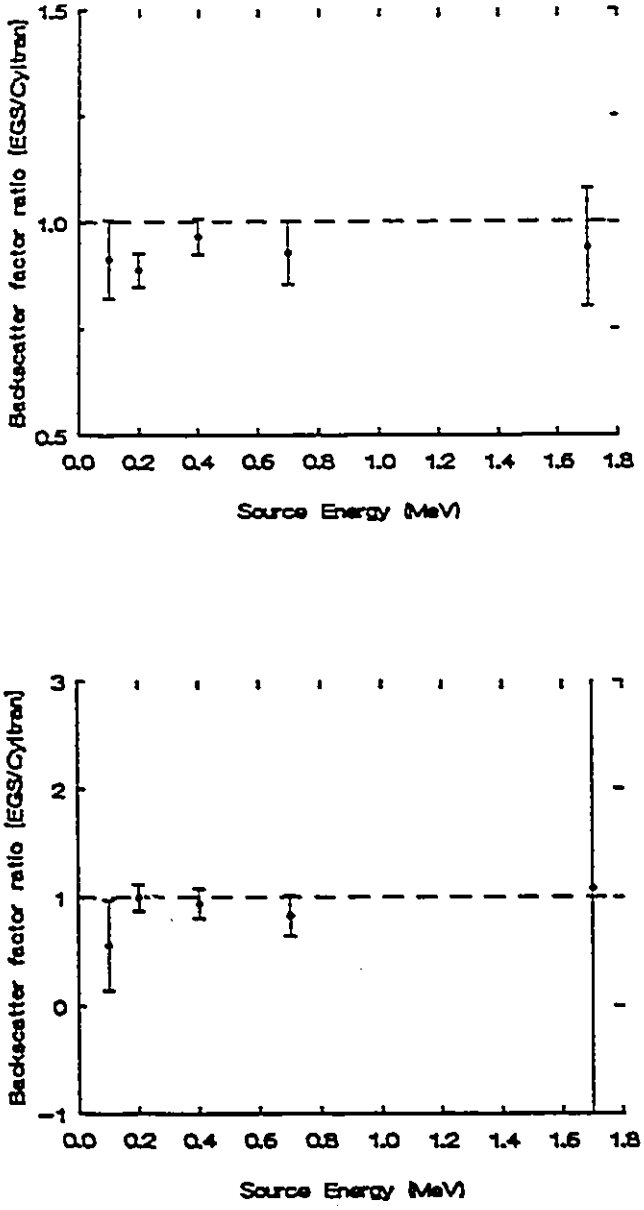

Fig 5.15 Ratio of monoenergetic dose backscatter factors, Thick detector window, point source Zeroeth simulations. Upper: bismuth/Mylar interface; Lower: aluminium/Mylar interface.

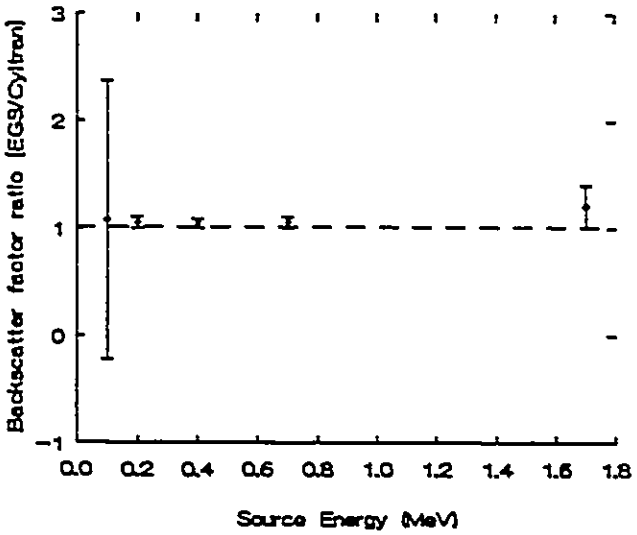

Fig 5.15(continued) Ratio of monoenergetic dose backscatter factors. Thick detector window, point source Zeroeth simulations. Air/Mylar interface.

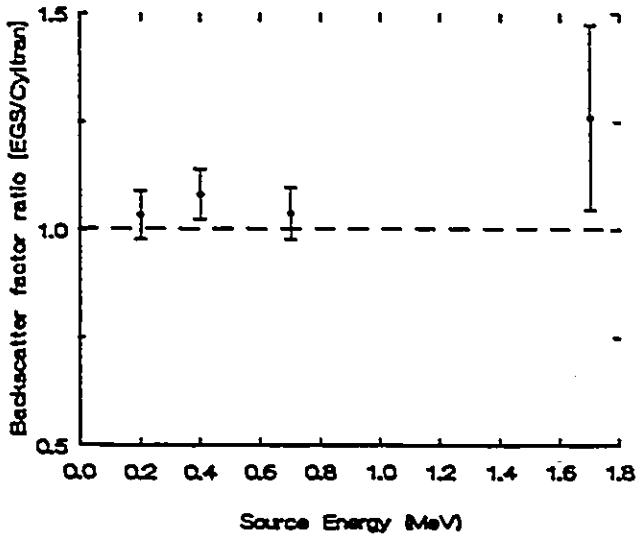

Fig 5.16 Ratio of monoenergetic dose backscatter factors. Thick detector window, point source Zeroeth simulations. Air/lucite interface.

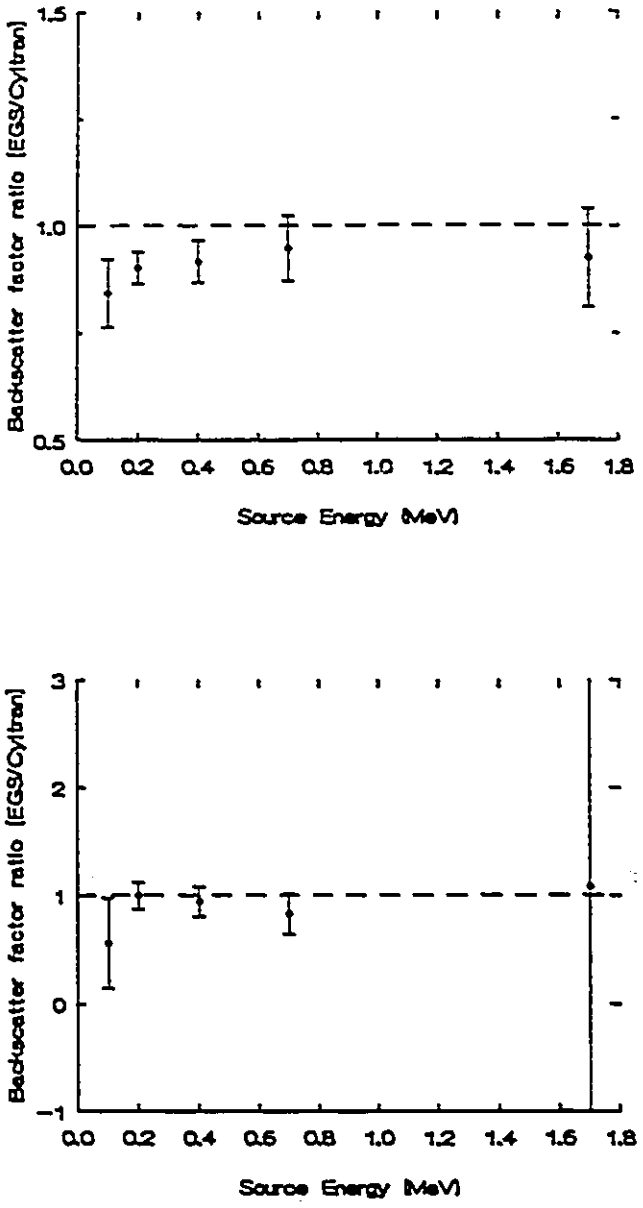

Fig 5.16(continued) Ratio of monoenergetic dose backscatter factors. Thick detector window, point source Zeroeth simulations. Upper: bismuth/lucite interface; Lower: aluminium/lucite interface.

(b) Thin Detector Window -

The same source geometry as above is used in Zeroeth simulations with the thin detector window. This window admits electrons below 70keV, the thick window cut-off, into the designated scoring region. The cut-off for the thin window is roughly 15keV.

The codes differ in similar ways at both cut-off energies. At 20keV source energy, with the thin window, the fractional energy deposited from EGS4/Dosrz is consistently lower, by about a factor of 10, than that from Cyltran. At other source energies, fractional energy deposited data from the two codes agree, within 7%, for the scatterers bismuth, aluminium, air and Mylar. The graphs in Figure 5.17 illustrate these observations.

Figure 5.18 shows ratios of monoenergetic backscatter factors, EGS4/Dosrz to Cyltran. The graphs for bismuth and aluminium are drawn so as to include the large differences between the codes at 20keV. Agreement between the codes for other source energies is about 20% to 30%. Additionally, the bismuth graph demonstrates that EGS4/Dosrz B(E) values are lower than those from Cyltran, for the most part. Therefore, for this interface, the Cyltran-calculated beta dose backscatter factor is larger than that determined using EGS4/Dosrz. For the aluminium/Mylar interface, at low energies, EGS4/Dosrz monoenergetic backscatter factors are larger than those from Cyltran but above 200keV this reverses. The beta dose backscatter factor from Cyltran also exceeds the value from EGS4/Dosrz at this interface (Table 5.3).

At the air interface in Figure 5.18, EGS4/Dosrz monoenergetic backscatter factors are larger than those from Cyltran for most source electrons, including ones which are heavily weighted in the ^{32}P beta spectrum (that is, 400keV to 700keV), and ones which deposit relatively large fractions of their energy in the detector (that is, 50keV to 100keV). EGS4/Dosrz consequently predicts a larger beta dose reduction factor than Cyltran in this case (Table 5.3).

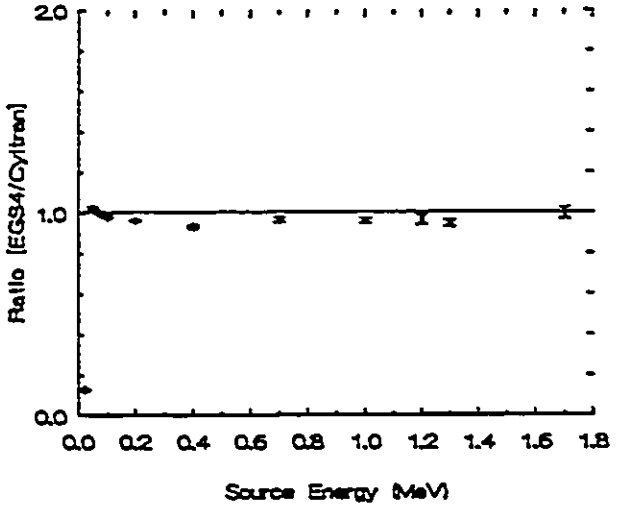

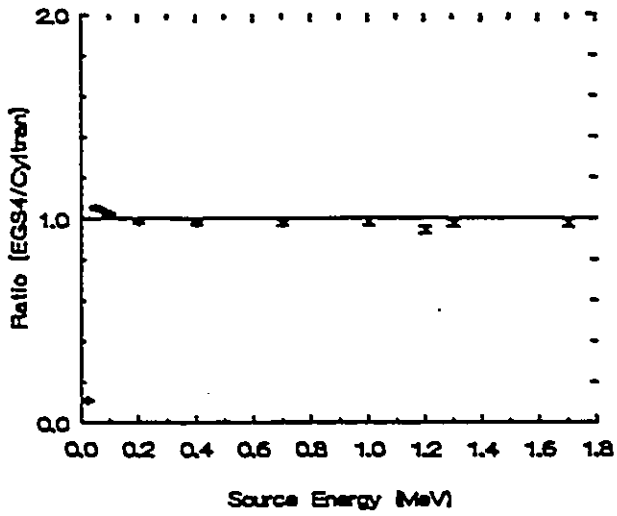

Fig 5.17 (a) Ratio of fractional energy deposited, Thin detector window, point source Zeroeth simulations. Upper: bismuth scatterer; Lower: aluminium scatterer.

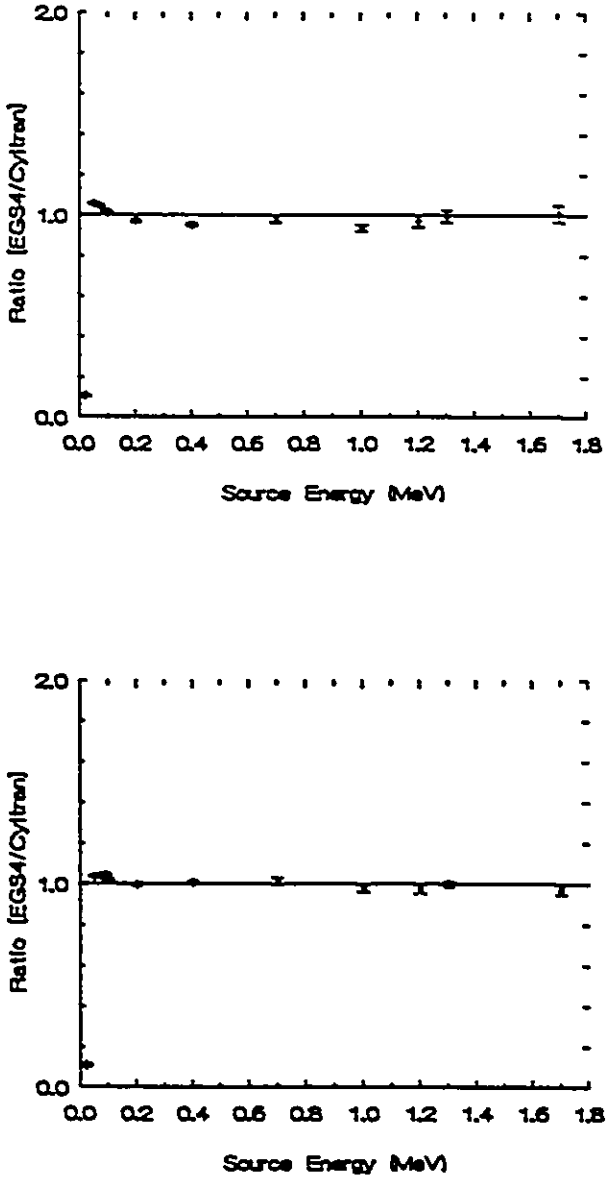

Fig 5.17 (b) Ratio of fractional energy deposited, Thin detector window, point source Zeroeth simulations. Upper: air scatterer; Lower: Mylar scatterer.

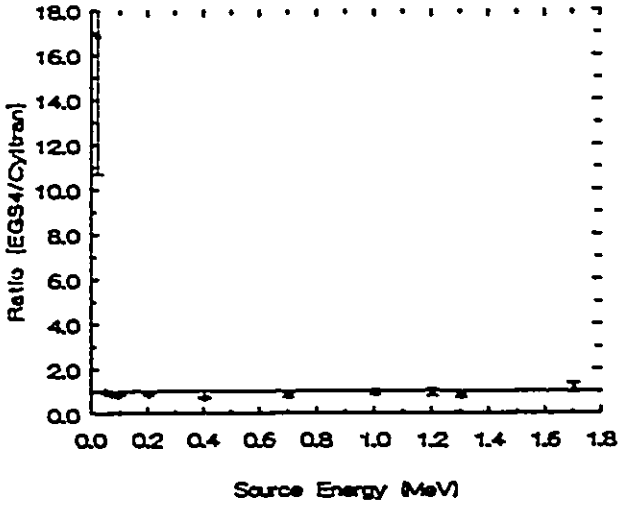

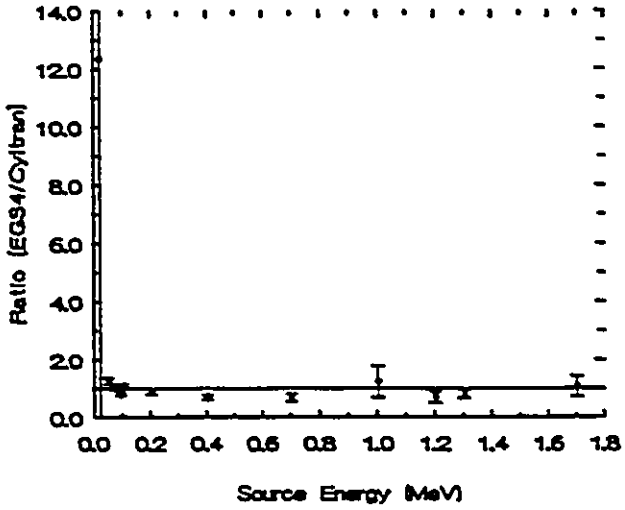

Fig 5.18 Ratio of monoenergetic backscatter factors, Thin detector window, point source Zeroeth simulations. Upper: bismuth/Mylar interface; Lower: aluminium/Mylar interface.

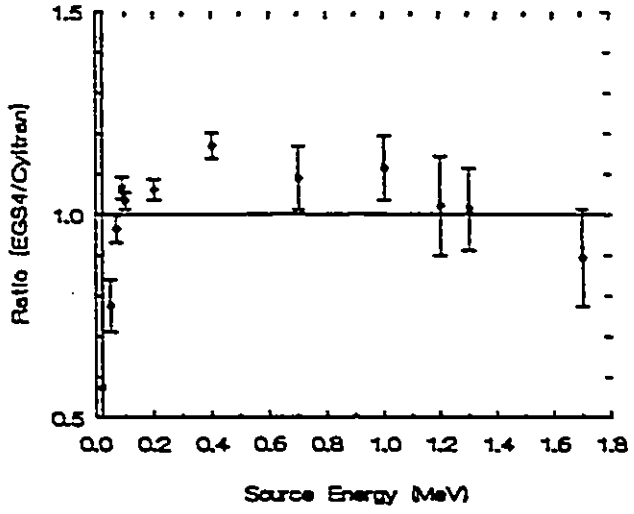

Fig 5.18(continued) Ratio of monoenergetic dose backscatter factors. Thin detector window, point source Zeroeth simulations. Air/Mylar interface.

Zeroeth Geometry, distributed source

Zeroeth geometry, thin detector window simulations with distributed sources for six scatterers, bismuth, copper, aluminium, Mylar, lucite and air, were done using both codes. Source diameters were 3.81cm and source energies ranged from 20keV to 1.7MeV, inclusive.

Except for 20keV source electrons, monoenergetic fractional energy deposited data, $\varepsilon(E)$, from both codes, and for the six scatterers, agree within about 10%. As observed for the point source, where the codes differ, for source energies greater than 200keV, values from Cyltran exceed those from EGS4/Dosrz, whereas for source energies between 50keV and 200keV, Cyltran values are lower than those from EGS4/Dosrz. At 20keV, EGS4/Dosrz fractional energy deposited data

are consistently a factor of about 10 lower than Cyltran fractional energy deposited data. These observations are demonstrated in Figure 5.19 which shows ratios of fractional energy deposited, EGS4/Dosrz to Cyltran, as a function of source energy.

Consistent with the energy deposited comparison, backscatter factors from the two codes for 20keV electrons differ by about 150% for the eight interfaces created with respect to Mylar and lucite using the scatterers listed above. Figures 5.20 through 5.23 compare EGS4/Dosrz and Cyltran monoenergetic dose backscatter factors, B(E), for these interfaces.

At bismuth interfaces, Figures 5.20 and 5.21, EGS4/Dosrz backscatter factors for 90keV to 400keV, 1.2MeV and 1.3MeV electrons are about 20% lower than those from Cyltran. Thus it follows that beta dose backscatter factors determined for bismuth interfaces are such that EGS4/Dosrz values are lower than those from Cyltran (Table 5.5).

At copper interfaces, Figures 5.20 and 5.21, although monoenergetic backscatter factors from the two codes agree within uncertainties for the most part, Cyltran values tend to be smaller than ones from EGS4/Dosrz. Not unexpectedly, whilst beta dose backscatter factors from the two codes agree within uncertainties , the EGS4/Dosrz beta dose backscatter factor is larger than that from Cyltran (Table 5.5).

At aluminium interfaces, Figures 5.22 and 5.23, clusters of disagreement between monoenergetic backscatter factors from the two codes are observed at source energies below 200keV and at 1.3MeV, where EGS4/Dosrz values are roughly half of Cyltran values. However, these discrepancies are nullified by the agreement at other source energies since beta dose backscatter factors from the two codes agree at these interfaces (Table 5.5).

Monoenergetic dose backscatter factors from the codes agree for most source energies at the air interfaces, (Figures 5.22 and 5.23), with the exception of a few discrepancies 20% or larger. It is not clear from these data that the EGS4/Dosrz beta dose reduction factor would be slightly less than that from Cyltran, as shown in Table 5.5.

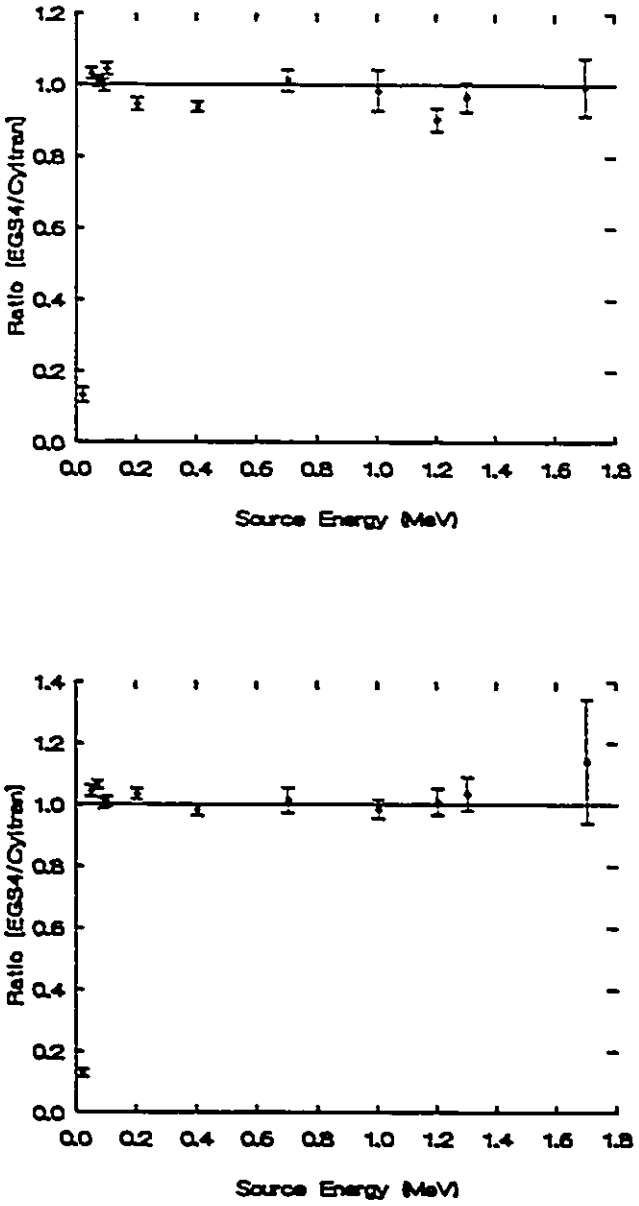

Fig 5.19 . Ratio of fractional energy deposited, Thin detector window, distributed source Zeroeth simulations. Upper: bismuth scatterer; Lower: copper scatterer.

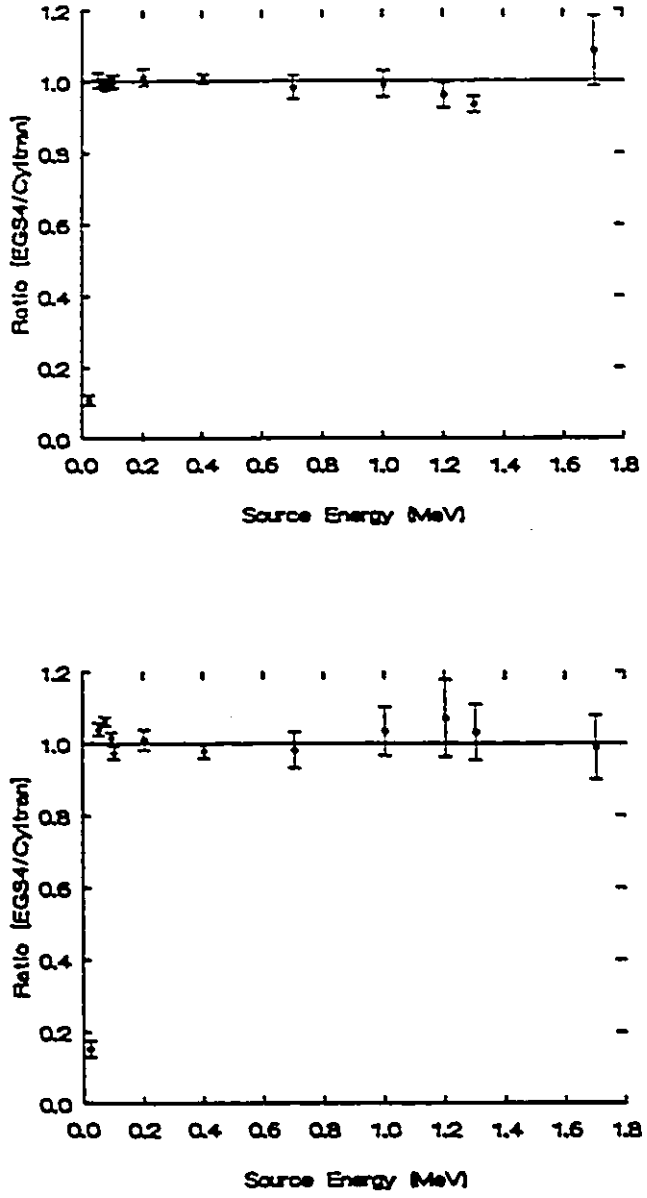

Fig 5.19(continued) Ratio of fractional energy deposited, Thin detector window, distributed source Zeroeth simulations. Upper: aluminium scatterer; Lower: air scatterer.

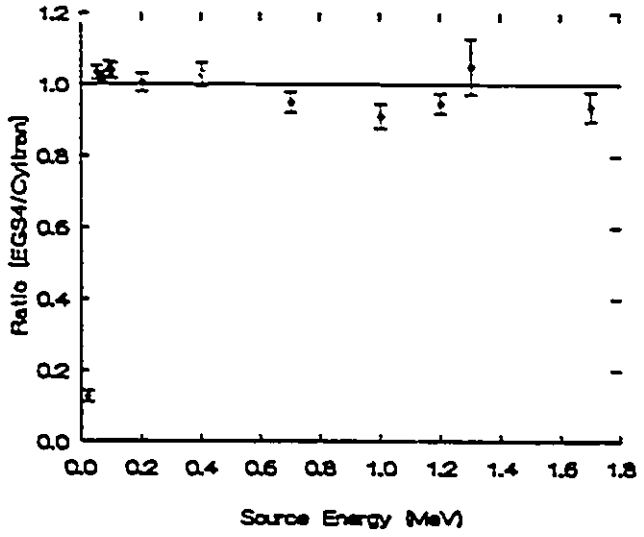

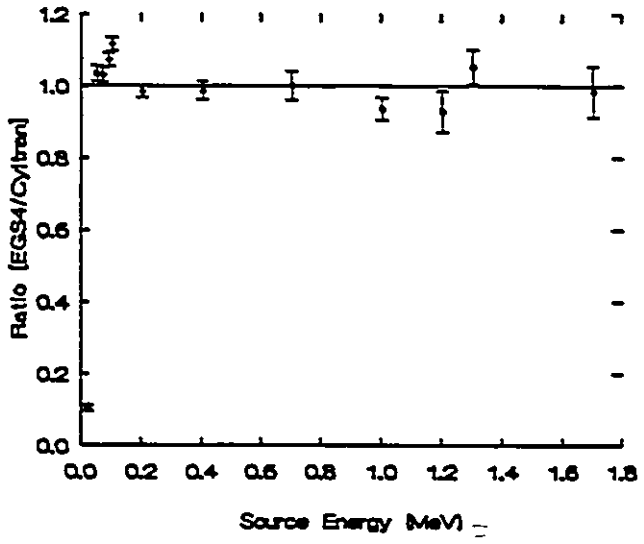

Fig 5.19(continued) Ratio of fractional energy deposited, Thin detector window, distributed source Zeroeth simulations. Upper: Mylar scatterer; Lower: lucite scatterer.

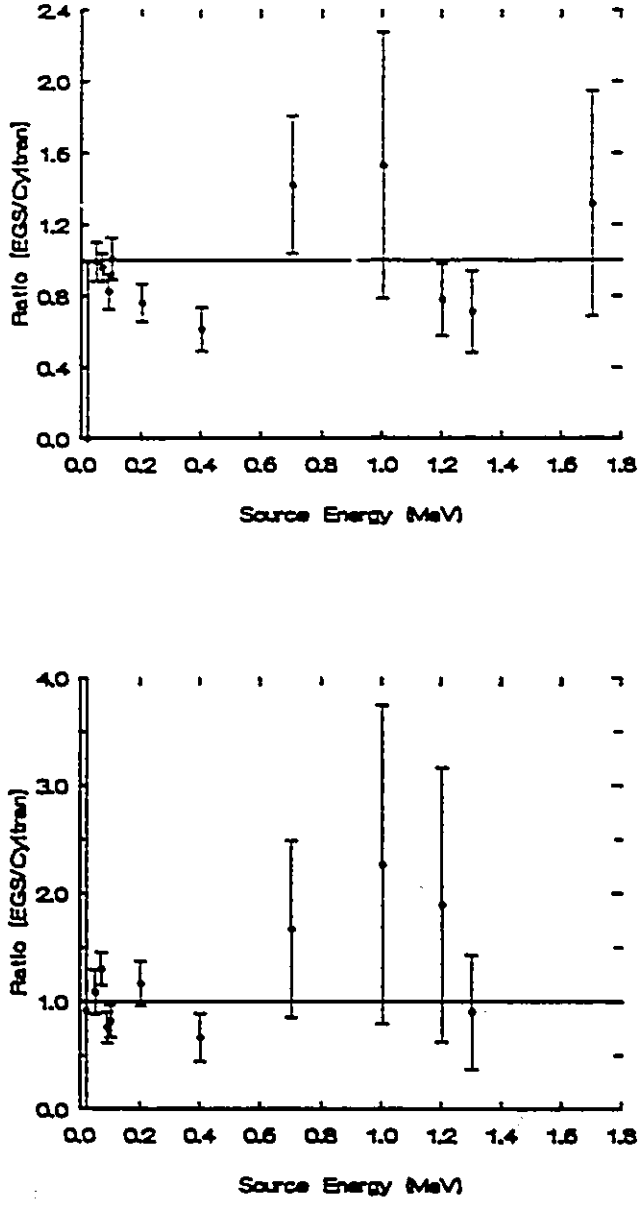

Fig 5.20 . Ratio of monoenergetic backscatter factors, Thin detector window, distributed source Zeroeth simulations. Upper: bismuth/Mylar interface; Lower: copper/Mylar interface.

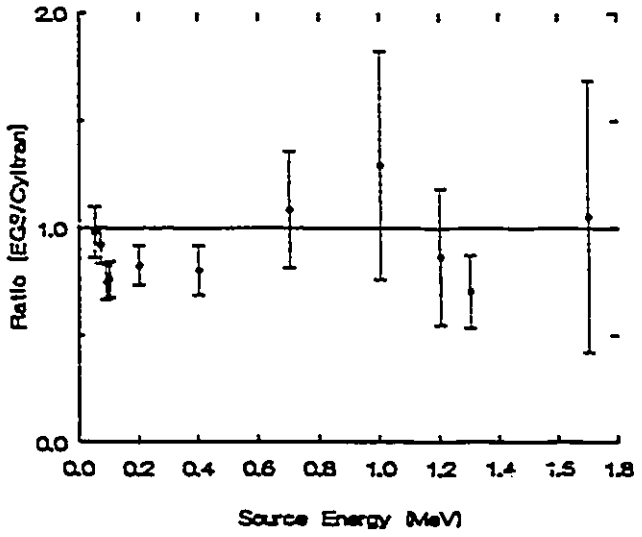

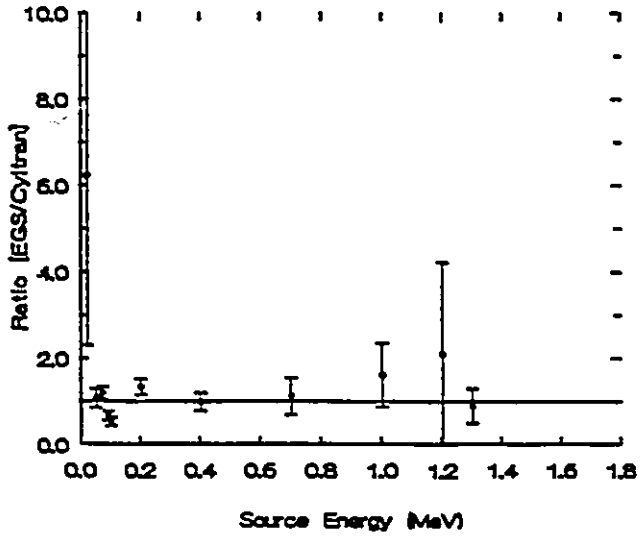

Fig 5.21 . Ratio of monoenergetic backscatter factors, Thin detector window, distributed source Zeroeth simulations. Upper: bismuth/lucite interface; Lower: copper/lucite interface.

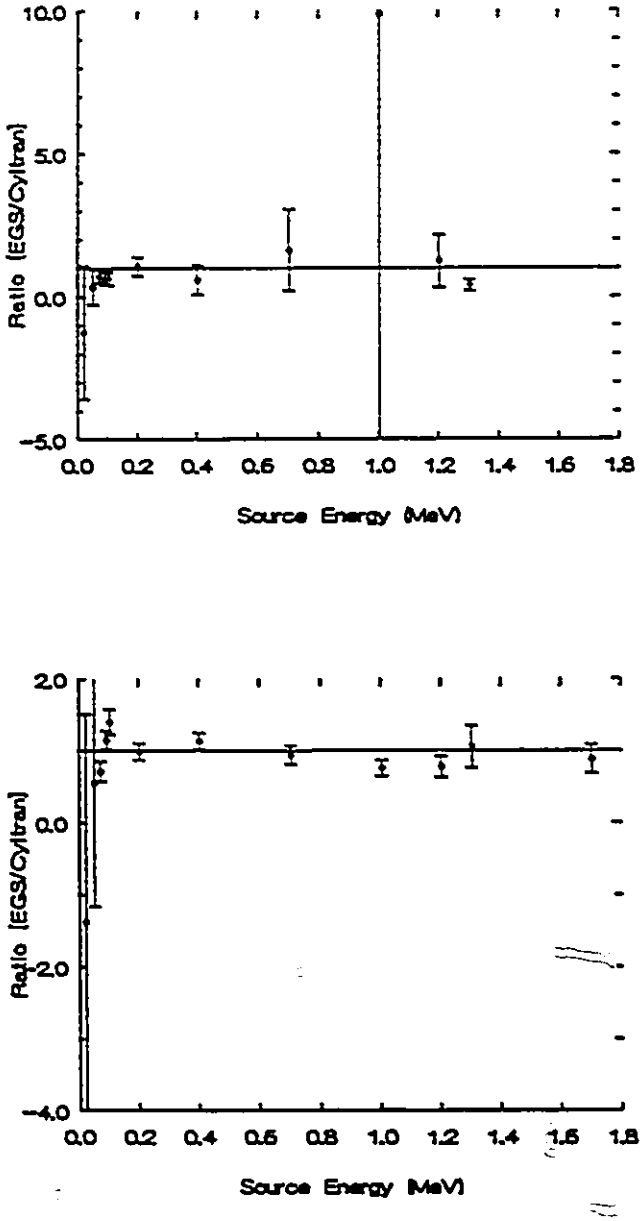

Fig 5.22 . Ratio of monoenergetic backscatter factors, Thin detector window, distributed source Zeroeth simulations. Upper: aluminium/Mylar interface; Lower: air/Mylar interface.

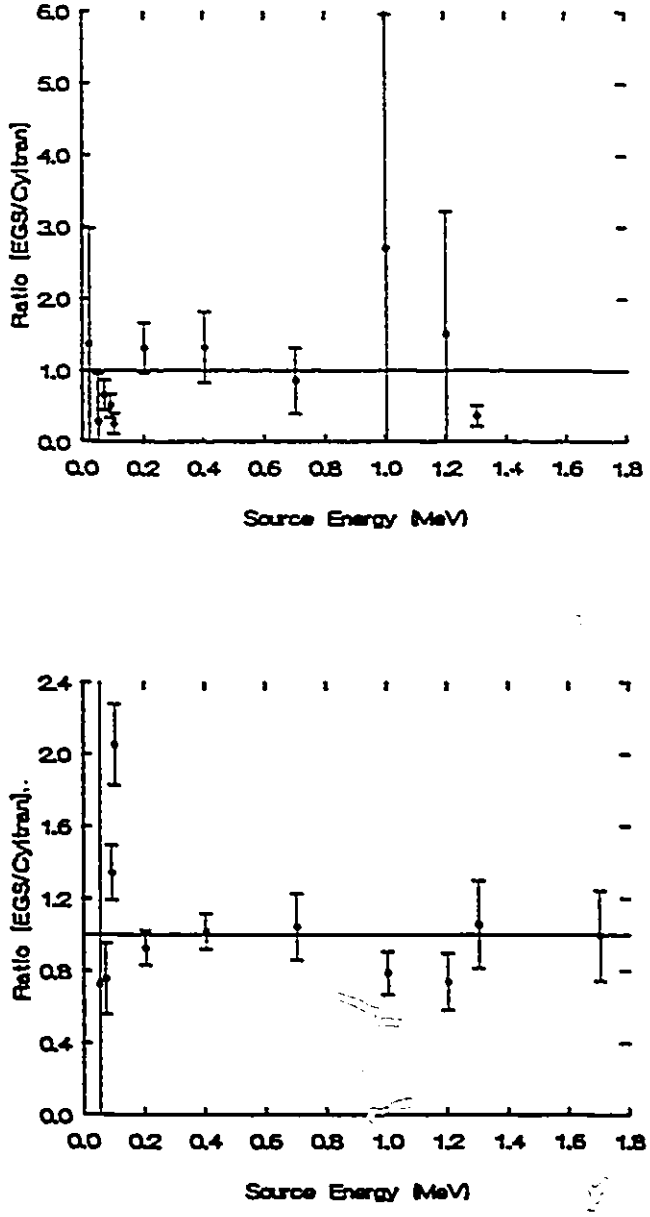

Fig 5.23 . Ratio of monoenergetic backscatter factors, Thin detector window, distributed source Zeroeth simulations. Upper: aluminium/lucite interface; Lower: air/lucite interface.

EGS4/Dosrz and Cyltran monoenergetic data are disturbingly and consistently different at 20keV. This discrepancy is similar to that in the thick window 70keV simulations, and may be due to differences in handling either energy-loss straggling or the termination of electron histories, or both, since these energies correspond to CSDA ranges that are roughly the window plus source substrate thicknesses.

ASD Geometry, point source

A 700keV point source was used in both codes for an ASD type simulation which scores the fractional energy deposited as a function of distance from the interface where the source is fixed. This source energy is approximately the average energy of the ^{32}P beta spectrum. Mylar, bismuth and air scatterers were used. In this simulation, when Mylar is the scatterer, there is, in effect, a homogeneous medium. When bismuth or air are the scatterers, bismuth/Mylar or air/Mylar heterogeneous media are created.

The homogeneous case is an example of good agreement between the energy deposited data from the two codes. The air interface exhibits agreement to within 3% between 5mg/cm^2 and 200mg/cm^2, and at the interface, there is an 8% discrepancy. The bismuth case shows 3% agreement between 5mg/cm^2 and 100mg/cm^2. There is a 12% discrepancy at the interface and about 10% differences between 100mg/cm^2 and 200mg/cm^2.

As for the Zeroeth simulations, discrepancies between the codes are such that Cyltran values exceed those from EGS4/Dosrz. Figure 5.24 illustrates ratios of Cyltran energy deposited data to EGS4/Dosrz energy deposited data, as a function of distance from the interface, for these three scatterers. The CSDA range of a 700keV electron in Mylar is about 270mg/cm^2; energy depositions beyond this depth are small and have large uncertainties, as seen in Figure 5.24.

Figure 5.25 illustrates ratios of backscatter factors as a function of distance from the interface for bismuth/Mylar and air/Mylar cases. The latter shows a 10% discrepancy between results from the two codes at the interface, followed by an improvement to about 6% from 5mg/cm^2 to 100mg/cm^2. Beyond this depth, uncertainties in the data from both codes become too large for definitive comparison. The bismuth/Mylar case shows 10% discrepancies between 5mg/cm^2 and 100mg/cm^2, and 30% between 100mg/cm^2 and 200mg/cm^2. At the interface, there is a considerable discrepancy between the backscatter factors from the two codes; the backscatter factor at 700keV is 5.8[1.1]% from EGS4/Dosrz and 19.8[1.9]% according to Cyltran. This resembles the differences in beta dose backscatter factors from the two codes for bismuth interfaces, noted in Section 5.3.1.

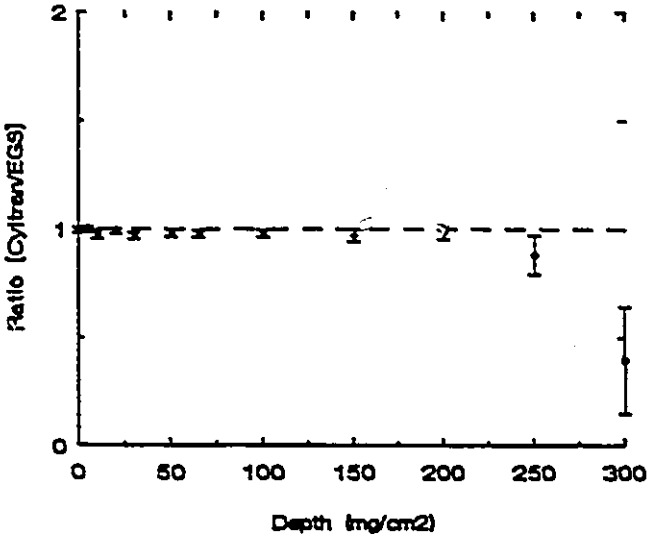

Fig 5.24 Ratio of fractional energy deposited for a 700keV point source ASD simulation. Mylar scatterer (that is, a homogeneous medium).

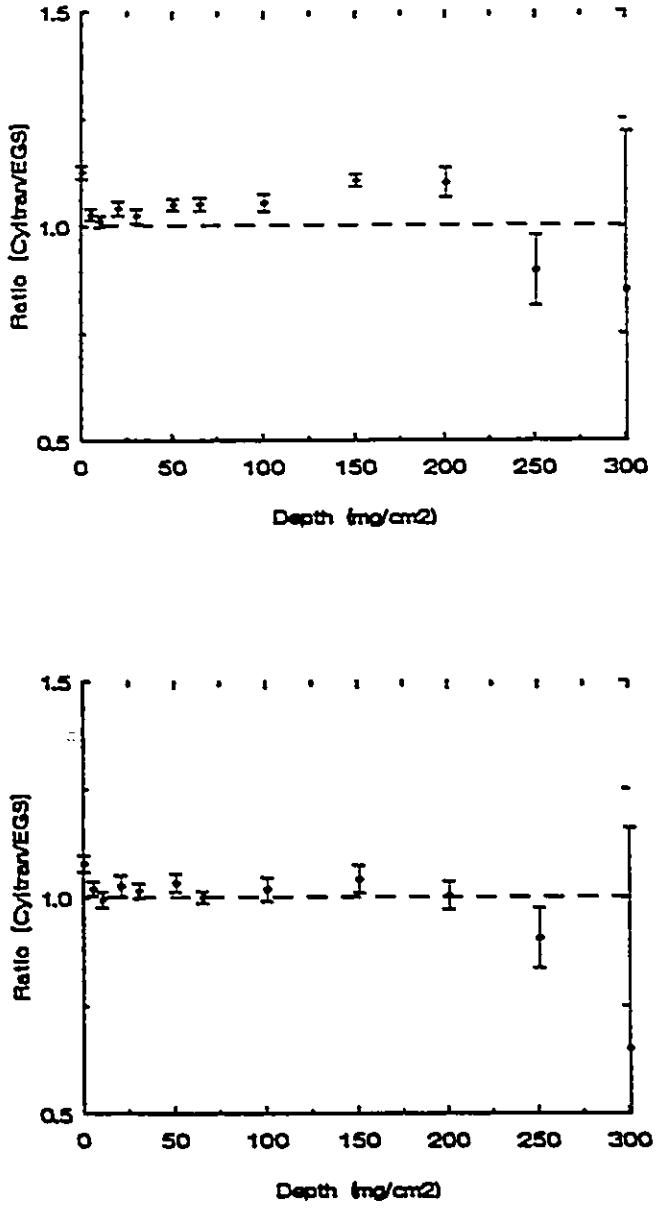

Fig 5.24(continued) Ratio of fractional energy deposited for a 700keV point source ASD simulation. Upper: bismuth scatterer; Lower: air scatterer.

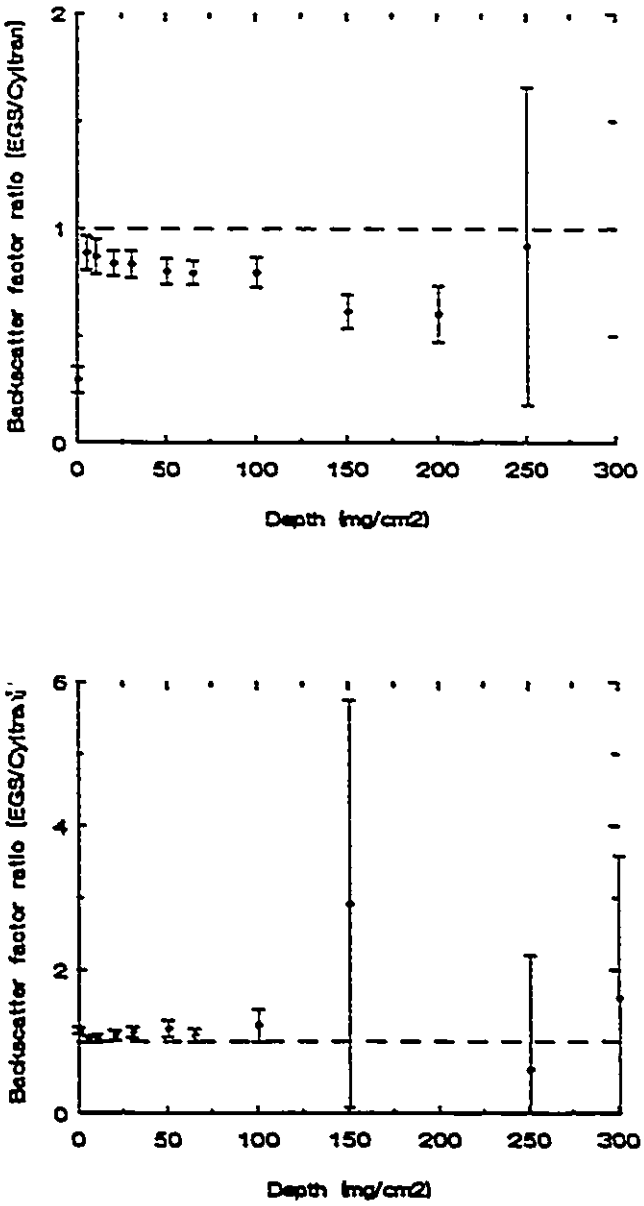

Fig 5.25 . Ratio of monoenergetic dose backscatter factors, 700keV point source ASD simulation. Upper: bismuth/Mylar interface; Lower: air/Mylar interface.

Comparisons of monoenergetic data from the two codes are not unfavourable. With regard to fractional energy deposition, there is agreement within about 10% for all cases considered, except for 20keV and 70keV source electrons in thin and thick window Zeroeth simulations. It is also noted that when data from the two codes differ, Cyltran predicts greater energy deposition than does EGS4/Dosrz for source electrons greater than 200keV and for source electrons between 50keV and 200keV, the reverse is observed.

Because it falls under the theme of this section, mention is made of the Eisen experiment simulation discussed in Chapter 8. The experiment also deals with electron backscattering; EGS4/Dosrz and Cyltran are used to simulate the transport of 2MeV electrons through a section of polystyrene and their subsequent backscatter from various materials.

Reasonable agreement between results from the codes is obtained, with a slight but systematic discrepancy observed in the depth-dose profiles (Figure 8.5). Interestingly, EGS4/Dosrz values are larger than Cyltran values in these cases but the data cannot be directly compared with observations made here because source geometry and location with respect to the interface are different.

CHAPTER 6

ANALYTICAL DOSIMETRIC CALCULATIONS OF BETA DOSE BACKSCATTER FACTORS

Two analytical methods, due to O'Brien et al and Radzievsky et al, which deal with beta dosimetry in heterogeneous media, are used here to calculate beta dose backscatter factors. Specifically, the first method, called the "One-Group" theory, is used to calculate dose enhancement or reduction at planar interfaces. The second method, the "Two-Group" theory, is used to calculate dose backscatter factors as a function of distance from a planar interface. In both cases, a beta source, ^{32}P, is located at the interface.

The "One-Group" method predicts a variation of backscatter factor with scatterer atomic number which is similar to that observed experimentally. In addition, calculated values agree with experimental backscatter factors to within 30%.

Results from the "Two-Group" theory are not in accordance with experimental results, however. Calculated and experimental backscatter factors do vary similarly near the interface, but at further distances, experimental and "Two-Group" values diverge.

6.1 The "One-Group" Method

The name derives from the assumption that the energy of a beta source can be represented by one value, its average energy. Consequently, the starting point of the method is the constant cross-section transport equation (O'Brien et al 1964). One dimension, perpendicular to the planar interface, is dealt with.

From Section 2.2, it follows that the electron flux in a medium is proportional to the dose rate due to these electrons in the medium. Therefore, dose ratios, from which dose backscatter factors are determined, are flux ratios. Using the notation introduced in Chapter 4,

$$R_{SL} = \frac{\text{flux in medium1, when material S is medium2}}{\text{flux in medium1, when lucite L is medium2}}$$

$$= \frac{\phi_{0_{1,S}}}{\phi_{0_{1,L}}} \quad . \tag{6.1}$$

Correspondingly, the dose ratio for a scatterer (S)/Mylar(M) interface is given by

$$R_{SM} = \frac{\phi_{0_{1,S}}}{\phi_{0_{1,M}}} \quad . \tag{6.2}$$

Medium 1 is analogous to the "base" of Section 4.1. For the present purpose, which is to compare dose backscatter factors calculated using this theory with experimental values, medium 1 is taken to be the soft-tissue equivalent lower electrode of the extrapolation chamber described in Chapter 4.

The geometry used in the calculations consists of a plane, infinite ^{32}P beta source sandwiched between two half-spaces. As stated above, one half-space, medium 1, is A-150 plastic. The other, medium 2, is varied by using each of the

following: air, carbon, aluminium, copper, cadmium, tungsten, bismuth, Mylar, lucite. The source is located at the interface, where the dose ratio is to be calculated.

The transport equation from which the electron fluxes are determined is given by the following.

$$\omega\frac{d\phi(\omega,x)}{dx} + \Sigma\phi(\omega,x) = Y(\omega,x) + \int_{-1}^{1} d\omega' \mu(\omega' \rightarrow \omega)\phi(\omega',x) \qquad (6.3),$$

where ω is the direction cosine of an electron at depth x, measured perpendicularly from the source; x is in g/cm^2,

$\phi(\omega,x)$ is the electron flux density ($\#e^- cm^{-2} s^{-1}$) in direction ω, at depth x;

Σ is the total interaction cross-section ($cm^2 g^{-1}$);

$Y(\omega,x)$ is the source strength ($\#e^- g^{-1} s^{-1}$) in direction ω; here, the source is defined to be at x=0, and for an isotropic source, total source strength Y_o, $Y(\omega) = Y_o/2$;

$\mu(\omega' \rightarrow \omega)$ is the differential mass scattering cross-section, $\frac{1}{\rho}\frac{d\mu_s}{d\omega}$; for isotropic scattering, $\mu(\omega' \rightarrow \omega) = \frac{1}{\rho}\frac{\mu_s}{2} = \frac{c}{2}\Sigma$, where c is the ratio of the scattering cross-section to the total cross-section.

Equation 6.3 becomes

$$\omega\frac{d\phi(\omega,x)}{dx} + \Sigma\phi(\omega,x) = \frac{Y_o}{2} + \frac{c\Sigma}{2}\int_{-1}^{1} d\omega' \phi(\omega',x) \qquad (6.4)$$

As mentioned in Chapter 2, the transport equation is not soluble analytically without invoking approximations. One approximation made here is to represent the directional electron flux density, $\phi(\omega,x)$, by a polynomial series -

$$\phi^{\pm}(\omega,x) = \sum_{i=1}^{L}(2i + 1)B_i^{\pm}(x)P_i^{\pm}(\omega) \quad , \tag{6.5}$$

where + denotes the forward direction, $0 \leq \omega \leq 1$ and - denotes the backward direction, $-1 \leq \omega \leq 0$,

$B_i(x)$ represents the spatial component of the series

and the angular part is given by $P_i^{+}(\omega) = P_i(2\omega - 1)$,

$P_i^{-}(\omega) = P_i(2\omega + 1)$, where P_i is the Legendre polynomial of degree i. (O'Brien et al 1964).

For L=0, the zeroeth order approximation for the directional flux density is obtained. This is the approach used by O'Brien et al (O'Brien et al 1964). For higher order approximations, the method of discrete ordinates is used to solve for $\phi(\omega,x)$ numerically (O'Brien et al 1974). In the L=0 approximation, Equation 6.5 becomes

$$\begin{aligned} \phi^{\pm}(\omega,x) &= \phi^{+}(x) \qquad \text{for } 0 \leq \omega \leq 1 \\ &= \phi^{-}(x) \qquad \text{for } -1 \leq \omega \leq 0. \end{aligned} \tag{6.6}$$

where $B_o^{\pm}(x)$ have been renamed $\phi^{\pm}(x)$.

Therefore, Equation 6.4 may be rewritten as follows,where it is understood that the directional flux densities are functions of x.

$$\omega\frac{d\phi}{dx} + \Sigma\phi = \frac{Y_o}{2} + \frac{c\Sigma}{2}\phi_o \quad . \tag{6.7}$$

Integration of the preceding equation over forward, +, ($0 \leq \omega \leq 1$) and backward, -, ($-1 \leq \omega \leq 0$) regions gives

$$\frac{d\phi_o^+}{dx} + \Sigma(2 - c)\phi_o^+ = Y_o + c\Sigma\phi_o^-$$

$$-\frac{d\phi_o^-}{dx} + \Sigma(2 - c)\phi_o^- = Y_o + c\Sigma\phi_o^+ \quad . \tag{6.8}$$

In the half-spaces, there is no source, so Equation 6.8 becomes

$$\frac{d\phi_o^+}{dx} + \Sigma(2 - c)\phi_o^+ = c\Sigma\phi_o^-$$

$$-\frac{d\phi_o^-}{dx} + \Sigma(2 - c)\phi_o^- = c\Sigma\phi_o^+ \quad . \tag{6.9}$$

These equations can be decoupled to give the following expressions for the flux densities in the forward (+) and backward (-) directions defined earlier.

$$\phi_o^+ = Ae^{\nu x} + Be^{-\nu x}$$

$$\phi_o^- = \frac{1}{\gamma}Ae^{\nu x} + \gamma Be^{-\nu x} \tag{6.10}$$

where A and B are undefined constants,

$$\gamma = \frac{2 - \alpha}{c} - 1, \quad \text{with} \quad \alpha = 2\sqrt{1 - c} \quad \text{and} \quad \frac{1}{\gamma} = \frac{2 + \alpha}{c} - 1;$$

and $\nu = \alpha\Sigma$.

Note that $\nu^2 = \Sigma[\Sigma - c\Sigma]$, is the product of the total interaction cross-section Σ and the mass absorption cross-section σ_a/ρ, where

$$\frac{\sigma_a}{\rho} = -\left(\frac{1}{\bar{E}}\right)\frac{1}{\rho}S(\bar{E}) \tag{6.11}$$

$\bar{E}$ is the average energy of the beta spectrum, and $\frac{1}{\rho}S(\bar{E})$ is the value of the mass stopping power at $\bar{E}$.

The scattering cross-section, $c\Sigma = \sigma_s/\rho$, is taken to be the transport cross-section, σ_t/ρ, evaluated at $\bar{E}$. (O'Brien et al 1964) The transport cross-section is that of Lewis (Lewis 1950).

The total flux density ϕ_o is given by

$$\phi_o = \phi_o^+ + \phi_o^- \quad . \tag{6.12}$$

When the two half-spaces are different media, there is a boundary where the source is located, as shown in the diagram below. The boundary is at x=0; the left half-space contains medium 1 and the right half-space, medium 2.

Using the general solution, Equation 6.10, the flux densities in the forward and backward directions in the two media are represented by the following.

$$\phi_{o,1}^+(x) = Ae^{\nu_1 x} \qquad \phi_{o,1}^-(x) = \frac{1}{\gamma_1}Ae^{\nu_1 x}$$

and $$\phi_{o,2}^+(x) = Be^{-\nu_2 x} \qquad \phi_{o,2}^-(x) = \gamma_2 Be^{-\nu_2 x} \tag{6.13}$$

Also, the total flux densities in media 1 and 2 are given by

$$\phi_{o,1}(x) = \phi_{o,1}^+(x) + \phi_{o,1}^-(x)$$

and $$\phi_{o,2}(x) = \phi_{o,2}^+(x) + \phi_{o,2}^-(x) \quad . \tag{6.14}$$

Consider electrons travelling in the direction shown in the following diagram. The cross-sectional area of this stream of electrons is $dA_\perp$, and the direction cosine is ω with respect to the normal to the interface.

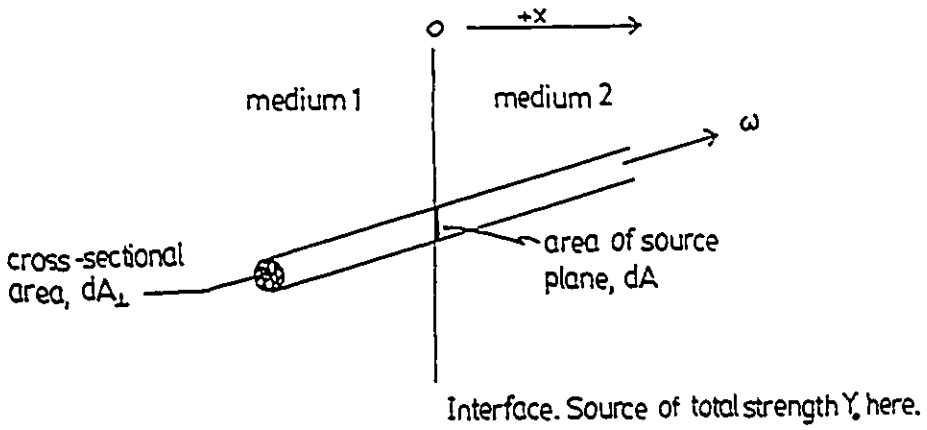

As noted earlier, the directional source strength, $Y(\omega)$, is $Y_o/2$ for an isotropic source. At the boundary, x=0, the following conditions apply from conservation of particles.

$$dA_\perp \phi_1(0) + \frac{Y_o}{2} dA = \phi_2(0) dA_\perp \qquad (6.15)$$

where $\phi_1(0)$ and $\phi_2(0)$ are the directional flux densities at the boundary.

Since $dA_\perp = dA\ \omega$, Equation 6.15 becomes

$$\omega\phi_2(0) - \omega\phi_1(0) = \frac{Y_o}{2} \ . \qquad (6.16)$$

After integration over angles in the forward and backward directions in each half-space, the following boundary conditions are obtained.

$$\phi^{+}_{o,2}(0) - \phi^{-}_{o,1}(0) = Y_o$$

$$-\phi^{-}_{o,2}(0) + \phi^{-}_{o,1}(0) = Y_o \quad . \tag{6.17}$$

Evaluating Equation 6.13 for x=0 and substituting in Equation 6.17 gives

$$B - A = Y_o \quad ,$$

and

$$\frac{1}{\gamma_1}A - \gamma_2 B = Y_o \tag{6.18}$$

from which the following expressions are derived.

$$A = Y_o \frac{\gamma_1(1+\gamma_2)}{(1-\gamma_1\gamma_2)}$$

and

$$B = Y_o \frac{(1+\gamma_1)}{(1-\gamma_1\gamma_2)} \tag{6.19}$$

From Equations 6.1, 6.2 and using Equations 6.13, 6.14 and 6.19, the dose ratios are given by

$$R_{SL} = \left[\frac{1-\gamma_L\gamma_{A-150}}{1-\gamma_S\gamma_{A-150}}\right] \cdot \left(\frac{1+\gamma_S}{1+\gamma_L}\right) \tag{6.20}$$

and

$$R_{SM} = \left[\frac{1-\gamma_M\gamma_{A-150}}{1-\gamma_S\gamma_{A-150}}\right] \cdot \left(\frac{1+\gamma_S}{1+\gamma_M}\right) \tag{6.21}$$

where A-150 denotes the Shonka plastic for medium 1 and the remaining notations are consistent with ones previously defined.
(Prestwich 1991)

Determination of the Parameters for the "One-Group" Dose Ratio Calculations -

The parameter γ in Equations 6.20 and 6.21 above requires knowledge of the scattering and absorption cross-sections, σ_s/ρ and σ_a/ρ. The latter cross-section is determined from the mass stopping power, S/ρ, which was defined in Section 2.1. The scattering or transport cross-section is taken from Lewis 1950 (O'Brien et al 1964) where, for multiply scattered electrons, it is given by

$$\sigma_{t,1} = n\int_{4\pi} \frac{d\sigma(\theta)}{d\Omega}[1 - P_1(\cos\theta)]\, d\Omega$$

where $\frac{d\sigma}{d\Omega}$ is the differential cross-section for single electron elastic scattering, as discussed in Section 2.1; a screened nuclear potential of the form $V(r) = \frac{Ze^2}{r}e^{-\frac{r}{a}}$, where a is the Thomas-Fermi atomic radius, is used. n is the number of scatterers per unit volume. To first order, the above becomes

$$\frac{\sigma_t}{\rho} = \frac{N_a}{A}\int_{4\pi} \frac{d\sigma(\theta)}{d\Omega}(1 - \cos\theta)\, d\Omega$$

where N_a is Avogadro's Number and A is the atomic weight of the medium. Evaluation, using V(r) above and in the Born approximation, gives, in units of $2\pi N_a r_o^2$,

$$\frac{\sigma_t}{\rho} = \frac{Z^2}{A}\frac{1}{\beta^2\varepsilon(\varepsilon+2)}\left[\ln\left(\frac{1}{\psi}\right) - 1\right] \qquad (6.22)$$

where ε is the kinetic energy of the electron in rest mass units,

r_o is the classical electron radius, $e^2/m_e c^2$,

β is the ratio of the electron speed to that of light,

Z is the atomic number of the medium, and

$\psi = (\theta_{min}/2)^2$, where θ_{min} is the minimum scattering angle or screening

angle. It is representative of the fact that scattering off a bare nucleus, given by the Rutherford cross-section of Equation 2.5, does not occur in reality since atomic electrons screen the nucleus from incident particles.

$\theta_{min} = \frac{\lambda\!\!\!^{-}}{a}$ where $\lambda\!\!\!^{-}$ is the electron's deBroglie wavelength.

Following O'Brien (O'Brien 1974), Equation 6.22 is modified to take account of electron-electron scattering by replacing Z^2 with $Z(Z+1)$, and to be applicable for energies outside the realm of the Born approximation. Also, the Thomas-Fermi radius is scaled. These alterations follow from Molière's treatment of multiple scattering (Birkhoff 1958; Scott 1963; O'Brien 1974). Equation 6.22 becomes, in the units of $2\pi N_a r_o^2$,

$$\frac{\sigma_t}{\rho} = \frac{Z(Z+1)}{A} \frac{1}{\beta^2 \varepsilon(\varepsilon+2)} \left[\ln\left(\frac{1}{\psi}\right) - 1 \right] \qquad (6.23)$$

where $\psi = (\theta_{min}/2)^2$, as before, but

$$\theta_{min} = \left(\frac{\lambda\!\!\!^{-}}{0.885a}\right)^2 \left(1.13 + 3.76\left[\frac{Z\alpha}{\beta}\right]^2\right) \quad \text{, with } \alpha = 1/137.$$

Mass absorption and scattering cross-sections were evaluated using $\bar{E}$= 694keV. Additional pieces of input information for the former, such as mean excitation energies and density effect parameters, (Equation 2.9), were taken from Berger and Seltzer 1983 and were defined in Section 2.1.

The cross-sections, in units of $2\pi N_a r_o^2$, are

$$\frac{\sigma_t}{\rho} = 0.267\frac{Z(Z+1)}{A}\left[\ln\left\{\frac{2.68134\times 10^5}{1.13Z^{\frac{1}{3}} + 2.44262\times 10^{-4}Z^{\frac{2}{3}}}\right\} - 1\right]$$

and

$$\frac{\sigma_a}{\rho} = 0.898\frac{Z}{A}\left\{2\ln\left(\frac{T}{I}\right) + 0.2762 - \delta(\bar{E})\right\}\left[1 + \frac{S_{rad}(\bar{E})/\rho}{S_{coll}(\bar{E})/\rho}\right] \quad (6.24)$$

where T is the kinetic energy of the electron in the same units of energy as I.

6.1.1 Results of the "One-Group" method

Table 6.1 contains dose backscatter factors for ^{32}P determined by the "One-Group" method. Experimental values measured for a distributed or planar ^{32}P source described in Chapter 4 are also included.

The "One-Group" method predicts that dose enhancement at material interfaces increases with atomic number of the scatterer. It shows that the dose enhancements with respect to lucite are greater than ones with respect to Mylar and that the magnitude of this effect decreases with increasing scatterer atomic number. The theory also predicts dose decrements at air/Mylar and air/lucite interfaces. Observation of these trends in experimental data lends support to the theory.

Quantitative comparison of experimental and calculated beta dose backscatter factors further substantiates the "One-Group" method. At most of the solid material interfaces, experimental and calculated backscatter factors agree to within 20% to 30%; experimental values are lower than calculated ones. There is excellent agreement between calculated and experimental beta dose backscatter factors at the aluminium interfaces.

At air interfaces, experimental and calculated values differ by 24%; experimental dose reductions are larger than calculated ones here. Air was treated as a purely absorbing medium for these calculations; that is, the scattering cross-section was made zero. This was done because in the experimental geometry, it is unlikely that electrons which are emitted from the finite source into the air are backscattered into the small detection volume.

Thirty percent discrepancies between "One-Group" and experimental backscatter factors are not unreasonable given the simplifying approximations used in the theory. All source electrons are assumed to have energies equal to the average energy of the beta spectrum; and zeroeth order approximations are used in flux determinations, as indicated earlier.

Assumption of constant electron energy predetermines that this method will not correctly predict the variation of backscatter factor with distance from the interface. Determination of electron flux to higher orders of approximation can improve its value at distance from the interface (O'Brien 1974); the flux is determined for example by the method of discrete ordinates (O'Brien 1974). However, the severe approximation of a constant energy remains, so that variation of backscatter factor with distance from the interface will not be accurate, and the simplicity of the calculation is sacrificed.

Although distributed source experimental data are directly compared with "One-Group" data, 'edge effects' are present only in the former. That is, the source is broader than the sensitive detector area in the experiment, but edgeless, or infinitely wide, and thin sources and scoring regions are used in the calculations. It may therefore be more appropriate to use averages of point and distributed source experimental data for comparing with "One-Group" data. This results in slightly smaller discrepancies, roughly 10% to 20%, between experimental and calculated backscatter factors but the former remain smaller than the latter at most solid material interfaces and experimental dose reductions at air interfaces remain smaller than calculated ones.

Table 6.1 Beta Dose Backscatter Factors for a Planar ^{32}P Source

Interface	"One-Group" Value %B	Experimental Value* %B [uncertainty]	Discrepancy[1]
Bismuth/Mylar	34.9	27.6 [0.3]	-26%
Tungsten/Mylar	33.4	27.7 [0.2]	-21%
Cadmium/Mylar	27.9	21.6 [0.3]	-29%
Copper/Mylar	19.3	15.8 [0.1]	-22%
Aluminium/Mylar	6.4	6.38 [0.03]	0%
Graphite/Mylar	-3.6	-2.1 [0.3]	-71%
Bismuth/lucite	36.3	29.4 [0.3]	-23%
Tungsten/lucite	34.8	29.4 [0.3]	-18%
Cadmium/lucite	29.2	23.1 [0.2]	-26%
Copper/lucite	20.5	17.7 [0.1]	-16%
Aluminium/lucite	7.4	7.96 [0.08]	7%
Air/lucite	-20.6	-27.2 [0.1]	24%
Air/Mylar	-21.4	-28.3 [0.1]	24%

* *Extrapolated "True Interface" values.*

[1] Discrepancy = [(Experiment - "One-Group") / Experiment] x 100%.

6.2 The "Two-Group" Method

The name arises from the treatment of electron transport in this theory. Electrons are depicted as moving radially outward from an isotropic source a certain distance, from where they diffuse or travel in random directions. The first stage is called the 'direct' component, and the second, the 'diffusion' component, hence the name "Two-Group".

Also fundamental to this method is that for a radionuclide to be a suitable candidate, its spectrum must be describable by sums of partial "quasi-equilibrium" spectra (Radzievsky et al 1980). The spectrum for ^{32}P is represented by the following.

$$\frac{dN}{dE}(^{32}P) \sim 1.47\,(1900\text{keV}) - 0.50\,(1000\text{keV}) + 0.03\,(330\text{ keV})$$

where the bracketed quantities are energies which correspond to range cut-offs used in formulating this sum (Radzievsky et al 1980).

The method consists of solving equations which represent the two-group fluence field. Parameters used in the solutions of these equations are empirical; also, the location of the source for the diffusion component is artificially chosen to be the source position.

The method is used to predict the dose backscatter factor variation with distance from a planar aluminium/water interface where a thin, distributed ^{32}P source is located. Backscatter factors in the water medium are calculated. This interface is chosen from a list of four media for which parameters for the model are provided, (Radzievsky and Komarov 1982), because it most closely resembles an aluminium/Mylar interface which is used in experimental work done here.

The diagram below depicts the problem geometry. A thin, infinite ^{32}P source is sandwiched between the two semi-infinite media. Medium 1 is water, medium 2, aluminium.

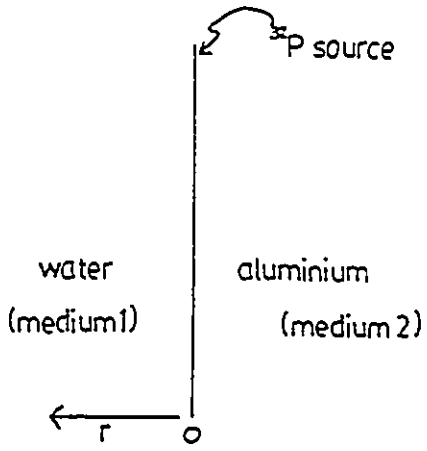

The dose D to medium 1 is the quantity of interest. It consists of two components, a directional and a diffusional one, as indicated next.

$$D = D_o + D_d \ . \tag{6.25}$$

where a subscript o denotes 'direct' and a subscript d, 'diffusion'. Equation 6.25 can be rewritten as

$$D = \sum_{i=1}^{N} D_{oi} + D_{di} \tag{6.26}$$

where

D_{oi} is the directional component of the dose due to the i^{th} partial source,

D_{di} is the diffusional component of the dose due to the i^{th} partial source.

For a partial source, the two component doses are given by

$$D_o = W_o \phi_o \tag{6.27}$$

and $$D_d = R_o^d W_o \phi_d \tag{6.28}$$

where W_o is the mean stopping power of the medium for the partial spectrum of interest; these values are taken from Figure 5 of Radzievsky et al 1980.

R_o^d is the ratio of the diffusional component stopping power to the directional component stopping power.

and ϕ_o and ϕ_d are the direct and diffusion constituents of the fluence field, respectively. These are defined as follows.

$$\phi_o(r) = \frac{e^{-kr}}{4\pi r^2} \tag{6.29}$$

and $$\phi_d(r) = \frac{Q}{4\pi Fr} e^{-\nu r} \tag{6.30},$$

where

k is the attenuation coefficient for the direct component;

ν is the analogous parameter for the diffusion component;

Q is the effective source for the diffusion component; and

F is the diffusion coefficient.

Therefore, there are five parameters which are given values determined empirically. The parameters are k, ν,F, Q, R_o^d, and their values, taken from the aforementioned references, are given in Table 6.2.

Let $D_{1,2}$ be the dose in medium 1 when medium 2 is one half-space bounding the source.

Let $D_{1,1}$ be the dose in medium 1 when the source is between identical materials.

$D_{1,2}$ and $D_{1,1}$ are evaluated by summing over the three partial spectra for ^{32}P, according to Equation 6.26. The solution of Equation 6.26 for the problem geometry of interest, given by Equations 7 and 8 of Radzievsky and Komarov

1982, is as follows.

$$D_{1,2}(r) = \sum_{i=1}^{N} A_i \frac{\sigma W_{o1}}{2} \left\{ E_1(k_{1i} r) + R_o^d \frac{2Q}{\nu_1 F_1 + \nu_2 F_2} e^{-\nu_{1,i} r} \right\} \quad (6.31)$$

and

$$D_{1,1}(r) = \sum_{i=1}^{N} A_i \frac{\sigma W_{o1}}{2} \left\{ E_1(k_{1i} r) + R_o^d \frac{Q}{\nu_1 F_1} e^{-\nu_{1,i} r} \right\} \quad (6.32)$$

where

r is the distance from the source, as indicated in the diagram above;

N is 3, corresponding to the three partial spectra of ^{32}P;

A_i is the amplitude of the i^{th} partial spectrum;

σ is the source strength per unit area; and

E_1 is the integral exponent, defined by

$$E_1(t) = \int_t^{\infty} t^{-1} e^{-t} \, dt \quad .$$

The dose ratio for aluminium with respect to water is determined from the ratio of Equations 6.31 and 6.32. Specifically, it is

$$R_{Al-H_2O}(r) = \frac{D_{1,2}(r)}{D_{1,1}(r)} \quad . \quad (6.33)$$

Table 6.2 Parameters for 'Two-Group' Determination of Dose Ratio in Water (for the geometry specified).

Partial Source, i	Partial Source Energy, E_i (MeV)	Amplitude A_i	CSDA Range for Partial Source Energy, S_{oi}(mg/cm^2)
1	1.9	1.47	925
2	1.0	-0.50	437
3	0.330	0.03	97.3

Partial Source i	Diffusion attenuation coefficient, $\nu_i = 9S_{oi}^{-1}$ (mg/cm^2)$^{-1}$	Mean Stopping Power for Partial Spectrum, W_{oi} (keV/(mg/cm^2))
1	0.00973	2.8
2	0.0206	3.1
3	0.0925	5.1

$Q = 0.5$

$R_o^d = 1.1$

$k_i = \nu_i$ and

$\nu_1 F_1 = 0.4$; and $\nu_2 F_2 = 0.3$ for the three partial sources.

6.2.1 Results of the "Two-Group" method

Dose ratios as a function of distance from an aluminium/water interface where a broad, isotropic ^{32}P source is located, are calculated from Equation 6.33 (Prestwich 1991). Backscatter factors thus obtained are shown in Figure 6.1, where depth refers to distance from the interface in the water medium. Analogous experimental data for an aluminium/Mylar interface are also included in this graph.

Disagreement between the curves in Figure 6.1 is evident. Experimentally, dose enhancement increases from 6% at the interface to 9% at about 30mg/cm^2 from the interface and thereafter decreases exponentially such that at 400mg/cm^2, the dose enhancement is 2%. Reduction of dose enhancement with increasing distance from the interface is anticipated for physical reasons.

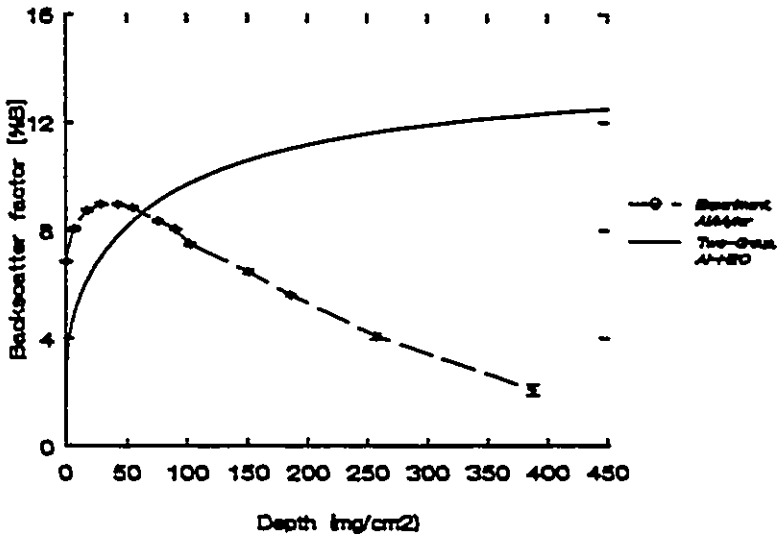

Fig 6.1 Variation of backscatter factor with distance from aluminium/Mylar (experimental) and aluminium/water ("Two-Group") interfaces where ^{32}P sources are located.

Dose enhancement results from greater energy deposition by electrons backscattered from aluminium compared with energy deposition in the homogeneous Mylar case. The energy of backscattered electrons is less than, or occasionally equal to the end-point energy of the ^{32}P beta spectrum. (Snyman and Clayton 1963; Kovarik 1910) Therefore, at a distance which corresponds to the range of this energy, or at some smaller distance, there should be no effect of backscattered electrons - the backscatter factor should be zero.

The "Two-Group" curve does show an initial increase in backscatter factor that is somewhat similar to the one observed experimentally. However, the calculated dose enhancement continues to increase beyond 100mg/cm^2 and almost plateaus around 12%. This is at odds with the physical rationale, presented in the preceding paragraph, to necessitate that dose enhancement be zero at 800mg/cm^2 from the interface. Previous calculations done elsewhere have found "Two-Group" curves similar to the one presented here (Kwok et al 1986).

Dose enhancement which persists with increasing distance from an interface is expected from the "Two-Group" model. At large distances from the interface, the integral exponent term in the expressions for dose, Equations 6.31 and 6.32, becomes negligible but the exponential term remains finite.

PART III. DISCUSSION AND CONCLUSIONS

CHAPTER 7

A DISCOURSE ON EXPERIMENTAL AND CALCULATED RESULTS

Interface beta dosimetry was investigated experimentally and using calculations. Calculational approaches included implementing two Monte Carlo codes, EGS4/Dosrz and Cyltran, and two analytical methods. Experimental work was done with the beta radioisotope, ^{32}P, and an extrapolation chamber as the radiation detector.

Sections 7.1 and 7.2 summarize the comparisons between results from calculations and experiments. The remaining section addresses previous and similar experimental and Monte Carlo work done elsewhere.

As discussed in Chapter 2, paths taken and energy deposition by electrons result from their interactions with atomic and sub-atomic constituents of a medium. Therefore, energy deposition which occurs when electrons are exposed to different media varies from that which occurs when they travel in a single medium. This difference in energy deposition translates into a difference in absorbed dose, which is investigated here.

This work considers the dose to a low atomic number, soft-tissue equivalent material when a beta source is sandwiched between the plane surfaces of this medium and another. When the other medium is not soft-tissue equivalent, the material arrangement is described as heterogeneous. A homogeneous case is one in which the two media are the same low atomic number, soft-tissue equivalent material; in the present discussion, this term also refers to situations where any soft-tissue equivalent material is a scatterer in the experiments.

The collecting electrode and upper electrode, or entrance window, of the extrapolation chamber constitute a low atomic number, soft-tissue equivalent

medium; the chamber's operational attributes, noted in Section 4.3.1, permit neglect of its sensitive region of air between the two electrodes. The collecting electrode is made of A-150, or Shonka, plastic and the entrance window is either conducting polyethylene or graphite-coated polypropylene. Mylar, also a soft-tissue equivalent material (White 1978), is used most frequently in experimental homogeneous medium arrangements because thin sheets of this material, needed for absorber type ASB and ASD measurements, are obtained the most readily.

The low atomic number, soft-tissue equivalent material or medium is hereinafter also referred to as the low atomic number material or medium.

The amount by which the dose to this medium changes for a heterogeneous case compared with a homogeneous one is the specific quantity of interest. It is the dose backscatter factor.

A positive dose backscatter factor means that the dose to the low atomic number material in the heterogeneous case is larger than in the homogeneous case. A negative dose backscatter factor means that the dose to the low atomic number material in the heterogeneous case is smaller than in the homogeneous case. The dose enhancements result from the backscattering of more electrons of the same energy, as well as higher energy electrons, from the non-soft-tissue equivalent medium compared with the low atomic number material. The dose reductions indicate that, relative to the homogeneous situation, there is a lack of electron backscattering from the non-soft-tissue equivalent material.

Lucite is a low atomic number material that is also used in Zeroeth type measurements. The experimental geometries are described in Sections 4.1 and 4.2.

Positive beta dose backscatter factors are obtained for heterogeneous cases where the non-soft-tissue equivalent material, or scatterer, has an atomic number which is higher than the effective atomic number of Mylar or lucite.

The dose enhancement is attributed to the greater amount of elastic nuclear scattering which occurs in higher atomic number materials; the Rutherford scattering cross-section varies as the square of the medium atomic number. Therefore, electrons are more likely to escape with greater energy from higher

atomic number materials than from lower atomic number materials. This is confirmed experimentally; monoenergetic electron backscatter or reflection experiments demonstrate that electrons backscattered from higher atomic number materials have greater energies than ones backscattered from lower atomic number materials (Chap 6, Mladjenović 1973).

Consistent with these monoenergetic results, experiments with ^{32}P show that backscattered energy spectra from high atomic number scatterers have larger fractions of higher energy electrons than backscattered spectra from low atomic number scatterers. They also show that maxima in backscattered spectra from high atomic number scatterers occur at higher energies and are larger than those in backscattered spectra from low atomic number scatterers. (Snyman and Clayton 1963).

Consequently, observation of beta dose backscatter factor variation with scatterer atomic number is not unexpected. Dose enhancements range from about 5½% for aluminium/Mylar interfaces to about 30% for bismuth/Mylar interfaces, for a ^{32}P point source (Table 4.2(b)).

The backscatter factor varies as log(Z+1), where Z is the scatterer atomic number, as shown in Figure 4.11. This is in keeping with other backscattering counting data, as noted in Section 4.4.2. Specifically, the variations of reflection coefficients and beta dose backscatter factors with scatterer atomic number are the same. The following further illustrates that backscatter factor experimental results are consistent with counting reflection experimental results.

The "saturation reflection thickness" is the minimum scatterer thickness which produces maximum backscattering. For ^{204}Tl and ^{90}Sr-^{90}Y, it is estimated to be about 1/5 of the range of the beta particles (Sharma and Singh 1979), where the range is calculated from the empirical formula of Katz and Penfold (Katz and Penfold 1952).

Beta dose backscatter factor variation with aluminium absorbers between the source and the backscatterer becomes negligible beyond 140mg/cm^2, as indicated in Figure 4.19. This thickness is roughly 1/5 of the range of ^{32}P beta particles in

aluminium and therefore agrees with the preceding "saturation reflection thickness" findings. The range of ^{32}P beta particles in aluminium is 789mg/cm^2, according to the Katz and Penfold formula.

The shapes of experimental backscatter factor depth profiles, ASD and ASB geometries, are described in Chapter 4.

In the ASD geometry, Mylar absorbers are positioned between the source and the detector. Electrons from the ^{32}P source are virtually in contact with the backscatterer; backscattered electrons as well as source electrons are then filtered by Mylar absorbers before reaching the point of measurement. The backscatter factor variation with Mylar absorber thickness or distance from the interface illustrates the following characteristics.

For solid interfaces such as aluminium/Mylar and bismuth/Mylar, backscatter factor ASD depth profiles (as in Figures 4.20 and 4.14) demonstrate that there is an initial increase in dose enhancement with distance from the interface, followed by a decline. These features have been addressed at greater length in Section 4.4.3.

The initial increase in backscatter factor is due to the greater penetrability and abundance of electrons backscattered from aluminium and bismuth compared with electrons backscattered from Mylar. The occurrence of a peak which is further from the interface in the bismuth profile than in the aluminium profile is consistent with the greater number of higher energy electrons which are backscattered from bismuth than from aluminium (Snyman and Clayton 1963).

In the ASB geometry, absorbers are positioned between the source and the (back)scatterer. Source electrons are filtered by Mylar absorbers before reaching the scatterer. Thus, the spectrum incident on the scatterer is reduced in energy in comparison to the source spectrum; the backscattered electrons are then further filtered before reaching the point of measurement.

'Source spectrum' refers to the electrons emitted from the beta source in situ in the experimental arrangements. It is also called the direct component to

distinguish it from backscattered electrons. In the ASB geometry, the source spectrum is seen unmodified by the detector whereas in the ASD geometry, both the source and the backscattered spectra are filtered by absorbers before detection. Also, in the ASB geometry, the Mylar backscattered term is constant; this is not the case in the ASD geometry, as noted earlier.

Therefore, in the ASB geometry with a solid material interface, the backscatter from the non-soft-tissue equivalent scatterer is the only contributing component to the measured energy deposition that varies with absorber thickness. From the definition of backscatter factor, it follows that the variation of ASB backscatter factors with distance from a solid material interface is purely decreasing and is faster than in the ASD geometry.

Dose reduction variation with distance from air interfaces in the ASB geometry exhibits two components. There is a faster decline near the interface, followed by a slower fall-off, as seen in Figure 4.17. The magnitude of the dose reduction decreases with increasing Mylar absorber thickness because a pure escape phenomenon, which takes place with no Mylar absorber, is not occurring. The Mylar absorbers introduce electron backscattering and the energy deposition from such backscattering increases with absorber thickness; consequently, the backscatter factor decreases.

Dose reduction variation with distance from air interfaces in the ASD geometry also exhibits two components, as seen in Figure 4.15. The ratio of source to source plus Mylar backscattered energy deposition is measured here. Each of these quantities is filtered, and therefore decreases, with distance from the interface. Therefore, the dose reduction diminishes with distance from the interface.

Experimental ASD and ASB profiles are fitted to sums of exponentials in Chapter 4. Although a quantitative and comprehensive explanation for the shapes of these profiles is lacking, analysis of direct and backscattered energy depositions determined using the Monte Carlo codes demonstrates that these components are not single exponentials; for example, the ASD direct component consists of two

exponentials. Therefore, it may not be inappropriate to use sums of exponentials to describe the profiles.

Beta dose backscatter factors measured with respect to lucite are larger than those measured with respect to Mylar. This is noted in Sections 4.4.2 and 4.5.2, and is consistent with Mylar having a larger scattering power than lucite. Energy deposited from a Mylar scatterer is larger than that from a lucite scatterer so that backscatter factors with respect to the former are smaller than ones with respect to the latter at solid interfaces; dose reductions with respect to Mylar are larger than ones with respect to lucite at air interfaces.

The ratio of backscatter factor with respect to lucite to backscatter factor with respect to Mylar decreases with increasing scatterer atomic number. This trend is called the "Mylar-lucite effect". For a ^{32}P point source, the preceding ratio is 1.92, 1.31 and 1.18 for aluminium, copper and bismuth scatterers, respectively.

The "Mylar-lucite effect" results from the differences in energy deposition by the various scatterers and the definition of the dose backscatter factor. As discussed earlier, energy deposition increases with scatterer atomic number; also, the energy deposited by a Mylar scatterer is greater than that deposited by a lucite one. Therefore, the ratio of 'the difference between the energy depositions by a high atomic number scatterer and lucite' to 'the difference between the energy depositions by the same high atomic number scatterer and Mylar' is smaller than an analogous ratio in which a scatterer of low atomic number replaces the high atomic number scatterer. Consequently, the "Mylar-lucite effect" is observed.

The effect of source geometry on beta dose backscatter factors is noted in Section 4.6. This effect is also evident in the ratio of backscatter factors with respect to lucite to ones with respect to Mylar since such ratios are smaller for distributed sources than for point sources. For a ^{32}P distributed source, this ratio is 1.24, 1.12 and 1.06 for aluminium, copper and bismuth scatterers, respectively. These values are smaller than the aforementioned point source values.

Distributed source dose backscatter factors are smaller than point source dose backscatter factors at solid material interfaces; the converse is found for dose reduction factors at air interfaces. These experimental findings are consistent with ^{32}P scattering experiments done previously elsewhere (Seliger 1952). The latter demonstrate that, in addition to a variation with scatterer atomic number, there is an angular dependence associated with beta particle backscattering. This is addressed at greater length in Section 4.6. The present experimental work finds that ratios of point to distributed source backscatter factors are of the order of 1.10 for solid material/Mylar interfaces and 1.20 for solid material/lucite interfaces. Analogous ratios for air interfaces are 0.92 and 0.86, respectively.

7.1 Monte Carlo / Experimental Results

The geometries used for Zeroeth and absorber - ASD and ASB - simulations are described in Section 5.2. Both Monte Carlo codes were used to calculate Zeroeth geometry beta dose backscatter factors for point and distributed ^{32}P sources. Cyltran was used to calculate beta dose backscatter factor variation from a material interface where the source was located; point and distributed sources were used in these ASD simulations. EGS4/Dosrz was used in ASB simulations to calculate the variation of beta dose backscatter factor with increasing source and scatterer, or interface, separation.

Zeroeth and ASB simulations mimic the experiments; dimensions and compositions of most of the materials used experimentally, such as the extrapolation chamber, are included. Simpler geometries are used in ASD simulations. In these, the detector is replaced by a cylinder of Mylar, 2cm long, 2cm diameter. The variation of backscatter factor with depth in this cylinder, away from the interface where the source is located, is determined. The scoring region size is equivalent to the sensitive air layer used in the extrapolation chamber during the ASD experiments. This simulation therefore approximates the ASD experiment

to the extent that the Shonka plastic of the chamber and the Mylar cylinder of the simulation are equivalent.

Since these two materials are both soft-tissue equivalent (White 1978), use of this simpler ASD geometry is justified. Therefore, any dramatic differences between experimental and Monte Carlo results cannot be attributed to the simulation geometry being inappropriate. Also, the saving on computing time which this simpler geometry affords is a bonus.

Quantitative comparison of the two codes is included in Chapter 5. Section 5.7 addresses the monoenergetic source energy deposited data which are output from the codes. Electron source energies were sampled from 0MeV to 1.7MeV, the end-point energy of the ^{32}P spectrum. The data from the two codes agree to within about 10% except for 20keV and 70keV source energies, for Zeroeth geometry thin and thick detector window simulations, respectively. In these cases, there is extreme disparity between results from the two codes. As noted in Section 5.7.1, a possible cause of the disagreement is the different ways in which the codes deal with energy-loss straggling or termination of electron histories, or both.

Although monoenergetic energy deposited data from the codes generally agree reasonably well, monoenergetic backscatter factors from the codes can exhibit poorer agreement since the latter are ratios of two energy deposited values. The quality of agreement between monoenergetic backscatter factors from the codes is usually reflected in a comparison of their beta dose backscatter factors, as shown in Section 5.7.1. For example, monoenergetic backscatter factors for the bismuth interface, Figures 5.17(a) and 5.18, indicate that beta dose backscatter factors from the codes will be different.

Zeroeth geometry simulations were done with bismuth, copper, aluminium and air as non-soft-tissue equivalent materials, and with Mylar and lucite as soft-tissue equivalent scatterers. Fourteen solid material interfaces were considered; these included simulations for the two source geometries and both detector windows. Five air interface simulations, also dealing with different combinations

of source geometry and detector window, were done. Both Monte Carlo codes were used for each simulation.

The agreement between experimental and Monte Carlo beta dose backscatter factors is generally good - discrepancies between experimental and Monte Carlo data are typically less than twenty percent. Individual comparisons are quantitated in Tables 5.2, 5.4 and 5.6.

Closer examination of the data reveals the following.

Point source simulations involving aluminium/Mylar interfaces are accountable for discrepancies between Monte Carlo and experimental results that are greater than twenty-five percent. Better agreement between experimental and Monte Carlo data is obtained for aluminium/lucite interfaces, and agreement between experimental and Monte Carlo beta dose backscatter factors for distributed source, aluminium interfaces is good. Although these inconsistent discrepancies between Monte Carlo and experimental data are puzzling, in order to keep them in perspective, it is important to note that the effect under discussion is small. Backscatter factors at aluminium interfaces are about 10%; thus, absolute differences of 3% translate into 30% discrepancies.

Interestingly, results from EGS4/Dosrz agree very well with experimental backscatter factors for all copper interfaces investigated; the agreement is to well within ten percent. Agreement between Cyltran and experimental beta dose backscatter factors is less impressive and somewhat confusing; it is marginal, that is, about ten percent, for copper/Mylar, point source cases, deteriorates to about twenty percent for copper/Mylar, distributed source cases, and is good for copper/lucite cases.

For bismuth interfaces, Cyltran beta dose backscatter factors agree better with experimental data than do those from EGS4/Dosrz. Agreement between EGS4/Dosrz and experimental results is in the neighbourhood of fifteen to twenty percent; and agreement between Cyltran and experimental data is about ten percent or better.

The discrepancy between EGS4/Dosrz and experimental bismuth interface

data is such that the backscatter factor from the code is smaller than the experimental value. This observation is consistent with the findings of a comparison between Goudsmit-Saunderson and Molière multiple-scattering theories which are used in Cyltran and EGS4/Dosrz, respectively. The Goudsmit-Saunderson formalism may be more appropriate for handling backscatter from high atomic number materials, particularly for low-energy electrons, since the Molière theory underestimates electron backscattering in these cases (Berger and Wang 1988).

However, the Monte Carlo/experimental comparison in this work cannot provide unequivocal evidence for preferring one of the multiple scattering theories. Adopting the stance taken by Rogers and Bielajew who also note differences between results from the codes with regard to high atomic number media (Rogers and Bielajew 1988), the following conclusion is reached.

Observations made about discrepancies between Monte Carlo and experimental backscatter factors at bismuth and aluminium interfaces indicate that further investigation is required in order to ascertain the causes of these discrepancies. There may be factors besides differences in multiple-scattering theories which contribute to these findings. Some examples of these factors may be scoring of energy deposited by low energy electrons and selection of electron step-size.

There is good agreement between Monte Carlo and experimental data for thin window, air interfaces, and slightly poorer, but still acceptable, agreement between Monte Carlo and experimental results for thick window, point source, air interface cases. For the thick window, point source cases, results from both codes exceed the experimental results by about fifteen percent. For the thin window, point source case, EGS4/Dosrz dose reduction factor is eight percent larger than the experimental value and the dose reduction factor from Cyltran agrees with the experimental value. Thin window, distributed source dose reduction factors from both codes are within five percent of experimental values.

Meticulous attention is given to quantifying the agreement between Monte

Carlo and experimental results. This is done with the aim of demonstrating whether Monte Carlo results are adequate for boundary dosimetry calculations in practical applications. In such situations, uncertainties less than 5% to 10% are desirable. For the geometry and beta radionuclide considered, this work indicates that both codes may be adequate for copper/soft-tissue equivalent and air/soft-tissue equivalent boundaries and that Cyltran is slightly more suitable for bismuth/soft-tissue equivalent boundaries. Further clarification is needed for aluminium boundaries.

The variation of beta dose backscatter factor with distance from an interface where a ^{32}P source is located, determined using Cyltran, agrees well with experimental results. The code effectively reproduces the shapes of the experimental ASD curves.

For both point and distributed sources, the code predicts that there is an increase in dose enhancement, from the Zeroeth value, with distance from solid material interfaces. The dose enhancement peaks and then decreases. This shape is the same as that determined experimentally. At air interfaces, Cyltran ASD dose reduction curves are similar to experimental ones.

The aluminium interface ASD profile for a ^{32}P point source, determined using Cyltran, contains values which are larger than experimental backscatter factors (Figure 5.4). This is consistent with Zeroeth geometry results noted before but, unfortunately, reasons for these discrepancies have not been determined. Agreement between Cyltran and experimental ASD bismuth profiles, for a ^{32}P distributed source, Figure 5.6, is good; the code correctly shows that the peak in the bismuth profile occurs further from the interface than does the peak in the aluminium profile, and that the decrease in dose enhancement is slower in the former case. For air interfaces, experimental and Cyltran dose reduction ASD profiles for point and distributed ^{32}P sources, Figures 5.4 and 5.6, also agree but, as noted for the aluminium profile, Monte Carlo values are somewhat larger than experimental values.

Moreover, the code not only satisfactorily reproduces the shapes of experimental ASD profiles, but it also predicts rates of decrease in backscatter factors that are consistent with experimental results. These decreases are characterized by relaxation lengths, defined in Section 4.4. For a point source, Cyltran ASD relaxation lengths are 357[51]mg/cm^2 and, 31[11]mg/cm^2 and 208[39]mg/cm^2 for aluminium/Mylar and air/Mylar interfaces, respectively. Corresponding experimental values are 174[6]mg/cm^2 and, 19.1[0.2]mg/cm^2 and 213[5]mg/cm^2. Absolute uncertainties are bracketed. For a distributed source, Cyltran ASD relaxation lengths are 435[132]mg/cm^2, 263[90]mg/cm^2 and 147[19]mg/cm^2 for bismuth/Mylar, aluminium/Mylar and air/Mylar interfaces, respectively. Corresponding experimental values are 588[69]mg/cm^2 and 238[11]mg/cm^2 for bismuth and aluminium interfaces, respectively, and 88[24]mg/cm^2 and 294[138]mg/cm^2 for the air interface.

EGS4/Dosrz ASB relaxation lengths also approximate experimental values. For a point source, experimental relaxation lengths are 26[4]mg/cm^2, and 2[1]mg/cm^2 and 28[1]mg/cm^2 for aluminium/Mylar and air/Mylar interfaces, respectively. Corresponding EGS4/Dosrz values are 36[1]mg/cm^2 and, 5[1]mg/cm^2 and 39[3]mg/cm^2.

In this geometry, the variation of backscatter factor with increasing source and scatterer separation is reproduced well by the Monte Carlo code for the air interface, as seen in Figure 5.8. Quantitative agreement is lacking in the dose enhancement profile; however, this is consistent with Zeroeth geometry results described in Section 5.3.1. Despite the dissimilarity in absolute values of beta dose backscatter factors, the calculated rate of decrease of dose enhancement with distance does not differ greatly from the experimental one, as demonstrated by their relaxation lengths.

In addition, EGS4/Dosrz ASB relaxation lengths are about six to eight times smaller than Cyltran ASD values. This is consistent with experimental findings, and is further evidence of the general agreement displayed between results from the

two codes for aluminium/Mylar and air/Mylar boundaries.

The Monte Carlo results indicate that there may be a "Mylar-lucite effect" such as the one observed experimentally. However, magnitudes of the associated uncertainties, and the few scatterer/soft-tissue boundaries simulated, make it difficult to discern a trend - ratios of backscatter factors with respect to lucite to ones with respect to Mylar only appear to decrease with increasing scatterer atomic number. These ratios, from EGS4/Dosrz Zeroeth, point source, thick window data, are 1.04[0.02], 1.06[0.01] and 1.11[0.02] for bismuth, copper and aluminium scatterers, respectively. Corresponding values from Cyltran data are 1.05[0.04], 1.07[0.05] and 1.13[0.10]. In contrast, the experimental "Mylar-lucite effect" is well-defined. The data are obtained from "true interface values" listed in Tables 4.2(b) and 4.5. Experimental uncertainties are considerably smaller than those associated with the Monte Carlo data. However, reductions of the latter necessitate impracticably long computing times.

A small set of Monte Carlo data is also only what is available for determining whether the simulations indicate that there is an effect of source geometry on beta dose backscatter factors. The findings are detailed in Section 5.3.3. Cyltran results indicate that point source dose enhancement factors are larger than distributed source ones and that point source dose reduction factors are smaller than distributed source ones; this agrees with experimental observations. However, EGS4/Dosrz beta dose backscatter factors do not indicate that there is a source geometry effect.

7.2 Analytical / Experimental Results

The "One-Group" and "Two-Group" methods, due to O'Brien et al (O'Brien et al 1964; O'Brien 1974) and Radzievsky et al (Radzievsky et al 1980; Radzievsky and Komarov 1982), respectively, are analytical approaches to boundary beta dosimetry. The first method is purely theoretical and the second is partly empirical. They were used, as described in Chapter 6, to calculate beta dose backscatter factors for an infinitely wide, thin and isotropic ^{32}P source located at material interfaces.

Predictions of the "One-Group" method agree with Zeroeth experimental beta dose backscatter factors to within about 20% for the interfaces considered in Section 6.1.2. Results from the theory exhibit an increase in dose enhancement with scatterer atomic number, and dose reductions at air interfaces. In addition, a "Mylar-lucite effect", defined earlier, is evident.

Qualitatively therefore, the "One-Group" method satisfactorily reproduces trends noted in experimental data. There is also reasonable quantitative agreement between theoretical and experimental backscatter factors, given the harsh approximations inherent in the theoretical approach.

The appealing simplicity of the "One-Group" method relies on its fundamental assumptions that the source spectrum can be represented by its average energy and that cross-sections governing electron interactions can be determined at this single energy. Applicability of the constant cross-section radiation transport equation, Equation 6.3, is thus assumed, and expressions for electron flux, and therefore dose rate and dose ratio, Equations 6.20 and 6.21, are determined.

These expressions depend on scattering and absorption cross-sections for the various materials used. The form of the scattering cross-section is from Lewis (Lewis 1950); and absorption cross-sections are determined from the stopping power, evaluated at the average energy (Equation 6.11). (O'Brien et al 1964)

The results from the "One-Group" method are acceptable. However, the

theory, as it is employed in Section 6.1, cannot accurately predict a variation of dose ratio with distance from an interface like experimental ASD profiles. The cross-sections are always evaluated at the same average energy whereas the average energy changes with distance from the source in reality.

The "Two-Group" method does not reproduce experimental ASD profiles either, as shown in Figure 6.1.

This method is based on a two-component description of the fluence field and on representing the beta spectrum as the sum of partial spectra. The latter relies on the shape of these spectra not changing with filtration (Radzievsky et al 1980) and the fluence field consists of direct and diffusion components (Radzievsky and Komarov 1982).

Although this description of the fluence field is used elsewhere (Fano 1954; Seliger 1952; Archard 1961), indications are that it may be inadequate for dealing with backscattering. The dose ratio expressions, Equations 6.31 through 6.33, lead to the physically unrealistic situation in which dose enhancement does not diminish at large distances from the interface.

Therefore, although by virtue of its empirical nature it is possible to alter the parameters of the "Two-Group" model in order to provide better agreement with experimental results, it is unlikely that this will be sufficient to rectify the aberrant behaviour of backscatter factor far from the source.

7.3 Comparison with Earlier Works

Experimental work which addresses dose perturbation at interfaces has been done elsewhere. Kwok et al measured backscatter factors with respect to polystyrene, for ^{32}P point and plane sources, at aluminium/polystyrene and air/polystyrene interfaces. Thermoluminescent dosimeters (TLDs), made of lithium fluoride and 31mg/cm^2 thick, were used. (Kwok et al 1987) Osanov and Podsevalov measured dose perturbations at air interfaces using a 16cm diameter extrapolation chamber; their backscatter factors are relative to air, not a soft-tissue equivalent material. (Osanov and Podsevalov 1971)

For the point source, Kwok et al measured a dose enhancement of 12[3]% at the aluminium/polystyrene interface and a dose reduction of 25[4]% at the air/polystyrene interface (Kwok et al 1987). These findings are consistent with backscatter factors measured in the present work; a quantitative comparison is not undertaken since the TLD measurements pertain to polystyrene which is not used here, are made over a thickness of 31mg/cm^2, and the thickness of the source covering is not specified. Plane source dose enhancement at 23-58mg/cm^2 from an aluminium/polystyrene interface is 8[3]% (Kwok et al 1987). While an effect due to source geometry is indicated, the experimental uncertainties, which are bracketed, prevent drawing such a conclusion unreservedly.

The extrapolation chamber used in the present work permits making measurements which are more sensitive and more precise than ones made with the TLDs described above. This is demonstrated by the relatively small uncertainties associated with the data in Chapter 4. In addition, these data clearly show that there is an effect of source geometry on beta dose backscatter factors.

The variation of backscatter factor with distance from an interface where a source is located was also considered using TLDs. The backscatter factors are shown to decrease exponentially with distance from the interfaces (Kwok et al

1987). Although this is similar to the ASD backscatter factor profiles discussed in Chapter 4, details of the variation are absent in the TLD graphs (Kwok et al 1987). This is due, at least in part, to the size of the dosimeter. For example, the peak in the distributed source ASD aluminium interface profile, Figure 4.20, is not seen in the comparable TLD profile because it occurs at about 30mg/cm^2 from the interface, a distance roughly equivalent to the size of the TLD. In addition, only three TLD measurements were made for each profile (Kwok et al 1987).

As mentioned in Chapter 1, a discrepancy between Monte Carlo and experimental beta dose backscatter factors at an air/soft-tissue equivalent interface was indicated in an earlier work. Cyltran, point sources of ^{147}Pm and ^{204}Tl, and lithium fluoride TLDs, 12mg/cm^2 thick, were employed (Yu 1989). Even though a vacuum was used instead of air in the simulations, the dose reduction determined using Cyltran was found to be considerably less than the experimental dose reduction. For ^{204}Tl, the dose reduction from Cyltran is 9[1]% and the experimental value is 23[7]% (Yu 1989).

Similar discrepancies between experimental and Cyltran ^{32}P dose backscatter factors at air/soft-tissue equivalent interfaces were not found in the present work. This is clear from the data in Tables 5.1 through 5.4.

The dose reduction factor for a point source of ^{204}Tl (E_o=764keV) was calculated using monoenergetic data from Zeroeth geometry, thin window, point source simulations; eight electron source energies, between 20keV and 700keV, inclusive, were used. The dose reduction factor was found to be 21.7[0.2]%. However, this does not prove that the calculated value of Yu is incorrect since details of the geometry simulated in that work are different from those of the Zeroeth geometry described earlier herein. Also, since dose backscatter factors for ^{204}Tl were not measured in this work, the calculated value of 21.7[0.2]% has not been confirmed by experiments done here. However, an estimate of the dose reduction factor for ^{204}Tl at an air/soft-tissue equivalent interface can be derived from extrapolation chamber measurements made by Osanov and Podsevalov

(Osanov and Podsevalov 1971) whose work is further discussed below. The estimate is 24% and it therefore lends support for the preceding calculated value. Although the TLD dose reduction factor agrees with this calculated value, the significance of this is questionable because of the relatively large thickness, 12mg/cm^2, of the TLD. Furthermore, the possibility that the TLDs respond preferentially to higher electron energies has not been discredited. The discrepancy noted by Yu thus remains unresolved.

Backscatter factors with respect to air were measured for point sources of ^{32}P, ^{204}Tl and ^{147}Pm using an extrapolation chamber (Osanov and Podsevalov 1971). The diameter of the chamber was 16cm and the high voltage electrode was made of aluminized Terylene film, 0.35mg/cm^2 thick (Osanov and Podsevalov 1971). This electrode is assumed to be the entrance window of the detector and is of comparable thickness to the thin detector window used in the present work. Exact positions of the source and scatterer are uncertain; they are located "near the high-voltage electrode" (Osanov and Podsevalov 1971).

Profiles comparable to ASD and ASB air/Mylar curves of Chapter 4 herein are given by Osanov and Podsevalov (Figures 1,3, Osanov and Podsevalov 1971). The shapes of their polyethylene/air profiles are similar to those of the air/Mylar profiles in the present work - they show that the backscatter factor decreases with distance from the interface - and their data are also fitted by exponentials.

Osanov and Podsevalov do not address backscatter factors for solid material interfaces. They measure the dose to a soft-tissue equivalent slab with a beta source atop it, and the subsequent increase in that dose when a scatterer is placed on the source.

Although solid material interfaces are not discussed explicitly by Osanov and Podsevalov, estimates of Zeroeth backscatter factors with respect to polyethylene have been derived from the graphs in Figure 1 of Osanov and Podsevalov (Osanov and Podsevalov 1971). For lead, aluminium and air scatterers, backscatter factors with respect to polyethylene are about 38%, 8% and

-23%. These agree with values obtained in the present work: for bismuth, aluminium and air scatterers, backscatterer factors with respect to lucite are 35.0[0.4]%, 10.5[0.6]% and -23.4[0.2]%, where bracketed quantities are uncertainties (Table 4.2(b), Chapter 4).

The following chapter considers another set of experimental results that deals with doses measured at and near aluminium/polystyrene and vacuum/polystyrene boundaries. Estimates of backscatter factors are obtained from these data and are compared with Monte Carlo calculations.

CHAPTER 8

THE EISEN EXPERIMENT

The two Monte Carlo codes, EGS4/Dosrz and Cyltran, described in Chapter 3, were used to simulate the 2MeV electron beam experiment of Eisen et al (Eisen et al 1972). In this experiment, depth-dose profiles in a polystyrene slab were measured; a broad 2MeV electron beam was incident on the polystyrene slab which was backed with various materials. These experimental data constitute standards for testing Monte Carlo calculations regarding the energy deposition of low energy electrons in a low atomic number medium and the handling of electron backscatter at material boundaries, features of the codes which were also tested using the experiments performed in this work (Chapter 4).

The Eisen experimental depth-dose profiles for the cases of polystyrene, aluminium and no backing material were compared with Monte Carlo-calculated depth-dose profiles. It was found that the Monte Carlo results agree reasonably well with each other, but there is some discrepancy between the experimental data and the calculated values. However, for reasons enlarged upon later, these discrepancies are viewed tentatively so as not to overrate their implications and draw unwarranted conclusions.

The dose backscatter factor, B, defined earlier in this work, quantitates dose reduction or enhancement at interfaces. Backscatter factors at the polystyrene/vacuum and polystyrene/aluminium interfaces, obtained from the two Monte Carlo codes, agree but large uncertainties associated with the experimental data preclude comparing the experimental and Monte Carlo results unambiguously.

The experimental data used in the comparison were obtained from the graph of Figure 8 in Eisen et al (Eisen et al 1972) since tabulated values were no longer available (Eisen 1990). In addition, it has been estimated that uncertainties of 10%

could be placed on these experimental data (Seltzer and Berger 1987); this is the result of combining a 6% experimental reproducibility and an 8% possible error in using a constant stopping power ratio to convert film dose to medium dose, assuming that the film does not perturb the electron fluence spectrum appreciably.

The upshot of this is that the "discrepancies" observed between Monte Carlo results and these data are not clear-cut. General trends of the experimental data agree with those of the Monte Carlo data as shown in Figures 8.2 through 8.4, but definitive, quantitative comparison is elusive. This is also evident in the comparison made by Rogers and Bielajew (Rogers and Bielajew 1990) where discrepancies indicated remain unexplained, and uncertainties on the data are absent.

Notwithstanding the imperspicuity of the comparison, the results are presented because of the scarcity of reference data such as these and to underscore the need for benchmark data.

An irrefutable observation and potential source of disagreement between Monte Carlo results and the Eisen experimental data is seen in Figures 8.6 through 8.8. The dose measured at the incident face is the same for all the backing materials, according to the Monte Carlo calculations whereas the experimental data indicate that there is an effect due to the backscatterer at this incident face.

8.1 Particulars of the Comparison

Figure 8.1 summarizes the experiment which was simulated. The experimental data, acquired from Figure 8 of Eisen et al (Eisen et al 1972), represent the depth-dose profiles in the $0.42 g/cm^2$ of polystyrene illustrated in Figure 8.1. Thin nylon film dosimeters were interspersed with cylindrical discs of various thicknesses which were used to build the polystyrene slab. Another cylinder of polystyrene backed against the first constituted a homogeneous medium. Inhomogeneous media were created by using backing materials other than

polystyrene.

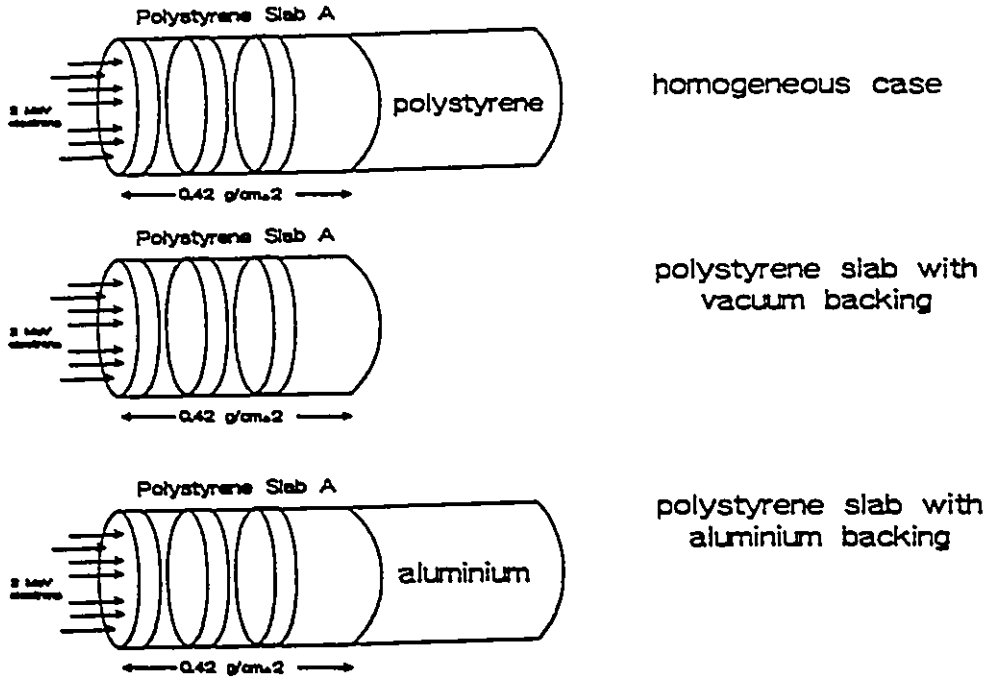

Depth-dose profiles in polystyrene slab A were measured by Eisen et al and calculated using EGS4/Dosrz and Cyltran. Thin nylon film dosimeters were interspersed between cylindrical discs of various thicknesses which were used to build slab A.

Fig 8.1 Summary of simulation of Eisen experiment.

The dosimeters were similar to polystyrene in their electron absorption characteristics (Eisen et al 1972). They were simulated as polystyrene, density 1.04g/cm^3, composition: C = 0.9226, H = 0.0774 (fraction by weight), and were 1cm square and 40μm thick.

The geometry used in the simulation was cylindrical; the scoring regions mimicking the dosimeters were therefore cylindrical. Their radii were 0.5cm, and their thicknesses were 40μm.

Cyltran simulation parameters included 50000 electron histories in 10 batches; electron and photon histories were terminated at 10keV and 1keV, respectively. Corresponding termination energies used in EGS4/Dosrz were 1keV; the maximum fractional energy loss per condensed history step was 0.04 and secondary particle production thresholds were 10keV and 1keV for electrons and bremsstrahlung photons, respectively. One hundred thousand (100000) histories in 10 batches were used.

8.2 Results

Figures 8.2 through 8.4 show the depth-dose profiles in the 0.42g/cm^2 slab. The experimental uncertainties are absent.

Figure 8.2 represents the homogeneous case, Figure 8.3, the polystyrene/aluminium case and Figure 8.4, the polystyrene/vacuum case. These graphs illustrate the agreement between the two Monte Carlo codes at the incident face and at the interface. The codes predict identical dose enhancement and dose reduction factors of approximately 17% and 23% at the aluminium and vacuum interfaces, respectively.

A small but systematic discrepancy between the codes is noted, however. In the region 0.12g/cm^2 to 0.30g/cm^2, EGS4/Dosrz predicts slightly higher doses ($\leq$ 8%) than Cyltran does. The discrepancy is most obvious for the polystyrene/vacuum depth-dose profiles. Figure 8.5 illustrates these observations in a graph of the ratio of 'EGS4/Dosrz to Cyltran' versus depth.

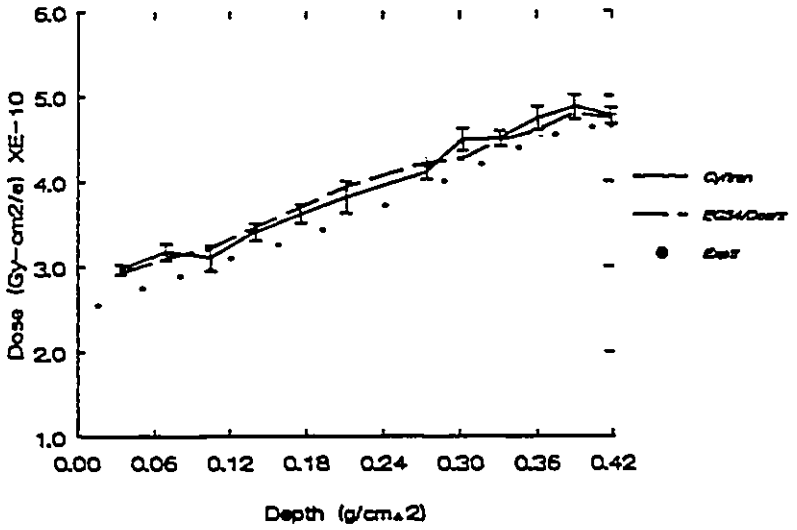

Fig 8.2 Depth-dose profiles in polystyrene slab A for the homogeneous case, as determined experimentally, and using EGS4/Dosrz and Cyltran Monte Carlo codes.

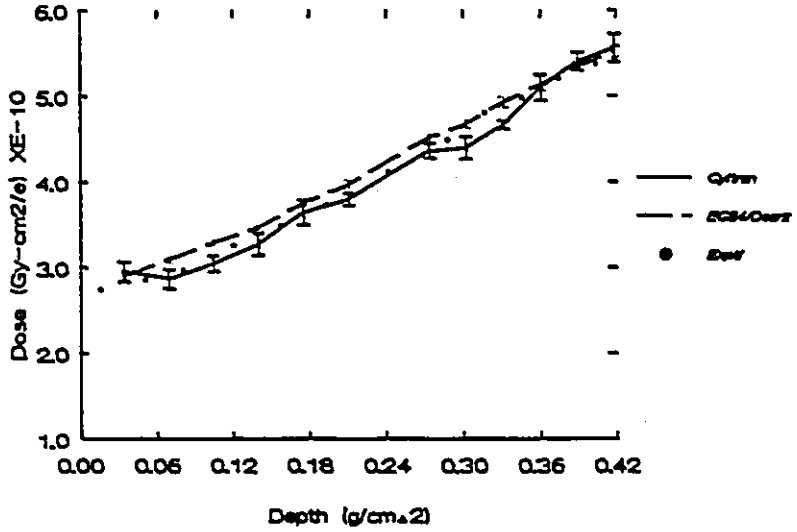

Fig 8.3 Depth-dose profiles in polystyrene slab A for the case of aluminium backing material, as determined experimentally and using EGS4/Dosrz and Cyltran Monte Carlo codes.

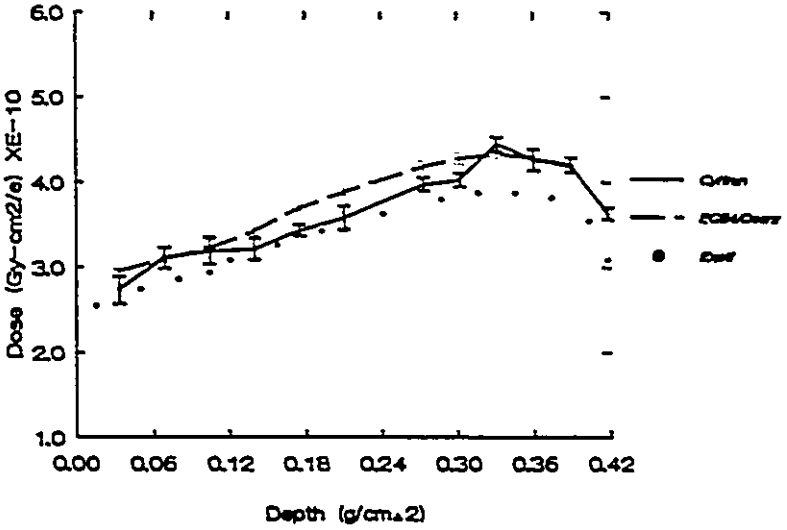

Fig 8.4 Depth-dose profiles in polystyrene slab A for the case of no backing material, as determined experimentally, and using EGS4/Dosrz and Cyltran Monte Carlo codes.

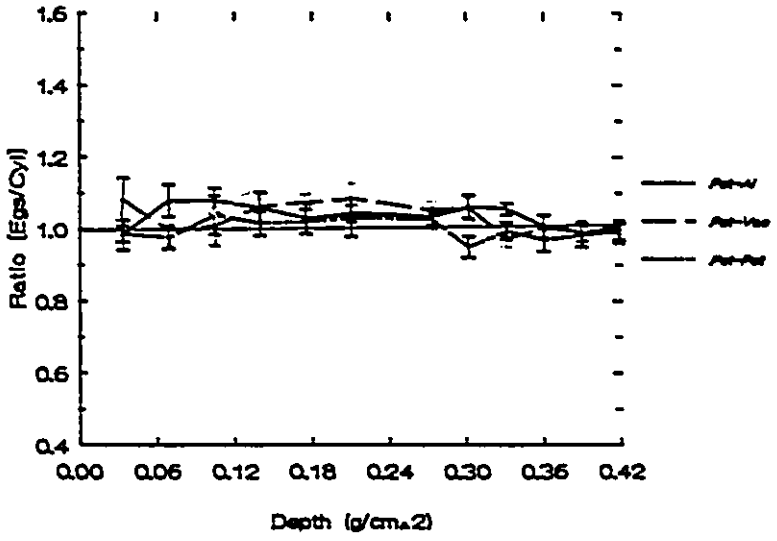

Fig 8.5 Ratio of Monte Carlo-calculated depth-dose profiles in polystyrene slab A for the homogeneous and two heterogeneous cases.

The experimental data agree, qualitatively, with the Monte Carlo results except for the polystyrene/vacuum case, where the dose decrement at the interface, resulting from electrons escaping from, and not returning to, the medium, is more pronounced in the experimental values.

It is important to note that the data in Figure 8 of Eisen et al (Eisen et al 1972) appear to be the result of smoothing of experimental data, and that the values used in this comparison were excerpted from this graph. This caveat is kept in mind hereinafter.

The experimental data for the homogeneous case, as for the case with no backing material, are lower than the Monte Carlo results. This is not observed in the polystyrene/aluminium case and points to the apparent anomaly in the experimental data mentioned earlier.

Figures 8.6. through 8.8 illustrate the inconsistency, namely, that the Monte Carlo codes predict the same doses at the incident face, regardless of the backscatterer, whereas the experimental data for the three cases do not converge at the incident face. Although it demands attention at first glance, its significance diminishes if a 6% experimental reproducibility and the above caveat are taken into account.

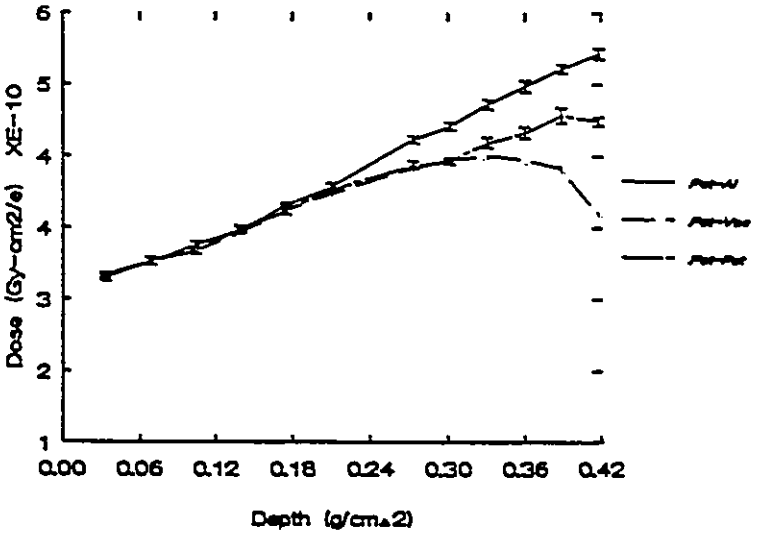

Fig 8.6 Depth-dose profiles in polystyrene slab A for the homogeneous and two heterogeneous cases, as determined using EGS4/Dosrz.

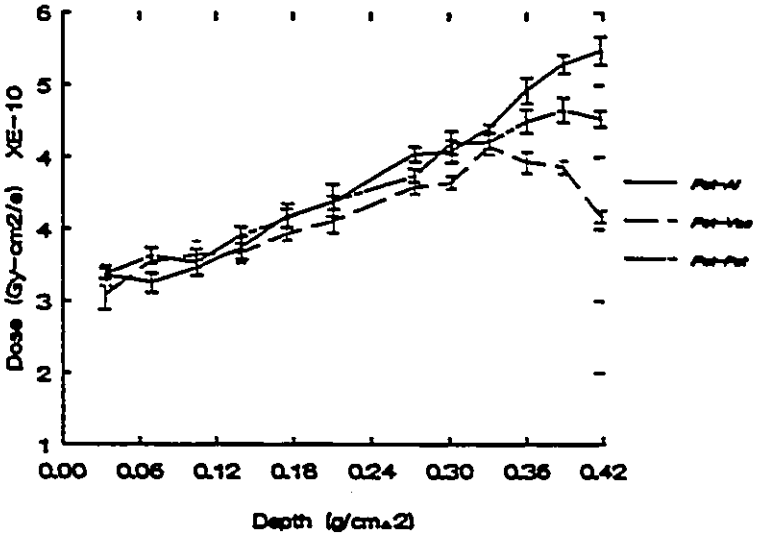

Fig 8.7 Depth-dose profiles in polystyrene slab A for the homogeneous and two heterogeneous cases, as determined using Cyltran.

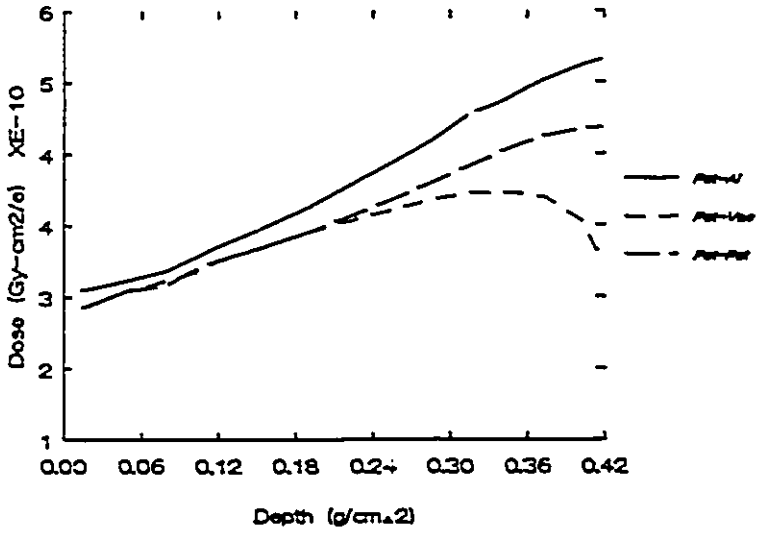

Fig 8.8 Depth-dose profiles in polystyrene slab A for the homogeneous and two heterogeneous cases, as determined experimentally.

Table 8.1 summarizes the dose backscatter factors derived from experimental and Monte Carlo data. A 6% uncertainty in the experimental data is used since the stopping power ratio error is not relevant in this situation where the film is considered equivalent to polystyrene with regard to its dosimetric properties (Eisen et al 1972).

Table 8.1 Backscatter factors determined from Eisen experimental data and from Monte Carlo data.

Backscatterer:	Aluminium			None (Vacuum)		
	Backscatter Factors, %B [uncertainty]					
Depth in Slab A (g/cm^2)	EGS4/ Dosrz	Cyltran	Expt	EGS4/ Dosrz	Cyltran	Expt
0.418*	16.8 [1.9]	16.7 [4.2]	17 [10]	-22.6 [1.1]	-23.5 [2.2]	-33 [6]
0.403			16 [10]			-23 [7]
0.389	11.4 [2.4]	10.9 [4.0]		-13.0 [1.9]	-13.4 [3.1]	
0.374			14.5 [9.7]			-16 [7]
0.360	11.8 [2.3]	7.3 [4.6]		-6.9 [1.7]	-9.9 [3.8]	

* *this is at the interface; depths are measured from the point at which the beam is incident on slab A.*

Seltzer and Berger (Seltzer and Berger 1987) state that their Monte Carlo calculations agree with the Eisen experimental data "to within the accuracy of the experiment". Although they do not address the vacuum interface, this statement describes the nature of the present comparison also. One is only justified in concluding that a definitive comparison cannot be realized because of the relatively large experimental uncertainties.

8.3 Relaxation Lengths

Relaxation lengths, as defined in Chapter 4, were obtained from the Eisen experimental and EGS4/Dosrz backscatter factor depth profiles. For this, the experimental data were normalized, at the incident face, to the value for the case of the aluminium backing material.

Relaxation lengths are 136[16]mg/cm^2 and 155[18]mg/cm^2 for the aluminium backscatterer, for EGS4/Dosrz and the experiment, respectively. Their agreement is marginal and is considerably better than that for the vacuum case, for which corresponding relaxation lengths are 47[4]mg/cm^2 and 84[4]mg/cm^2. The bracketed quantities are uncertainties.

Although Monte Carlo and experimental relaxation lengths differ, they exhibit similar trends. That is, they both indicate that the fall-off of backscatter factor with distance from the interface is faster when there is no backscatterer, as compared to when aluminium is the backing material. Specifically, EGS4/Dosrz data suggest that the decline is roughly twice as fast for vacuum than for aluminium.

This was not observed in the experiments done with beta sources in this work (Chapter 4), where relaxation lengths were found to be 174[6]mg/cm^2 for an aluminium/Mylar interface, and 33[4]mg/cm^2 and 213[5]mg/cm^2 for an air/Mylar interface using a point source. Corresponding values for a distributed beta source were 238[11]mg/cm^2, and 88[24]mg/cm^2 and 294[138]mg/cm^2.

The similarities between relaxation lengths from the Eisen experimental data and from the present experimental work are interesting. However, there are significant differences between the two experiments. A major one is source geometry. The Eisen experiment uses a broad parallel electron beam whereas isotropic sources are used in this work. In addition, a beta radionuclide, ^{32}P, is used in the latter while 2MeV electrons are used in the former. Source positions in relation to the interface also differ. Beta sources in the ASD experimental geometry are at the interface, while the electron beam is filtered by about 400mg/cm^2 of

polystyrene before encountering the backscatterer. Direct comparison of relaxation lengths from these two experiments is consequently tenuous.

CHAPTER 9

CONCLUSIONS

9.1 Beta Dose Point Kernels

The beta dose point kernel for a radionuclide is the spatial dose distribution produced by a unit activity point source of that nuclide. It is used in determining the spatial dose distribution resulting from a non-uniformly distributed source - the source or activity distribution is convolved with the beta dose point kernel.

Beta dose point kernels have been calculated for various radionuclides in an infinite water medium (Prestwich et al 1989; Simpkin and Mackie 1990; Cross et al 1982). The methods used in the first two references include the effects of energy-loss straggling in electron transport whereas the less accurate CSDA model is used in the last reference, as noted in Chapter 1. A beta dose point kernel is determined by summing monoenergetic dose point kernels which are weighted according to the energy spectrum of the beta radionuclide under consideration.

Experiments done in this work, Chapter 4, ascertained the variation of backscatter factor with distance from several material interfaces. The backscatter factor is a measure of how the dose to a soft-tissue equivalent medium changes when this homogeneous medium is replaced by two dissimilar media, one soft-tissue equivalent and one not.

It is therefore possible that a homogeneous medium beta dose point kernel can be modified by a backscatter factor in order to determine doses near boundaries. The following is an example to illustrate the potential applicability of this concept. The dosimetry of skin surface contamination by "hot spots" of ^{32}P is considered. Geometrical differences between the experiment and isotropic beta dose point kernels are ignored at present.

The homogeneous dose point kernel for ^{32}P is represented by $F_H(t)$, where t is the distance from the source. The variation of backscatter factor with distance from the skin/air interface where the source is located is given by $\bar{B}(t)$, which is the double exponential analytical representation determined in Chapter 4 for the ASD point source air interface geometry. Then, the modified dose point kernel for this heterogeneous situation is given by $F_I(t)$, where

$$F_I(t) = \bar{B}(t) \cdot F_H(t) \quad .$$

Convolution of $F_I(t)$ with the activity distribution on the skin surface gives an estimate of the dose as a function of distance into the skin.

This concept can be similarly applied to the other cases mentioned in Chapter 1. It may therefore play a role in the macrodosimetry involved in radioimmunotherapy.

9.2 Summary

The objectives of this work were elucidated in Section 1.2. In brief, they were as follows -

(i) to produce experimental data which could be used to test numerical and analytical boundary beta dosimetry calculations;

(ii) to provide information of potential relevance to "hot particle" dosimetry and the dosimetry associated with radioimmunotherapy;

(iii) to investigate the variation of dose perturbation with distance from boundaries; and

(iv) to resolve discrepancies between experimental and Monte Carlo results pertaining to air interfaces that were noted in another work.

The extent to which these goals have been realized is summarized next.

Air interface discrepancies similar to those discussed by Yu (Yu 1989) were

not found in the comparison between Monte Carlo and experimental results in this work. As discussed in Section 7.3, reasons for the discrepancy noted by Yu are not known.

The variations of dose backscatter factor with distance from interfaces were investigated. Two geometries were considered; one dealt with the variations of backscatter factor with increasing distance from interfaces where sources were fixed (ASD geometry); the other determined the variations of backscatter factor with increasing source and interface separation (ASB geometry).

The variations were found to be adequately described by sums of exponentials. Parameters of these analytical representations for the material and source geometries considered were therefore determined. In particular, relaxation lengths, which quantitate the rate of decrease of dose perturbation with distance from an interface, were parameters frequently used to characterize these variations.

Furthermore, the potential applicability of these backscatter factor depth profiles was indicated in Section 9.1. With regard to radioimmunotherapy, their role is likely to be limited to the dosimetry done to roughly quantitate the "tumour versus healthy tissue" dose. Microdosimetry is required in order to assess the efficacy of radioimmunotherapy as a clinically viable cancer treatment (Humm and Cobb 1990).

Experiments done in this work quantified the changes in absorbed dose in a soft-tissue equivalent medium due to the introduction of a non-soft-tissue equivalent medium using simple and well-specified geometry. Moreover, the experimental uncertainties were sufficiently small so that definitive comparison with calculated data was achieved. For these reasons, the experimental results are considered benchmark data.

The Monte Carlo codes, EGS4/Dosrz and Cyltran, were found to compare satisfactorily with experimental ^{32}P backscatter factor results for the interfaces addressed, as described in Chapter 5.

Beta dose backscatter factors from Cyltran for bismuth/soft-tissue

equivalent interfaces agree slightly better with experimental values than do those from EGS4/Dosrz. A generalization of this statement to all high atomic number scatterers is possible, but cannot be based on the small sample studied in this work.

The "One-Group" theory (O'Brien et al 1964) predicts beta dose backscatter factors which agree with experimental results to within about 20%. However, the assumption of a single, constant source energy limits the accuracy of this theory. The "Two-Group" method (Radzievsky and Komarov 1982) deals with depth-dose profiles with regard to boundary beta dosimetry. Despite this, backscatter factor depth profiles determined using this method differ markedly from comparable experimental profiles.

9.3 Future Work

The discrepancies between Monte Carlo and experimental results at air interfaces noted in the work of Yu (Yu 1989), where thermoluminescent dosimeters were used, warrant further investigation.

Also, differences between the two codes noted in Chapters 5 and 7, such as the preferential performance of Cyltran at bismuth interfaces, should be considered.

Experimental work to determine the effect of source energy on beta dose backscatter factor could be investigated. Other radionuclides such as ^{204}Tl, ^{147}Pm, ^{90}Y are possible candidates. This information would be useful dosimetric data; for example, it could be used to determine whether the performance of the "One-Group" method depends on source energy.

There is a need for work in analytical boundary beta dosimetry. Perhaps the "Two-Group" method can be altered to improve its behaviour at large distances from the interface. Experimental data could be used to determine parameters of such a new empirical model.

In addition, the concept of a modified point kernel, suggested in Section 9.1, could be developed. The Monte Carlo method would be a useful tool in such

an undertaking. It might also be worthwhile to calculate monoenergetic dose point kernels for soft-tissue equivalent media other than water in order to quantitate variations among these materials since, as seen in this work, there are small but measurable differences between Mylar, lucite and Shonka plastic.

APPENDIX A

SOURCES FOR SOME EXPERIMENTAL MATERIALS

Material	*Source*
Aquadag	Acheson Colloids (Canada) Ltd Brantford, Ontario N3T 5P9 (519-752-5461)
Electrometer Keithley, model 614	Keithley Instruments, Inc 28775 Aurora Road Cleveland, Ohio 44139
Mylar, ~0.35mg/cm^2	Steinerfilm, Inc 987 Simonds Road Williamstown, MA 01267
Mylar, 1/2 thou	Day International (Canada) Ltd Cadillac Plastic Division 91 Kelfield Street Rexdale, Ontario M9W 5A4 (416-249-8311)
Myar, 14 thou, 1 thou	Warehoused Plastic Sales, Inc 13 Blackburn Street Toronto, Ontario M4M 2B3

Phosphorus-32	NEN DuPont Canada. Inc Medical Products Department Biotechnology Division Wilmington, DE 19898 *ordered via* NEN DuPont Canada. Inc Biotechnology Systems 7070 Mississauga Road Box 2200 - Streetsville Mississauga L5M 2H3
Repeating Dispenser and Microlitre Syringe	(*ordered via* Fischer Scientific. Inc from) Hamilton Company P.O.Box 10030. Reno Nevada 89520-0012
Shonka plastic	Exradin 1950 University Lane Lisle. Illinois 60532 (708-968-5666)

APPENDIX B

COMPUTER PROGRAMME FOR DATA ACQUISITION AND ANALYSIS

```
20 REM ----- written by Kenrick Chin
30 REM -----  version 1.00, 10 Jan 1999
32 REM --- edited 99-07-31
33 REM --- for aluminium and absorber backscatter measurements
34 DIM XMEAN(8),VAR(8),Y(8),SUM(2),SQ(2),DATI100:,VPN(2),AVPS(2)
35 DIM A(1000)
36 DIM PROGZ(40)
37 DIM SSQ(2)
40 DATA &H8B55,&H83EC,&H06CS,&H7E8B,&HEE00,&H0020,&H80A6,&HF574
42 DATA &HDE83,&H0F24,&HD88A,&H0439,&HE800,&H0010,&H80A6,&HF075
44 DATA &H18E8,&H4900,&HF375,&H1DB9,&HCA5D,&H0002,&H06BA,&HEC03
46 DATA &H02A6,&HF874,&H05BA,&HEC03,&H8F24,&HD1CD.&H83E3,&HD1D1
48 DATA &HD1E3,&H03E3,&HB4DA,&H0300,&HC3B3,&H0000,&H0000,&H0000
50 FOR I = 1 TO 40
51   READ PROGZ(I)
52 NEXT I
60 PORTC = &H306
61 CONTROL = PORTC + 1
64 OUT CONTROL,151
65 OUT PORTC,16
90 KEY OFF
100 REM --- INITIALIZE ---
150 V$="a:"
160 D$="a.dat"
165 E$="b.dat"
170 LINE INPUT "filename? ";C$
190 B$=V$+C$+D$
195 F$=V$+C$+E$
201 OPEN B$ FOR OUTPUT AS #1
205 OPEN F$ FOR OUTPUT AS #2
240  FOR I=1 TO 8
250   PRINT "current position no is" I
260   INPUT "current position number?"; IOJ
270   IF (I=IOJ) THEN GOTO 274 ELSE PRINT "wrong position number" : GOTO 999
274   FOR L=1 TO 2
275    INPUT "1 for pos polarity, 2 for negative?"; M
280   SUM(M)=0!
290   SQ(M)=0!
295   FOR KM=1 TO 250!
297   NEXT KM
```

```
300  FOR J=1 TO 100
310   GOSUB 5000
320   DAT(J)=IDAT/100*
330   SUM(M)=SUM(M)+DAT(J)
340   SQ(M)= SQ(M)+DAT(J)^2
350  NEXT J
360  AVPN(M)=SUM(M)/100*
362 SSQ(M)=0*
365 FOR JV=1 TO 100
367  SSQ(M)=SSQ(M)+(DAT(JV)-AVPN(M))^2
369 NEXT JV
370 VPN(M)=SSQ(M)/99*
375 PRINT AVPN(M),VPN(M)
376  PRINT#2, AVPN(M),VPN(M)
378 TWOSIG=2*ISQR(VPN(M))
380 FOR MM=1 TO 100
382  IF (ABS(DAT(MM)-AVPN(M))>TWOSIG) THEN PRINT "data more than 2 stddevs away from mean" DAT(MM)
384 NEXT MM
385  NEXT L
386  IMEAN(I)=(AVPN(1)+AVPN(2))/2*
390  VAR(I)=(VPN(1)+VPN(2))/4*
395  PRINT #1,IMEAN(I),VAR(I)
396  Y(I)=1*/VAR(I)
400  TWOSID=2*ISQR(VAR(I))
440  PRINT "next position is" I+1
450 NEXT I
455 REM --- variance in distribs,not in means. There is a factor of
456 REM ---  100 on the loose and this is taken care of later.
460 UPSCT=IMEAN(1)*Y(1)+IMEAN(4)*Y(4)+IMEAN(5)*Y(5)+IMEAN(8)*Y(8)
470 LWSCT=Y(1)+Y(4)+Y(5)+Y(8)
480 UPTISS=IMEAN(2)*Y(2)+IMEAN(3)*Y(3)+IMEAN(6)*Y(6)+IMEAN(7)*Y(7)
490 LWTISS=Y(2)+Y(3)+Y(6)+Y(7)
500 WMWSCT=UPSCT/LWSCT
510 WMWTIS=UPTISS/LWTISS
520 UWCSCT=SQR(1*/(LWSCT*100*))
530 UWCTIS=SQR(1*/(LWTISS*100*))
540 CHISQ=(IMEAN(1)-WMWSCT)^2/(VAR(1)/100*)+(IMEAN(4)-WMWSCT)^2/(VAR(2)/100*)+(IMEAN(5)-WMWSCT)^2/(VAR(5)/100*)+(IMEAN(8)-WMWSCT)^2
/(VAR(8)/100*)
550 CHI=(IMEAN(2)-WMWTIS)^2/(VAR(2)/100*)+(IMEAN(3)-WMWTIS)^2/(VAR(3)/100*)+(IMEAN(6)-WMWTIS)^2/(VAR(5)/100*)+(IMEAN(7)-WMWTIS)^2/(
VAR(7)/100*)
560 DF=3*
570 RTCHSQ=SQR(CHISQ/DF)
580 RTCHI=SQR(CHI/DF)
590 IF (CHISQ<DF) THEN ERRSCT=UWCSCT ELSE ERRSCT=UWCSCT*RTCHSQ
600 IF (CHI<DF) THEN ERRTIS=UWCTIS ELSE ERRTIS=UWCTIS*RTCHI
```

```
610  PRINT WMNSCT,WMNTIS
620  PRINT #1,WMNSCT,ERRSCT
630  PRINT #1,CHISQ
640  PRINT #1,WMNTIS,ERRTIS
650  PRINT #1,CHI
660  PRINT #2,WMNSCT,ERRSCT,CHISQ
670  PRINT #2,WMNTIS,ERRTIS,CHI
710  RATIO=WMNSCT/WMNTIS
720  UNCRAT=SQR((ERRSCT/WMNSCT)^2+(ERRTIS/WMNTIS)^2)*RATIO
730  PERRAT=(RATIO-1!)*100!
740  UNCPER=UNCRAT*100!
750  PRINT #1, RATIO,UNCRAT,PERRAT,UNCPER
760  PRINT PERRAT,UNCPER
770  CLOSE#1
780  CLOSE#2
999 STOP
5000 REM --- GET DATA FROM ELECTROMETER
5100 GETTLDZ = VARPTR(PROGZ(1)) : CALL GETTLDZ(XZ)
5105 XDAT = XZ
5140 RETURN
```

APPENDIX C

DEPENDENCE OF BACKSCATTER FACTOR ON CHAMBER THICKNESS

C.1 Details of the ANOVA

```
10 REM --- one way ANOVAs
20 REM --- 90-12-17
30 LINE INPUT "file name,with extension?"; A$
40 B$="a:"
50 C$=B$+A$
60 OPEN C$ FOR OUTPUT AS #1
70 INPUT "no. of interfaces?"; L
80 FOR J=1 TO L
90   LINE INPUT "name of interface?"; BD$
100  WRITE#1,BD$
110   INPUT "no of turns?"; K
120   TOT=0
130   SSQT=0
140   SSQG=0
150   N=0
160   FOR I=1 TO K
162     INPUT "chamber thickness?"; MCI
170    PRINT "this is turn no ", MCI
180    INPUT "no of values?"; NI
190    N=N+NI
200    Sum=0
210    FOR M=1 TO NI
220     INPUT "backscatter factor"; B
230     TOT=TOT+B
240     SSQT=SSQT+B^2
250     Sum=Sum+B
260     WRITE#1,MCI,B
270    NEXT M
280    SSQG=SSQG+Sum^2/NI
290    NEXT I
300    C=TOT^2/N
310    TSS=SSQT-C
320    AGSS=SSQG-C
330    WGSS=TSS-AGSS
340    GDF=K-1
350    EDF=N-K
360    WRITE#1,TSS,AGSS,WGSS,GDF,EDF
370    AGMS=AGSS/GDF
380    WGMS=WGSS/EDF
390    F=AGMS/WGMS
400    WRITE#1,"among grp mean sq is",AGMS
410    WRITE#1,"within grp mean sq is",WGMS
420    WRITE#1,"F is ", F
430  NEXT J
440 STOP
450 END
```

$F_{critical}$, that is, $F_{\alpha(1)=0.05,\nu_1=k-1,\nu_2=N-k}$, is looked up in statistical tables. The null hypothesis is rejected if $F > F_{critical}$. k = number of turns of the chamber; N = the number of values; ν_1 = numerator degrees of freedom; and ν_2 = denominator degrees of freedom.

The critical F values used for the appropriate numbers of degrees of freedom which depend on the number of turns (k) and on the total number of values in the set (N) are as follows -:

Numerator Degrees of Freedom, ν_1	Denominator Degrees of Freedom ν_2	$F_{critical}$
3	4	6.59
2	3	9.55
3	9	3.86
3	5	5.41

Checkmarks on the following pages of data indicate that the null hypothesis cannot be rejected. The null hypothesis is that the backscatter factor is independent of number of turns of the chamber.

The leading integer in the data sets is the chamber thickness or inter-electrode spacing, in mm or number of turns. The subsequent number is the measured backscatter factor, %B.

C.2 Zeroeth, Thick Window Data for ^{32}P Point Source

```
"al"    aluminium/lucite ✓
1,10.71
1,10.86
2,10.28
2,10.35
3,11.01
3,10.93
4,11.24
4,10.78
.7324219,.6098633,.1225586,3,4
"among grp mean sq is",.2032878
"within grp mean sq is",3.063965E-02
"F is ",6.634794
"nl"    air/lucite ✓
1,-22.08
1,-21.79
3,-21.21
3,-21.27
4,-21.89
4,-21.04
2,-21.54
2,-21.55
.907959,.5026856,.4052735,3,4
"among grp mean sq is",.1675619
"within grp mean sq is",.101318
"F is ",1.653815
"am"    aluminium/Mylar ✓
1,7.31
1,7.25
1,8.45
1,8.33
2,7.78
2,7.71
3,8.07
3,8.17
4,7.7
4,7.68
4,7.75
4,7.84
4,7.85
1.476929,.2038574,1.273071,3,9
"among grp mean sq is",6.795248E-02
"within grp mean sq is",.1414524
"F is ",.4803912
```

```
"nm"    air/Mylar
1,-24.01
1,-23.61
2,-23.62
2,-23.53
3,-23.29
3,-23.21
4,-24.24
4,-24.02
.9404297,.8291016,.1113281,3,4
"among grp mean sq is",.2763672
"within grp mean sq is",2.783203E-02
"F is ",9.929825
"as"    aluminium/A-150plastic ✓
1,12.47
1,12.38
1,11.23
2,11.44
2,11.54
3,11.53
3,11.69
4,11.8
4,11.8
1.380859,.4068604,.973999,3,5
"among grp mean sq is",.1356201
"within grp mean sq is",.1947998
"F is ",.6962025
"ns"    air/A-150plastic ✓
1,-21.36
1,-20.75
2,-20.83
2,-20.56
3,-20.78
3,-20.72
4,-21.24
4,-20.67
.5590821,.1726074,.3864746,3,4
"among grp mean sq is",5.753581E-02
"within grp mean sq is",9.661865E-02
"F is ",.5954938
```

```
"bt"    cortical bone/soft-tissue ✓
1,9.859999
1,9.49
1,8.04
2.5,8.62
2.5,8.270001
4,8.399999
4,8.21
2.926697,.9967651,1.929932,2,4
"among grp mean sq is",.4983826
"within grp mean sq is",.4824829
"F is ",1.032954
"at"    air/soft-tissue ✓
1,-20.17
1,-20.2
2.5,-20.27
2.5,-20.23
4,-20.75
4,-20.19
.2470703,8.911133E-02,.157959,2,3
"among grp mean sq is",4.455567E-02
"within grp mean sq is",.052653
"F is ",.8462132
"cl"    copper/lucite ✓
1,24.92
1,22.65
2.5,23.56
2.5,23.66
4,24.38
4,24.23
3.115235,.5229492,2.592285,2,3
"among grp mean sq is",.2614746
"within grp mean sq is",.8640951
"F is ",.3025994
```

```
"cm"    copper/Mylar ✓
1,22.02
1,19.71
2.5,20.48
2.5,20.17
4,21.12
4,20.86
3.249512,.4997559,2.749756,2,3
"among grp mean sq is",.2498779
"within grp mean sq is",.9165852
"F is ",.2726183
"dl"    cadmium/lucite ✓
1,33.25
1,29.41
2.5,30.61
2.5,31
4,32.68
4,32.38
10.62012,3.126465,7.493653,2,3
"among grp mean sq is",1.563232
"within grp mean sq is",2.497884
"F is ",.6258227
"dm"    cadmium/Mylar ✓
1,30.25
1,26.25
2.5,27.34
2.5,27.64
4,28.88
4,28.39
9.522949,1.357422,8.165528,2,3
"among grp mean sq is",.678711
"within grp mean sq is",2.721843
"F is ",.2493572
```

```
"wl"    tungsten/lucite ✓
1,41.82
1,37.7
2.5,39.06
2.5,39.49
4,40.37
4,40.79
10.4082,1.740234,8.667969,2,3
"among grp mean sq is",.8701172
"within grp mean sq is",2.889323
"F is ",.3011492
"wm"    tungsten/Mylar ✓
1,39.04
1,32.97
2.5,36.29
2.5,34.5
4,36.93
4,36.88
22.3335,2.307129,20.02637,2,3
"among grp mean sq is",1.153565
"within grp mean sq is",6.675456
"F is ",.1728069
"zl"    bismuth/lucite
1,39.71
1,39.92
2.5,41.26
2.5,41.24
4,42.44
4,41.85
5.720703,5.523438,.1972656,2,3
"among grp mean sq is",2.761719
"within grp mean sq is",6.575521E-02
"F is ",42
```

```
"zm"    bismuth/Mylar
1,36.02
1,36.41
2.5,37.68
2.5,37.72
4,38.47
4,38.45
5.291992,5.214844,7.714844E-02,2,3
"among grp mean sq is",2.607422
"within grp mean sq is",2.571615E-02
"F is ",101.3924
"rl"    carbon/lucite ✓
1,-1.39
1,-.765
2.5,-.11
2.5,-.58
4,-.32
4,-.59
.9663212,.5241088,.3422125,2,3
"among grp mean sq is",.3120544
"within grp mean sq is",.1140708
"F is ",2.73562
"rm"    carbon/Mylar ✓
1,-3.41
1,-4.11
2.5,-2.75
2.5,-3.37
4,-2.9
4,-3.01
1.209274,.7660294,.443245,2,3
"among grp mean sq is",.3830147
"within grp mean sq is",.1477483
"F is ",2.592346
```

C.3 Zeroeth, Thin Window Data for ^{32}P Point Source

```
"zm"    bismuth/Mylar
4,33.77
4,33.71
3,32.74
3,32.71
2,31.8
2,31.71
1,30.74
1,30.37
11.17578,11.09961,7.617188E-02,3,4
"among grp mean sq is",3.69987
"within grp mean sq is",1.904297E-02
"F is ",194.2906
"zl"    bismuth/lucite
4,37.29
4,37.91
3,37.3
3,37.18
2,36.51
2,36.53
1,34.06
1,35.105
11.61328,10.86524,.7480469,3,4
"among grp mean sq is",3.621745
"within grp mean sq is",.1870117
"F is ",19.36641
"wm"    tungsten/Mylar
4,30.07
4,33.47
3,33.35
3,31.68
2,32.86
2,31.33
1,31.59
1,31.69
9.262696,.9130859,8.34961,3,4
"among grp mean sq is",.304362
"within grp mean sq is",2.087402
"F is ",.145809
```

```
"wl"    tungsten/lucite
4,34.53
4,37.94
3,38.52
3,36.55
2,36.75
2,36.62
1,35.6
1,35.27
12.43066,4.613282,7.817383,3,4
"among grp mean sq is",1.53776
"within grp mean sq is",1.954346
"F is ",.7865415
"dm"    cadmium/Mylar
4,22.87
4,23.5
3,22.7
3,22.56
2,21.71
2,21.5
1,20.89
1,19.84
10.01929,9.238037,.78125,3,4
"among grp mean sq is",3.079246
"within grp mean sq is",.1953125
"F is ",15.76625
"dl"    cadmium/lucite
4,26
4,27.3
3,26.87
3,26.65
2,26.11
2,25.93
1,25.72
1,24.54
4.94043,3.358399,1.582031,3,4
"among grp mean sq is",1.119466
"within grp mean sq is",.3955078
"F is ",2.830453
```

```
"cm"     copper/Mylar
4,18.64
4,18.53
3,18.04
3,18.26
2,17.55
2,17.28
1,16.73
1,16.55
4.464112,4.381104,8.300781E-02,3,4
"among grp mean sq is",1.460368
"within grp mean sq is",2.075195E-02
"F is ",70.37255
"cl"     copper/lucite
4,21.75
4,22.08
3,22.11
3,22.11
2,21.79
2,21.83
1,21.02
1,21.02
1.430908,1.376221,.0546875,3,4
"among grp mean sq is",.4587403
"within grp mean sq is",1.367188E-02
"F is ",33.55357
"am"     aluminium/Mylar
4,7.19
4,6.86
3,6.64
3,6.96
2,6.76
2,6.26
1,5.83
1,5.87
1.790711,1.559265,.2314453,3,4
"among grp mean sq is",.5197551
"within grp mean sq is",5.786133E-02
"F is ",8.982771
```

```
"al"     aluminium/lucite
4,10.02
4,10.44
3,10.5
3,10.46
2,10.53
2,10.2
1,9.04
1,9.729999
1.865234,1.483765,.3814697,3,4
"among grp mean sq is",.4945883
"within grp mean sq is",9.536743E-02
"F is ",5.186134
"nm"     air/Mylar
4,-25.23
4,-25.18
3,-25.5
3,-25.36
2,-25.79
2,-25.83
1,-26.13
1,-26.13
1.015625,1.003906,1.171875E-02,3,4
"among grp mean sq is",.3346354
"within grp mean sq is",2.929688E-03
"F is ",114.2222
"nl"     air/lucite
4,-23.26
4,-22.79
3,-22.85
3,-22.8
2,-23.04
2,-23
1,-24.02
1,-23.35
1.18457,.8481446,.3364258,3,4
"among grp mean sq is",.2827149
"within grp mean sq is",8.410644E-02
"F is ",3.361393
```

```
"bt"    cortical bone/soft-tissue
4,7.43
4,8.28
3,8.22
3,8.33
2,7.99
2,8.09
4,7.28
4,7.69
1.12384,.66745,.4563904,3,4
"among grp mean sq is",.2224833
"within grp mean sq is",.1140976
"F is ",1.949939
"nt"    air/soft-tissue
4,-22.16
4,-22.03
3,-22.18
3,-22.14
2,-22.41
2,-22.385
1,-22.95
1,-22.89
.8532715,.842041,1.123047E-02,3,4
"among grp mean sq is",.2806803
"within grp mean sq is",2.807617E-03
"F is ",99.97101
"as"    aluminium/A-150plastic
4,11.71
4,11.27
3,11.26
3,11.5
2,11.09
2,10.86
1,10.31
1,10.405
1.732178,1.575501,.1566773,3,4
"among grp mean sq is",.5251668
"within grp mean sq is",3.916931E-02
"F is ",13.40761
```

```
"ns"    air/A-150plastic
4,-22.4
4,-22.12
3,-22.26
3,-22.29
2,-22.46
2,-22.45
1,-22.93
1,-23.14
.8540039,.7924805,6.152344E-02,3,4
"among grp mean sq is",.2641602
"within grp mean sq is",1.538086E-02
"F is ",17.1746
"ra"    carbon/Mylar
4,-3.2
4,-3.38
3,-3.64
3,-3.5
2,-4.09
2,-4.17
1,-4.05
1,-4
.9583816,.9279251,3.045654E-02,3,4
"among grp mean sq is",.3093084
"within grp mean sq is",7.614136E-03
"F is ",40.62291
```

C.4 Zeroeth, Thin Window Data for ^{32}P Distributed Source

```
"zm"     bismuth/Mylar
4,29.58
4,29.55
3,29.19
3,29.23
2,28.7
2,28.74
1,27.9
1,27.89
3.14209,3.139649,2.441406E-03,3,4
"among grp mean sq is",1.046549
"within grp mean sq is",6.103516E-04
"F is ",1714.667
"zl"     bismuth/lucite
4,31.31
4,31.27
3,30.96
3,30.94
2,30.44
2,30.61
1,29.74
1,29.75
2.680176,2.664551,.015625,3,4
"among grp mean sq is",.8881836
"within grp mean sq is",3.90625E-03
"F is ",227.375
"wm"     tungsten/Mylar
4,29.23
4,28.92
3,28.7
3,28.65
2,28.44
2,28.51
1,28.02
1,27.8
1.486816,1.410156,7.666016E-02,3,4
"among grp mean sq is",.4700521
"within grp mean sq is",1.916504E-02
"F is ",24.52654
"wl"     tungsten/lucite
4,31
4,30.37
3,30.5
3,30.36
2,30.22
2,30.28
1,29.62
1,29.32
1.902832,1.647949,.2548828,3,4
"among grp mean sq is",.5493165
"within grp mean sq is",6.372071E-02
"F is ",8.620689
"dm"     cadmium/Mylar
4,22.87
4,22.89
3,22.71
3,22.68
2,22.275
2,22.35
1,21.63
1,21.77
1.642334,1.62915,1.318359E-02,3,4
"among grp mean sq is",.5430501
"within grp mean sq is",3.295899E-03
"F is ",164.7654
"dl"     cadmium/lucite
4,24.53
4,24.46
3,24.35
3,24.3
2,24.05
2,24.06
1,23.43
1,23.45
1.289063,1.285645,3.417969E-03,3,4
"among grp mean sq is",.4285482
"within grp mean sq is",8.544922E-04
"F is ",501.5239
```

```
"cm"     copper/Mylar
4,16.82
4,16.68
3,16.625
3,16.6
2,16.41
2,16.34
1,15.99
1,16.04
.6354981,.6215821,1.391602E-02,3,4
"among grp mean sq is",.207194
"within grp mean sq is",3.479004E-03
"F is ",59.55556
"cl"     copper/lucite
4,18.35
4,18.23
3,18.09
3,18.04
2,17.97
2,18
1,17.75
1,17.59
.4165039,.3947754,2.172852E-02,3,4
"among grp mean sq is",.1315918
"within grp mean sq is",5.432129E-03
"F is ",24.22472
"am"     aluminium/Mylar
4,6.87
4,6.83
3,6.71
3,6.78
2,6.63
2,6.66
1,6.52
1,6.44
1,6.49
.1876526,.1806946,6.958008E-03,3,5
"among grp mean sq is",6.023153E-02
"within grp mean sq is",1.391602E-03
"F is ",43.28217
```

```
"al"     aluminium/lucite
4,8.270001
4,8.270001
3,8.21
3,8.19
2,8.140001
2,8.16
1,7.97
1,8.01
8.618164E-02,.0848999,1.281738E-03,3
"among grp mean sq is",2.829997E-02
"within grp mean sq is",3.204346E-04
"F is ",88.31746
"nm"     air/Mylar
4,-27.32
4,-27.21
3,-27.4
3,-27.43
2,-27.68
2,-27.7
1,-28.01
1,-28.08
.713379,.7045899,8.789062E-03,3,4
"among grp mean sq is",.2348633
"within grp mean sq is",2.197266E-03
"F is ",106.8889
"nl"     air/lucite
4,-26.37
4,-26.31
3,-26.43
3,-26.5
2,-26.65
2,-26.65
1,-26.99
1,-27.02
.5078125,.5029297,4.882813E-03,3,4
"among grp mean sq is",.1676432
"within grp mean sq is",1.220703E-03
"F is ",137.3333
```

```
"bt"    cortical bone/soft-tissue ✓
4,6.295
4,6.38
3,6.18
3,6.34
2,6.23
2,5.98
1,6.24
1,5.97
.1652222,6.111573E-02,8.410644E-02,3,4
"among grp mean sq is",2.703858E-02
"within grp mean sq is",2.102661E-02
"F is ",1.285922
"nt"    air/soft-tissue
4,-25.59
4,-25.62
3,-25.66
3,-25.67
2,-25.95
2,-25.95
1,-26.19
1,-26.16
.4213867,.4199219,1.464844E-03,3,4
"among grp mean sq is",.139974
"within grp mean sq is",3.66211E-04
"F is ",382.2222
"as"    aluminium/A-150plastic ✓
4,8.92
4,8.810001
3,8.890001
3,8.84
2,8.76
2,8.84
1,8.810001
1,8.62
5.877686E-02,.0302124,2.856445E-02,3,4
"among grp mean sq is",.0100708
"within grp mean sq is",7.141114E-03
"F is ",1.410256
```

```
"ns"    air/A-150plastic
4,-25.91
4,-25.92
3,-26
3,-25.99
2,-26.21
2,-26.21
1,-26.55
1,-26.56
.4916992,.491211,4.882813E-04,3,4
"among grp mean sq is",.163737
"within grp mean sq is",1.220703E-04
"F is ",1341.333
"ra"    carbon/Mylar
4,-1.56
4,-1.57
3,-1.59
3,-1.61
2,-1.99
2,-1.88
1,-2.06
1,-2.285
.5333958,.5017834,.0316124,3,4
"among grp mean sq is",.1672611
"within grp mean sq is",7.903099E-03
"F is ",21.16399
```

APPENDIX D

ESTIMATION OF SHOT NOISE

Interaction of radiation with the inter-electrode air in the ionization chamber causes the creation of ion pairs, that is, electrons and positively charged ions. By applying a potential across the electrodes, these ion pairs are collected during a certain time and therefore the ionization current can be measured.

Radioactive decay and the interaction of radiation with matter are random processes which are describable by Poisson statistics. The creation of ion pairs may also be treated using Poisson statistics. In this estimation therefore, the uncertainty associated with the number of ion pairs, N, namely, the shot noise, is given by $\sqrt{N}$.

The number of ion pairs, N, which gives rise to a particular ionization current, I, is determined as follows. The charge, Q, collected during time τ, is given by $Q = I\tau$. τ is obtained from particulars of the electrometer; the time, t, required for the current to settle to 1% of its final value is 600ms. Assuming an exponential decrease in the current - $0.01 = e^{-t/\tau}$ - τ is found to be about 130ms. For a typical current of 50pA, $Q = 6.5 \times 10^{-12}$ C. The number of ion pairs $N = Q / 1.602 \times 10^{-19}$ C $\approx 4 \times 10^{7}$. Therefore, the relative or fractional uncertainty, or shot noise, is $1/\sqrt{N} \approx 1.6 \times 10^{-4}$, or about 0.02%.

REFERENCE LIST

Andreo, P. 1988. Electron Pencil-Beam Calculations. Chap 20 In *Monte Carlo Transport of Electrons and Photons.* eds. T. M. Jenkins, W. R. Nelson and A. Rindi. New York: Plenum Press.

Arfken, G. 1985. *Mathematical Methods for Physicists.* Toronto: Academic Press, Inc.

Attix, F. H. 1986. *Introduction to Radiological Physics and Radiation Dosimetry.* Toronto: John-Wiley and Sons, Inc.

Baily, N. A. 1980. Electron Backscattering. *Medical Physics 7(5): 514-519.*

Berger, M. J. 1973. *Improved Point Kernels for Electron and Beta-Ray Dosimetry.* NBSIR73-107. National Bureau of Standards, Washington DC 20234.

Berger, M. J. 1963. Monte Carlo Calculations of the Penetration and Diffusion of Fast Charged Particles. Chap In *Methods in Computational Physics* eds. B. Alder, S. Fernbach and M. Rotenberg. New York: Academic Press. pp: 135-215.

Berger, M. J. and S. M. Seltzer. 1983. *Stopping Powers and Ranges of Electrons and Positrons.* 2nd ed. NBSIR82-2550-A. U. S. Department of Commerce, National Bureau of Standards, Washington, D. C. 20234. December 1982.

Berger, M. J. and S. M. Seltzer. 1968. *ETRAN Monte Carlo Code System for Electron and Photon Transport Through Extended Media.* CCC-107. Radiation Shielding Information Centre, Oak Ridge National Lab.

Berger, M. J. and R. Wang. 1988. Multiple-Scattering Angular Deflections and Energy-Loss Straggling. Chap 2 In *Monte Carlo Transport of Electrons and Photons* eds. T. M. Jenkins, W. R. Nelson and A. Rindi. New York: Plenum Press.

Bethe, H. A. 1953. Molière's Theory of Multiple Scattering. *Physical Review 89(6): 1256-1266.*

Bielajew, A. F. 1991. private communication.

Bielajew, A. F. and D. W. O. Rogers. 1987. PRESTA: The Parameter Reduced Electron-Step Transport Algorithm for Electron Monte Carlo Transport. *Nuclear Instruments and Methods in Physics Research B18: 165-181.*

Birkhoff, R. D. 1958. The Passage of Fast Electrons Through Matter. Chap In *Encyclopedia of Physics, Vol 34 - Corpuscles and Radiation In Matter II* ed. S. Flügge. Berlin: Springer-Verlag. pp: 53-138.

Boag, J. W. 1964. Ionization Dosimetry at High Intensity. Chap In *Proceedings of the International School of Physics <<Enrico Fermi>>, Course XXX, Radiation Dosimetry* ed. G. W. Reed. 5th - 17th Aug, 1963. Vienna on Lake Como, Villa Monastero. New York: Academic Press.

Boag, J. W. 1963. Space Charge Distortion of the Electric Field in a Plane-Parallel Ionization Chamber. *Physics in Medicine and Biology 8(4): 461-467.*

Braden, C. H., G. E. Owen, J. Townsend, C. S. Cook and F. B. Shull. 1948. Discrepancies Caused by Source Charging in Beta Spectrometers. (Letter to the Editor) *Physical Review 74(10): 1539-1540.*

Bruivinis, I. A. D., W. A. F. Mathol and P. Andreo. 1989. Inclusion of Electron Range Straggling in the Fermi-Eyges Multiple-Scattering Theory. *Physics in Medicine and Biology 34(4): 491-507.*

Berger, M. J. and R. Wang. 1988. Multiple-Scattering Angular Deflections and Energy-Loss Straggling. Chap 2 In *Monte Carlo Transport of Electrons and Photons* eds. T. M. Jenkins, W. R. Nelson and A. Rindi. New York: Plenum Press.

Bethe, H. A. 1953. Molière's Theory of Multiple Scattering. *Physical Review 89(6): 1256-1266.*

Bielajew, A. F. 1991. private communication.

Bielajew, A. F. and D. W. O. Rogers. 1987. PRESTA: The Parameter Reduced Electron-Step Transport Algorithm for Electron Monte Carlo Transport. *Nuclear Instruments and Methods in Physics Research B18: 165-181.*

Birkhoff, R. D. 1958. The Passage of Fast Electrons Through Matter. Chap In *Encyclopedia of Physics, Vol 34 - Corpuscles and Radiation In Matter II* ed. S. Flügge. Berlin: Springer-Verlag. pp: 53-138.

Boag, J. W. 1964. Ionization Dosimetry at High Intensity. Chap In *Proceedings of the International School of Physics <<Enrico Fermi>>, Course XXX, Radiation Dosimetry* ed. G. W. Reed. 5th - 17th Aug, 1963. Vienna on Lake Como, Villa Monastero. New York: Academic Press.

Boag, J. W. 1963. Space Charge Distortion of the Electric Field in a Plane-Parallel Ionization Chamber. *Physics in Medicine and Biology 8(4): 461-467.*

Braden, C. H., G. E. Owen, J. Townsend, C. S. Cook and F. B. Shull. 1948. Discrepancies Caused by Source Charging in Beta Spectrometers. (Letter to the Editor) *Physical Review 74(10): 1539-1540.*

Bruivinis, I. A. D., W. A. F. Mathol and P. Andreo. 1989. Inclusion of Electron Range Straggling in the Fermi-Eyges Multiple-Scattering Theory. *Physics in Medicine and Biology 34(4): 491-507.*

Carlson, B. G. and K. D. Lathrop. 1968. Transport Theory: The Method of Discrete Ordinates. Chap 3 In *Computing Methods in Reactor Physics.* ed. H. Greenspan, C. N. Kelber and D. Okrent. New York: Gordon and Breach Science Publishers.

Charlton, D. E. 1970. Energy Dissipation Near an Interface: A More Realistic Approach to Electron Range and Stopping Power. *Radiation Research 44: 575-593.*

Clark, R. K., S. S. Brar and L. D. Marinelli. 1955. Ionization of Air by Beta Rays from Point Sources. *Radiology 64: 94-103.*

Cross, W. G., H. Ing, N. O. Freedman and J. Mainville. 1982. *Tables of Beta-Ray Dose Distributions in Water, Air and Other Media.* AECL-7617. Chalk River Nuclear Laboratories, Chalk River, Ontario.

Cross, W. G. 1969. Distribution of Absorbed Beta Energy in Solid Media. *Canadian Journal of Physics 47: 75-83.*

Cross, W. G. 1967. The Distribution of Absorbed Energy from a Point Beta Source. *Canadian Journal of Physics 45: 2021-2039.*

Cross, W. G. 1967a. *Tables of Beta Dose Distributions.* Atomic Energy of Canada Limited Report. AECL-2793.

Dressel, R. W. 1966. Retrofugal Electron flux from Massive Targets Irradiated with a Monoenergetic Primary Beam. *Physical Review 144(1): 332-343.*

Eckelman, W. C., C. H. Paik and R. C. Reba. 1980. Radiolabelling of Antibodies. *Cancer Research 40: 3036-3042.*

Eisen, H. 1990. private communication.

Eisen, H., M. Rosenstein and J. Silverman. 1972. Electron Depth-Dose Distribution Measurements in Two-Layer Slab Absorbers. *Radiation Research 52: 429-447.*

Enge, H. 1966. *Introduction to Nuclear Physics.* Don Mills, Ontario: Addison-Wesley (Canada) Ltd.

Evans, R. D. 1955. *The Atomic Nucleus.* London: McGraw Hill Book Co., Inc.

Everhart, T. E. 1960. Simple Theory Concerning the Reflection of Electrons from Solids. *Journal of Applied Physics 31(8): 1483-1490.*

Eyges, L. 1948. Multiple Scattering with Energy Loss. *Physical Review 74: 1534-1535.*

Failla, G. 1937. The Measurement of Tissue Dose in Terms of the Same Unit for all Ionizing Radiations. *Radiology 29: 202.*

Fano, U. 1954. Principles of Radiological Physics. Chap 1 In *Radiation Biology, Volume 1, Pt 1.* ed. A. Hollaender. New York: McGraw-Hill Book Company, Inc.

Fermi, E. 1940. The Ionization Loss of Energy in Gases and in Condensed Materials. *Physical Review 57: 485-493.*

Ford, R. L. and W. R. Nelson. 1978. *The EGS Code System: Computer Programs for the Monte Carlo Simulation of Electromagnetic Cascade Showers (Version 3).* SLAC-210, Stanford Linear Accelerator Center (June 1978).

French, A. P. 1971. *Newtonian Mechanics.* London: W. W. Norton & Company.

Gasciorowicz, S. 1974. *Quantum Physics.* New York: John Wiley and Sons, Inc.

Goudsmit, S. and J. L. Saunderson. 1940. Multiple Scattering of Electrons. *Physical Review 57: 24-29.*

Halbleib, J. A., T. A. Mehlhorn and R. P. Kensek. 1987. Version 2.1 of ITS, Sandia National Laboratories Memo, Dec 11th, 1987, In *Documentation for CCC-467/ITS 2.1 Code Package, RSIC Computer Code Collection.* Sandia National Laboratories, Albuquerque, New Mexico.

Halbleib, J. A. and T. A. Mehlhorn. 1984. *ITS: The Integrated Tiger Series of Coupled Electron/Photon Monte Carlo Transport Codes.* SAND84-0573, Nov 1984. Radiation Shielding Information Center, Sandia National Laboratories, Albuquerque, New Mexico.

Halbleib, J. A. and W. H. Vandevender. 1976. Computer Code Abstract. *Nuclear Science and Engineering 61: 288-289.*

Harvey, J. R., B. J. MacFarlane, R. G. Shipton and I. M. G. Thompson. 1975. (Letter to the Editor) Conversion of Beta-ray Dose Rates Measured in Air to Dose Rates in Skin. *Physics in Medicine and Biology 20(4): 652-656.*

Hine, G. J. and G. L. Brownell. 1956. *Radiation Dosimetry.* New York: Academic Press.

Humm, J. L. and L. M. Cobb. 1990. Nonuniformity of Tumor Dose in Radioimmunotherapy. *Journal of Nuclear Medicine 31(1): 75-83.*

ICRU 35. 1984. *Radiation Dosimetry: Electron Beams with Energies between 1 and 50 MeV.* International Commission on Radiation Units and Measurements, 7910 Woodmont Ave., Bethesda, Maryland 20814. U.S.A.

Jaszczak, R. J., K. L. Greer and R. E. Coleman. 1985. SPECT Quantification of Regional Radionuclide Distributions. In *Proceedings of the Fourth International Radiopharmaceutical Dosimetry Symposium*, Nov 5-8, Oak Ridge, Tennessee. CONF-851113-(DE86010102). pp: 82-96.

Jette, D., L. H. Lanzl, A. Pagnamenta, M. Rozenfeld, D. Bernard, M. Kao and A. M. Sabbas. 1989. Electron Dose Calculation Using Multiple-Scattering Theory: Thin Planar Inhomogeneities. *Medical Physics 16(5): 712-725.*

Jette, D. and A. F. Bielajew. 1989. Electron Dose Calculation Using Multiple-Scattering Theory: Second Order Multiple-Scattering Theory. *Medical Physics 16(5): 698-725.*

Jette, D. 1988. Electron Dose Calculation Using Multiple-Scattering Theory. A Gaussian Multiple-Scattering Theory. *Medical Physics 15(2): 123-137.*

Jette, D. 1983. The Application of Multiple Scattering Theory to Therapeutic Electron Dosimetry. *Medical Physics 10(2): 141-146.*

Jordan, T. M. 1986. Adjoint Electron Monte Carlo Calculations. *Transactions of the American Nuclear Society 52: 382-383.*

Katz, L. and A. S. Penfold. 1952. Range-Energy Relations for Electrons and the Determination of Beta-Ray End-Point Energies by Absorption. *Reviews of Modern Physics 24(1): 28-44.*

Köhler, G. and C. Milstein. 1975. Continuous Cultures of Fused Cells Secreting Antibody of Predicted Specificity. *Nature 256: 495-497.*

Kovarik, A. F. 1910. Absorption and Reflexion of the ß-Particles by Matter. *Philosophical Magazine, 6th series, 20: 849-866.*

Kwok, C. S., P. J. Bialobzyski, S. Yu and W. V. Prestwich. 1990. Effect of Tissue Inhomogeneity on Dose Distribution of Point Sources of Low-Energy Electrons. *Medical Physics 17(5): 786-793.*

Kwok, C. S., M. Irfan, M. K. Woo and W. V. Prestwich. 1987. Effect of Tissue Inhomogeneity on Beta Dose Distribution of ^{32}P. *Medical Physics 14(1): 98-104.*

Kwok, C. S., M. Irfan, M. K. Woo and W. V. Prestwich. 1986. Effect of Tissue Inhomogeneity on Beta Dose Calculation. In *Proceedings of the Fourth International Radiopharmaceutical Dosimetry Symposium.* Nov 5-8. Oak Ridge, Tennessee. CONF-851113-(DE86010102). pp: 562-573.

Landau, L. 1944. On the Energy Loss of Fast Charged Particles by Ionization. *Journal of Physics 8(4): 201-205.*

Landau, L. D. and E. M. Lifshitz. 1976. *Quantum Mechanics. Non-Relativistic Theory.* New York: Permagon Press.

Larson, S. M., J. A. Carrasquillo, J. C. Reynolds, I. Hellstrom, K. E. Hellstrom, J. C. Mulshine and L. E. Matis. 1986. Therapeutic Applications of Radiolabelled Antibodies: Current Situations and Prospects. *Nuclear Medicine and Biology 13(2): 207-213.*

Leichner, P. 1986. SPECT in the Quantitative Imaging of Radiolabelled Antibodies. In *Proceedings of the American College of Nuclear Physicians and the Society of Nuclear Medicine Clinical SPECT Symposium,* Sept 22-23, Washington, DC. pp: 98-100.

Lewis, H. W. 1950. Multiple Scattering in an Infinite Medium. *Physical Review 78(5): 526-529.*

Lockwood, G. J., G. H. Miller and J. H. Halbleib. 1980. *Calorimetric Measurement of Electron Energy Deposition in Extended Media..Theory vs Experiment.* SAND79-0414.

Loevinger, R. 1956. The Dosimetry of Beta Sources in Tissue. The Point-Source Function. *Radiology 66: 55-62.*

Loevinger, R. 1954. The Dosimetry of Beta Radiations. *Radiology 62: 74-82.*

Loevinger, R. 1953. Extrapolation Chamber for the Measurement of Beta Sources. *Review of Scientific Instruments 24(10): 907-914.*

Loevinger, R. 1950. Distribution of Absorbed Energy around a Point Source of ß Radiation. *Science 112: 530-531.*

Mackie, T. R. 1990. Applications of the Monte Carlo Method in Radiotherapy. Chap 6 In *The Dosimetry of Ionizing Radiation, Vol. III.* eds. K. R. Kase, B. E. Bjarngard and F. H. Attix. San Diego, California: Academic Press, Inc.

McCracken, D. D. 1955. The Monte Carlo Method. *Science 192: 90-96.*

McGervey, J. D. 1983. *Introduction to Modern Physics.* New York: Academic Press, Inc.

McGregor, M. 1988. Dosimetry in Cancer Treatment Research. *Health Physics Society Newsletter 16(7): 4.*

Mladjenovic, M. 1973. *Radioisotope and Radiation Physics, An Introduction.* New York: Academic Press.

Mott, N. F. 1931. On the influence of radiative forces on the scattering of electrons. *Proceedings of the Cambridge Philosophical Society 27: 255-267.*

Mott, N. F. and H. S. W. Massey. 1949. *The Theory of Atomic Collisions.* Oxford: The Claredon Press.

Nelson, W. R., H. Hirayama and D. W. O. Rogers. 1985. *The EGS4 Code System.* SLAC-265. Dec 1985. Stanford University, Stanford, California: Stanford Linear Accelerator.

Nieminen, R. M. 1988. Stopping Power for Low-Energy Electrons. *Scanning Microscopy 2(4): 1917-1926.*

O'Brien, K. 1974. The Subcutaneous Beta-ray Dose Rate from Fission Products Deposited on the Skin. *Health Physics 26: 122-127.*

O'Brien, K., S. Sampson, R. Sanna and J. E. McLaughlin. 1964. The Application of "One-Group" Transport Theory to ß-Ray Transport. *Nuclear Science and Engineering 18: 90-96.*

Osanov, D. P. and Y. N. Podsevalov. 1971. Dose Function for a Plane Infinite Thin Source. *Soviet Atomic Energy 31: 1025-1027.*

Pook, E. A. and T. M. Francis. 1975. Conversion of Beta-Ray Dose Rates Measured in Air to Dose Rates in Skin. (Letter to the Editor) *Physics in Medicine and Biology 20: 147-149.*

Prestwich, W. V. 1991. private communication.

Prestwich, W. V. 1990. private communication.

Prestwich, W. V., J. Nunes and C. S. Kwok. 1989. Beta Dose Point Kernels for Radionuclides of Potential Use in Radioimmunotherapy. *Journal of Nuclear Medicine 30(6): 1036-1046.*

Prestwich, W. V. 1986. private communication.

Radzievsky, G. B. and N. A. Komarov. 1982. Dose Distributions from ß-radiation in Heterogeneous Media: "Two-Group" Method of Calculation. *Journal of Applied Radiation and Isotopes 33: 733-743.*

Radzievsky, G. B., N. A. Komarov, A. N. Glagolev and E. R. Shepeleva. 1980. Distributions of Absorbed Energy from ß-Radiation in Homogeneous Media. *International Journal of Applied Radiation and Isotopes 31: 431-436.*

Rogers, D. W. O. 1984. Low Energy Electron Transport with EGS. *Nuclear Instruments and Methods in Physics Research 227: 535-548.*

Rogers, D. W. O. and A. F. Bielajew. 1990. Monte Carlo Techniques of Electron and Photon Transport for Radiation Dosimetry. Chap 5 In *The Dosimetry of Ionizing Radiation, Vol. III.* eds. K. R. Kase, B. E. Bjarngard and F. H. Attix. New York: Academic Press. pp: 427-540.

Rogers, D. W. O. and A. F. Bielajew. 1988. A Comparison of EGS4 and ETRAN. Chap 14 In *Monte Carlo Transport of Electrons and Photons. Proceedings of the International School of Radiation Damage and Protection. Eighth Course: Monte Carlo Transport of Electrons and Photons Below 50MeV,* Sept 24 - Oct 3, 1987, Enrice, Sicily, Italy. New York: Plenum Press.

Rossi, B. 1952. *High Energy Particles.* New York: Prentice-Hall, Inc.

Roy, R. R. and R. D. Reed. 1968. *Interactions of Photons and Leptons with Matter.* New York: Academic Press.

Rutherford, E. 1911. The Scattering of α and β Particles by Matter and the Structure of the Atom. *Philosophical Magazine 20: 669-688.*

Sandison, G. A. and L. S. Papiez. 1990. Dose Computation Applications of the Electron Loss Model. *Physics in Medicine and Biology 35(7): 979-997.*

Schneider, D. O. and D. V. Cormack. 1959. Monte Carlo Calculations of Electron Energy Loss. *Radiation Research 11: 418-429.*

Scott, W. T. 1963. Reviews of Modern Physics. The Theory of Small-Angle Multiple Scattering of Fast Charged Particles. *The American Physical Society 35(2): 231.*

Seliger, H. H. 1952. The Backscattering of Positrons and Electrons. *Physical Review 88(2): 408-412.*

Seltzer, S. M. and M. J. Berger. 1987. Energy Deposition by Electron, Bremsstrahlung and Co Gamma-Ray Beams in Multi-Layer Media. *Applied Radiation and Isotopes 38(5): 349-364.*

Sharkey, R. M., R. D. Blumenthal, H. J. Hansen and D. M. Goldenberg. 1990. Biological Considerations for Radioimmunotherapy. *Cancer Research (supplement) 50: 964s-969s.*

Sharma, K. K. and M. Singh. 1979. Variation of Beta Ray Backscattering with Target Thickness. *Journal of Applied Physics 50(3): 1529-1532.*

Sherbini, S. and S. W. Porter. 1983. *A Review of the Current Deficiencies in Personnel Beta Dosimetry, with Recommendations.* NUREG/CR-3296, U. S. Regulatory Commission, Washington, D. C.

Simpkin, D. J. and T. R. Mackie. 1990. EGS4 Monte Carlo Determination of the beta dose kernel in water. *Medical Physics 17(2): 179-186.*

Snyman, G. C. and C. G. Clayton. 1963. Some Observations on the Scattering of ß-Particles by Thick Absorbers. *International Journal of Applied Radiation and Isotopes 14: 183-188.*

Spencer, L. V. 1959. *Energy Dissipation of Fast Electrons.* National Bureau of Standards Monograph 1, Sept 10th 1959.

Spencer, L. V. 1955. Theory of Electron Penetration. *Physical Review 98(6): 1597-1615.*

Spiers, F. W. 1949. The Influence of Energy Absorption and Electron Range on Dosage in Irradiated Bone. *British Journal of Radiology 22: 521-533.*

Storchi, P. R. M. and H. Huizenga. 1989. On a Numerical Approach of the Pencil Beam Model. *Physics in Medicine and Biology 30(5): 467-473.*

van der Zwan, L. and K. W. Geiger. 1986. *The β⁻ Calibration Facility at the National Research Council of Canada.* Report No. PIRS-0093.

Vaughan, A. T. M., P. Anderson, P. W. Dykes, C. E. Chapman and A. R. Bradwell. 1987. Limitations to the Killing of Tumours using Radiolabelled Antibodies. *British Journal of Radiology 60: 567-578.*

Werner, B. L., C. S. Kwok and I. J. Das. 1988. Dose Distributions in Regions Containing Beta Sources: Large Spherical Source Regions in a Homogeneous Medium. *Medical Physics 15(3): 358-363.*

Werner, B. L. 1985. The Perturbation of Electron Beam Dose Distributions at Medium Interfaces. *Medical Physics 12(6): 754-763.*

Wessels, B. W. 1990. Current Status of Animal Radioimmunotherapy. *Cancer Research(supplement) 50: 970s-973s.*

White, D. R. 1978. Tissue Substitutes in Experimental Radiation Physics. *Medical Physics 5(6): 467-479.*

Yu, Sui-Ki. 1989. *Dosimetry of Electron Sources Near Planar Tissue Interfaces.* MSc Project Report. McMaster University, Hamilton, Ontario.

Zerby, C. D and F. L. Keller. 1967. Electron Transport Theory, Calculations and Experiment. *Nuclear Science and Engineering 27: 190-218.*